Analysis of shear-wave response to fractures: A full waveform study of microseismic fracture imaging

Baban Mustafa Yousef

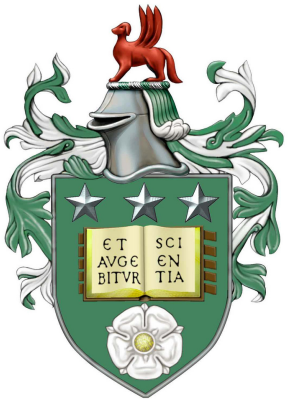

Submitted in accordance with the requirements for the degree of

Doctor of Philosophy

The University of Leeds

School of Earth and Environment

September 2016

Declaration

The candidate confirms that the work submitted is his own, except where work which has formed part of a jointly authored publication has been included. The contribution of the candidate and the other authors to this work has been explicitly indicated below. The candidate confirms that appropriate credit has been given within the thesis where reference has been made to the work of others.

Some parts of the work presented in this thesis have been published in the following articles:

Journal articles

Yousef, B. M., and Angus, D. A. (2016). When do fractured media become seismically anisotropic? some implications on quantifying fracture properties. *Earth and Planetary Science Letters, 444, 150159. 2016.*

Yousef, B. M., and Angus, D. A. (2016). Analysis of fracture induced scattering of microseismic shear-waves. *Studia Geophysica et Geodaetica, Submitted.*

Expanded abstracts

Yousef, B., Angus, D., Hildyard, M., Verdon, J., and Perry, M. (2013). Full waveform model validation of microseismic shear-wave splitting fracture parameter inversion. *In Second EAGE Workshop on Naturally Fractured Reservoirs.*

Yousef, B. M., Angus, D. A., Hildyard, M. W., Verdon, J. P., and Perry, M. (2014). Measuring shear-wave splitting using seismic anisotropy. *In 76th EAGE Conference and Exhibition.*

Acknowledgments

This research is the result of collaboration with many colleagues at Leeds University and I may not be able to list every single person's name. Without them this PhD research work wouldn't have come to a successful end.

First of all, I must express my great gratitude to my excellent supervisor Doug Angus for his valuable time, patience, guidance and constant encouragement helping and enthusing me through the most difficult moments of this research. I have benefited a lot from his knowledge and experience not only in academic research but also the rest of life. I have received inspiration from each academic discussion with him and he has been very supportive and patient, as well as helpful in improving the writing quality of my thesis and scientific papers. My thanks to him for keeping my research in the right direction.

Also I am very grateful to my co-supervisor Mark Hildyard for his supervision and his helpful suggestions, invaluable discussions, continual instruction and sound criticism in the use of the FD algorithm WAVE. Through this process he has inspired me and my research by encouraging and guiding me on how to best accomplish tasks and remedy any deficiencies. I would like to thank the Institute of Applied Geoscience members for help they have given me. I am very grateful for the enjoyable life in Leeds with office mates and friends, Yanxiao He, Ekbal Hussain, David Bekaert, Taher Rabizadeh, Javed Haneef, Tom Lynch, David Price, Andrea Vidal Dura, Pilar Ramírz García, Lisa Roach, Alif Mohd Jelani, and Hannah Bentham. Thanks for their help and advice. I am thankful to James Verdon for sponsoring my visit to Bristol University for two days and helping me learn SHEBA and INSAFF.

I would also like to acknowledge Kurdistan regional government for their financial support of my PhD study. I wish to thank the SEE IT staff, especially Richard Rigby for his time-and-time-again help with my computer issues.

I would like to give my most sincere thanks to my wife, as without her continuous care, emotional support and constant encouragement over the entire stages of my thesis, I wouldn't complete my PhD.

I would like to give my most sincere to my parents. Doing a PhD can be stressful at times but knowing there is someone who has your back at all times makes everything so much easier. Without your support, this thesis would simply not exist.

This thesis is dedicated to those who covered me with their sincere and endless love:

my parents, wife and daughter.

Abstract

Naturally fractured reservoirs are playing an important role in exploration geophysics. As fractures can control the permeability and pore pressure of the reservoir, it is crucial to study the fracture characterisation. The thesis is mainly including the estimated seismic anisotropy from shear-wave splitting (SWS) observations and the study of the S-wave scattering characteristics of fractured media as well. A suite of synthetic fractured media with a broad range of fracture parameters is generated. The range of fracture parameters was chosen based on the numerical simulation and also where there is a lack of research in the literature.

An automated approach of SWS analysis is performed which is suitable to cope with large volume of SWS measurements. The SWS analysis was automatically performed using cross-correlation and eigenvalue minimisation methods by using a cluster analysis technique. The automated quality measuring is obtained from the misfit calculation of both methods to estimate SWS measurements. This method leads to detect 7% and 4% high quality SWS of 6624 SWS measurements for the single and the double fracture sets models, respectively. This method is crucially beneficial as it reduces the number of inspection of SWS measurements. The SWS measurements are obtained from the receivers distribution at near-surface as well as four boreholes. The parametrisation study of SWS shows that the number of models with good SWS decreases with increasing fracture length size. Moreover, by increasing normal and tangential compliance by one order of magnitude while keeping compliance ratio constant leads to models with good SWS in most cases.

The simulation of synthetic microseismic event provides suitable S-wave sources that result in SWS measurements to image fracture parameters (i.e., fracture density and orientation). The δV_S, the difference between the fast and slow shear-waves velocities along the raypath, varied between 0% and 14% which is influenced by the

fracture density. As the discrete fractures are superimposed in an isotropic medium, so the anisotropy is interpreted in terms of the fracture strike and fracture density by implementing an inversion method based on the effective medium theory (EMT). The inversion was performed for a single fracture set (i.e., HTI) and double orthogonal fracture sets (i.e., orthorhombic symmetry system). The fracture strike inversion is more constrained than the fracture density due to the limited ray coverage and inversion algorithm assumptions.

In the subsequent part of the thesis, I confirm the general scale-dependence of seismic anisotropy and provide new results specific to SWS. I find that SWS develops under conditions when the ratio of wavelength to fracture size (λ_S/d) is greater than 3, where Rayleigh scattering from coherent fractures leads to an effective anisotropy such that effective medium model (EMM) theory is qualitatively valid. When $1 < \lambda_S/d < 3$ there is a transition from Rayleigh to Mie scattering, where no effective anisotropy develops and hence the SWS measurements are unstable. When $\lambda_S/d < 1$ I observe geometric scattering and begin to see behaviour similar to transverse isotropy. I find that seismic anisotropy is more sensitive to fracture density than fracture compliance ratio. More importantly, I observe that the transition from scattering to an effective anisotropic regime occurs over a propagation distance between 1 to 2 wavelengths depending on the fracture density and compliance ratio.

Finally, I use different methods including the RMS envelope analysis, shear-wave polarisation distortion, differential attenuation analysis and peak frequency shifting to assess the scattering behaviour of parametrised models in which the propagation direction is either normal or parallel to the fracture surfaces. The quantitative measures show strong observable deviations for fractures size on the order of or greater than the dominant seismic wavelength within the Mie and geometric scattering regime for both propagation normal and parallel to fracture strike. The results suggest that strong

scattering is symptomatic of fractures having size on the same order of the probing seismic wave.

Contents

List of Figures

List of Tables

List of Symbols and abbreviations

Symbols

a	Fracture size	m
α	Fracture strike	$^\circ$
C, C_{ijkl}	Stiffness tensor	Pa
H	Average fracture spacing	m
D	Distance	m
ϵ	Fracture density	number/m^3
$\mathbb{Q}$	Shear-wave splitting quality	dimensionless
dh	Grid spacing	m
V_P	Compressional-wave	m/s
V_S	Shear-wave	m/s
λ_P	P-wave wavelength	m
λ_S	S-wave wavelength	m
S_1	Fast S-wave	m/s
S_2	Slow S-wave	m/s
δt	Delay time	s
δV_S	Percentage difference between fast and slow shear waves	dimensionless
ϕ	S_1 Polarisation direction	$^\circ$
B_N, B_T	Normal and tangential effective media compliances of fracture sets	Pa^{-1}
Z_N, Z_T	Normal and tangential individual fracture compliances	mPa^{-1}
Q^{-1}	Attenuation	dB (or dB/cycle)
t_q	Envelope width time	s
$\overline{t_q}$	Normalised envelope width time	s
f	Frequency	Hz
$\chi_{Parallel}$	RMS amplitude ration for the *Parallel* model	dimensionless
χ_{Normal}	RMS amplitude ration for the *Normal* model	dimensionless
$\varepsilon, \gamma, \delta$	Thomson's parameters	dimensionless
ε_{kl}	Strain	dimensionless
σ_{ij}	Stress	Pa
μ, λ	Lamé parameter	Pa
k	Wavenumber	m^{-1}
ν	Poisson's ratio	dimensionless
E	Young's modulus	Pa
θ	Arrival azimuth	$^\circ$
β	Arrival inclination	$^\circ$

Abbreviations

RMS	Root-Mean-Square
PSD	Power Spectral Density
LWA	Long Wave Approximation
HFA	High-Frequency Approximation
SWS	Shear-wave splitting
VSP	Vertical Seismic Profile
VTI	Vertical transverse isotropy
HTI	Horizontal transverse isotropy
XC	Cross-correlation method
EV	Eigenvalue method
LS	Linear slip

Chapter 1

Introduction

In this chapter I provide a general overview of the thesis. First I discuss the general ideas and concepts related to fracture characterisation, seismic modelling in fractured media and fracture detection using shear wave data. Next I provide the aims and objectives of this study. Finally, I summarise the thesis structure as well as the software and programs used.

1.1 Background and motivation

Natural fractures in reservoirs play an important role in the geomechanical and fluid-flow behaviour of the subsurface. Thus, fracture characterisation in general and knowledge of the orientation and density of fractures specifically is important in petroleum reservoir production to enhance hydrocarbon recovery and hence increase economic performance of naturally fractured reservoirs. Fractures have a significant influence on the multi-

physical response of hydrocarbon reservoirs, yet they are still poorly understood and their properties largely underestimated in situ. The investigation of natural fractures should start from an early stage of production, in terms of effectively locating wells and during the well-construction stage (e.g., Bratton et al., 2006).

Seismic anisotropy is a useful attribute for characterisation and detection of fabric within most reservoir rocks. There are different length-scales of rock fabric that lead to seismic anisotropy, such as mineral alignment (e.g., Valcke et al., 2006), grain-scale fabric (e.g., Hall et al., 2008; Verdon et al., 2008; Angus et al., 2009), large scale sedimentary layers (e.g., Bacus,1962) and presence of aligned fracture sets (e.g., Hudson, 1980, 1981). Furthermore, depending on the wavelength of the seismic signal and the length-scale of elastic heterogeneity, an elastic medium may or may not appear seismically anisotropic (e.g., Winterstein, 1990). A set of cracks or fractures may render a rock seismically anisotropic if they are preferentially aligned parallel to the maximum primary horizontal stress. The most common anisotropic mechanisms in hydrocarbon reservoir are horizontally aligned fabric, consisting of a combination of sedimentary layering, grain-scale and mineral alignment. Such layering leads to a vertically transverse isotropic symmetry system. Another source of anisotropy displays coherent vertical alignment due to the presence of subvertical fracture sets.

Seismic velocity is one of the key seismic attributes, and in the presence of coherent seismic heterogeneity shows directional dependence. In the case of fractures, waves propagate faster parallel to the fracture surface than those propagating normal to the fracture surface. The measurement of azimuthal velocity variation of P-waves from travel-times was first used to confirm the presence of seismic anisotropy in the Earth (Hess, 1964). There are other key seismic attributes, however, such as amplitude and seismic polarisation. Several methods have been developed to analyse seismic reflection data, vertical seismic profile (VSP) data and cross-hole data. For instance, amplitude

variation with offset (AVO) as well as amplitude variation with offset and azimuth (AVOA) have been employed to characterise fractured media (e.g., Lynn et al., 1996; Sayers & Rickett, 1997; Hall & Kendall, 2000; Lynn et al., 2003). Interval normal moveout P-wave analysis is another attribute to image fractures (e.g., Tsvankin, 1997; Bakulin et al., 2000).

Similar to P-waves, S-waves can be affected by a set of aligned fractures. For instance, the S-wave AVOA technique can be utilised to characterise fracture orientation (e.g., Hall & Kendall, 2000). The sensitivity of S-waves can be utilised as a means to characterise the fracture strike and density and also the fracture infill (Kendall & Kendall, 1996). Using both P- and S-waves in the AVOA analysis, Lynn et al. (1995) provide a more robust method to determine fracture parameters.

Willis et al. (2003, 2006) introduce a method in which the interval transfer function of the upper and bottom interface of a naturally fractured reservoir is calculated based on the scattered wave field. Scattered coda energy analysis is capable of constraining the fracture density and fracture orientation as well as fracture spacing. Moreover, recent anisotropic attenuation analysis has been developed, such as for small-scale oriented fractures (e.g., Rathore et al., 1995; Chichinina et al., 2006). Chichinina et al. (2006) utilise the azimuthal variation of attenuation with offset (QVOA) as a means to characterise fractures and were able to robustly constrain fracture orientation of saturated fractures. In a previous study by Hall & Kendall (2000), there was ambiguity in the estimated fracture orientation due to the trade-off between fracture infill material and crack aspect ratio.

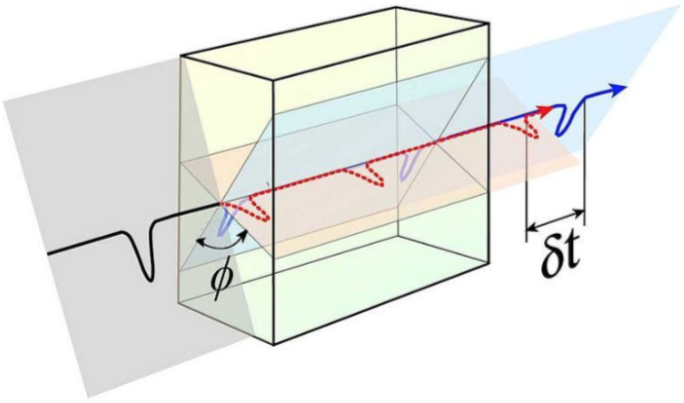

Figure 1.1: Schematic illustration of shear-wave splitting in a fractured medium. The delay between fast and slow S-waves δt and the polarisation direction of the fast S-wave is ϕ. Figure is from Wikipedia.)

1.2 Seismic anisotropy and shear-wave splitting

One of the best diagnostic wave phenomenon of anisotropic media within the Earth is shear-wave splitting (SWS). SWS occurs when a shear wave encounters an anisotropic medium; the shear-wave is split into two perpendicular polarised shear-wave components with different wave speeds (e.g., Crampin, 1981; Savage, 1999). The polarisation and delay time will persevere outside the anisotropic region. Figure 1.1 illustrates a schematic of shear-wave splitting in a anisotropic medium, where the S-wave splits into two S-waves with a time delay. The two SWS parameters are the fast polarisation direction (ϕ) and the delay time between fast and slow S-waves (δt). The δt parameter is a measure of the anisotropy strength of the medium along the raypath. Usually δt is normalised by the raypath length yielding an estimate of the percentage difference between the fast and slow shear-wave velocities (δV_S). In a simple case, the ϕ parameter corresponds to the fracture strike if the S-wave propagates subvertically.

SWS measurements have been extensively used in seismological studies: in studies of deformation in the deep-mantle (e.g., Lay et al., 1998; Kendall & Silver, 1998),

upper-mantle (e.g., Silver & Chan, 1988; Savage, 1999) and recently in more applied seismic settings such as in the exploitation of petroleum reservoirs (i.e, microseismic monitoring). In the literature, SWS measurements have been presented in numerous well-established techniques (e.g., Ando & Ishikawa, 1980; Vidale, 1986; Silver & Chan, 1991; Menke & Levin, 2003; Wuestefeld et al., 2010). The technique of Silver & Chan (1991) is likely the most prevalent approach. This technique is based on a grid search over the two SWS parameters (ϕ and δt). The estimation of SWS parameters is performed by two complementary approaches: attempts to minimise the energy on the transverse component or by minimising the second eigenvalue of the particle motion covariance matrix (λ_2). Wuestefeld et al. (2010) found that minimising λ_2/λ_1 leads to the most efficient and robust results for the estimation of SWS parameters in this approach.

1.3 Shear-wave splitting inversion

The interpretation of SWS results may be non-unique or require an oversimplification of the subsurface, such as assuming that the fast polarisation direction represents the actual strike rather than an average or effective fracture strike, and also that δV_S is related to fracture density (Verdon et al., 2009). The prediction of the SWS pair (δt, ϕ) is dependent on the raypath orientation relative to the major fracture orientation (Verdon et al., 2009). In addition, the presence of fractures in sedimentary layers increases the complexity of the overall anisotropic elasticity of the medium. Thus it is important to take into account the relative contribution of each cause.

There have been several attempts in the past to invert SWS measurements for fracture properties and/or anisotropy parameters from various data. For instance, Horne & MacBeth (1994) used a genetic algorithm to invert SWS observations for fracture

parameters from VSP datasets from the Conoco test site in Oklahoma. Šílenỳ & Plomerová (1996) inverted global SWS observations recorded in southern Sweden to characterise the symmetry axis and the thickness of upper-mantle. Teanby et al. (2004b) inverted SWS on microseismic data at the Valhal field in the North Sea. In their study, the elastic constants were calculated using the effective medium theory of Schoenberg & Sayers (1995) and also the approach of Hall & Kendall (2000) to allow the inclusion of multiple crack sets. They subsequently compute synthetic seismograms using ray tracing and Maslov asymptotic theory (Guest & Kendall, 1993), where the synthetic data were processed similar to the real data to estimate ϕ and δt following the calculation of misfit (i.e., the comparison of synthetic with real data). Yang et al. (2005) developed an inversion algorithm to tackle the inherent non-linearity in the inversion and applied their inversion scheme on SWS measurements from Geysers geothermal reservoir in California. Rial et al. (2005) inverted SWS observations from natural and induced geothermal reservoirs for fracture parameters such as strike, dip, aspect ratio, density, and fluid-content. Verdon et al. (2009) developed an inversion approach that can be used for media containing fractures and sedimentary layering and allows for non-vertically propagating raypaths. To assess the sensitivity of the inversion approach to raypath orientation, Verdon et al. (2009) construct a suite of synthetic models based on effective medium theory, and conclude that despite the source-receiver geometry, the strike is most accurately constrained.

In the previous discussion of SWS measurement inversion, it was assumed that the anisotropic parameters are uniform along the raypath in the anisotropic region between source and receiver. Wookey (2012) proposed an advanced inversion algorithm using a non-linear neighbourhood algorithm to determine the parameter space specified by an anisotropic model incorporating a number of non-uniform domains. The algorithm allows quantification of spatially varying model spaces by determination of non-uniform

anisotropic models.

1.4 Aims and objectives of the thesis

1.4.1 Aims and objectives

Recent research has focused on the integration of geomechanics, fluid-flow and seismic modelling to characterize fractured reservoirs. This requires knowledge of the crack or fracture properties (e.g., compliances) on both the geomechanical and seismological scale. However, populating the geomechanical and/or seismic model with crack and fracture properties is based primarily on laboratory core data, which are several orders smaller in length scale than observed in fractured reservoirs. Also, there is scarce field-scale measurements. Properties such as fracture compliance (and thereby the compliance ratio) influence the deformation behaviour and hence the fluid pathways within fractured reservoirs. Effective medium theories have been implemented extensively to model fractured media. However, effective medium models (EMMs) are limited by the model assumptions where as the alternative discrete fracture model (DFM) approach makes no restriction on the fracture size relative to seismic wavelength. As such, in this thesis I study the feasibility of measuring and inverting for fracture properties using EMM using finite-difference (FD) synthetic waveform modelling of wave propagation through a DFM. The aim of this PhD thesis is to:

* Study whether observations of seismic anisotropy from S-waves can constrain fracture properties. To do this, I investigate the feasibility of using SWS analysis to invert for fracture density and fracture strike quantitatively for different fracture properties.

* Calibrate fracture compliance against fracture size from numerical parametrisation

of discrete fracture modelling.

* Examine under what conditions fractured media become seismically anisotropic. To do this, I study the development of SWS as a shear wave propagates through a suite of discrete fractured models.

* Integrate the analysis of scattering characteristics of S-waves for a range of scattering regimes and study the implication of different S-wave polarisations with propagation parallel and normal to the fracture planes.

The objectives of this project are threefold: (1) perform a parametric study using full waveform FD synthetics to model seismic anisotropy in fractured media and examine the relationship between seismic anisotropy measurements and fracture properties, (2) examine the heterogeneity-to-anisotropy transition of fractured media over a range of scattering regimes, encompassing scales where EMM and DFM are valid, and (3) examine the scattering characteristics of S-waves in fractured media by observing the widening effect and frequency spectral ratio.

The outcomes from this study will provide quantitative bounds on the feasibility and errors in inverting for fracture strike and density of discrete fractured media using an inversion algorithm based on effective medium theory. In addition, provide an quantitative criteria to distinguish fractured media in transition from heterogeneity to anisotropy. Furthermore, study the quantitative behaviour of S-wave scattering from fractured media in relation to the specific S-wave polarisation and orientation.

1.5 Time frame and work content

The research in this PhD project was completed within 4 years, starting in October 2012. Table 1.1 summarises the time frame and work content for this PhD project as a

reference.

1.6 Thesis structure

There are three principal topics in this thesis: (1) assessing the inversion of fracture parameters for discrete fractured media, (2) study when heterogeneous fractured media become seismically anisotropic, and (3) examine the scattering characteristics of S-wave from discrete fractured media. The first topic involves generating an ensemble of discrete fractured media with different fracture size, fracture compliance, fracture density and fracture compliance ratio, where the synthetic data are inverted for fracture properties using SWS measurements from ensemble of models. The second topic is dedicated to understanding under what conditions a heterogeneous discrete fractured medium becomes seismically anisotropic. Finally, the third topic focuses on the scattering characteristics of S-waves using different analysis techniques. The thesis is composed of eight chapters, where this chapter discusses the motivation and objectives behind this PhD thesis. The remainder of the thesis is organized as discussed below and shown schematically in Figure 1.2.

Chapter 2 reviews the basic principles of the classification of naturally fractured reservoirs based on the definition of Narr et al. (2006) and provide a general definition of cracks and fractures used in this study. Also, I review the publications covering the background theories involved in this study to assess what has been done and provide motivation for my research.

In Chapter 3, I review the basic theories involved in my thesis. I introduce the concept of finite-difference modelling of seismic waves and give a detailed explanation of the algorithm WAVE that I implement to generate the synthetic waveforms. I discuss the seismic moment tensor as a microseismic source representation in the FD model. I

Project course	Course of work	Term
Literature review	• Classifying fractures • Review the theories in FD and shear-wave splitting • Review effective medium model versus discrete fracture medium • Fracture compliance	6 months
Seismic modelling of discrete fracture medium (DFM) using both dilatational point source and moment tensor (MT) source types	• Theory of finite-difference • WAVE algorithm • Theory of seismic anisotropy • Shear-wave splitting and its parameters	10 months
Inverting fracture strike and density	• Model parameters • SWS for single and double fracture sets • Inversion results	8 months
Parametrisation the SWS measurements	• Model parametrisation • Numerical FD model • Anisotropy vs heterogeneity	8 months
Scattering characteristics of shear-wave response in DFM	• Model parameters • Analysis of SWS-wave coda • RMS envelope analysis • Distortion of S-wave polarisation • Differential attenuation analysis	7 months
Thesis writing	Eight chapters are presented in this PhD project	9 months

Table 1.1: Time frame and work content for this PhD project.

review seismic wave propagation in anisotropic media with different symmetry systems, as well as review effective and discrete fractured media representation. Finally, I present the workflows used in the shear-wave splitting analysis and the inversion algorithm for fracture characterisation.

In Chapter 4, I study the feasibility of inverting for fracture properties using S-wave data. The fractured media are modelled for a broad range of fracture size, normal and tangential compliances, density and normal to tangential compliance ratio. I use the concept of seismic anisotropy to image subsurface fractures using an inversion algorithm based on effective medium theory. The findings from this chapter have been presented at 76th EAGE Conference and Exhibition 2014 in Yousef et al. (2014).

In Chapter 5, I provide some insight into several fundamental questions: Under what conditions do fractured media become seismically anisotropic? How do we define the transition region from scattering to anisotropy? How should we consider this transition in our quantitative estimates of fracture properties? To answer these questions, I study the development of SWS since wave propagates through a suite of fractured media using the DFM approach. I explore the range of fracture properties that result in effective anisotropy using heterogeneous yet coherent discontinuities by simulating the interaction of seismic wave with fractures. This chapter is a more detailed expansion of the work presented in Yousef & Angus (2016).

In Chapter 6, I examine the scattering characteristics of shear-waves for a range of scattering regimes. I perform qualitative and quantitative analysis of shear-wave coda energy for a different initial shear-wave polarisations and propagation paths normal and parallel to the fracture planes. The envelope broadening of shear-waves due to the scattering is analysed by implementation of root-mean-square envelope analysis. Next, I carry out differential attenuation analysis of shear-waves to compare my results with Hudson (1981) and Carter & Kendall (2006). Finally, I investigate the frequency

content of the dataset.

Chapter 7 discusses the relevance of the results within this thesis and Chapter 8, summarizes the main conclusions and presents a summary of recommendations for future research.

The appendices begin with a description of the software and programs adopted in the thesis. The appendices describe the detail effective elastic constants of fractured media based on the Hudson's model as well as Liu's model. In addition, the inversion results and their errors for both single and double fracture sets are listed in Appendix D. Finally, the calculations of excess compliance tensors based on the linear slip EMM using six different means are written.

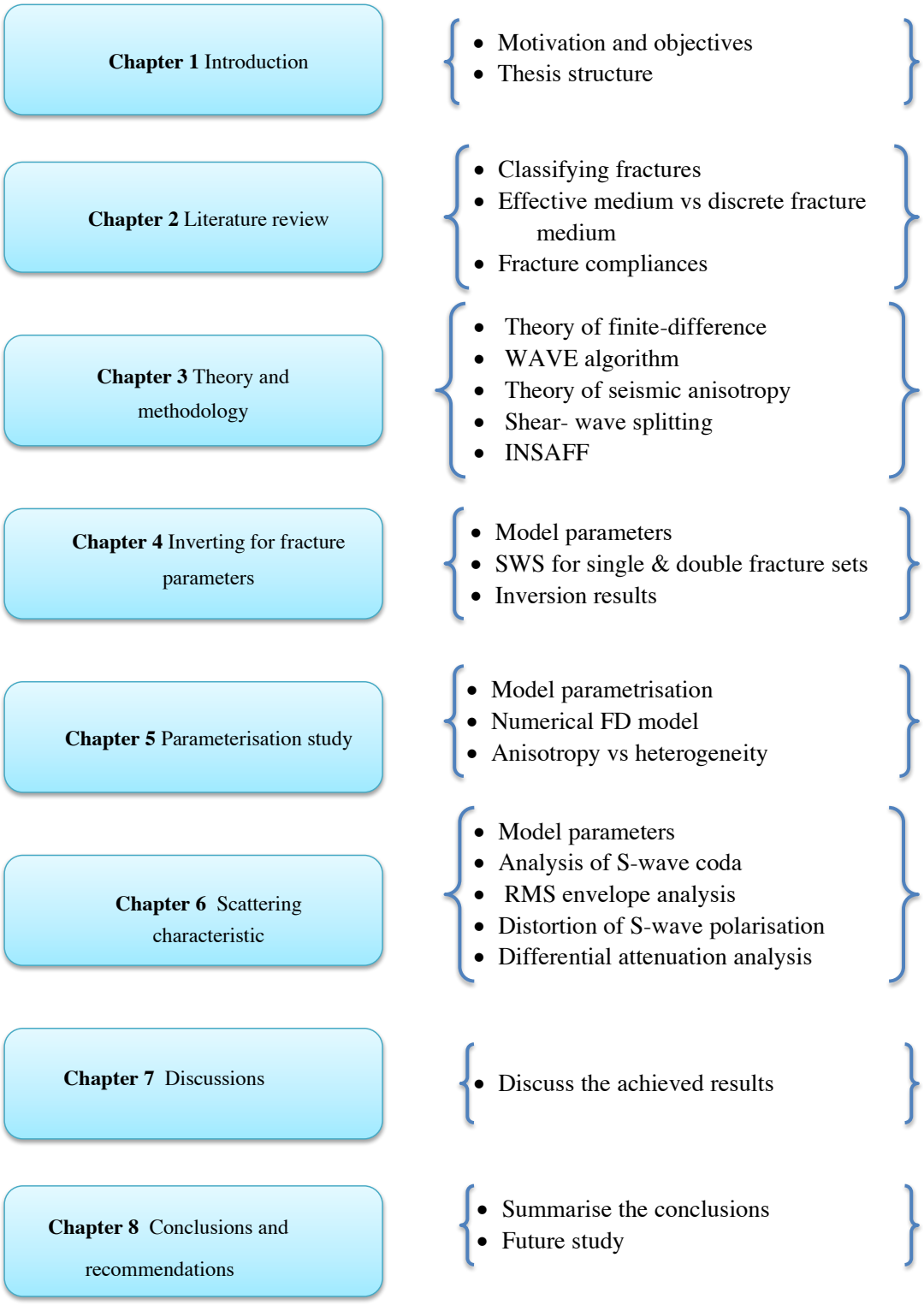

Figure 1.2: Thesis structure and chapter contents.

Chapter 2

Natural fractures and their modelling

2.1 Classification of naturally fractured media

Fractures are ubiquitous structural features in the Earth's upper crust. They are evident at most outcrops and it is likely that most reservoirs contain some natural fractures (see Figure 2.1). They are common in conventional reservoirs such as carbonate and unconventional reservoirs such as tight gas and shale gas (Engelder et al., 2009). Fractures can affect different aspects of reservoir management, including drilling, well completion, well placement, data collection and enhanced oil recovery (EOR) strategy. Therefore, the early recognition of fractures leads to better field development plans of recoverable reserves: as well, fractures play a critical factor on EOR strategy of naturally fractured reservoirs.

There are different terminologies for fractures, but in this thesis the terminology I use is based on Narr et al. (2006) who define a fracture as a discontinuity caused by

(a) Canyon Lake, Texas, USA)

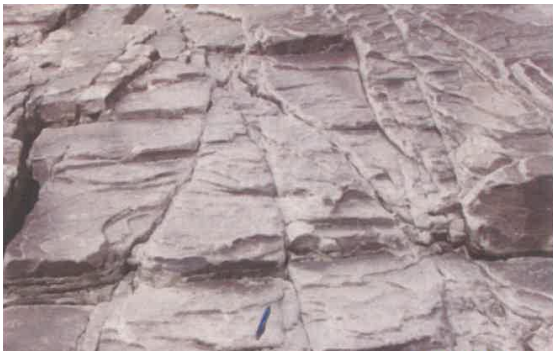

(b) tight gas sand (Piceance Basin, Colorado, USA)

(c) shale gas (Marcellus formation at Appalachian Basin, USA)

Figure 2.1: Typical fracture outcrops in hydrocarbon reservoirs. Figure from Liu & Martinez (2012).

brittle failure due to deformation or physical diagenesis. Fracture is a general term that comprises various natural and induced features including crack, joint, fault and vein (Narr et al., 2006). There are different fracture types based on the force orientation during failure, such as joints and faults in fractured sandstones as well as joints, faults and veins in fractured carbonates. Furthermore, fluid-flow properties vary according to the type of fractures. Therefore, it is essential to properly classify fracture types to predict fracture orientation as a whole and therefore planning of optimum drilling direction.

Joints are natural fractures caused by natural tensile forces and thus are extensional opening mode cracks. The walls of a joint are pulled away from each other during

formation (see Figure 2.2). Thus, there is no shearing displacement parallel to the fracture walls. Due to the lack of shear displacement in the joint formation, joints can be called cracks or tensile fractures (Van der Pluijm & Marshak, 2005). In stratified rocks, joints are typically almost normal to layering and commonly confined to boundaries between stratified layers or discontinuities in rocks. A joint set consists of a collection of parallel joints approximately equally spaced. Joints can have an impact on fluid flow in a fractured reservoir, for example joint spacing can influence the effective drainage of the rock matrix and permeability. Fracture height can influence gravity-induced drainage from a reservoir, where tall joints are more effective than short joints (Narr et al., 2006).

Faults, on the other hand, experience some shear failure, where shear displacement has occurred. Faults can enhance the flow of fluid through rocks, or they can act as barrier to fluid flow resulting in the compartmentalisation of petroleum reservoirs. Faults can play paradoxically in fluid flow; depending on their openness and composition within the fault zone they may either create porous storage or permeable pathway in reservoir, which influence hydrocarbon accumulation and migration. The orientation of both joints and faults are controlled mainly by the Earth's stress field, which varies in direction and magnitude with location (Nelson, 2001; Narr et al., 2006; Fossen, 2010). In fact, the orientation of faults depends on the tectonic setting and is less influenced by bedding, whereas for joints bedding plays a significant role (Narr et al., 2006).

2.1.1 Fracture characterisations

Is is impractical to provide a detailed scan of all fractures within a reservoir. However, fracture network characterisations can be estimated through a range of measurements. Fracture characterisation can be examined directly from geological aspects; such as surface outcrops and well logging observations. Surface outcrop observations can assist

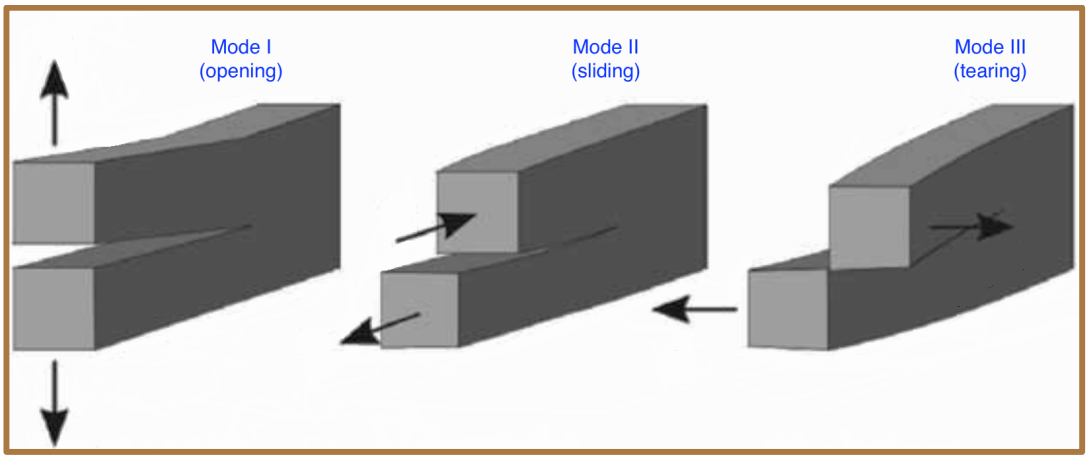

Figure 2.2: Various modes of fractures: model I is an extensional opening fracture, model II is a sliding and model III is a tearing fracture. Model II and III are shear movements. Figure is modified from Liu & Martinez (2012).

in understanding the fracture evolution process which is still with large uncertainty. In contrast, well-log imaging techniques can provide detailed information of fracture properties (i.e, fracture orientation, density, bedding, permeability and fluid content) but has limited sampling of the reservoir volume and is dependent on whether fractures intersect the borehole wall. The interpretation of logging data is essential to calibrate seismic cross-well sections as well as characterising the fluid flow behaviour around wells. Furthermore, logging subsurface exploration is an expensive method as a few kilometres of depths need to be drilled.

The prediction of naturally fractured reservoir behaviour is difficult due to the geological complexity and heterogeneity, and also presence of fluid and thereby the flow-related parameters such as viscosity and temperature. The flow behaviour is unpredictable in well-based scale observations as the sample volume of fractured reservoir is smaller than the real representative elemental volume (Liu & Martinez, 2012). This results from the multi-scale variation of subsurface fractures, from millimetre to kilometre scale (for detailed descriptions, see Narr et al., 2006; Nelson, 2001; Aguilera, 1998).

Alternatively, fractures can been characterised indirectly by a variety of geophysical seismic methods, such as vertical seismic profile (VSP) method, reflection seismic method, time-lapse surface and microseismic monitoring. Over the last few decades, seismic methods have developed significantly, in terms of seismic acquisition, processing, analysis and interpretation to aid in characterising fractures. Fractures can lead to various wave phenomena, such as mode conversions, duplex waves as well as seismic anisotropy. In this thesis, I examine the induced anisotropy and scattering effects on shear-wave propagation.

2.2 Modelling fractured media

There are two general approaches to define fracture systems: ”effective medium theories” (EMTs) or ”effective medium models” (EMMs) and discrete fracture models (DFMs). In this section, I review the concepts of both EMM and DFM representations of fractured media.

2.2.1 Effective medium model

The analysis of fracture induced seismic anisotropy has been traditionally performed based on EMT. In this theory, a heterogeneous medium with a distribution of discrete fractures (inclusions or other heterogeneous features) is mathematically replaced with an equivalent homogeneous medium. Done correctly, the homogeneous medium and the heterogeneous fractured medium have the same elastic properties (Liu & Martinez, 2012). In principle, the EMT approach is valid if the seismic wavelength is much greater than the scale of fractures: at least ten fractures per wavelength (Hobday & Worthington, 2012).

Garbin & Knopoff (1973) first discuss the behaviour of wave propagation through aligned parallel fractures, where they demonstrate the variation of shear-wave polarisation with direction without using the concept of effective anisotropy. Crampin (1978) uses the conclusions of Garbin & Knopoff (1973) to measure the seismic elastic constants for a parallel vertically fractured medium. Hudson (1981) derives the overall anisotropic elastic constants for velocity and attenuation in cracked media with a sparse distribution of cracks. Although there are several EMT, the model of Hudson (1981) is the most widely applied EMT in fractured media. I will follow this discussion by introducing two types of EMT models: (1) the inclusion-based model (e.g., Hudson, 1980, 1981; Chapman et al., 2003), and (2) the slip-interface or displacement-discontinuity model (e.g., Schoenberg, 1980; Pyrak-Nolte et al., 1990; Schoenberg & Sayers, 1995; Liu et al., 2000).

2.2.1.1 Hudson's model

The Hudson (1980, 1981) models predict the effective properties of embedded fractures with small, thin and penny-shaped ellipsoidal cracks or inclusions in an isotropic background medium. His model is based on a scattering theory analysis of the mean wavefield. The effective stiffness matrix is expressed as Mavko et al. (2009),

$$\mathbf{C}_{ij}^{eff} = \mathbf{C}_{ij}^{0} + \mathbf{C}_{ij}^{1} + \mathbf{C}_{ij}^{2}, \tag{2.1}$$

where $\mathbf{C}_{ij}^{0}$ is the isotropic background tensor, and $\mathbf{C}_{ij}^{1}$ and $\mathbf{C}_{ij}^{2}$ are the first- and second-order corrections, respectively (see Appendix B). Note that in Hudson's model, the cracks are assumed to be isolated, thereby there is no connection between cracks. In addition, it is reported that Hudson's model is applicable for low crack densities and small fracture sizes (Cheng, 1993). However, Cheng (1993) suggests a new second-order equation when the crack density is high and aspect ratio is small.

In fact, Hudson's model is applicable for various crack (or inclusion) types: (1) weak infill inclusion, (2) dry cracks by setting the inclusion volume modulus to zero, and (3) fluid-saturated cracks by setting the inclusion shear modulus to zero. Although, Hudson's model is a high-frequency approximation with respect to fluid flow (i.e., cracks are isolated), Mavko et al. (2009) propose using Hudson's model to model dry cracks and also using Brown & Korringa (1975) to model saturated rock.

Hudson & Liu (1999) developed the model of Cheng (1993) to describe the overall fracture interface using the averaging process of Schoenberg & Douma (1988). They classify the fracture model into three models: model (a) the fracture as a cumulative planar distribution of small cracks, model (b) represent fractures as a group of contacts, and model (c) represents fractures as a thin layer of weak solid material with a constant aperture as shown in Figure 2.3. Model (c) can be assumed as an earlier state of fracturing, in which, by increasing fluid pressure the fracture surfaces are opened up. Increasing the effective stress closes the surfaces and is represented by model (b). In the later stage, further increases in stress renders growing contact surface and thus leads to model (a).

2.2.1.2 Linear slip model

Schoenberg (1980) proposed the Linear Slip (LS) model as another type of EMT to model fractured media in which fractures and faults are considered as long interfaces with negligible thickness, compared to the small dispersed cracks in Hudson's model. The LS model describes the displacement discontinuity as an imperfectly bonded interface between two elastic media (i.e., fracture or fault) while the stress remains continuous.

The relation between difference in displacement $\Delta\mathbf{u}$ is assumed to depend on the traction vector $\mathbf{t}$ across the fracture as,

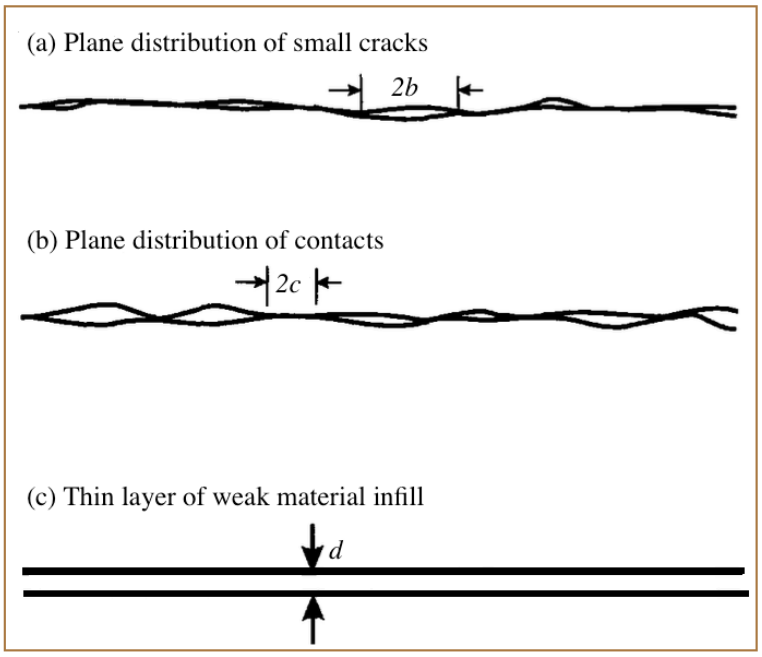

Figure 2.3: Schematic description of the three fracture models. (a) a plane distribution of small isolated cracks, (b) a plan distribution of imperfect contacts or rough surface and (c) thin layer of week material infill. Figure is modified from Hudson & Liu (1999).

$$\Delta \mathbf{u}_i = \mathbf{Z}_{ij}\mathbf{t}_j, \tag{2.2}$$

where $\mathbf{Z}$ is the individual fracture compliance (also known as specific compliance) having dimension length/stress.

The overall effective elastic compliance tensor $\mathbf{S}$ of a medium with fractures is given by Schoenberg & Sayers (1995) as,

$$\varepsilon_{ij} = (S^b_{ijkl} + S^f_{ijkl})\sigma_{kl}, \tag{2.3}$$

where the average strain ε is related to the average stress σ over a representative volume V. The S^b_{ijkl} and S^f_{ijkl} are the compliance of background medium and the excess compliance caused by the presence of the fractures.

The additional strain is given by Schoenberg & Sayers (1995) as,

$$S^f_{ijkl}\sigma_{kl} = \frac{1}{2V}\sum_r \int_{S_r} ([u_i]n_j + [u_j]n_i)\, dS, \tag{2.4}$$

where $[u_i]$ denotes the ith component of the jump discontinuity in the displacement on fracture surface S_r. However, by assuming that all fractures are aligned with the fixed normal $\mathbf{n}$, it is possible to replace each fracture in V by an average fracture having a surface area S and a linear slip boundary as,

$$[u_i] = Z_{il}\,\sigma_{lq}\,n_q, \tag{2.5}$$

where $\sigma_{lq}\,n_q$ is the lth component of the traction on the fracture surface, $[u_i]$ is the average displacement discontinuity on the fracture and the quantities Z_{il} depends on the interior conditions and infill of the fractures (Liu et al., 2000).

Substituting Equation 2.5 into 2.4, the excess compliance in Equation 2.4 can be expressed in terms of the fracture compliance tensor $\mathbf{Z}$ with components Z_{ij},

$$S^f_{ijkl} = \frac{D_f}{4}\left(Z_{ik}n_l n_j + Z_{jk}n_l n_i + Z_{il}n_k n_j + Z_{jl}n_k n_i\right), \tag{2.6}$$

where $D_f = N_f S/V$ and n_l are the components of the local unit normal to the fracture surface.

For a single set of rotationally invariant fractures with normal $\mathbf{n}$=(1,0,0) direction, the individual compliance of the fracture can be described by the normal compliance Z_N and the tangential compliance Z_T. Therefore, the Equation 2.4 can be rewritten,

$$Z_{ij} = Z_N n_i n_j + Z_T(\delta_{ij} - n_i n_j) = Z_T\delta_{ij} + (Z_N - Z_T)n_i n_j. \tag{2.7}$$

Then by substitution of Equation 2.7 into Equation 2.6, the excess compliance is

derived as,

$$S^f_{ijkl} = \frac{D_f}{4}\left[Z_T\left(\delta_{ik}n_l n_j + \delta_{jk}n_l n_i + \delta_{il}n_k n_j + \delta_{jl}n_k n_i\right) + 4(Z_N - Z_T)n_i n_j n_k n_l\right]. \tag{2.8}$$

However, Sayers & Kachanov (1991) and Sayers (2010) expressed Equation 2.8 in the following form in order to utilise it to calculate the effective elastic compliance,

$$S^f_{ijkl} = \frac{1}{4}\left[B_T\left(\delta_{ik}n_l n_j + \delta_{jk}n_l n_i + \delta_{il}n_k n_j + \delta_{jl}n_k n_i\right) + 4(B_N - B_T)n_i n_j n_k n_l\right]. \tag{2.9}$$

where D_f is included in B_N and B_T.

The excess compliance can be derived in the following form by Schoenberg & Sayers (1995),

$$S^f_{ijkl} = \begin{bmatrix} B_N & 0 & 0 & 0 & 0 & 0 \\ 0 & 0 & 0 & 0 & 0 & 0 \\ 0 & 0 & 0 & 0 & 0 & 0 \\ 0 & 0 & 0 & 0 & 0 & 0 \\ 0 & 0 & 0 & 0 & B_T & 0 \\ 0 & 0 & 0 & 0 & 0 & B_T \end{bmatrix}. \tag{2.10}$$

Note that for an isotropic background medium with a single set of aligned fractures, the medium is transversely isotropic (TI) with its symmetry axis normal to the fractures. The overall effective compliance of a TI medium depends only on two background elastic parameters, μ and λ (i.e., Lamé parameter), and the two non-negative fracture compliances Z_N and Z_T. Unlike B_N and B_T, which describe the equivalent medium compliance of a full fracture set and have dimension 1/stress (Pa^{-1}), Z_N and Z_T are the

compliances of the individual fractures with dimension length/stress (m/Pa). The $Z_{N,T}$ and $B_{N,T}$ can be related thorough the following equation

$$B_{N,T} = \frac{Z_{N,T}}{H}, \tag{2.11}$$

where H is the average fracture spacing in a direction normal to the fracture direction. Note that the fracture set with different $B_{N,T}$ can have the same $Z_{N,T}$ if their spacing is appropriately scaled (Worthington, 2008).

2.2.1.3 The linear slip model within finite difference simulation

The LS model can be implemented within the finite-difference (FD) method easily if fractures and faults are parallel to the FD grid but with some difficulty for arbitrarily oriented fractures. Coates & Schoenberg (1995) suggest a method to calculate the elastic compliance matrix of the FD grid intersected by the linear slip interface. Figure 2.4 depicts a fault or fracture with length of Δl crossing a 2D cell with area ΔA. In the case of insignificant thickness h, the overall compliance for the fractured cell is given (e.g., Nichols et al., 1989; Hood, 1991)

$$S = S_b + S_f = S_b + \frac{\Delta l}{\Delta A} \begin{bmatrix} 0 & 0 & 0 \\ 0 & 0 & 0 \\ 1 & 0 & 0 \\ 0 & 1 & 0 \\ 0 & 0 & 1 \\ 0 & 0 & 0 \end{bmatrix} \underline{Z} \begin{bmatrix} 0 & 0 & 1 & 0 & 0 & 0 \\ 0 & 0 & 0 & 1 & 0 & 0 \\ 0 & 0 & 0 & 0 & 1 & 0 \end{bmatrix}, \tag{2.12}$$

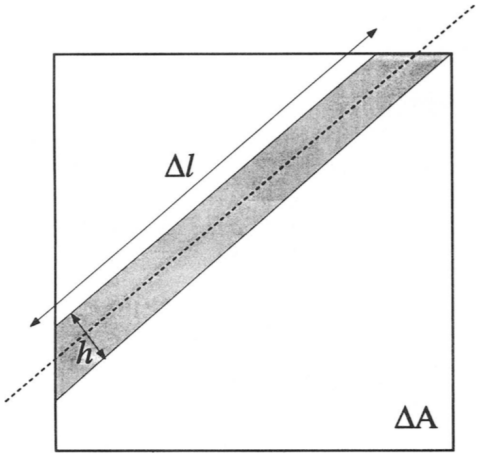

Figure 2.4: A fault (dashed line) passing through a 2D cell of area ΔA. Δl is the length of the fault segment lying within the cell and h is the thickness of the fault (which in the limit goes to zero). Figure from Coates & Schoenberg (1995).

where S_b is the background compliance matrix, S_f is the excess compliance matrix caused by the fault or fracture, and $\dfrac{\Delta l}{\Delta A}$ is the coefficient used when 2D cells are considered while $\dfrac{\Delta a}{\Delta V}$ is used for 3D cells instead (Δa is the area of the 3D fracture in the cell and ΔV is the volume of the cell). To extend the expression to the 3D case, Δl is replaced by Δa, and the area ΔA is replaced by the volume ΔV of the cell. Z is a 3×3 fracture characteristic matrix. When the fracture normal is parallel to the X3-axis, Z is given as (Schoenberg & Muir, 1989),

$$\underline{Z} = \begin{bmatrix} Z_N & 0 & 0 \\ 0 & Z_T & 0 \\ 0 & 0 & Z_T \end{bmatrix}. \tag{2.13}$$

Therefore the excess compliance matrix is,

$$S_f = \frac{1}{L}\begin{bmatrix} 0 & 0 & 0 & 0 & 0 & 0 \\ 0 & 0 & 0 & 0 & 0 & 0 \\ 0 & 0 & Z_N & 0 & 0 & 0 \\ 0 & 0 & 0 & Z_T & 0 & 0 \\ 0 & 0 & 0 & 0 & Z_T & 0 \\ 0 & 0 & 0 & 0 & 0 & 0 \end{bmatrix}, \tag{2.14}$$

where $\frac{1}{L} \equiv \frac{\Delta l}{\Delta A}$ for the 2D case and $\frac{1}{L} \equiv \frac{\Delta a}{\Delta V}$ for the 3D case. If the fault or fracture is not horizontal, the effective compliance is calculated by rotating to the coordinate system using Bond transformation. For example, when the normal of vertical fracture is along the X1-axis, the effective compliance matrix is given:

$$S = S_b + \frac{1}{L}\begin{bmatrix} Z_N & 0 & 0 & 0 & 0 & 0 \\ 0 & 0 & 0 & 0 & 0 & 0 \\ 0 & 0 & 0 & 0 & 0 & 0 \\ 0 & 0 & 0 & 0 & 0 & 0 \\ 0 & 0 & 0 & 0 & Z_T & 0 \\ 0 & 0 & 0 & 0 & 0 & Z_T \end{bmatrix}. \tag{2.15}$$

Schoenberg's linear slip theory is more practical for observing the seismic response of individual fractures than Hudson's model, in which both predict the overall elastic properties of a fractured medium (Hou, 2014).

A general explicit expression for various fracture models was proposed by Liu et al. (2000) based on LS theory as shown in Figure 2.3. Liu et al. (2000) classify the natural fractures into three models similar to Hudson & Liu (1999) (see Section 2.2.1.1).

Liu et al. (2000) calculate the overall compliance of a fractured medium which is associated with the elastic constants of the isotropic host medium (i.e., Lamé parameter) and different geometrical inclusion variables such as average radius of a fracture, average radius of welded regions and average fracture aperture. In model (a), the variables mainly involve the crack density and the two terms U_{11} and U_{33} (for more detail see Appendix C), which can be calculated based on Hudson (1981). A more detailed derivation of this theory can be found in Appendix C. This model is consistent with Hudson's crack theory, where cracks are randomly distributed in a volume. In Model (b) the fracture density variable is different from the crack density. Furthermore, this model is suitable for only dry fractures. This model is consistent with the rough surface model of White (1983). In model (c) the infill is assumed to be weak, so the infill parameters (two Lamé parameters and viscosity) and the probing wavelet frequency are considered. This model is in agreement with Backus (1962) for horizontal thin layers. Both models (a) and (b) can be equivalently replaced by model (c) in which the fracture is modelled as an equivalent thin layer with constant thickness of weak infill. Model (c) can be used to represent hydraulic fractures.

In Liu et al. (2000), the fracture density is assumed to be smaller than 0.1, though resultant estimations of different EMT models claim that the theory may be applicable for crack density up to 0.5. Moreover, Liu et al. (2000) indicate that, in the three types of models the assumption of the compliance ratio $Z_N/Z_T \approx 1$ is valid for dry cracks if the crack Poisson's ratio ν rages $0.1 \leqslant \nu \leqslant 0.25$. For liquid-filled cracks, $Z_N = 0$, therefore $Z_N/Z_T = 0$.

2.2.2 Discrete fractured medium

DFM is an approach where fractures are modelled explicitly, incorporating both the geometry and explicit fracture properties. Since fractures control the flow and transport

properties within reservoirs (e.g., Dershowitz et al., 2004), modelling fractures as discrete features allows for a much more direct link between seismic attributes with fractures and flow parameters. However, modelling fractures as discrete features may be costly in terms of computational resources (memory and simulation time) as well as practicalities of constructing deterministic models. Moreover, EMMs are generally applicable where the size of inclusions are substantially less than the probing seismic wavelength which is often the case for surface seismic surveys. In contrast, using numerical analysis of DFM seems to be the only approach to simulate wave propagation in fractured media without the restriction of the size-to-wavelength ratio (Vlastos et al., 2003). If the fracture dimensions and spacing are comparable to the seismic wavelength, the discrete fracture model (DFM) is more appropriate, which is independent of the fracture size and spacing. This is because, fractures scatter P-waves and S-waves, leading to a complex seismic signature. This effect is dependent on some conditions as discussed by Willis et al. (2006): (1) the orientation of source-receiver pairs relative to the fracture orientation, (2) the fracture spacing, (3) the wavelength of seismic wave, and (4) the compliance of the fractures. Furthermore, DFMs have been implemented in FD grids using EMT dealing with multiple scattering without having any limitations on the fracture density.

To understand the seismic response of a discrete fracture, several modelling studies (e.g., Yi et al., 1998; Groenenboom & Falk, 2000; Nihei et al., 2002; Vlastos et al., 2003; Willis et al., 2006) and laboratory experiments (e.g., Pyrak-Nolte et al., 1987, 1990; Hsu & Schoenberg, 1993; Nihei et al., 1999; Pyrak-Nolte & Roy, 2000; Xian et al., 2001) have been performed. These studies have significantly illustrated wave propagation phenomena developed around a single fracture and multiple sets of fractures. The resultant wave phenomena from these situations are seismic scattering and wave guiding (Grandi Karam, 2008). Seismic coda waves can reveal valuable information about

fracture geometry and properties (Vlastos et al., 2003; Willis et al., 2006). Vlastos et al. (2003) studied the effect of different spatial distributions of fractures with the same fracture density using the 2D pseudospectral method. They observed that varying spatial distribution leads to different frequency content in the recorded wavefield which is consistent with the results of Leary & Abercrombie (1994). In addition, the ratio of fracture size to wavelength is independent of spatial distribution of fractures. Willis et al. (2006) propose a scattering index (SI) method to detect the fracture orientation from 3D field data.

2.3 Fracture compliance

The compliance ratio (Z_N/Z_T) plays an important role in the detection of fracture fluid infill and its properties. A common approach to model Z_N and Z_T is to assume that the fracture is represented by penny-shaped voids (e.g., Hudson, 1981; Sayers & Kachanov, 1995; Hudson et al., 1996). In these models Z_N/Z_T is governed by the fluid filling the fractures. If the fractures are dry (Sayers & Kachanov, 1995), the compliance can be estimated simply as,

$$Z_N/Z_T = 1 - \nu/2, \tag{2.16}$$

where ν is the Poisson's ratio of the background medium. Since ν is normally in the range $0.1 \leq \nu \leq 0.25$ for reservoir rocks, $Z_N/Z_T \approx 1$. Cracks have been referred to as scalar cracks where $Z_N/Z_T = 1$.

The presence of fluid in fractures results in an decrease in Z_N, while Z_T is unchanged, so $Z_N/Z_T \rightarrow 0$ (e.g., Hudson, 1981). However, if fluid can flow between fractures, or between fracture and the rock matrix, then Z_N/Z_T can be controlled by the time that fluid can drain out of the cracks, which is controlled by the fracture and the

bulk rock permeability as well as fluid viscosity (e.g., Hudson et al., 1996; Chapman et al., 2003; Baird et al., 2013). If fluid can fully drain out of the cracks, then the cracks are compliant and Z_N/Z_T is given by Equation 2.16. If the fluid is viscous, and the permeability of rock is low, or the frequency of the seismic wave is high enough, then the fluid will not have sufficient time to escape the fractures. Therefore, liquid will trapped within the cracks and $Z_N/Z_T \rightarrow 0$.

Figure 2.5 and Table 2.1 provide a compilation of published measurements of Z_N/Z_T from laboratory and field studies. These studies can be categorised into four groups: (1) core samples without discrete fractures to image grain-scale discontinuities (Sayers, 1999; Sayers & Han, 2002; MacBeth & Schuett, 2007; Verdon et al., 2008; Angus et al., 2009), (2) representative or synthetic samples with known crack distributions (Hsu & Schoenberg, 1993; Rathore et al., 1994; Far, 2011), (3) core samples with only one single large scale fracture (Pyrak-Nolte et al., 1990; Lubbe et al., 2008), and (4) field scale measurement of a major fracture zone (Hobday & Worthington, 2012).

Verdon et al. (2008) and Angus et al. (2009) inverted ultrasonic measurements of core samples without fractures in order to determine the compliance of grain-scale microfractures. Verdon et al. (2008) used a group samples from the Clair reservoir and found $0.68 < Z_N/Z_T < 1.06$. Angus et al. (2009) compiled a large body of data from the literature, and found $0.25 < Z_N/Z_T < 1.5$. Likewise, Sayers & Han (2002) utilised ultrasonic measurements performed by Han et al. (1986) on both dry and water-saturated sandstone samples, finding $0.25 < Z_N/Z_T < 3$ for the dry samples, and $0.05 < Z_N/Z_T < 1.1$ for water-saturated. In addition, Sayers (1999) inverted ultrasonic measurements on dry shale samples performed by Johnston & Christensen (1993), and on water-saturated shale samples by Hornby et al. (1994) obtaining $0.47 < Z_N/Z_T < 0.8$ for dry samples, and $0.26 < Z_N/Z_T < 0.41$ for water- shale samples. In another study, MacBeth & Schuett (2007) measured Z_N/Z_T for ultrasonic data for both undamaged

Table 2.1: Published measurements of Z_N/Z_T from both laboratory and field studies. Table from Verdon & Wüstefeld (2013).

	Reference	**Experiment type**	$\mathbf{Z_N/Z_T}$
1	Verdon et al. (2008)	Dry samples. Ultrasonic measurement on grain-scale fabrics. Data from Hall et al. (2008)	0.68 - 1.06
2	Angus et al. (2009)	Dry samples. Ultrasonic measurement on grain-scale fabrics. Data collated from a range of literature sources.	0.25 - 1.5
3(a)	Sayers & Han (2002)	Dry samples. Ultrasonic measurement on grain-scale fabrics. Data from Han et al. (1986)	0.25 - 3
3(b)		As above, water saturated.	0.05 - 1.1
4(a)	Sayers (1999)	Dry samples. Ultrasonic measurement on shale samples. Data from Johnston & Christensen (1993) and Vernik (1993)	0.47 - 0.8
4(b)		As above, water saturated. Data from Hornby et al. (1994)	0.26 - 0.41
5(a)	MacBeth & Schuett (2007)	Dry samples. Ultrasonic measurement on grain-scale fabrics. Undamaged sample.	0 - 0.6
5(b)		As above, sample thermally damaged.	0 - 1.2
6(a)	Hsu & Schoenberg (1993)	Representative medium of compressed perspex plates. Ultrasonic measurements on dry, unfilled samples.	0.8 - 1.0
6(b)		As above, but cracks contain rubber pellet inclusions	0.1
7(a)	Far (2011)	Representative medium of compressed perspex plates. Ultrasonic measurements on dry samples.	0.11 - 0.75
7(b)		As above, honey saturated.	0.16 - 1.6
8	Rathore et al. (1994)	Synthetic sample containing a population of cracks. Ultrasonic data reanalysed by Hudson et al. (2001)	0.46
9(a)	Pyrak-Nolte et al. (1990)	Quartz monzonite samples containing a single fracture. Ultrasonic measurements on dry samples.	0.2 - 0.77
9(b)		As above, water saturated.	0.04 - 0.48
10(a)	Lubbe et al. (2008)	Limestone samples cut and reassembled to create a single fracture. Ultrasonic measurements on dry samples.	0.2 - 0.55
10(b)		As above, honey saturated.	0.02 - 0.05
11	Hobday & Worthington (2012)	Hammer seismic imaging of outcrop of Caithness Flagstone. Water saturated	≤ 0.1

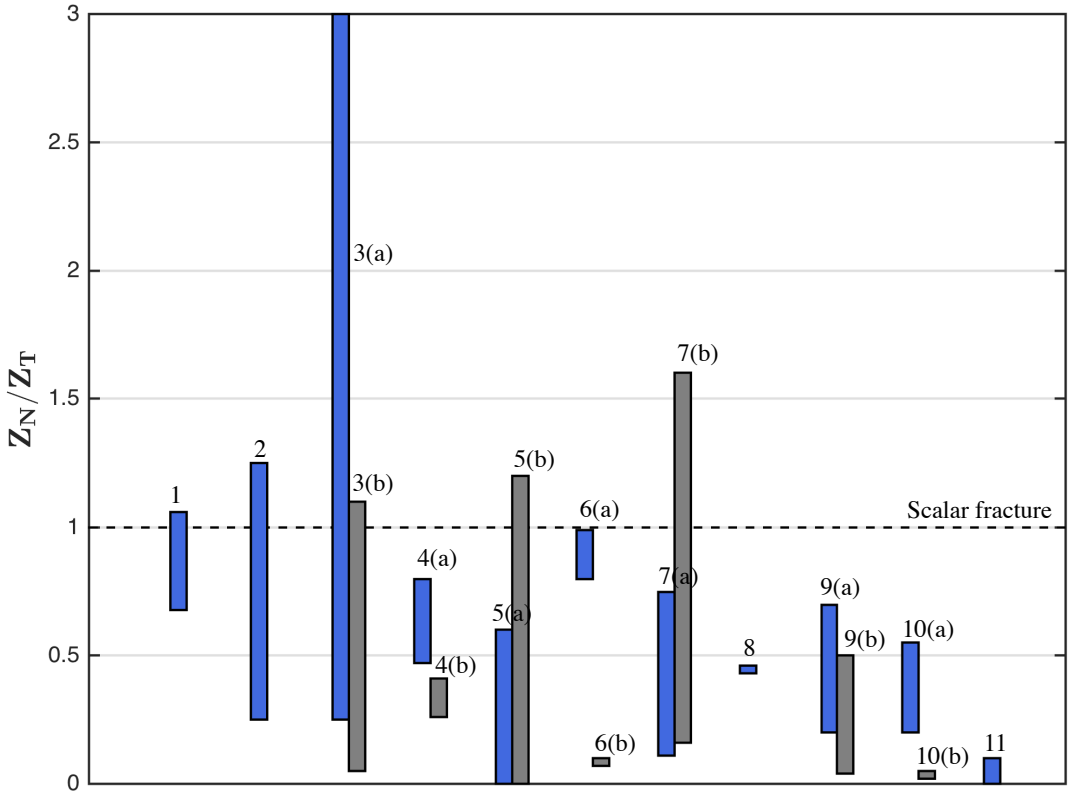

Figure 2.5: Published values of Z_N/Z_T from laboratory and field studies. Label number correspond to the studies listed in Table 1. Figure is modified from Verdon & Wüstefeld (2013).

core and heat damaged core, producing intra/intergranular fractures. They shown that for the initial sample before heating $0< Z_N/Z_T <0.6$, while for the sample after heating $0< Z_N/Z_T <1.2$. MacBeth & Schuett (2007) noted that pre-existing microfractures were diagenetically infilled, while the heat induced microcracks had smoother faces and were unfilled.

Hsu & Schoenberg (1993) in a major experiment, proposed representative samples roughened with perspex plates to create samples containing discontinuities. In these samples the fracture geometry, distribution and properties could be well constrained. Therefore, these properties could be attributed directly by observations. Hsu & Schoenberg (1993) examined their samples with ultrasonic measurements, achieving

0.8$< Z_N/Z_T <$1 for dry samples, while for samples filled with honey Z_N/Z_T decrease to 0.1. In a similar approach, Far (2011) created a representative sample of compressed perspex plates. Far's finding showed that Z_N/Z_T ranged between 0.11$< Z_N/Z_T <$0.75 for unfilled samples. Far (2011) also revealed that when the the samples of perspex plates whose discontinuities were filled with rubber pellets led to an increase in Z_N/Z_T as high as 1.6.

In a different approach, Rathore et al. (1994) created a synthetic fractured rock in which the crack distributions were known. Ultrasonic measurements of P- and S-waves were measured at different angles to the fracture set. Although Rathore et al. (1994) did not estimate Z_N/Z_T, Hudson et al. (2001) used the frequency-dependent model of Hudson et al. (1996) to fit the results of Rathore et al. (1994).

Pyrak-Nolte et al. (1990) measured the compliance of a core sample of quartz monzonite with a single fracture. Unlike earlier mentioned studies (i.e., grain-scale), the sample of Pyrak-Nolte et al. (1990) represented a large scale fracture in the rock. For dry samples Pyrak-Nolte et al. (1990) found 0.20$< Z_N/Z_T <$0.77, while for water-saturated samples the compliance ratio decreased to 0.04$< Z_N/Z_T <$0.48. Likewise, Lubbe et al. (2008) cut a limestone core to provide a representative sample with one fracture and found 0.20$< Z_N/Z_T <$0.55 for dry samples while for honey saturated sample a significant reduction to 0.02$< Z_N/Z_T <$0.05.

Interestingly, all previous laboratory measurements were limited to centimetre-scale, so there was a lack of upscaling in the Z_N/Z_T measurements. However, Hobday & Worthington (2012) performed a field scale of measure Z_N/Z_T. They used a hammer seismic to estimate Z_N/Z_T of a water-saturated outcrop of Upper Caithness Flagstone, revealing that $Z_N/Z_T \leq$0.1.

Recently, Verdon & Wüstefeld (2013) developed a method to invert SWS measurements obtained from the microseismic Cotton Valley data with fracture length scales of

0.5 to 10 m. Verdon & Wüstefeld (2013) found that the effective compliance ratio was $B_N/B_T = 0.74 \pm 0.4$.

In addition to knowing the Z_N/Z_T values, the choice of fracture compliance is a key step in the seismic modelling of fractured media. Figure 2.6 plots a compilation of laboratory and field estimation of dynamic fracture compliance (as explained earlier) against fracture length scale. Apparently, there is lack of upscaled measurements between 10 and 100 m fracture length.

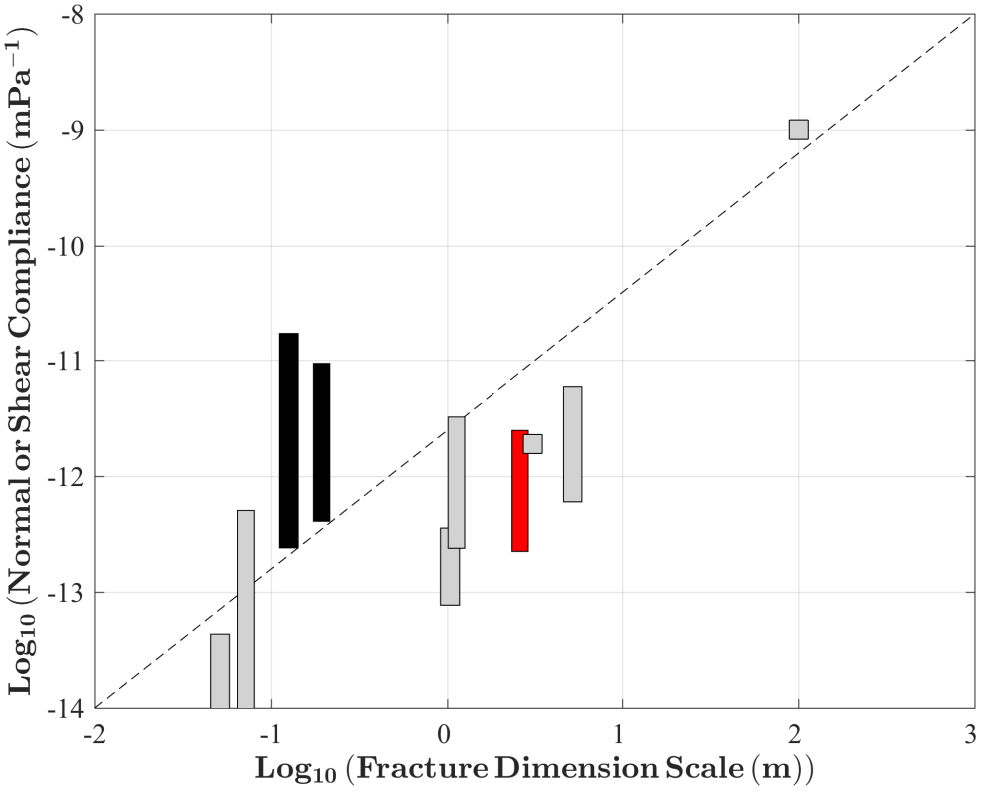

Figure 2.6: Fracture compliance as a function of fracture length scale. Grey is the compilation of laboratory and field data by Worthington (2008). Black bars are data from Far (2011). Red is data from Verdon & Wüstefeld (2013). Figure is modified from Worthington (2008).

2.4 Summary

Fracture is a general term that comprises various natural and induced features including, cracks, joints, faults and veins. Naturally occurring fractures are ubiquitous structural features in the Earth's crust, especially in most hydrocarbon reservoirs. So knowledge of their orientation and density is important to increase production rates. Although fracture network characterisations can be understood through various direct measurements, seismic methods are indirect approaches in which seismic waves travelling through fractures are affected due to the fractures' mechanical properties such as compliance and fluid saturation, and by geometrical properties as well.

There are two general approaches to define fracture systems: effective medium models" models (EMMs) and discrete fracture models (DFMs). So, in this section I reviewed the different theories of EMM in fractured media involved in this study.

The EMT can be categorised into two types of models: inclusion-based model (e.g., Hudson, 1980, 1981; Chapman et al., 2003), and the displacement-discontinuity model (e.g., Schoenberg, 1980; Pyrak-Nolte et al., 1990; Schoenberg & Sayers, 1995; Liu et al., 2000).

Hudson's model includes some assumptions and limitations in which fractures are penny-shaped with small aspect ratio and a small fracture density. Though Hudson's model estimates frequency-independent behaviour of fractured models, the model of Chapman et al. (2003) considers frequency-dependent behaviour based on squirt-flow mechanism. In addition, Chapman's model can treat the effect of different scales of fractures. Schoenberg (1980) proposed the LS model as another type of EMT to model fractured media. The LS model describes the displacement discontinuity at an imperfectly bonded interface between two elastic media while the stress remains continuous.

Alternatively, DFM is an approach where fractures are modelled explicitly. Mod-

elling fractures as discrete features allow for a much more direct link between seismic attributes with fractures and flow parameters. Unlike EMM, DFM seems to be the only way to simulate wave propagation in the fractured media without the restriction of the size-to-wavelength ratio.

The choice of fracture compliance values is an essential step in the seismic modelling of fractured media. The compilation of laboratory and field research reveals that there is linear relation between fracture compliance and fracture size. However, there is lack of estimation for the fractures with lengths from a few meters to a hundred meters. This is likely the range that most fractures in reservoirs occur. Therefore, it is essential to understand how fracture compliance might vary over this range and whether they are detectable using seismic techniques. So in this thesis I intend to fill the gap of study for this range of fracture sizes by modelling synthetic discrete fractured media.

Chapter 3

Theory and methodology

3.1 Introduction

In this Chapter, I provide an overview of the basic theory involved in my thesis. First I present the concept of finite-difference (FD) modelling of seismic waves and detail the algorithm WAVE that I use to create the synthetic waveforms. I discuss the seismic moment tensor representation of the seismic source, which is used to describe the microseismic source in the FD models. Next I discuss wave propagation in anisotropic media, anisotropy symmetry systems, and equivalent and discrete fractured media representation. Finally, I present the method of shear-wave splitting analysis and the inversion algorithm for fracture characterisation.

3.2 Finite-difference method (FD)

Seismic numerical modelling methods are valuable approaches to simulate wave propagation within the Earth. Seismic numerical modelling can be categorised within three end-member approaches: finite-difference, integral-equation and ray-tracing methods. The FD method is a grid based method often referred to as a full-wave equation method since the method does not make any restrictions about the wave solution. The FD method can be very accurate if the model is sufficiently discretised in space and in time. However, compared to other techniques, such as analytical solutions and ray-tracing, the FD method can be computationally intensive due to the fine grid sampling required (e.g., Carcione et al., 2002). The FD method is widely used to simulate the whole seismic wavefield including direct waves, primary and multiple reflected waves, refracted waves, surface waves, diffracted waves and converted waves. It should be noted that there are other methods that require the discretization of the time and space variables, such as the pseudospectral (PS) (e.g., Kosloff & Baysal, 1982) and the finite-element (FE) methods (e.g., Lysmer & Drake, 1972; Schlue, 1979), which yield highly accurate full waveform synthetics.

There are two types of schemes used in the FD method: (1) the explicit scheme, where the wavefield at any grid point can be propagated to the next time step using an explicit FD formulation that uses only values of wavefield at previous time steps; and (2) the implicit scheme (e.g., Emerman et al., 1982 and Mufti, 1985), where the wavefield at a specific time step is calculated simultaneously at all grid points based on the values for the current and past time steps, and requires implementing the inverse of a system matrix (Moczo et al., 2007).

For a 2D medium, Virieux (1986) represents the velocity-stress formulation for the second-order hyperbolic system as

$$
\begin{aligned}
\frac{\partial^2 \mathrm{u}_x}{\partial t^2} &= \frac{1}{\rho}\left(f_x + \frac{\partial \sigma_{xx}}{\partial x} + \frac{\partial \sigma_{xz}}{\partial z}\right), \\
\frac{\partial^2 \mathrm{u}_z}{\partial t^2} &= \frac{1}{\rho}\left(f_z + \frac{\partial \sigma_{xz}}{\partial x} + \frac{\partial \sigma_{zz}}{\partial z}\right), \\
\sigma_{xx} &= (\lambda + 2\mu)\frac{\partial \mathrm{u}_x}{\partial x} + \lambda \frac{\partial \mathrm{u}_z}{\partial z}, \\
\sigma_{zz} &= (\lambda + 2\mu)\frac{\partial \mathrm{u}_z}{\partial z} + \lambda \frac{\partial \mathrm{u}_x}{\partial x}, \\
\sigma_{xz} &= \mu\left(\frac{\partial \mathrm{u}_z}{\partial x} + \frac{\partial \mathrm{u}_x}{\partial z}\right),
\end{aligned}
\tag{3.1}
$$

where σ_{ij} denotes the stress tensor, u_x and u_z denote the displacement components, ρ denotes the bulk density, $\lambda(x, z)$ and $\mu(x, z)$ denote the elastic moduli (Lamé parameters), and f_x and f_z represent the applied force. Equation 3.1 can be rewritten as a system of first-order hyperbolic equations

$$
\begin{aligned}
\frac{\partial v_x}{\partial t} &= \frac{1}{\rho}\left(f_x + \frac{\partial \sigma_{xx}}{\partial x} + \frac{\partial \sigma_{xz}}{\partial z}\right), \\
\frac{\partial v_z}{\partial t} &= \frac{1}{\rho}\left(f_z + \frac{\partial \sigma_{xz}}{\partial x} + \frac{\partial \sigma_{zz}}{\partial z}\right), \\
\frac{\partial \sigma_{xx}}{\partial t} &= (\lambda + 2\mu)\frac{\partial v_x}{\partial x} + \lambda \frac{\partial v_z}{\partial z}, \\
\frac{\partial \sigma_{zz}}{\partial t} &= (\lambda + 2\mu)\frac{\partial v_z}{\partial z} + \lambda \frac{\partial v_x}{\partial x}, \\
\frac{\partial \sigma_{xz}}{\partial t} &= \mu \frac{\partial v_z}{\partial x} + \mu \frac{\partial v_x}{\partial z},
\end{aligned}
\tag{3.2}
$$

where v_x and v_z denote the velocity components.

The general concept of the FD method is to numerically approximate the partial derivatives using finite difference stencils typically derived using Taylor series expansions (e.g., Tannehill et al., 1997) or more advanced approaches such as pseudospectral methods (e.g., Fornberg, 1998). The explicit and implicit FD schemes differ in terms

of how the time derivatives are approximated. For the explicit method, the wavefield at a specific time is computed from the data at previous time steps. For the implicit method, the wavefield is computed from the wavefield at previous and future values. The implicit scheme requires more computational effort due to the need for inverting a large system matrix. However, the implicit method is unconditionally stable unlike the explicit method. In general, explicit schemes can be computationally accurate if the time step is restricted by the stability criteria (Carcione et al., 2002). The stability criterion is governed by the maximum phase velocity c_{max} and the minimum grid spacing dx_{min},

$$dt \leqslant \frac{2}{\pi\sqrt{n}} \left(\frac{dx_{min}}{c_{max}} \right) , \tag{3.3}$$

where n stands for n-D space. To limit numerical dispersion there is a constraint on the grid spacing

$$dx \leqslant \frac{c_{min}}{2f_{max}} , \tag{3.4}$$

where f_{max} is the maximum source frequency and c_{min} is the minimum phase velocity (e.g., Carcione et al., 2002). Equation 3.4 implies that the grid spacing should not be larger than the smallest wavelength in order to avoid aliasing.

3.3 WAVE

In this thesis I use the FD program WAVE (Napier & Malan, 1997; Hildyard, 2007) that is based on an explicit FD technique. WAVE is a staggered grid, fourth-order accurate in space and second-order accurate in time FD algorithm for isotropic 2D and 3D elastic media. WAVE was developed specifically for modelling wave propagation through fractures within an isotropic background medium and has been shown to accurately model the seismic response due to fractures in mining and radioactive waste storage

environments (Hildyard & Young, 2002; Hildyard, 2007). The model is discretised into an orthogonal grid with each discrete node containing component dependent properties such as stress and velocity, where fractures (and openings) are modelled as zero-width discontinuities (Hildyard, 2007). A summary of some previous applications of the program is given in Napier & Malan (1997), while a technical overview can be found in Hildyard et al. (1995). WAVE is capable of accurately modelling diffraction, refraction, reflection and transmission of stress waves (Daehnke et al., 1996).

WAVE is being used in this thesis because it is computationally efficient in both two-dimensions (2D) and three-dimensions (3D). Specifically, WAVE is unique in that it models fractures as explicit discontinuities and so does not require making the assumption of an effective medium. Although WAVE is limited in terms of the geometries of the fractures that can be modelled (i.e., the fractures must be parallel to the primary grid axes, and thereby are orthogonal in the case of multiple fracture sets), it allows studying the influence of fracture properties on the wavefield. The most common approach for modelling the seismic behaviour of fractured rock is to use an effective medium representation of the fracture network. While much has been achieved with these methods, there are limitations such as the applicable frequency range, the types of fracture properties which can be studied, and non-uniform influences for example due to the stress-field (e.g., Hildyard, 2007). The alternative approach is to model fracture networks as discrete elements that can encapsulate individual fracture behaviour. The discrete fracture representation means that we do not need to make any assumptions about the model, enabling the solution to simulate more accurately the interaction of seismic waves with fractures systems. Using a discrete fracture representation allows models to capture the influence of the stress state, as well as specific fracture properties such as fracture size, filling and compliance.

WAVE as well as other FD algorithms solve the first-order equations on a staggered

grid (e.g., Madariaga, 1976; Aki & Richards, 1980; Virieux, 1986) due to computational efficiency. The explicit solutions can be divided into two main types: solution to the first-order hyperbolic wave equation (e.g., Madariaga, 1976; Virieux, 1986 (see Equation 3.2) and solution to the second order hyperbolic wave equation (e.g, Kelly et al., 1976; Virieux, 1986 (see Equation 3.1).

WAVE uses a staggered mesh with central differences (e.g., Madariaga, 1976; Aki & Richards, 1980; Graves, 1996). In the central difference formulation two values are used at half distance from nodal points where the value at the nodal point will be calculated from. The velocity and stress variables in WAVE are obtained by consecutively solving the constitutive equation for stresses from velocity, and the equation of the motion for velocities from stress values (Hildyard, 2001). Hence velocities and stresses are staggered in time by $\Delta t/2$, where Δt is the time step between samples in the staggered grid. Figure 3.1 shows the positions of the grid variables in the 2D and 3D WAVE grids. Figure 3.2 depicts part of the 2D staggered grid for some unit cells in WAVE. Velocities are calculated from the equation of motion (Newton's law) and stresses from the constitutive equation (Hooke's law).

3.4 Explicit fracture models

The discrete fracture model is generated independently and then embedded within the isotropic medium (Hildyard, 2001). The concept of fracturing is based on collection of flat open fractures that are randomly distributed in a prescribed fracture volume. The crack density ϵ is related to fracture size per unit of volume and is defined by O'Connell & Budiansky (1974) as,

$$\epsilon = \frac{2N}{\pi V}\langle\frac{A^2}{P}\rangle, \tag{3.5}$$

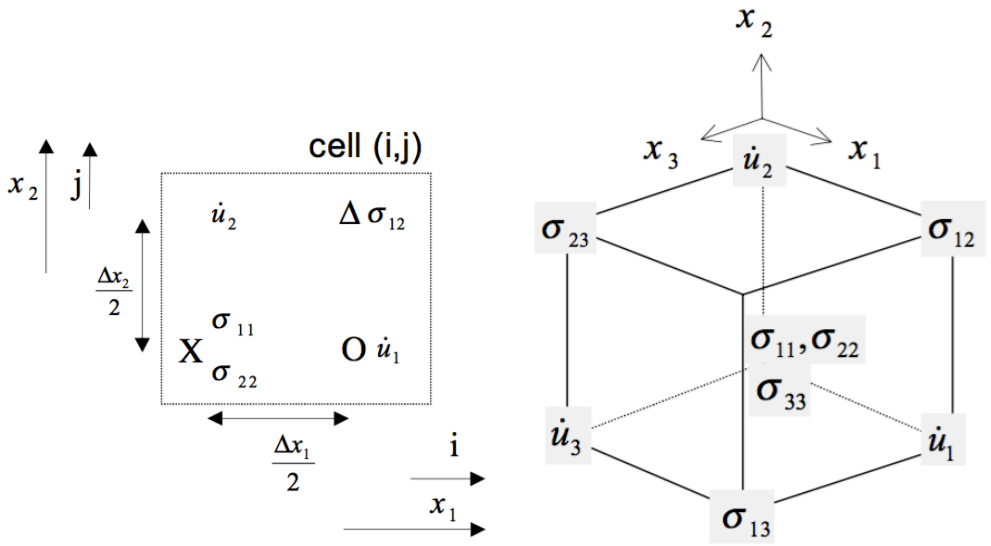

(a) (b)

Figure 3.1: 2D and 3D unit cell in WAVE staggered grid, showing the position of the velocity and stress components distributed around the cell. Figure from Hildyard (2001).

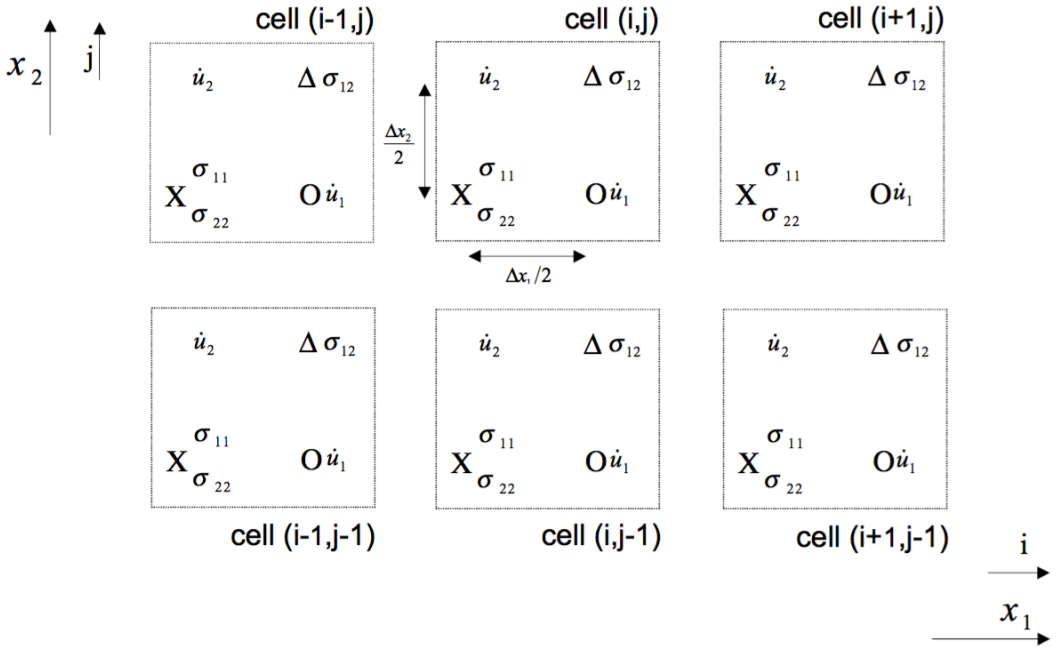

Figure 3.2: Part of the 2D staggered grid in WAVE. Figure from Hildyard (2001).

where N is the number of fractures within the medium volume V, A the crack area, P the crack perimeter and brackets denote an average. This is a dimensionless definition of fracture density. For circular cracks with radius a, crack density is defined

$$\epsilon = \frac{N}{V} \sum a^3. \tag{3.6}$$

In WAVE cracks are defined,

$$\epsilon = \frac{1}{\pi V} \sum \frac{A^2 B^2}{A + B}, \tag{3.7}$$

where A and B are the crack side lengths. Based on Equations 3.5-3.7, the same crack density for the different scale of crack length size can be obtained.

The program CRACKGN generates a random crack realisation that can be implemented in WAVE. It renders three orthogonal directions of cracks with a specified crack density for three axes. Cracks are distributed linearly in the specified fracture volume with fracture intersections being avoided. This limits the generation of cracks for small size fractures with high fracture density that can skew the random distribution for high density fractures (Hildyard, 2001).

3.5 Moment Tensor (MT)

The physics of the seismic source and its description have been studied significantly in global seismology. The source within the solid Earth can be categorised into shear sources and volumetric sources. A shear or faulting source is associated with slip across a fracture plane while a volumetric source is a sudden expansion or contraction throughout a volumetric source region. The seismic source can be described mathematically in two different ways: in terms of a body force imposed to a certain element of the

medium containing the source or by a discontinuity in displacement or strain across a rupture or fault (e.g., across a fault plane or surface of volumetric source).

Aki & Richards (2002) discuss the equivalence of the body-force and displacement discontinuity concept. Equivalent forces are the typical approach to approximate the seismic source, that can be incorporated into the linear wave equation by neglecting non-linear effects in the near source region (Aki & Richards, 2002). Equivalent forces generate a displacement discontinuity at the Earth's surface that is similar to those generated by a fault (e.g., earthquake) source or volumetric source. The seismic source or point source is small compared to the seismic wavelength and is described by its magnitude (M_0) and fault plane solution (e.g., Honda, 1962; Herrmann, 1975). The seismic moment tensor (MT) is the most common approach used to describe the seismic point source (e.g., Kanamori & Given, 1982). Gilbert (1971) introduced the seismic moment tensor to evaluate displacements at the free surface, where the displacement could be formulated as a sum of moment tensor elements convolved with the corresponding Green's function. The Green's function is the impulse response of the medium between source and receiver (Jost & Herrmann, 1989). The Green's function depends on the source and receiver coordinates, the Earth or velocity model, and is a tensor (Aki and Richards, 1980). Gilbert (1973) first uses the linearity between the moment tensor and Green's function elements to calculate moment tensor elements from observations (moment tensor inversion).

Figure 3.3 describes how a point source can be described by a system of double couples M_{ij}, which consist of nine components of the moment tensor. Based on symmetry, $M_{ij} = M_{ji}$, and so the nine components reduce to six independent components. Based on Aki & Richards (2002) the MT for a double couple mechanism is defined

$$M_{ij} = \mu A(u_i n_j + u_j n_i), \tag{3.8}$$

where μ is shear modulus, A is the area of the fault, u_i indicates the ith slip vector component on the fault surface and n_i indicates the ith component of the normal vector to the fault plane. The vectors $\mathbf{u}$ and $\mathbf{v}$ can be determined from the strike Φ, dip Υ and slip Λ of the fault (Aki & Richards, 2002)

$$\begin{aligned}\mathbf{u} = \bar{u}(cos\Lambda\ \cos\Phi + \cos\Upsilon\ \sin\Lambda\ \sin\Phi)\mathbf{e_x} \\ +\bar{u}(\cos\Lambda\ \sin\Phi - \cos\Upsilon\ \sin\Lambda\ \cos\Phi)\mathbf{e_y} \\ -\bar{u}(\sin\Upsilon\ \sin\Lambda)\mathbf{e_z},\end{aligned} \tag{3.9}$$

where $\bar{u}$ is the mean displacement on the fault plane and $\mathbf{e_x}$ is the unit X-component of the X-axis. The fault normal $\mathbf{v}$ is

$$\mathbf{v} = -\sin\Upsilon\sin\Phi\mathbf{e_x} + \sin\Upsilon\cos\Phi\mathbf{e_y} - \cos\Upsilon\mathbf{e_z}\,. \tag{3.10}$$

The strike Φ is measured clockwise from North ($0 \leqslant \Phi \leqslant 2\pi$), the dip Υ is measured down from horizontal ($0 \leqslant \Upsilon \leqslant \pi/2$) and slip (or rake) Λ is measured in the fault plane with the angle between direction of strike and slip ($-\pi \leqslant \Lambda \leqslant \pi$). These parameters are depicted in Figure 3.4.

The scalar seismic moment can be obtained

$$M_0 = \mu A\bar{u}. \tag{3.11}$$

The Cartesian components of the symmetric moment M_0, based on Equation 3.8-3.11 can be defined in terms of strike, dip and slip angles

$$M_{xx} \quad = \quad -M_0(\sin\Upsilon\cos\Lambda\sin 2\Phi + \sin 2\Upsilon\sin\Lambda\sin^2\Phi)$$

$$
\begin{aligned}
M_{yy} &= M_0(\sin\Upsilon\cos\Lambda\sin 2\Phi - \sin 2\Upsilon\sin\Lambda\cos^2\Phi) \\
M_{zz} &= M_0(\sin 2\Upsilon\sin\Lambda) \\
M_{xy} &= M_0(\sin\Upsilon\cos\Lambda\cos 2\Phi + 0.5\sin 2\Upsilon\sin\Lambda\sin 2\Phi) \\
M_{xz} &= -M_0(\cos\Upsilon\cos\Lambda\cos\Phi + \cos 2\Upsilon\sin\Lambda\sin\Phi) \\
M_{yz} &= -M_0(\cos\Upsilon\cos\Lambda\sin\Phi - \cos 2\Upsilon\sin\Lambda\cos\Phi).
\end{aligned}
\tag{3.12}
$$

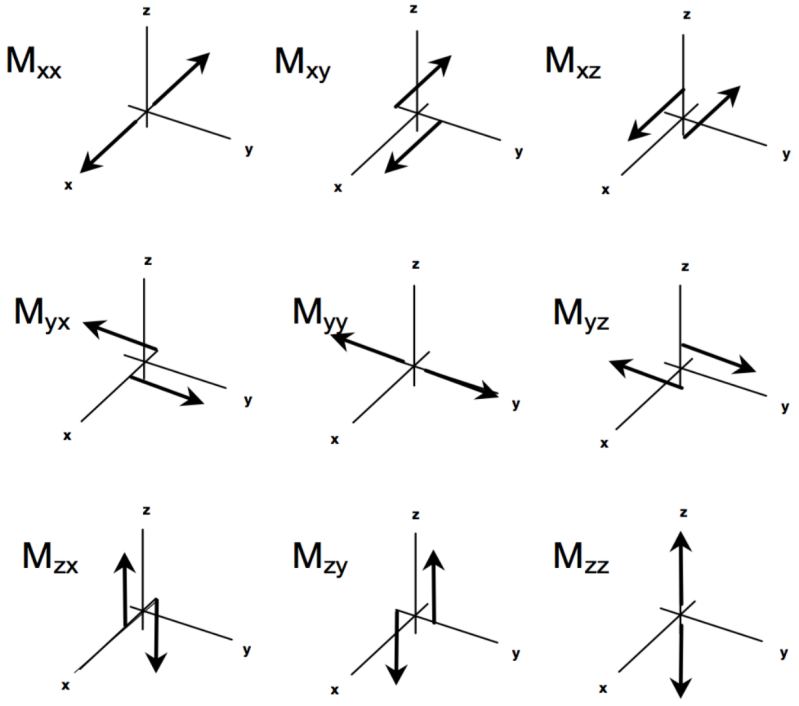

Figure 3.3: The nine possible couples that describe a seismic point source. In this notation (M_{ij}), i and j are the force direction and the axis along which the force acts, respectively. Figure is modified from Aki & Richards (2002).

The equivalent forces and source mechanism can be determined from the eigenvalues and eigenvectors of the moment tensor (Jost & Herrmann, 1989). If the sum is positive, the source is explosive type, whereas it is implosive if the sum is negative. Since the

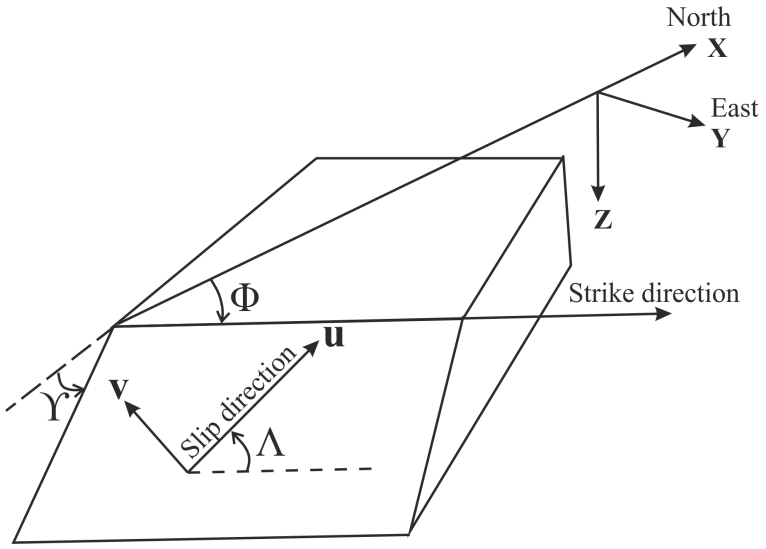

Figure 3.4: Definition of fault-plane parameters in the Cartesian coordinates (x,y,z). The strike Φ is measured clockwise from North ($0 \leqslant \Phi \leqslant 2\pi$), the dip Υ is measured down from horizontal ($0 \leqslant \Upsilon \leqslant \pi/2$) and slip (or rake) Λ is measured in the fault plane with the angle between direction of strike and slip ($-\pi \leqslant \Lambda \leqslant \pi$). $\mathbf{u}$ and $\mathbf{v}$ are the slip vector and fault normal vector, respectively. Figure is modified from Aki & Richards (2002).

seismic moment tensor is symmetric and real, M_{ij} can be decomposed in different ways, such as into isotropic and deviatoric terms. The deviatoric component represents a double couple source if one eigenvalue equals zero. Otherwise, if none of the eigenvalues equals zero, the moment tensor can be defined by a major and minor double couple (Kanamori & Given, 1981), or a double couple and a compensated linear vector dipole (CLVD) (Knopoff & Randall, 1970). In this thesis the moment tensor I implement is a pure double couple source. For a pure double couple source, the principal axis (i.e., the eigenvector) corresponding to the negative eigenvalue is the pressure axis, the principal axis corresponding to the positive eigenvalue is the tension axis, and the null axis is associated with the eigenvalue of zero.

Figure 3.5 shows the Cartesian and spherical polar coordinates used for the analysis of radial and transverse components (i.e., r, θ and ϕ) of the radiated seismic wavefield from a seismic source. The P- and S-wave radiation patterns in the far field are given by

Aki & Richards (2002), respectively

$$\begin{aligned} A_P &= \sin 2\theta \cos\varphi \, \hat{\mathbf{r}} \\ A_S &= \cos 2\theta \cos\varphi \, \hat{\boldsymbol{\theta}} - \cos\theta \sin\varphi \, \hat{\boldsymbol{\varphi}}, \end{aligned} \tag{3.13}$$

where A_P is the radial component which is explicitly proportional to ($\sin 2\theta \cos\varphi \, \hat{\mathbf{r}}$), and A_S is the transverse component which is proportional to ($\cos 2\theta \cos\varphi \, \hat{\boldsymbol{\theta}} - \cos\theta \sin\varphi \, \hat{\boldsymbol{\varphi}}$). It can be seen from Equation 3.13 that the far field displacement terms can be obtained from the two radiation patterns of a double couple source.

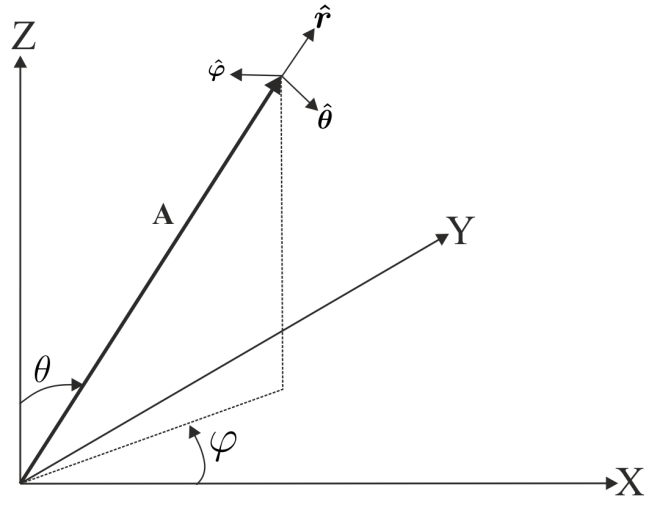

Figure 3.5: Cartesian and spherical polar coordinates for analysis of radial and transverse components of displacement radiated by a double couple. Figure is modified from Aki & Richards (2002).

Figure 3.6 shows how the radial (P) wave (Figure 3.6a) and transverse (S) wave (Figure 3.6b) displacement radiation pattern due to a double couple source, where the arrows at the centre denote the orientation of shear dislocation. In Figure 3.6a the radiation pattern is proportional to $\sin 2\theta$. The plus sign indicates outward direction (compres-

sional) first motion while the minus sign indicates inward direction (dillational) first motion of the radial wave (i.e, P-wave). Figure 3.6b depicts the pattern of displacement due to the a double couple source which is proportional to $\cos 2\theta \cos \varphi \, \hat{\boldsymbol{\theta}} - \cos \theta \sin \varphi$. Again the central arrows depict the orientations of shear dislocation and arrows on each lope indicates the direction of the shear-wave displacement.

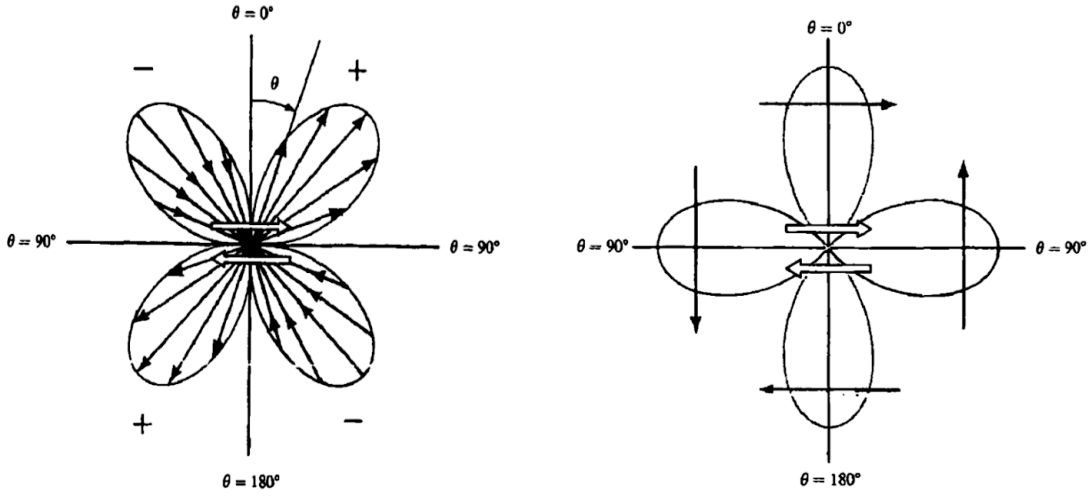

Figure 3.6: Radiation pattern of radial (a) and transverse (b) component of displacement due to the a double couple source mechanism. Figure from Aki & Richards (2002).

3.6 Seismic anisotropy

Seismic anisotropy is defined to be the dependence of seismic velocity upon propagation direction or angle (Thomsen, 2002). The angle refers to the polar angle (from vertical) as well as azimuthal angle. Seismic anisotropy has become a powerful tool in geophysics with vast applications from mantle convection, plate boundaries and lithospheric structure (e.g., Silver, 1996; Nataf et al., 1984) to hydrocarbon exploration and extraction (e.g., Kendall et al., 2007; Verdon et al., 2011a) and monitoring of CO2 storage sites (e.g., Verdon et al., 2011b). There are several causes of seismic anisotropy in the earth

but in the upper crust it can be influenced by two main factors; structural anisotropy and stress-related anisotropy. Seismic anisotropy can result from various causes: (1) intrinsic anisotropy due to preferentially aligned minerals, crystals and grains (e.g., Valcke et al., 2006; Hall et al., 2008), (2) preferred orientation of rock fabric, cracks, fractures and joints (e.g., Hudson, 1981), (3) rock layering in sedimentary rocks (e.g., Backus, 1962), (4) direct stress-induced anisotropy (e.g., Nur & Simmons, 1969 and Crampin & Zatsepin, 1997). In hydrocarbon exploration, seismic velocity (or travel time) is one of the key seismic attributes, and in the presence of the seismic anisotropy shows directional dependence. There are other key seismic attributes, however, such as amplitude and seismic polarization.

The concept of anisotropy is closely related to geophysical concept of heterogeneity. A medium is anisotropic when its properties change with propagation direction at a specific location, whereas the medium is heterogeneous if its properties change with location for a specific direction (Winterstein, 1990). The concept of anisotropy and heterogeneity are scale dependent. It means that when the wavelength is larger than the scale length of the heterogeneity, the medium may behave as an anisotropic medium, whereas if the seismic wavelength is comparable to or less than the scale length of the heterogeneity, the medium can be treated as a heterogeneous medium. For instance, on the larger scale shales appear homogeneous, but on the microscopic scale, shales are heterogeneous (Figure 3.7).

Seismic anisotropy in the Earth can be complicated due to the numerous sources of anisotropy. However, analysis of seismic anisotropy can still yield useful characterisation of the source of anisotropy. In sedimentary rocks, there are two common types of seismic anisotropy: transverse isotropy (TI) with vertical symmetry axis (VTI), which is observed in most sedimentary rocks due to the presence of horizontal layering, and horizontal transverse isotropy (HTI) which is observed in many fractured reservoirs.

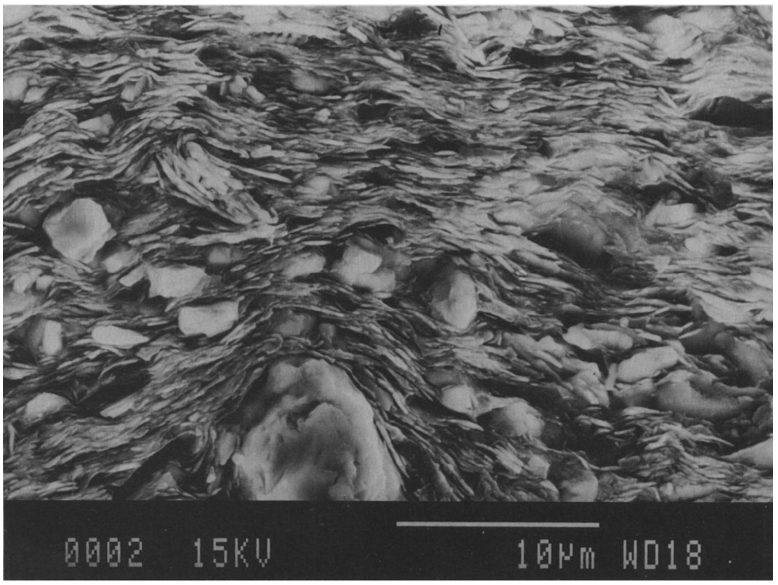

Figure 3.7: Scanning electron microphotograph of a shale. Shale (platey particles) in the small scale appears a heterogeneous medium. Figure from Hornby et al. (1994).

VTI and HTI are also referred to as polar anisotropy and azimuthal anisotropy. In general, VTI is related to layering or bedding, whereas HTI is related to vertically oriented fracture or joint sets.

Fractures or small cracks in hydrocarbon reservoirs can have preferred orientations due to a variety of stress-induced processes, such as subcritical crack growth leading azimuthal anisotropy (Crampin, 1981; Crampin et al., 1983). Typically, fracture-induced anisotropy is equivalent to HTI media if the scale of the fractures or cracks are much smaller than the seismic wavelength of the probing wave. Studies have shown that the response of waves is sensitive to fracture properties, such as fracture orientation and fracture density, which can be used to as an indirect means to characterise fractured reservoirs (e.g., Liu & Gao, 2013; Tsvankin & Grechka, 2011). The strength of anisotropy is proportional to the crack density (ϵ) of the fracture system.

A fractured medium can be dry or fluid saturated, which can influence the overall stiffness of the medium. Thus, it is necessary to understand the effect of fracture properties, such as fracture infill, on the overall stiffness of the medium. The aligned

fractures exhibit effective anisotropy in the limit of low frequency waves (i.e, long-wavelength approximation, LWA) where the fluid flows between fractures and pore space. This happens due to the equilibration of pore fluid pressure with dynamic pressure changes caused by the transient wave that sometimes result in anisotropy frequency dependence (Zatsepin & Crampin, 1997; Liu et al., 2003; Maultzsch et al., 2003; Baird et al., 2014; Galvin & Gurevich, 2015).

There are a number of attributes that can be used to characterise fractured reservoirs: P-to-S mode conversion where the S-wave splitting of the upgoing S-wave is valid for the analysis of fractured medium (e.g., Rüger, 1997; Qian et al., 2007; Far & Hardage, 2016). Lynn (2004) use P-wave data because it is easier and cheaper to acquire with high resolution than S-wave and converted PS-wave methods. Using P-wave seismic attribute includes various attributes such as amplitude, velocity, travel time and AVO/AVOA gradient are observed to be related to the fracture size (e.g., Vlastos et al., 2003), density (e.g., Pearce, 2003; Vlastos et al., 2003, fracture spacing (Willis et al., 2004a) and orientation (e.g., Pérez et al., 1999; Vlastos et al., 2003).

3.6.1 Hooke's law for isotropic media

In an isotropic elastic medium the stress and strain are linearly related by Hooke's law using two constants (i.e., Lamé parameters λ and μ),

$$\sigma_{ij} = \lambda\delta_{ij}\varepsilon_{kk} + 2\mu\varepsilon_{ij} \tag{3.14}$$

or alternatively in terms of Young's modulus E and Poisson's ratio ν (Mavko et al., 2009) in the following form

$$\varepsilon_{ij} = \frac{1}{E}[(1+\nu)\sigma_{ij} - \nu\delta_{ij}\sigma_{kk}], \tag{3.15}$$

where σ_{ij} is the stress tensor, σ_{kk} is the sum of 3 principal stresses, ε_{ij} is the strain tensor, and δ_{ij} is the Kronecker delta function.

3.6.2 Hooke's law for general anisotropic media

In general anisotropic elastic media the relationship between stress σ_{ij} and strain ε_{ij} is given through a fourth-rank stiffness or compliance tensor as follows

$$\sigma_{ij} = C_{ijkl}\varepsilon_{kl}, \tag{3.16}$$

or alternatively:

$$\varepsilon_{ij} = S_{ijkl}\sigma_{kl}, \tag{3.17}$$

where C_{ijkl} is the stiffness tensor and S_{ijkl} is the compliance tensor. Both matrices have the subscribe values $i = 1, 2, 3$ and $j = 1, 2, 3$.

There are several different symmetry systems of anisotropic media, which may result in different physical properties and wave phenomena. The elastic tensor C_{ijkl} (or its inverse, $S = C^{-1}$) is $3 \times 3 \times 3 \times 3$ tensor (i.e, 81 components in total). However, due to the symmetry of stress and strain tensors, the independent components reduce from 81 to 21 components. The subscripts in the stiffness and compliance tensors can be simplified to J and K by using Voigt notation,

$$\begin{array}{c|cccccc} ij(kl) & 11 & 22 & 33 & 23 = 32 & 13 = 31 & 12 = 21 \\ \downarrow & \downarrow & \downarrow & \downarrow & \downarrow & \downarrow & \downarrow \\ J(K) & 1 & 2 & 3 & 4 & 5 & 6 \end{array} . \tag{3.18}$$

Therefore the strain and stress components will be as,

$$\begin{bmatrix} \varepsilon_1 \\ \varepsilon_2 \\ \varepsilon_3 \\ \varepsilon_4 \\ \varepsilon_5 \\ \varepsilon_6 \end{bmatrix} = \begin{bmatrix} \varepsilon_{11} \\ \varepsilon_{22} \\ \varepsilon_{33} \\ 2\varepsilon_{23} \\ 2\varepsilon_{13} \\ 2\varepsilon_{12} \end{bmatrix} \tag{3.19}$$

$$\begin{bmatrix} \sigma_1 \\ \sigma_2 \\ \sigma_3 \\ \sigma_4 \\ \sigma_5 \\ \sigma_6 \end{bmatrix} = \begin{bmatrix} \sigma_{11} \\ \sigma_{22} \\ \sigma_{33} \\ \sigma_{23} \\ \sigma_{13} \\ \sigma_{12} \end{bmatrix} \tag{3.20}$$

Finally, the Voigt convention of the elastic stiffness is formed as

$$\boldsymbol{C} = \begin{bmatrix} C_{11} & C_{12} & C_{13} & C_{14} & C_{15} & C_{16} \\ C_{12} & C_{22} & C_{23} & C_{24} & C_{25} & C_{26} \\ C_{13} & C_{23} & C_{33} & C_{34} & C_{35} & C_{36} \\ C_{14} & C_{24} & C_{34} & C_{44} & C_{45} & C_{46} \\ C_{15} & C_{25} & C_{35} & C_{45} & C_{55} & C_{56} \\ C_{16} & C_{26} & C_{36} & C_{46} & C_{56} & C_{66} \end{bmatrix}. \tag{3.21}$$

In addition to the symmetry system (i.e, the symmetry of elastic properties) of a medium, there is another concept of symmetry which is the symmetry of the constituents (e.g, solid grains) of a medium (Winterstein, 1990). In fact, the symmetry system of a medium is always as high as or higher than the symmetry of its constituents. Furthermore, by increasing the symmetries, fewer independent parameters are needed to characterise the media. Winterstein (1990) introduced symmetry systems by using sets of parallel planar cracks into a homogeneous isotropic rock. Hexagonal symmetry system is related to a medium with one set of vertical or horizontal fractures. A medium with hexagonal symmetry system is most commonly considered in exploration geophysics. For such media, the elastic stiffness tensor has the following form

$$\boldsymbol{C}_{VTI} = \begin{bmatrix} C_{11} & C_{11}-2C_{66} & C_{13} & 0 & 0 & 0 \\ C_{11}-2C_{66} & C_{11} & C_{13} & 0 & 0 & 0 \\ C_{13} & C_{13} & C_{33} & 0 & 0 & 0 \\ 0 & 0 & 0 & C_{55} & 0 & 0 \\ 0 & 0 & 0 & 0 & C_{55} & 0 \\ 0 & 0 & 0 & 0 & 0 & C_{66} \end{bmatrix} \tag{3.22}$$

$$\boldsymbol{C}_{HTI} = \begin{bmatrix} C_{11} & C_{13} & C_{13} & 0 & 0 & 0 \\ C_{13} & C_{33} & C_{33}-2C44 & 0 & 0 & 0 \\ C_{13} & C_{33}-2C44 & C_{33} & 0 & 0 & 0 \\ 0 & 0 & 0 & C_{44} & 0 & 0 \\ 0 & 0 & 0 & 0 & C_{55} & 0 \\ 0 & 0 & 0 & 0 & 0 & C_{55} \end{bmatrix}. \tag{3.23}$$

Another symmetry system considered in this thesis is orthorhombic symmetry which is formed by embedding two sets of orthogonal and vertical fractures in an isotropic medium. However, there are other forms of orthorhombic symmetry system; one set of fractures embedded in a VTI background medium or even two sets of vertical and orthogonal fractures in a VTI background medium (Bakulin et al., 2000). The elastic stiffness of an orthorhombic symmetry medium is

$$\boldsymbol{C}_{Orth} = \begin{bmatrix} C_{11} & C_{12} & C_{13} & 0 & 0 & 0 \\ C_{12} & C_{22} & C_{23} & 0 & 0 & 0 \\ C_{13} & C_{23} & C_{33} & 0 & 0 & 0 \\ 0 & 0 & 0 & C_{44} & 0 & 0 \\ 0 & 0 & 0 & 0 & C_{55} & 0 \\ 0 & 0 & 0 & 0 & 0 & C_{66} \end{bmatrix} . \tag{3.24}$$

In comparison to the TI or hexagonal symmetry system (with five independent elastic stiffness constants), the orthorhombic symmetry system medium has nine independent elastic stiffness constants.

Thomsen (1986) reveals that for sedimentary rock, anisotropy is weak. So, to simplify the description of weak anisotropic, Thomsen (1986) introduced an alternative notation for VTI media in terms of seismic velocities and three anisotropic parameters as

$$\begin{aligned} V_{P0} &= \sqrt{\frac{c_{33}}{\rho}} , \qquad \varepsilon = \frac{C_{11} - C_{33}}{2C_{33}} , \\ V_{S0} &= \sqrt{\frac{C_{44}}{\rho}} , \qquad \gamma = \frac{C_{66} - C_{44}}{2C_{44}} , \\ \delta &= \frac{(C_{13} + C_{44})^2 - (C_{33} - C_{44})^2}{2C_{33}(C_{33} - C_{44})} , \end{aligned} \tag{3.25}$$

where V_{P0} and V_{S0} are respectively the vertical P- and S-wave velocity, ρ is the bulk density, ε and γ represent the strength of the P- and S-wave anisotropy, respectively, and δ represents the P-wavefront ellipticity. In general, for most sedimentary rocks that are weakly anisotropic, the anisotropy parameters ε, γ and δ are less than 0.2. If the

anisotropic is weak, the quadratic expression above for δ can be simplified (Thomsen, 2002)

$$\delta \to \delta_{weak} = \frac{C_{13} - C_{33} + 2C_{44}}{C_{33}}. \tag{3.26}$$

The phase velocity of seismic waves in weakly anisotropic rocks can be defined (Thomsen, 1986)

$$\begin{aligned} V_P(\theta) &= V_{P0}\left(1 + \delta sin^2\theta cos^2\theta + \varepsilon sin^4\theta\right) , \\ V_{SV}(\theta) &= V_{S0}\left(1 + \frac{\alpha^2}{\beta^2}\left(\varepsilon - \delta\right) sin^2\theta cos^2\theta\right) , \\ V_{SH}(\theta) &= V_{S0}\left(1 + \gamma sin^2\theta\right) , \end{aligned} \tag{3.27}$$

where V_P, V_{SV} and V_{SH} are the phase velocities for the P-, SV- and SH-waves, respectively, and θ is the angle between the wavefront normal and the symmetry axis.

3.7 Shear-wave splitting analysis

3.7.1 Introduction

Seismic anisotropy is manifested in many ways, such as leading to anisotropic velocity models and amplitude versus offset and azimuth (AVOA) anomalies in reflection seismology. Shear-wave splitting (SWS) from P-to-S mode converted waves in reflection seismic data and transmitted S-waves in microseismic data represents the most unambiguous measure of seismic anisotropy (e.g., Wookey, 2012). When an S-wave

propagating within an isotropic medium encounters an anisotropic medium, the shear wave splits into a fast (S_1) and a slow (S_2) wave component depending on the initial S-wave polarisation and the allowable polarisations defined by the anisotropic elasticity tensor (e.g., Angus et al., 2004). SWS measures the associated S_1 polarisation direction (ϕ) and the delay time (δt) between the S_1 and the S_2 waves (e.g., Shearer, 2009). This delay time is proportional to the length of the ray path inside the anisotropic material and the strength of the seismic anisotropy (e.g., Wuestefeld et al., 2011). Figure 3.8 shows a schematic of SWS in the two common TI symmetry models, HTI and VTI media. Depending on the initial polarisation of the incident S-wave, the medium can split the incident S-wave into the S_1 and S_2 waves. There is no splitting where the initial S-wave polarisation is parallel to the fracture plane or perpendicular to the fracture plane (see Figure 3.8).

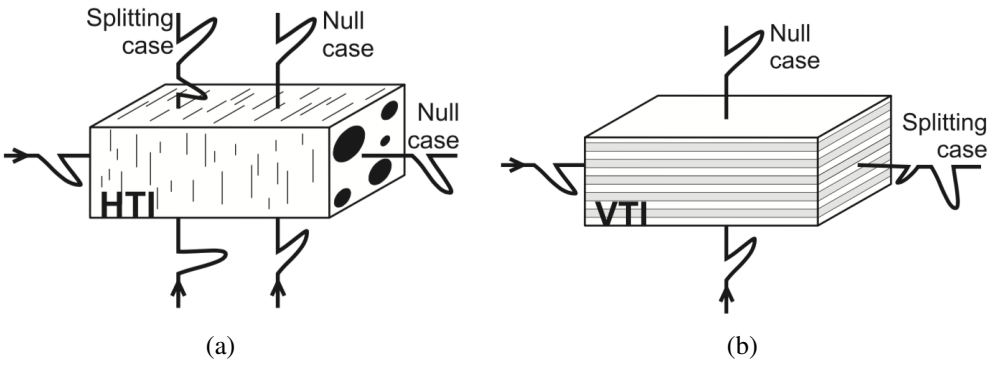

Figure 3.8: Shear-wave splitting in two common TI anisotropy: (a) HTI and (b) VTI. Shear-wave splitting occurs for non-parallel rays to the symmetry axis. Specific combination of symmetry axis and initial polarisation leads null splitting results. Figure from Wuestefeld et al. (2010).

Significant contributions to our understanding of the Earth's subsurface developed through the analysis of SWS; seismic anisotropy was observed to be widespread within the crust (e.g., Crampin et al., 1980) and upper mantle (e.g., Ando & Ishikawa, 1980). Within the crust, seismic anisotropy measured from shear-waves has identified the

presence of coherent and often critically stressed fractures (e.g., Crampin, 1978; Hudson, 1981; Crampin, 1984; Crampin & Peacock, 2005).

Historically, SWS methods involved manual analysis of waveforms (e.g., Buchbinder, 1985; Booth et al., 1985a; Booth & Crampin, 1985b) and so were subjective and time consuming, especially for large datasets which were becoming increasingly common (e.g., Aster et al., 1990; Ryall & Savage, 1974). Shih et al. (1989) and Savage et al. (1989) developed an objective and automated approach for calculating SWS in which the aspect ratio of particle motion is projected onto an orthogonal plane, where the fast polarisation direction is estimated by maximising the aspect ratio as a function of strike, and the delay time is estimated by finding the maximum correlation between the S_1 and S_2 waves (e.g., Shih et al., 1989). Although additional enhancements were also proposed by Aster et al. (1990), there were several limitations with this approach. For example, these methods did not automatically select the analytical window for SWS and only used a small subset of the waveform (Teanby et al., 2004a). The subjective window choice gave widely varying results for even slightly different window choices and the use of limited waveform information caused the SWS calculations more susceptible to noise (Teanby et al., 2004a). The issue of using the whole waveform instead of a small subset was solved by Silver & Chan (1991) and was later expanded on by Teanby et al. (2004a) to enable selecting the analytical window objectively and automatically.

In this study, I use the SHEar-wave Birefringence Analysis (SHEBA) algorithm developed by Teanby et al. (2004a) to conduct the analysis of SWS. In SWS analysis, the δt is used to characterise the strength of anisotropy along the raypath. The δt parameter is normalised by the path length to estimate the percentage velocity anisotropy δV_S (i.e., difference between S_1 and S_2 velocity). The δV_S parameter is computed using the following relationship: $100 \times (V_{S1} - V_{S2})/((V_{S1} + V_{S_2})/2)$.

3.7.2 Methodology

3.7.2.1 Rotation to the ray frame and filtering

In microseismic monitoring, the rays are not always subvertical and so the S-wave energy will not be predominantly on the horizontal components. Thus, to improve the clarity of S-waves and also to have more accurate shear-wave splitting measurements, the seismic data in the acquisition frame (i.e., geographical coordinate system) are rotated to the ray frame coordinate (L-SH-SV). The L-axis is the ray direction which contains the P-wave, and SH- and SV-axes contain the S-waves which are normal to the L-axis. Rotation to the ray frame is performed using the P-wave particle motion to point out the direction of the ray, using the *protate* algorithm presented by Al-Anboori (2005). The P-wave particle motion is parallel or near parallel to the ray direction in isotropic or weakly anisotropic media (Al-Harrasi, 2010). Next, a P-wave window is selected manually, whose length varies from one to many cycles dependent on the separation of the P- and S-wave. The rotation angles in the horizontal and vertical planes are estimated based on the least absolute residuals ($L1$ norm) perpendicular to the line. The uncertainty of this method is measured by a bootstrap technique (Press, 1989). For cases where the P-wave can not be picked, or the rotation is not acceptable, the data are rotated using the azimuth and inclination assuming a straight source-receiver path. Figure 3.9 depicts the rotation from the geographic to ray frame coordinate. After rotation the data are filtered using a Butterworth bandpass filter between 10 Hz and 1500 Hz, which is the range of the expected frequencies. Since the manual P-wave window picking is a time consuming process, Al-Harrasi (2010) presents a fixed P-wave window relative to the P-wave time pick following the construction of the hodograms by looping over the chosen event.

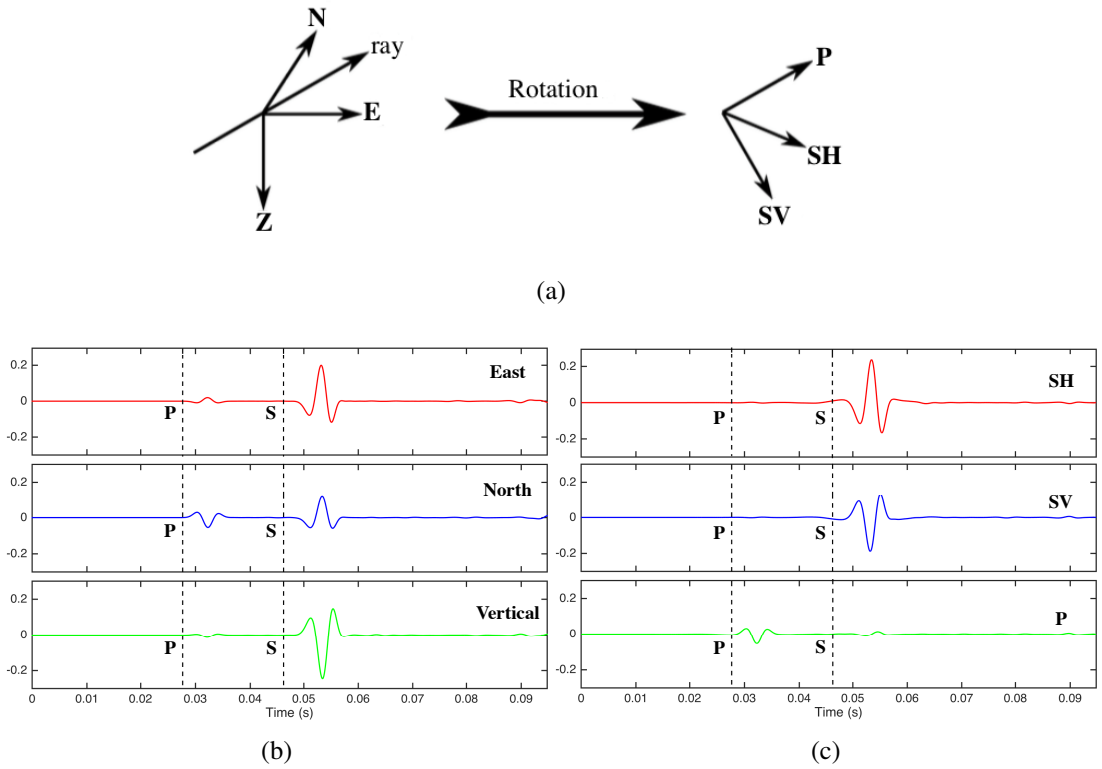

Figure 3.9: Rotation from geographic to ray coordinate. (a) Schematic illustrate of rotation. seismograms before (b) and after (c) rotation to ray frame. Notice the S-wave energy on the SH- and SV- axes are increased, while the P-wave energy are minimised. P-wave energy increases on P-axis while s-wave energy is minimised. The part (a) is modified from Al-Harrasi (2010).

3.7.2.2 Cluster analysis

A standard technique for measuring SWS is the method of Silver & Chan (1991). The technique requires a manual selection of the S-wave window, where the SWS parameters ϕ and δt are estimated using a grid search over ϕ and δt. In fact, if the SWS has occurred, the S-wave particle motion is elliptical. So, the grid search attempts to linearise the particle motion which is stable and reliable. An issue encountered with manual selection is that the SWS calculation is sensitive to the chosen S-wave window. Teanby et al. (2004a) introduced an automated approach to remove the subjective window of the results by incorporating a cluster analysis technique in SWS analysis. The cluster

approach of Teanby et al. (2004a) performs the SWS analysis to achieve the best cluster of results over many windows around the S-wave. This results in the most stable and reliable result for ϕ and δt.

The automation approach initiates by setting up a grid analysis window. The grid analysis incorporates the construction of many windows with different lengths. Figure 3.10 depicts a schematic of the grid window analysis. The analysis begins with choosing the window before the S-wave time pick (T_S) which varies between T_{beg_0} and T_{beg_1}. Similarly, the window after T_S expands between T_{end_0} and T_{end_1}. The analysis window starts at T_{beg} and ends at T_{end}. T_{beg} is allowed to vary with N_{beg} steps of ΔT_{beg} and similarly T_{end} is allowed to vary with N_{end} steps of ΔT_{end}. Therefore, the total number of windows will be $N = N_{beg} \times N_{end}$. The two boundaries of the SWS analysis window are defined as,

$$T_{beg} = T_{beg_1} - (i-1)\Delta t_{beg} \qquad \text{for} : i = 1 \ldots\ldots N_{beg} \tag{3.28}$$

$$T_{end} = T_{end_0} + (j-1)\Delta t_{end} \qquad \text{for} : j = 1 \ldots\ldots N_{end} \tag{3.29}$$

T_{beg_0}, T_{beg_1}, T_{end_0} and T_{end1} are defined relative to T_S. Generally, by increasing the number of windows, the window length increases. The window analysis for $N = 250$ is shown in figure 3.11. The window parameters must be chosen precisely such that no more phases aside from the S-wave are included. However, by increasing N the cluster analysis becomes more time consuming. Considering the results of the window analysis with different N, I choose $N = 30$ (i.e., $N_{beg} = 5$ and $N_{end} = 6$) for this study. Based on the uncertainty in the picking time and the dominant period of the source (5.5 ms) in this study, I choose $T_{beg1} = 2$ ms before T_S and $T_{beg0} = 5$ ms. T_{end0} and T_{end1} are set to 10 ms and 12 ms, respectively.

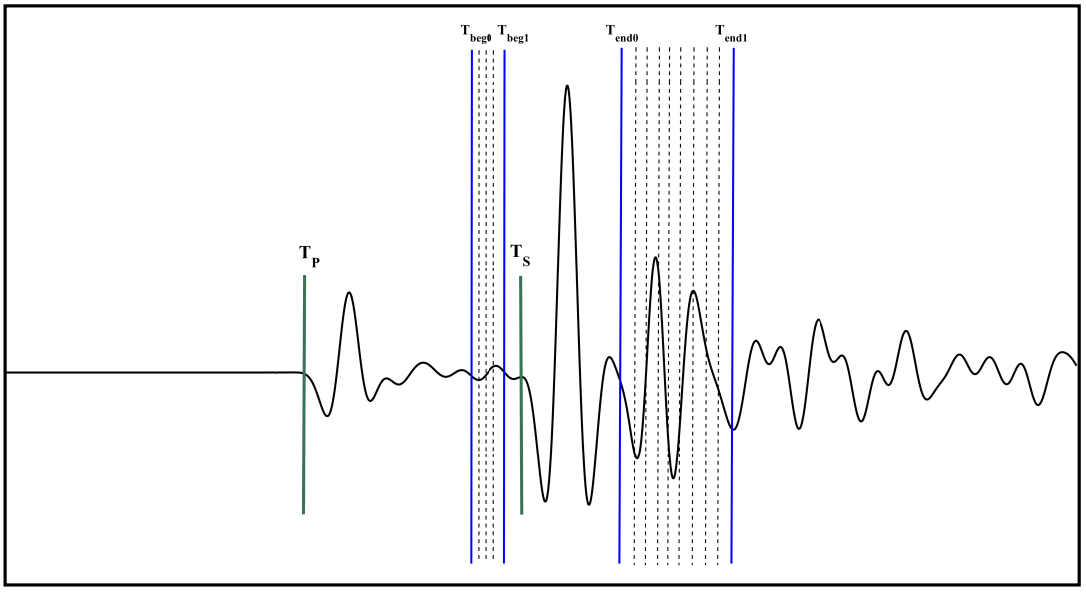

Figure 3.10: Cluster analysis of SWS. T_P and T_S depicts the onset of P- and S-waves respectively. The start of analysis window is expanded between T_{beg0} and T_{beg1} while the end of window is expanded between the T_{end0} and T_{end1}.

3.7.2.3 Choice of automation parameters

Implementation of Teanby et al. (2004a) requires a number of guidelines that must be considered:

- The analysis window should be expanded over several dominant periods to reduce the cycle skipping effects and reduce the influence of noise.
- The window should not be so long to include P-wave or the secondary phase of S-waves. These are can reduce the reliability of splitting measurements.
- Large N and small Δt can render more reliable estimation. N_{end} should be larger than N_{beg}.
- T_{beg_1} should be selected slightly before the onset of the S-wave keeping in mind the uncertainty of the S-wave onset.

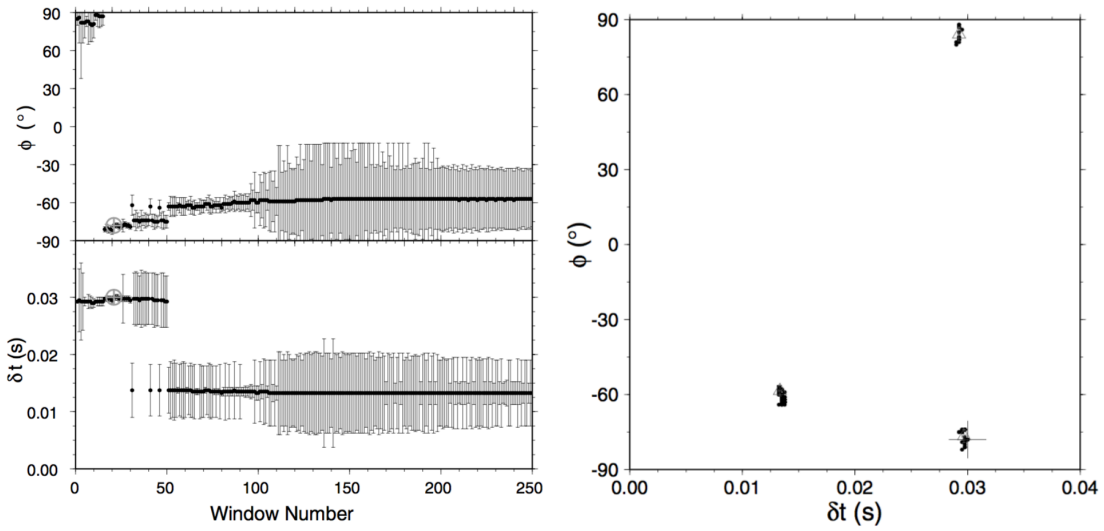

Figure 3.11: Shear-wave splitting cluster analysis. (a) Measurements of δt and ϕ obtained from 250 different analysis windows plotted against window number. (b) Stable results correspond to plateaus with small error bars which is denoted by the gray crosshairs. Figure from Teanby et al. (2004a).

3.7.2.4 Quality of the splitting measurements

There are two common techniques to estimate the splitting parameters. The first type (so-called multi-event technique) performs the analysis: on a suite of stations from different azimuths, simultaneously. Vinnik et al. (1989) proposed the stacking of transverse components with weights dependent on azimuth. In this approach, ϕ is derived from the maximum weighted amplitude and δt is retrieved from the maximum stacked amplitude of the transverse component. However, the method is deprived of error calculation. Chevrot (2000) proposed to project the transverse components on the amplitudes of the time derivatives of radial components known as splitting components. The fast S-wave polarisation and time delay are estimated by the best fit of the phase and amplitude, respectively. The method is applicable when the signal-to-noise ratio (S/N) is low. The multi-event technique has been applied in some teleseismic studies (e.g., Vinnik et al., 1989; Dricker et al., 1999; Menke & Levin, 2003; Long & van der Hilst, 2006).

The second type of technique calculates the splitting parameters based on each

raypath (Ando & Ishikawa, 1980; Fukao, 1984; Silver & Chan, 1991). The technique is based on a grid search to remove the effects of splitting. Two methods are used to compare the results of SWS; the cross-correlation method (XC hereafter) and the eigenvalue method (EV hereafter). Both methods are automated methods which use the cluster technique of Teanby et al. (2004a). The XC method rotates the seismograms in the ray frame and seeks the orientation where the cross-correlation coefficient is maximum and thus leading to the SWS parameters ϕ_{XC} and δt_{XC} (e.g., Ando & Ishikawa, 1980). The EV method rotates the shear components and applies a time-shift in the ray frame to return the most singular covariance matrix based on its eigenvalues λ_1 and λ_2 (e.g., Fukao, 1984). Silver & Chan (1991) performed this by maximising λ_1 or λ_1/λ_2 and minimising λ_2 or λ_2/λ_1. Wuestefeld et al. (2010) found that minimising λ_2/λ_1 renders the most reliable results for the SWS parameters ϕ_{XC} and δt_{XC}. The grid search in both methods (EV and XC) vary between 0 ms and 5 ms for Δt, and between -90° and 90° for ϕ.

An increase in confidence of the results can be achieved by stacking multiple error surfaces (Wuestefeld et al., 2010). Wolfe & Silver (1998) proposed stacking with normalised error surfaces while Restivo & Helffrich (1999) performed the stacking of error surfaces with S/N. An alternative stacking method was presented by Teanby et al. (2004a) in which the results are stacked from neighbouring stations in a vertical borehole array.

The process of SWS is sensitive to the window selection and so can lead to several pitfalls (see Vecsey et al., 2007). Moreover, the SWS process includes some manual steps, such as picking and visual control of the waveforms and diagnostic plots (e.g., Teanby et al., 2004a; Wüstefeld et al., 2008). Therefore, Wuestefeld et al. (2010) modified the method of Wüstefeld & Bokelmann (2007) to present a numerical value for SWS quality ($\mathbb{Q}$). The method begins with the calculation of two parameters:

the ratio between the delay times in the XC and EV methods ($\Delta = \delta t_{XC}/\delta t_{EV}$) and the normalised misfit between the fast polarisation between the two methods ($\Omega = (\phi_{EV} - \phi_{XC})/45°$). The parameter Δ varies between 0 and ∞, whereas the parameter Ω ranges between 0 and 1. The SWS measurements can be classified as good, poor and good null based on values of Δ and Ω. Ideal good measurements are achieved when the measurements from both methods are identical (i.e., $\Delta = 1$, $\Omega = 0$). In contrast, the ideal null occurs when $\delta t_{XC} = 0$ ($\Delta = 0$) and the fast polarisation differ by 45° ($\Omega = 1$). So the quality of SWS measurements are determined based on how far the values vary between these two ideal extreme points. Wuestefeld et al. (2010) defined d_{null} as distance from $\Omega = 1$ and d_{good} as distance from the ideal good ($\Delta = 1$) as

$$
\begin{aligned}
d_{null} &= \sqrt{2(\Delta^2 + (\Omega - 1)^2)} \\
d_{good} &= \sqrt{2((\Delta - 1)^2) + \Omega^2)} \\
\mathbb{Q} &= \begin{cases} -(1 - d_{null}): & \text{for } d_{null} < d_{good} \\ (1 - d_{good}): & \text{for } d_{null} \geq d_{good}. \end{cases}
\end{aligned}
\tag{3.30}
$$

The $\mathbb{Q}$ ranges from +1 (good) to 0 (poor) and -1 (good null). I define the quality category ranges as: good ($\mathbb{Q} \geqslant 0.75$), fair ($0.75 > \mathbb{Q} \geqslant 0.25$), poor ($0.25 > \mathbb{Q} \geqslant -0.25$), fair null ($-0.25 > \mathbb{Q} \geqslant -0.75$) and good null ($-0.75 > \mathbb{Q}$). The quality of each window $\mathbb{Q}_{win}$ varies in the automated cluster analysis. So, Wuestefeld et al. (2010) suggest a way to estimate the best quality $\mathbb{Q}_{best}$ for a event with N cluster windows as

$$
\mathbb{Q}_{event} = \omega_1 \frac{\sum \mathbb{Q}_{win}}{N} + \omega_2 \mathbb{Q}_{best}, \tag{3.31}
$$

where $\omega_{1,2}$ are weighting factors that determine the average and best quality, respectively.

I chose $\omega_1 = \frac{1}{3}$ and $\omega_2 = \frac{2}{3}$.

3.7.2.5 Workflow of automated S-wave splitting

The workflow of the automated SWS using cluster analysis is shown in Figure 3.12. By assuming that the direct P- and S-waves have previously been picked and the geometrical information regarding the source and receivers are available, SWS is performed using the following steps:

- Rotation from geographic to ray frame coordinates (i.e, E-N-Z to L-SH-SV) by maximising the P-wave energy on L-component.
- Performing SWS using cluster analysis for 30 different windows, taking into consideration that the S-wave window excludes the P-wave. The splitting parameters (ϕ and δt) are estimated using both XC and EV techniques.
- Quality determination ($\mathbb{Q}$) of SWS measurements by comparing the results of both methods. Select good measurements for inversion or interpretation.

3.8 Fracture inversion

There have been several studies that have used SWS results to infer (e.g., Teanby et al., 2004b; Al-Harrasi et al., 2011) or invert (e.g., Verdon et al., 2009; Verdon et al., 2011b; Verdon & Wüstefeld, 2013) for various fracture properties, such as fracture density and orientation. The inversions use sets of delay times and fast polarisation directions along with source-to-receiver information such as ray path azimuth, inclination, and propagation distance. Unlike SWS seismic anisotropy studies, application of SWS fracture inversion has been limited due to its inherent complexity as a non-linear problem (Horne & MacBeth, 1994). One of the first attempts at solving this problem

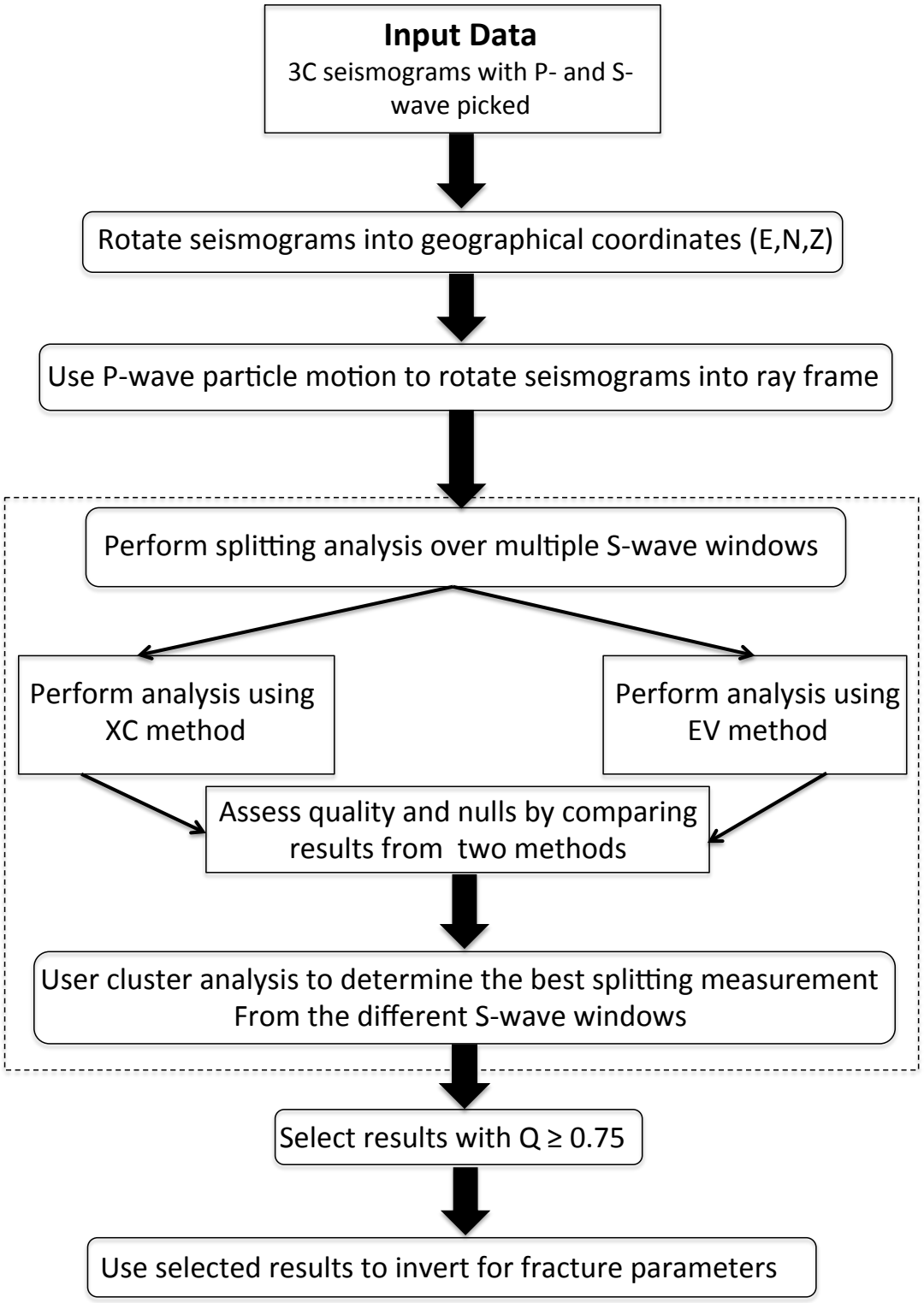

Figure 3.12: Workflow of automated S-wave splitting. Figure is modified from Wuestefeld et al. (2010).

was done using forward modelling, either using trial and error or a pre-calculated database of SWS attributes (MacBeth, 1991), yet this was time consuming (Horne & MacBeth, 1994). The lack of efficient inversion algorithms for fracture inversion led to more sophisticated inversion schemes, such as trying to linearise the problem using degenerate perturbation theory for weakly anisotropic cases (Chapman & Pratt, 1992) and genetic algorithms (Horne & MacBeth, 1994). Both of these methods only considered fracture distribution in two-dimensions (2D), which was mainly due to the increase in mathematical complexity and computational expense associated with 3D (Horne & MacBeth, 1994). Rial et al. (2005) developed a method allowing 3D variations, where the theoretical values of the delay time and fast polarisation angle could be calculated by evaluating the eigenvectors and eigenvalues of a Kelvin-Christoffel matrix (this corresponds with an elastic stiffness matrix devised by MacBeth, 1999). Those theoretical values would be compared with the values calculated from measured data, then the pair with the best root-mean-square (RMS) misfit is chosen, and finally the desired properties are calculated from their theoretical relationships (Rial et al., 2005). A similar approach was made by Verdon et al. (2009, 2011b) by using more comprehensive rock physics models that allow for the inversion of multiple fracture sets and fracture properties. This approach has been extended to allow for fracture compliance inversion (Verdon & Wüstefeld, 2013). A problem with these methods is that they consider the whole medium in which the ray propagates to be an effective fractured medium, which can lead to an underestimate of the fracture density. While there exist other approaches that allow spatial variation in anisotropy and isotropic regimes (Abt & Fischer, 2008; Wookey, 2012), they tend to be under-determined problems due to requiring significantly more model parameters (Verdon et al., 2009).

A common approach to modelling fractures is to assume an effective medium representation of the fracture volume. Effective medium theories are employed when

the size of inclusions is substantially less than the seismic wavelength (e.g. Liu et al., 2000) and are a popular approach for modelling fractures since only general properties of the fracture system are required (i.e., we do not need a deterministic model). In the inversion approach, the additional compliance approach of (Schoenberg & Sayers, 1995) is used to represent the influence of fractures on the elasticity tensor. Specifically, the fracture compliance for each fracture set ($\mathbf{\Delta S}$) is added to the background rock compliance ($\mathbf{S_b}$):

$$\mathbf{S} = \mathbf{S_b} + \mathbf{\Delta S_1} + \mathbf{\Delta S_2} + ... + \mathbf{\Delta S_m}, \tag{3.32}$$

where $\mathbf{m}$ is the number of fracture sets present ($\mathbf{m}$ =1 for the single fracture case and $\mathbf{m} = 2$ for the orthogonal fracture case). The background rock compliance ($\mathbf{S_b}$) represents the unfractured rock and can be either isotropic or anisotropic (e.g., vertical transverse isotropy if layering is present) as demonstrated by Verdon et al. (2009). Based on the approach of Schoenberg & Sayers (1995) and for a set of vetical fracture, in a VTI medium, $\mathbf{\Delta S_i}$ is given by the following matrix for each fracture set (Verdon et al., 2011b):

$$\mathbf{\Delta S_i} = \begin{bmatrix} B_N^i & 0 & 0 & 0 & 0 & 0 \\ 0 & 0 & 0 & 0 & 0 & 0 \\ 0 & 0 & 0 & 0 & 0 & 0 \\ 0 & 0 & 0 & 0 & 0 & 0 \\ 0 & 0 & 0 & 0 & B_{Tv}^i & 0 \\ 0 & 0 & 0 & 0 & 0 & B_{Th}^i \end{bmatrix}, \tag{3.33}$$

where B_N^i is the normal compliance of a fracture set while B_{Tv}^i, and B_{Th}^i are the vertical

and horizontal components of the shear compliances. B^i_{Tv} can be set to equal B^i_{Th} if the background rock is isotropic (Verdon et al., 2009), which is the case in this thesis. These compliances can be computed using the following equations by Hudson (1981) for penny-shaped fractures (Verdon et al., 2011b):

$$B^i_N = \frac{4}{3}\frac{\epsilon_i C^r_{11}}{C^r_{66}(C^r_{11} - C^r_{66})} \tag{3.34a}$$

$$B^i_{Th} = \frac{16}{3}\frac{\epsilon_i C^r_{11}}{C^r_{66}(3C^r_{11} - 2C^r_{66})} \tag{3.34b}$$

$$B^i_{Tv} = \frac{16}{3}\frac{\epsilon_i C^r_{33}}{C^r_{44}(3C^r_{33} - 2C^r_{44})}, \tag{3.34c}$$

where ϵ_i is the density of the ith fracture set. Note that all of the fracture densities are based on Hudson (1981) dimensionless fracture density definition (Equation 3.6) using the low-frequency limit, such that the compliance of a fracture set is only dependent on the fracture density (ϵ_i) and the Lamé parameters of the isotropic background rock.

The presence of liquid between cracks and equant pores may be taken into account in the calculation of fracture compliance. This happens when the pressure gradient within the liquid can equalise by moving between cracks and equant pores within the low-frequency limit. Essentially, the liquid between the cracks does not cause any deformation and hence does not contribute to the compliance of the fracture. Finally, equation 3.33 is substituted into equation 3.32 to calculate the total compliance ($\mathbf{S}$), which is then inverted for rock stiffness or elasticity ($\mathbf{C}$) (Verdon et al., 2009). Note that C_{ij} in equation 3.34a (where $i, j = 1$ to 6) are the elastic components in Voigt notation (see Equation 3.21).

3.8.1 Inversion algorithm

In this thesis I use the fracture inversion algorithm INSAFF (Verdon et al., 2009). The fracture inversion algorithm INSAFF starts by performing a grid search over the model free parameters and computes the elastic stiffness tensor ($\mathbf{C}$) for each case (Verdon et al., 2009). It calculates the theoretical fast and slow S-wave velocities and polarisation directions for each $\mathbf{C}$ and subsequent SWS parameters using the Christoffel equation

$$(C_{ijkl}P_jP_k - \rho\delta_{il})g_l = 0, \tag{3.35}$$

where P_j is the jth component of the slowness, g_l is the lth component of the polarisation and ρ is the rock density. The polarisation g_l can be derived

$$det|a_{ijkl}n_jn_k - \nu_n^2\delta_{il}| = 0, \tag{3.36}$$

where a_{ijkl} is the elastic tensor normalised by ρ, n_i is the wave normal, and ν_n is the nth phase velocity. For each arrival azimuth θ and inclination β, the Christoffel equation is used to calculate the SWS parameters (i.e, δV_S and ϕ). The SWS predictions are compared to the observed SWS values by computing the RMS misfits. To calculate the overall misfit, the misfits of δV_S and ϕ are normalised by their minimum values. Finally, the model which minimises the RMS misfit is chosen as the best fitting model (Verdon et al., 2009). From all SWS measurements only those in the good SWS category are included in the inversion process. The overall misfit is performed by computing the 90% confidence interval using an F-test (see for e.g., Silver & Chan, 1991, in appendix). The workflow for these processes is shown in Figure 3.13. To do the inversion, in this study, the free parameters are constrained to fracture density ϵ and fracture strike azimuth α.

Implicitly, the INSAFF algorithm is based on the assumption that the physical properties of the rock which shear-waves have travelled through are constant. INSAFF

has been extended to invert for the strike and density of two fracture sets (Verdon et al., 2011b) and to invert for the strike, tangential compliance, and the compliance ratio for one fracture set (Verdon & Wüstefeld, 2013). To make the approach efficient and reduce the number of free parameters, I assume that each fracture set contributes equally to the excess compliance. This assumption is reasonable given no a priori knowledge of the orthogonal fracture system (i.e., no knowledge of dominant fracture set). However, with real microseismic data that contain many recorded microseismic events (on the order of 100 or more), this restriction can be relaxed as there should be more SWS measurements to constrain the inversion.

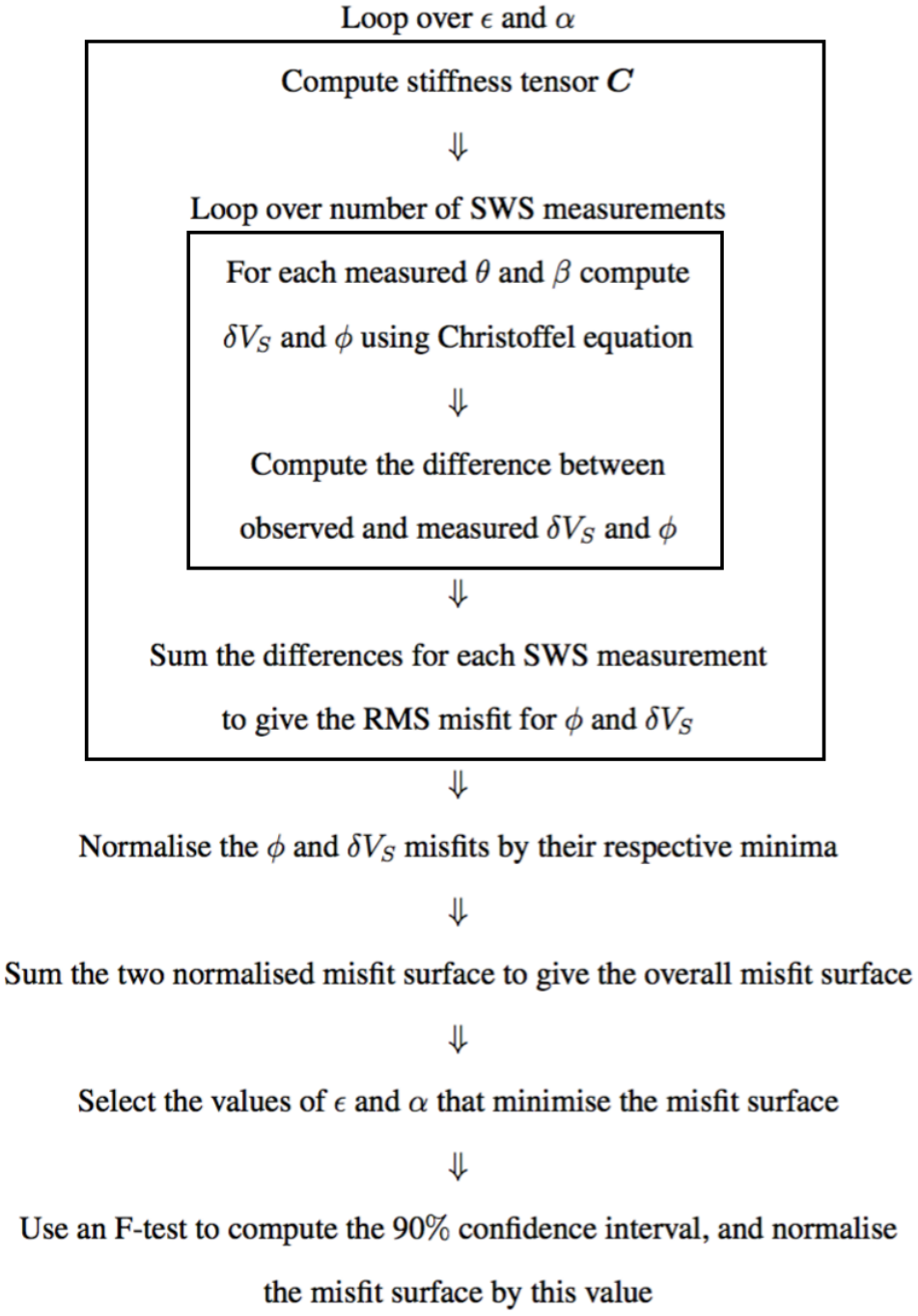

Figure 3.13: Workflow for the inverting for fracture parameter (α and ϵ) from SWS measurements. Figure is modified from Verdon et al. (2009).

3.9 Summary

In this Chapter, I reviewed the theoretical concepts of anisotropy. Due to tectonic and sedimentation processes in the subsurface, vertical fracturing and horizontal layering are pervasive features in hydrocarbon reservoirs. Therefore, the study of anisotropy is of great interest for exploration geophysicists to seismically characterise fractures.

Seismic numerical modelling is a valuable approach to simulate wave propagation in a medium. I explained the 3D FD forward modelling approach as a means to study the seismic response of discrete vertical fractured media. To do this, a MT source and discrete fracture volume are separately inserted in an isotropic background medium.

Shear-wave splitting is selected as a robust attribute to characterise fractured media in terms of evaluating the strength of anisotropy and thereby as a means to invert for fracture properties such as fracture strike and fracture density by implementation of the fracture inversion algorithm INSAFF. An automated SWS analysis cluster is implemented to reduce computational requirements. The quality of SWS measurements are evaluated by a numerical value including two different XC and EV methods. The integration of all these concepts and algorithms will be used to study shear-wave anisotropy and scattering response of fractured media.

Chapter 4

Inverting shear-wave splitting measurements for fracture parameters

4.1 Introduction

The observation of seismic anisotropy can be an indicator of the presence of fractures. Thus the imaging of seismic anisotropy within the Earth's subsurface can enable significant spatial and temporal characterisation of fracture properties. Seismic anisotropy in sedimentary rocks can result from several phenomena over a broad range of length-scales. These length-scales include mineral alignment (e.g., Valcke et al., 2006), grain scale alignment (e.g., Arne Johansen et al., 2004; Hall et al., 2008), large scale layering (e.g., Backus, 1962) and the presence of the aligned fracture sets (e.g., Hudson, 1981).

In this thesis I focus on seismic anisotropy due to fracture alignment. Fractures are discontinuities in the Earth's crust and can result from various types of rock failure when

the stress state exceeds the rock yield strength. Fractures occur over a range of scales, from continental scale (e.g., mega-fault) to micro-scale (e.g., micro cracks or grain boundaries). Fractures display themselves as seismological discontinuities and, in the case of aligned or coherent fractures sets, can appear to be effectively homogeneous and seismically anisotropic (e.g., Wuestefeld et al., 2011; Yousef & Angus, 2016). Seismic anisotropy refers to the situation where medium elastic properties change with direction of propagation and/or polarisation. As such, seismic anisotropy can be diagnosed in many ways, such as azimuthal velocity variation, amplitude variation with offset and azimuth (AVOA), and shear-wave splitting (SWS) analysis.

Although azimuthal variation in velocity and reflection amplitude of P- and S-waves can be diagnostic of anisotropy, shear-wave splitting (SWS) is the least ambiguous indicator of seismic anisotropy. When a shear-wave from an isotropic medium enters an anisotropic region it splits into two orthogonally polarised waves, the S_1-wave will travel faster than the S_2-wave. The degree of splitting depends on the initial S-wave polarisation in the isotropic medium and the allowable polarisation defined by the anisotropic elasticity tensor (e.g., Angus et al., 2004). SWS measures the polarisation direction (ϕ) of the fast S_1-wave and the delay time (δt) between the S_1- and the S_2- waves (e.g., Shearer, 2009). This delay time is proportional to the length of the raypath inside the anisotropic medium and the strength of the seismic anisotropy (e.g., Wuestefeld et al., 2011). The delay time δt is normalised by the path length between the source and the receiver to yield a percentage difference in S-wave velocity δV_S.

In hydrocarbon reservoirs, shear waves can be generated from two different sources: (1) passive seismic or microseismic events in and around the reservoir caused by stress changes, and (2) active seismic or controlled sources, using either a shear source or from P-to-S conversions. In reflection surveys, seismic waves travel subvertically and so the fast polarisation direction is generally interpreted to be the direction of a fracture strike,

while δV_S indicates the strength of fracturing. There have been several studies that have used SWS results to infer (e.g., Teanby et al., 2004b; Al-Harrasi et al., 2011) or invert (e.g., Verdon et al., 2009; Verdon et al., 2011b; Verdon & Wüstefeld, 2013; Yousef et al., 2013, 2014) for various fracture properties, such as fracture density (ϵ) and fracture orientation (α). SWS inversion techniques use sets of delay times and fast polarisations along with source-to-receiver information such as raypath azimuth, inclination, and travel distance (e.g., Verdon et al., 2009; Wookey, 2012) to image fracture zones and estimate in situ fracture properties.

In this Chapter, I study the feasibility of inverting for fracture strike (α) and density (ϵ) for several fracture models having one set of fractures or two sets of orthogonally aligned fractures using microseismic SWS measurements. To do this, I generate a suite of 96 fracture models for each single and double fracture sets with varying fracture size, density, stiffness and effective compliance ratio. For each model, I generate full waveform microseismic synthetics using the 3D finite-difference (FD) algorithm WAVE (Hildyard, 2007). The seismic anisotropy induced by the fractures is measured using shear-wave splitting (SWS) delay times and fast polarisation directions utilising the algorithm SHEBA (Teanby et al., 2004a). Based on an effective medium fracture model, the SWS measurements are inverted for the fracture model parameters (α and ϵ) using the algorithm INSAFF (Verdon & Wüstefeld, 2013; Verdon et al., 2011b; Verdon et al., 2009). I subsequently compare the inversion results to the true model to evaluate the feasibility of the inversion approach in extracting fracture properties from SWS data.

4.2 Model

In this section, I simulate wave propagation through a suite of elastic models: one subset of models having a single set of aligned fractures and another subset having two

Property	**Value**
P-wave (m/s)	5700
S-wave (m/s)	3200
V_P/V_S	1.78
λ_P (m)	31.4
λ_S (m)	17.6
Density (kg/m^3)	2600
Dominant period (s)	0.0055
Dimension (x, y, z) (m)	(300, 300, 300)

Table 4.1: Physical properties of the background (isotropic) medium.

orthogonally aligned fracture sets within a homogeneous isotropic medium (Yousef et al., 2014). The isotropic background model has P-wave velocity of 5700 m/s, S-wave velocity of 3200 m/s and density of 2600 kg/m^3 (see Table 4.1). For each model, a total of 69 3C receivers are used (see Figure 4.1), with 20 receivers placed in vertical boreholes (four boreholes each containing 5 receivers) and the remaining 49 receivers forming a planar near-surface square array (the near surface array is buried to eliminate free surface noise contamination). The dimension of the elastic model is 300 m$\times$ 300 m $\times$ 300 m. A microseismic source is defined having a Ricker wavelet with time duration of 5.5 ms. The source mechanism is a moment tensor having a seismic moment magnitude of 1×10^{11} N m and a strike-slip double-couple mechanism with strike 90°, dip of 90° and slip 45°. To reduce the computational time and allow exploring the influence of fracture properties on the fracture inversion, I simulate one event for each fracture model. In practice, numerous microseismic events would be recorded during microseismic monitoring and so many source-receiver SWS measurements would be used to invert for fracture properties. However, the synthetic data are noise free and so allow studying the feasibility of inverting microseismic SWS for fracture properties from fewer source-receiver measurements.

A total of 96 models have been generated by varying the fracture size (6, 10, 20 and

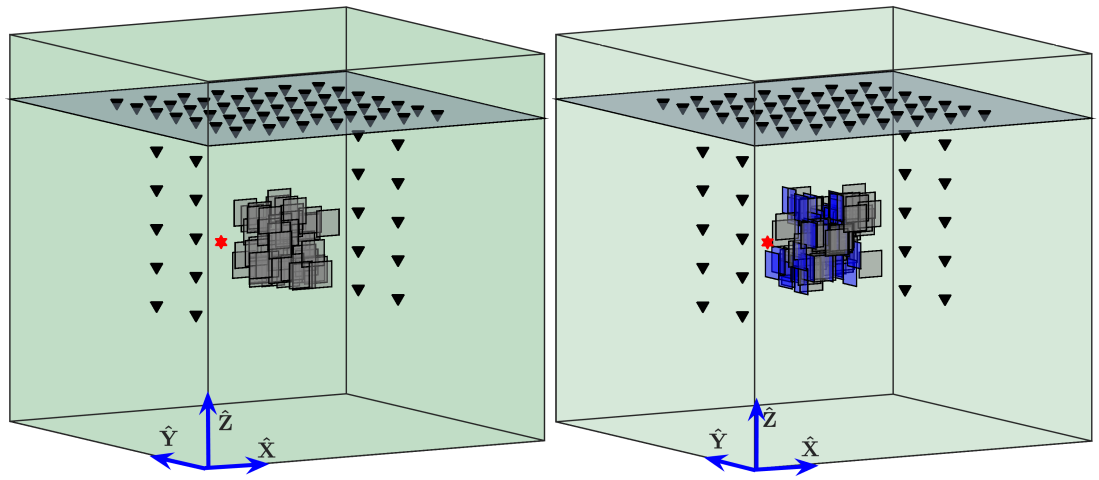

(a) (b)

Figure 4.1: Geometry of the 3D FD model with (a) one set of aligned fractures and (b) two sets of aligned fractures. The red star represents the location of the micro-seismic source (located in the centre of the left edge of the fracture zone), the triangles represent the surface and borehole receivers and the grey and blue rectangles within the sub-volume schematically represent the vertical fractures.

50 m), fracture density (0.02, 0.04, 0.08 and 0.1) and fracture compliance ratio (0.33, 0.60 and 1.00). The fracture stiffness values are divided into high stiffness models and low stiffness model. The low stiffness models have values of (1, 5 and 6)$\times 10^{10}$ Pa.m^{-1} for the normal fracture stiffness K_N and (1, 3 and 2)$\times 10^{1}$ Pa.m^{-1} for the shear fracture stiffness K_S. Similar values for the HS models have been chosen with the exception that these models have higher stiffness by one order of magnitude (i.e., multiplied by 10^1). These values were chosen based on the range of values observed in the field and laboratory (e.g., Lubbe & Worthington, 2006; Verdon & Wüstefeld, 2013). For the orthogonal double fracture sets, fracture properties are kept identical between the fracture sets to simplify the modelling procedure. Table 4.2 lists the fracture parameters for the 96 models in this chapter.

$Z_N/Z_T = 0.33$												
Fracture density	0.02			0.04			0.08			0.1		
size (m)	$K_N\ (Pa/m)$	$K_S\ (Pa/m)$	Model	$K_N\ (Pa/m)$	$K_S\ (Pa/m)$	Model	$K_N\ (Pa/m)$	$K_S\ (Pa/m)$	Model	$K_N\ (Pa/m)$	$K_S\ (Pa/m)$	Model
6	6×10^{10}	2×10^{10}	S6LD2	6×10^{10}	2×10^{10}	S6LD4	6×10^{10}	2×10^{10}	S6LD8	6×10^{10}	2×10^{10}	S6LD1
6	6×10^{11}	2×10^{11}	S6HD2	6×10^{11}	2×10^{11}	S6HD4	6×10^{11}	2×10^{11}	S6HD8	6×10^{11}	2×10^{11}	S6HD1
10	3×10^{10}	1×10^{10}	S10LD2	3×10^{10}	1×10^{10}	S10LD4	3×10^{10}	1×10^{10}	S10LD8	3×10^{10}	1×10^{10}	S10LD1
10	3×10^{11}	1×10^{11}	S10HD2	3×10^{11}	1×10^{11}	S10HD4	3×10^{11}	1×10^{11}	S10HD8	3×10^{11}	1×10^{11}	S10HD1
20	3×10^{9}	1×10^{9}	S20LD2	3×10^{9}	1×10^{9}	S20LD4	3×10^{9}	1×10^{9}	S20LD8	3×10^{9}	1×10^{9}	S20LD1
20	3×10^{10}	1×10^{10}	S20HD2	3×10^{10}	1×10^{10}	S20HD4	3×10^{10}	1×10^{10}	S20HD8	3×10^{10}	1×10^{10}	S20HD1
50	3×10^{9}	1×10^{9}	S50LD2	3×10^{9}	1×10^{9}	S50LD4	3×10^{9}	1×10^{9}	S50LD8	3×10^{9}	1×10^{9}	S50LD1
50	3×10^{10}	1×10^{10}	S50HD2	3×10^{10}	1×10^{10}	S50HD4	3×10^{10}	1×10^{10}	S50HD8	3×10^{10}	1×10^{10}	S50HD1
$Z_N/Z_T = 0.6$												
Fracture density	0.02			0.04			0.08			0.1		
size (m)	$K_N\ (Pa/m)$	$K_S\ (Pa/m)$	Model	$K_N\ (Pa/m)$	$K_S\ (Pa/m)$	Model	$K_N\ (Pa/m)$	$K_S\ (Pa/m)$	Model	$K_N\ (Pa/m)$	$K_S\ (Pa/m)$	Model
6	5×10^{10}	3×10^{10}	S6LD2	5×10^{10}	3×10^{10}	S6LD4	5×10^{10}	3×10^{10}	S6LD8	5×10^{10}	3×10^{10}	S6LD1
6	5×10^{11}	3×10^{11}	S6HD2	5×10^{11}	3×10^{11}	S6HD4	5×10^{11}	3×10^{11}	S6HD8	5×10^{11}	3×10^{11}	S6HD1
10	5×10^{10}	3×10^{10}	S10LD2	5×10^{10}	3×10^{10}	S10LD4	5×10^{10}	3×10^{10}	S10LD8	5×10^{10}	3×10^{10}	S10LD1
10	5×10^{11}	3×10^{11}	S10HD2	5×10^{11}	3×10^{11}	S10HD4	5×10^{11}	3×10^{11}	S10HD8	5×10^{11}	3×10^{11}	S10HD1
20	5×10^{9}	3×10^{9}	S20LD2	5×10^{9}	3×10^{9}	S20LD4	5×10^{9}	3×10^{9}	S20LD8	5×10^{9}	3×10^{9}	S20LD1
20	5×10^{10}	3×10^{10}	S20HD2	5×10^{10}	3×10^{10}	S20HD4	5×10^{10}	3×10^{10}	S20HD8	5×10^{10}	3×10^{10}	S20HD1
50	5×10^{9}	3×10^{9}	S50LD2	5×10^{9}	3×10^{9}	S50LD4	5×10^{9}	3×10^{9}	S50LD8	5×10^{9}	3×10^{9}	S50LD1
50	5×10^{10}	3×10^{10}	S50HD2	5×10^{10}	3×10^{10}	S50HD4	5×10^{10}	3×10^{10}	S50HD8	5×10^{10}	3×10^{10}	S50HD1
$Z_N/Z_T = 1.0$												
Fracture density	0.02			0.04			0.08			0.1		
size (m)	$K_N\ (Pa/m)$	$K_S\ (Pa/m)$	Model	$K_N\ (Pa/m)$	$K_S\ (Pa/m)$	Model	$K_N\ (Pa/m)$	$K_S\ (Pa/m)$	Model	$K_N\ (Pa/m)$	$K_S\ (Pa/m)$	Model
6	1×10^{10}	1×10^{10}	S6LD2	1×10^{10}	1×10^{10}	S6LD4	1×10^{10}	1×10^{10}	S6LD8	1×10^{10}	1×10^{10}	S6LD1
6	1×10^{11}	1×10^{11}	S6HD2	1×10^{11}	1×10^{11}	S6HD4	1×10^{11}	1×10^{11}	S6HD8	1×10^{11}	1×10^{11}	S6HD1
10	3×10^{10}	3×10^{10}	S10LD2	3×10^{10}	3×10^{10}	S10LD4	3×10^{10}	3×10^{10}	S10LD8	3×10^{10}	3×10^{10}	S10LD1
10	3×10^{11}	3×10^{11}	S10HD2	3×10^{11}	3×10^{11}	S10HD4	3×10^{11}	3×10^{11}	S10HD8	3×10^{11}	3×10^{11}	S10HD1
20	1×10^{9}	1×10^{9}	S20LD2	1×10^{9}	1×10^{9}	S20LD4	1×10^{9}	1×10^{9}	S20LD8	1×10^{9}	1×10^{9}	S20LD1
20	1×10^{10}	1×10^{10}	S20HD2	1×10^{10}	1×10^{10}	S20HD4	1×10^{10}	1×10^{10}	S20HD8	1×10^{10}	1×10^{10}	S20HD1
50	3×10^{9}	3×10^{9}	S50LD2	3×10^{9}	3×10^{9}	S50LD4	3×10^{9}	3×10^{9}	S50LD8	3×10^{9}	3×10^{9}	S50LD1
50	3×10^{10}	3×10^{10}	S50HD2	3×10^{10}	3×10^{10}	S50HD4	3×10^{10}	3×10^{10}	S50HD8	3×10^{10}	3×10^{10}	S50HD1

Table 4.2: Summary of fracture properties for all 96 models.

4.3 SWS results

The first step in processing SWS involves picking the arrival times of the P- and S-waves from the 3C synthetic seismograms. From all 96 models, 6624 3C seismograms are processed. After picking the 3C seismograms, each 3C seismogram is rotated from the global coordinate (east,north,vertical) into the local (source-receiver) ray coordinate, with one coordinate being the ray direction (containing primarily the P-wave energy) and the other coordinates perpendicular to the ray direction (one is the S_V direction and the other the S_H direction)(see Figure 3.9). After rotation, I use SHEBA to calculate the SWS delay time δt and fast polarisation direction (ϕ). To do this the seismograms are filtered using a Butterworth bandpass filter between 10 Hz and 1500 Hz, which is the range of the expected frequencies. After some parameter and quality control tests, a P-wave window size of 0.02 s is chosen, where I allow the S-wave window size to vary slightly around 0.01 s (the maximum δt value is constrained to be 3 ms). Next, SWS analysis is performed for each 3C seismogram. For each measurement, a diagnostic plot is created and is used to determine whether the SWS result is good, null or bad. A SWS measurement is classified using an automated quality control value ($\mathbb{Q}$) and is a measure of how similar the SWS measurement parameters of the cross-correlation (XC) and Eigenvalue (EV) techniques are (see section 3.7.2.4). In addition to the automated quality control measure, the SWS measurements can be assessed using the diagnostic plots from the EV method. A SWS measurement is considered reliable by determining when (1) the energy on the corrected transverse component has been minimised, (2) the S_1- and S_2-waves have similar waveforms, and (3) the elliptical S-wave particle motion in the SV-SH plane has been linearised after the splitting correction. The value of $\mathbb{Q}$ ranges from -1 to +1, where $\mathbb{Q} = -1$ denotes a null result (i.e., no anisotropy and hence no SWS), $\mathbb{Q} = 0$ denoting a poor result (i.e., unreliable) and $\mathbb{Q} = +1$ denoting a good result (i.e., SWS present). I define a $\mathbb{Q}$ value of greater than or equal to 0.75

to be a good SWS result for the synthetic seismograms based on trial and error (i.e., $\mathbb{Q} < 0.75$ resulted in inaccurate fracture inversions). Figure 4.2 shows an example of a SWS diagnostic plot with a good quality factor ($\mathbb{Q} = 0.96$) and an example of the null result ($\mathbb{Q} = -0.98$). For the good quality factor (Figure 4.2a) the particle motion is ellipsoidal before correction and is linearised after correction while for the null SWS (Figure 4.2b) the particle motion is linear before and after the correction.

4.3.1 Single fracture set vs double fracture sets

For the models with one fracture set, the strike of the fracture set is $\alpha = 90^\circ$ from north (i.e., the Y-axis), whereas for the double fracture set model the fracture sets have strike $\alpha = 0^\circ$ and 90° (i.e., the fractures are orthogonal along the X- and Y-axes). Figure 4.3 depicts the ray coverage in the vertical (inclination) and horizontal (azimuth) planes. There is good azimuth coverage with the exception of a reduction in azimuthal coverage between 210° and 300°. The range of inclination covers mainly between 0° and 60° with some coverage between 60° and 110°. Out of 6624 source-receiver combination there are 445 good SWS measurements ($\approx 7\%$) for the single fracture set models after using the quality control. In contrast, for the double fracture set models there are 261 good SWS measurements ($\approx 4\%$). This is likely due to the additional fracture set which reduces the amount of coherent scattering that would allow SWS to develop.

Figure 4.4 is a histogram of the azimuth and inclination values for the all models and including all the 6624 SWS measurements. This figure shows that the inclination of the ray paths are mostly between 20° and 60°, but with good azimuthal coverage. Figure 4.5 is a histogram for azimuth and inclination of the good SWS measurements for the both single and double fracture set models. The figure shows that the majority of the raypaths are between 40° and 120° azimuth travelling subhorizontally through the fracture volume. There is no azimuth coverage between 0° and 40° as well as 140° and

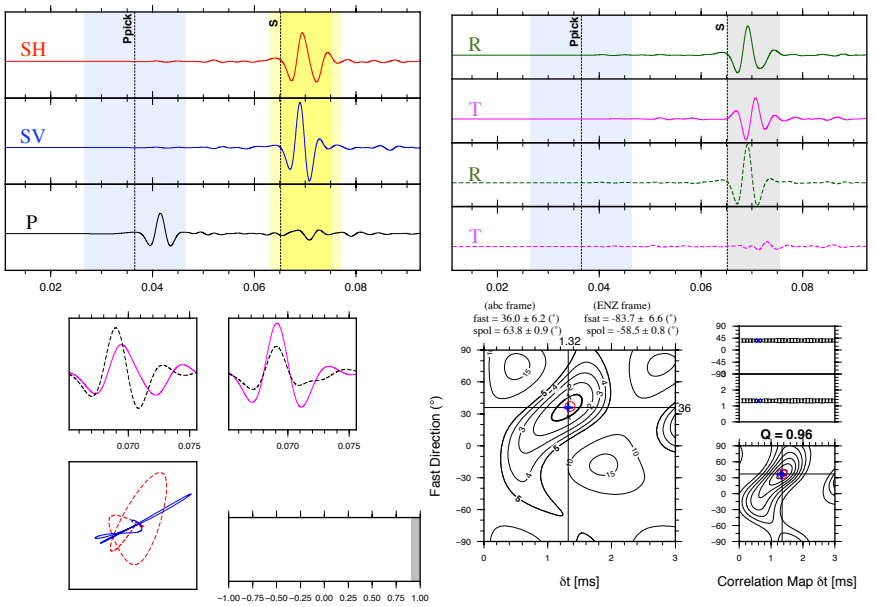

(a)

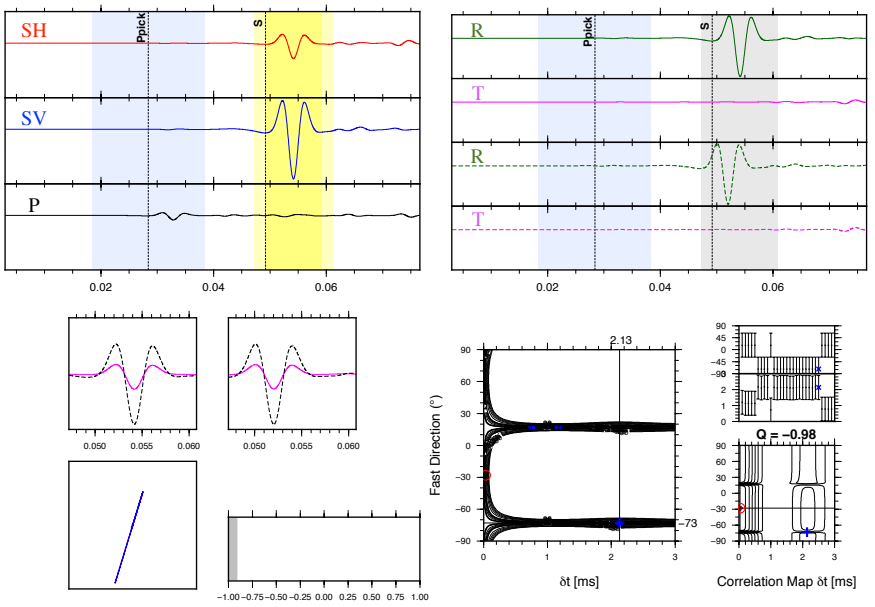

(b)

Figure 4.2: Example of (a) good SWS measurement ($\mathbb{Q} = 0.96$) and (b) null splitting ($\mathbb{Q} = -0.98$). For (a) and (b); (top-left) 3 component waveforms in local ray coordinates; (top-right) radial and transverse components before (top 2 traces) and after (bottom 2 traces) splitting correction; (middle-left) fast (dashed) and slow (solid) S waves before (left) and after (right) correction; (bottom-left) particle motion in SV-SH coordinate frame before (dashed) and after (solid) correction; (bottom-right) error surfaces of the eigenvalue (left) and cross-correlation (lower right) methods (see Wuestefeld et al., 2010, for details). The best result of the two methods are shown as blue + and red circle for the eigenvalue and cross-correlation method, respectively; and (middle-right) fast axis (top) and δt variations for each window including corresponding error bars.

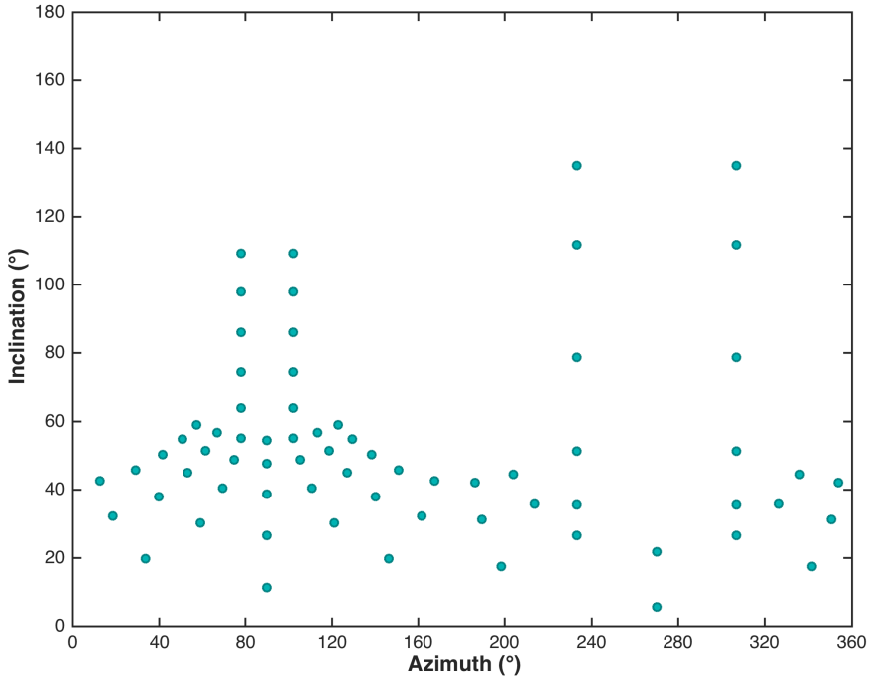

Figure 4.3: Distribution of source-receiver azimuth and inclination for the fracture model array.

180° since the raypaths do not travel through the fracture volume where SWS would develop. The highest azimuthal counts in the histogram are for the vertical borehole arrays.

Figure 4.6 is a histogram of the measurement quality ($\mathbb{Q}$) for the whole SWS measurements and also for the good SWS measurements. It can be seen for the whole dataset that most of the SWS measurements fall in the category of good null ($\mathbb{Q} < -0.75$). However, the histogram for good SWS $\mathbb{Q}$ reveals that the majority of $\mathbb{Q}$ values are larger than 0.90. For the case of data with good signal-to-noise ratio where the S-wave signals are clear or for data with large number of SWS measurements, the threshold could be increased to higher values such as 0.80 or even 0.90. As such, the measure allows a reduction in the required visual examination of the diagnostic plots (Al-Harrasi, 2010). Since the dataset is noise free and the model geometry is designed to maximise S-wave anisotropy, I can automatically control and choose the high SWS

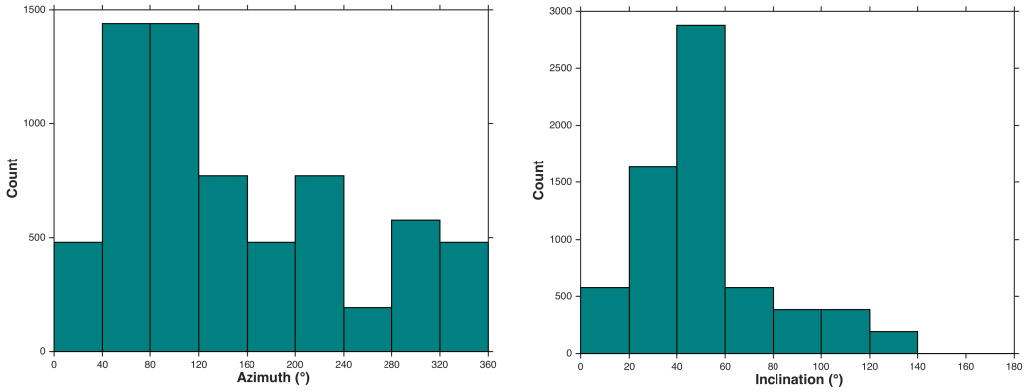

(a) (b)

Figure 4.4: Histogram of azimuth and inclination for the whole SWS dataset (6624 measurements).

measurement quality reliably from the large volume of data. Similarly, Wuestefeld et al. (2010) applied this approach to a Valhall microseismic dataset, where the results of their automated SWS analysis being equivalent with the manual results of Teanby et al. (2004b).

Figure 4.7 shows the distribution of $\mathbb{Q}$ against the difference between initial S-wave polarisation and ϕ in the shear-wave plane (i.e., SV-SH plane). The null measurements can be seen clearly in this figure. Good quality SWS measurements require a separation of at least 20° from the null direction. The scatter reveals that higher $\mathbb{Q}$ values occur when the difference is approximately 45°, and lower $\mathbb{Q}$ values when differences equal to 0° and 90°. This figure confirms that the automated quality control approach has a physical basis. However, it would be expected that the signal-to-noise ratio can robustly affect this limitation (Wuestefeld et al., 2010).

To make the SWS less subjective, the $\mathbb{Q}$ value is introduced and is calculated from the combination of both the EV and XC techniques. Both techniques behave differently, particularly in the vicinity of the null direction, where the XC technique fails to extract proper values of ϕ_{XC} and δt_{XC}. This occurs because of the absence or the weakness of S-wave energy on the transverse component close to the null. In fact, correlation

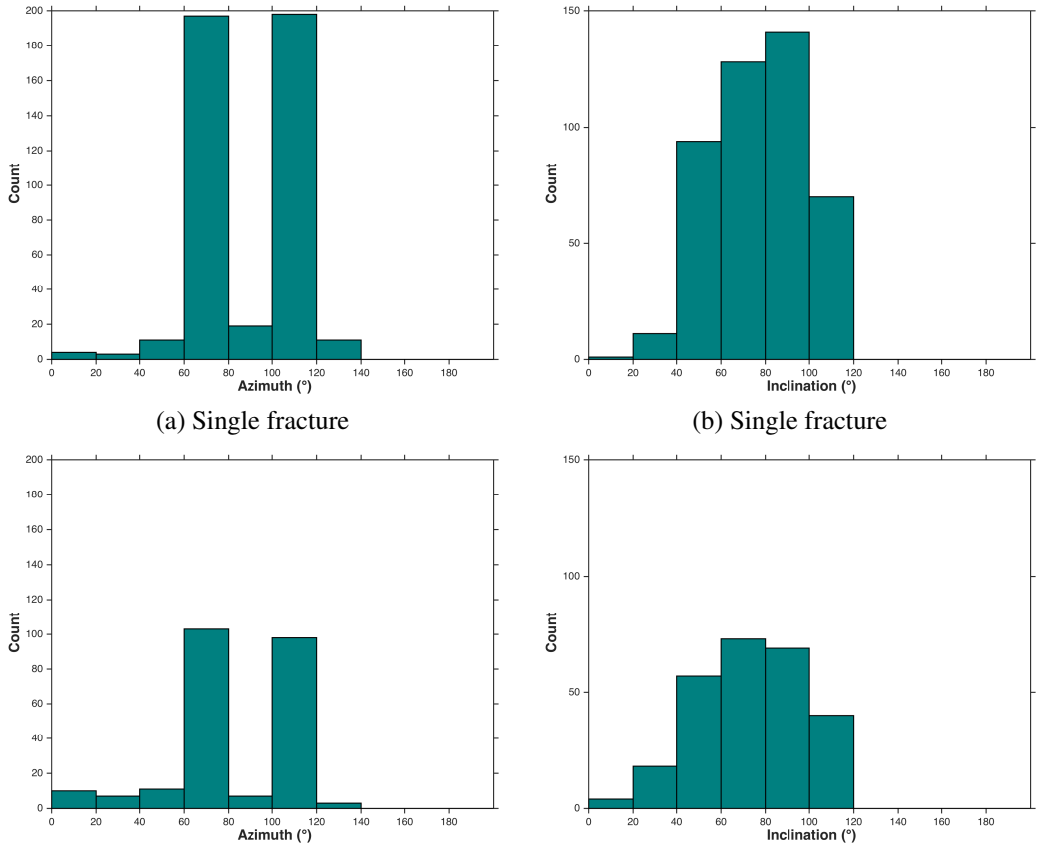

(a) Single fracture (b) Single fracture

(c) Double fracture (d) Double fracture

Figure 4.5: Histogram of azimuth and inclination of the good SWS for the single and double fracture sets.

can only be found if the transferred energy by the rotations of the grid search from the initial polarization component to the transverse component is much more strong. The correlation is maximum for a rotation of 45° and obviously results in zero timelag between the two S-wave components. Therefore, the techniques should not be used alone (Wüstefeld & Bokelmann, 2007). The $\mathbb{Q}$ value is crucial for reliable fracture inversion of anisotropy measurements; the results of the inversion are dependent on the $\mathbb{Q}$ values of the input SWS measurements.

In SWS analysis, the δt is used to characterise the strength of anisotropy along the raypath. The δt parameter is normalised by the path length to estimate the percentage velocity anisotropy δV_S (i.e., difference between S_1 and S_2 velocity). The δV_S parameter

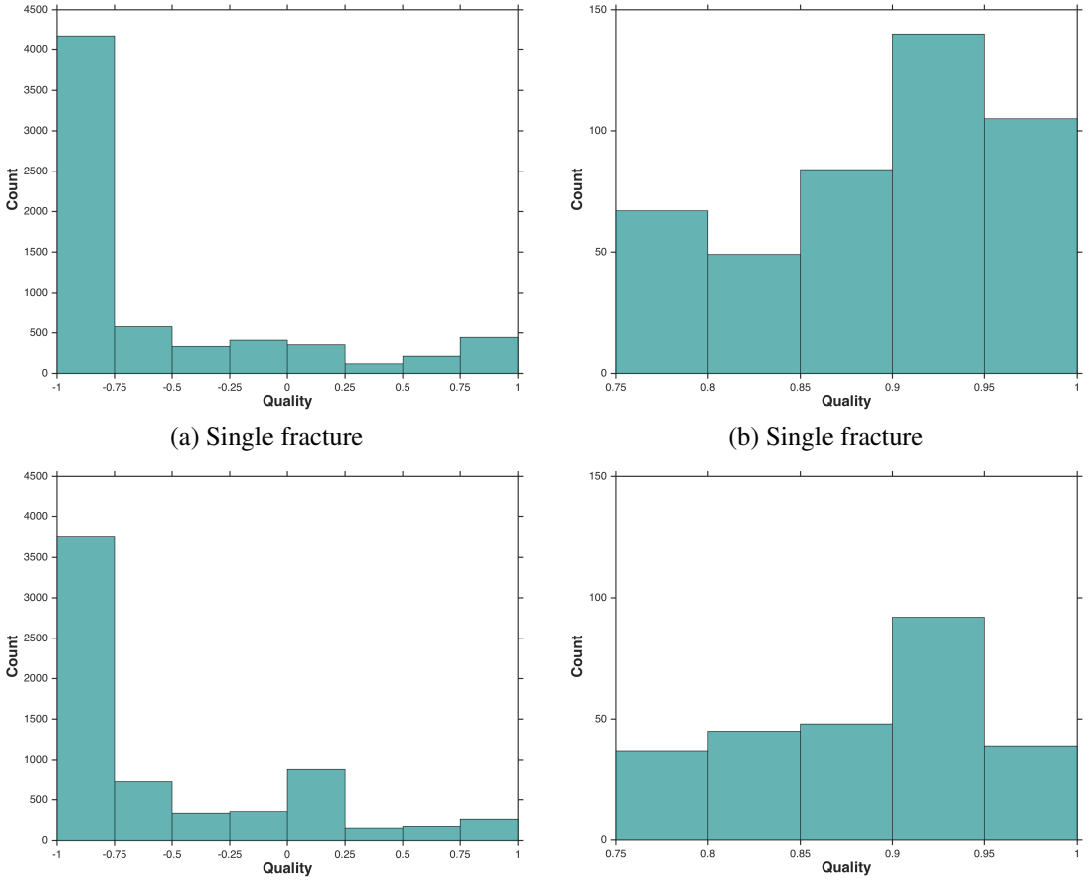

(a) Single fracture

(b) Single fracture

(c) Double fracture

(d) Double fracture

Figure 4.6: Histogram of SWS $\mathbb{Q}$ values: (a) for all SWS measurements of single fracture set, (b) for good, $\mathbb{Q} \geqslant 0.75$, SWS measurements of single fracture set, (c) for all SWS of double fracture set, and (d) for good SWS of double fracture set.

is computed using the following relationship: $100 \times (V_{S1} - V_{S2})/V_{S(ave)}$, where $V_{S(ave)}$ is the average S-wave velocity. The maximum S-wave velocity anisotropy δV_S for the single and double fracture sets are 16.3% and 21.2%, respectively.

Figure 4.8 shows the variation of δV_S against direct distance between the source and receiver for the whole dataset and $\mathbb{Q} \geq 0.75$ for the single and double fracture set models, respectively. The distances range between approximately 50 m and 200 m for the whole dataset. For the whole dataset it can be seen that δV_S decreases by increasing source-receiver distance. However, the large δV_S values at short distances have very

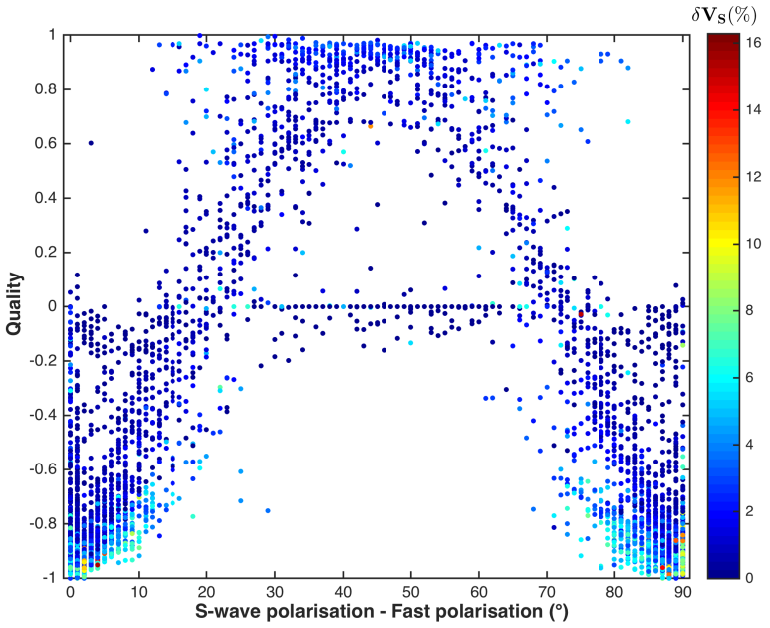

(a) Single fracture

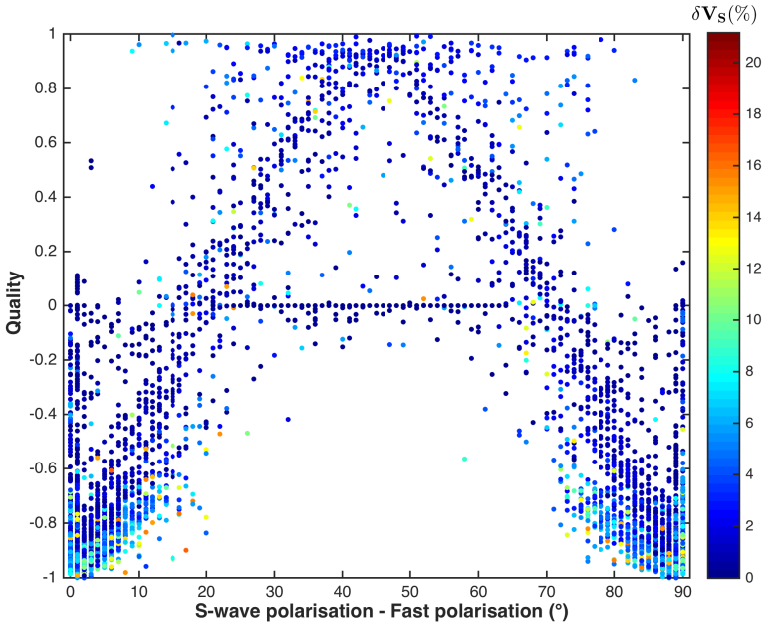

(b) Double fracture

Figure 4.7: The SWS quality versus difference between initial source polarisation and the fast S-wave polarisation (ϕ) in the S-plane for the whole dataset. The colour depicts the percentage of shear-wave splitting δV_S. Note that the colour scales are not normalised between the two models.

low $\mathbb{Q}$ values, and so indicates the importance of having quality control of the specific SWS values used. For the $\mathbb{Q} \geq 0.75$ dataset the δV_S values are less than 6% for the single fracture set and 15% for the double fracture set models. Furthermore, for good quality SWS measurements the raypath are approximately greater than or equal to 100 m, or approximately 5 wavelengths. In the double fracture models it can be seen that the distribution of good $\mathbb{Q}$ range over a broader propagation distance from 100-200 m, while for the single fracture models is narrower (i.e., approximately between 130-180 m). However, the magnitude of anisotropy is higher in the double fracture model compared to the single fracture model.

The number of good SWS measurements is a key parameter in the inversion for fracture parameters. Based on trial and error and considering the stability of the inversion results for each model, I perform the fracture inversion with a minimum of 5 SWS with $\mathbb{Q} \geq 0.75$, generally leading to a stable inversion. Figure 4.9 maps the number of good SWS measurements for each of the 96 models. For the case of the single fracture set, the number of models with more than 5 good $\mathbb{Q}$ values for the compliance ratios Z_n/Z_T =0.33, 0.60 and 1.00 are 10, 8 and 17, respectively, whereas for the double fracture sets the number of models are 13, 8 and 3 respectively.

Figures 4.10-4.11 plot the histograms of δt and δV_S for the whole dataset and good SWS data for both single and double fracture sets. Figure 4.10 shows that the δV_S distribution decreases from 1% to 14%, and that δt is approximately constant between 0 to 3 ms with higher number of SWS measurements at 0 ms and 3 ms. In contrast, in Figure 4.11, there is a skewed distribution of δV_S centred around roughly 1.8% for both single and double fracture sets. In terms of the δt values, the distribution for the double fracture set models are roughly constant between 0.25 to 2.75 ms. For the single fracture set models the range is similar but with a skewed distribution centred towards lower δt values.

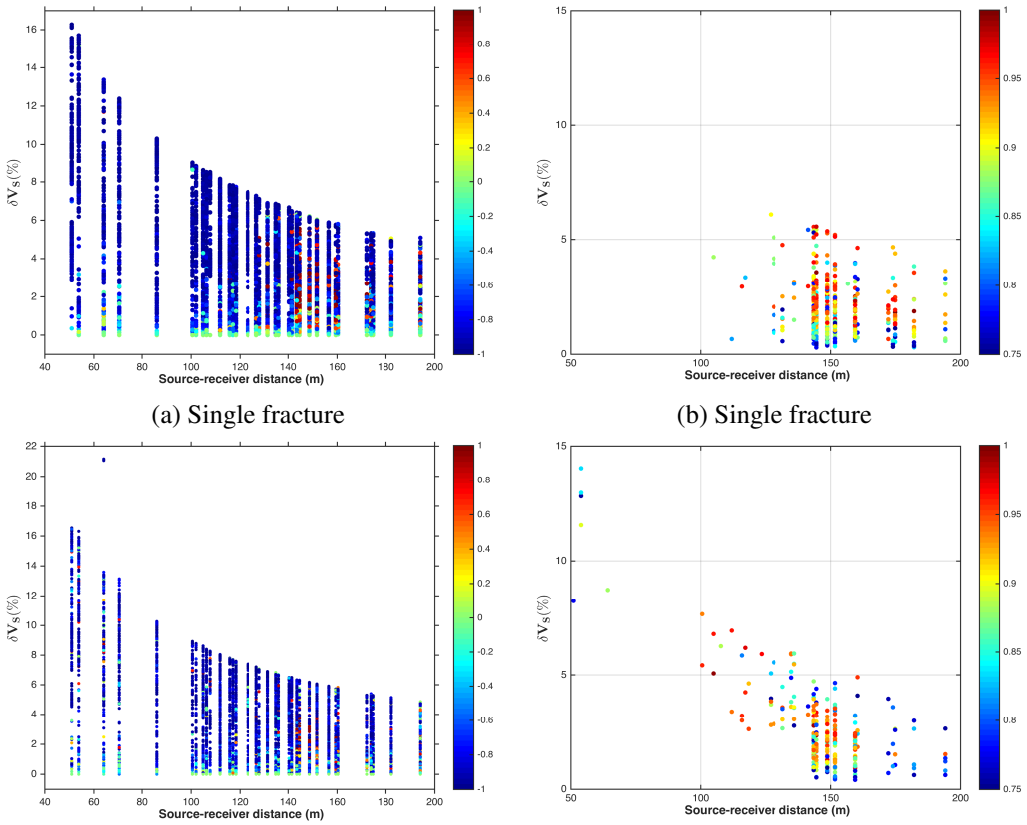

(a) Single fracture

(b) Single fracture

(c) Double fracture

(d) Double fracture

Figure 4.8: Variation of δV_S with length of raypath: single fracture model for (a) whole dataset and (b) for good SWS results ($\mathbb{Q} \geq 0.75$), and double fracture model for (c) whole dataset and (d) for good SWS results. Colour indicates the quality index ($\mathbb{Q}$) of the SWS measurements.

In Figure 4.12, I plot the published compliance values versus fracture size a (grey rectangles) from literature (Lubbe, 2005; Pyrak-Nolte et al., 1990; Hardin et al., 1987; Lubbe & Worthington, 2006; King et al., 1986 and Worthington & Hudson, 2000) as well as the model values (see table 4.2) generated in this chapter. For the three compliance ratios $Z_N/Z_T = 0.33$, 0.60 and 1.00 and fracture sizes a =6, 10, 20 and 50 m the results are categorised into good, unstable and no SWS. The models with good SWS are those that have 5 or more good SWS values $\mathbb{Q} \geq 0.75$ (red), the models with unstable SWS have less than 5 good SWS values (blue) and the models with no

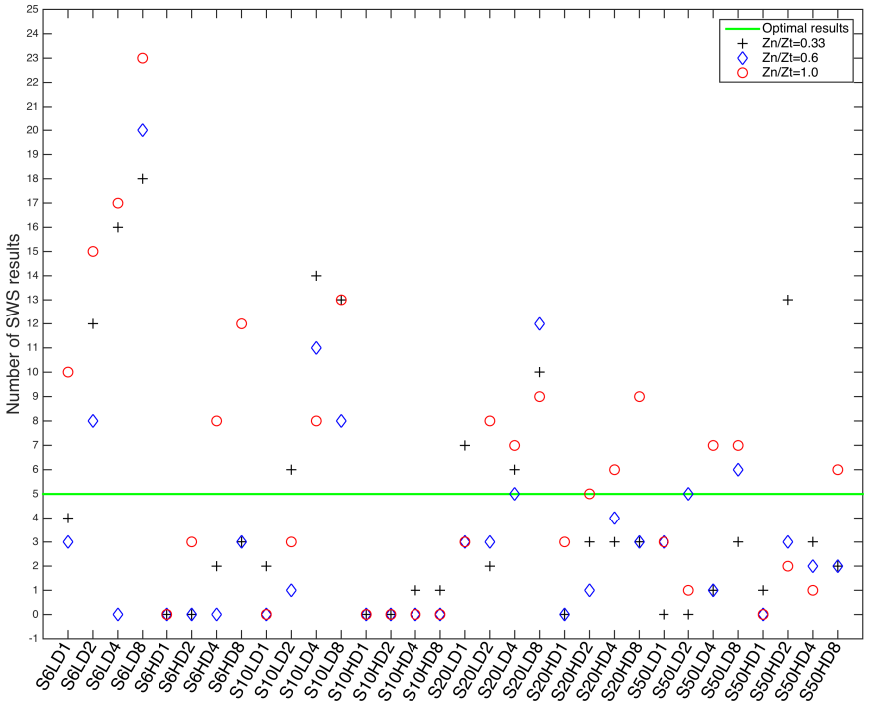

(a) Single fracture

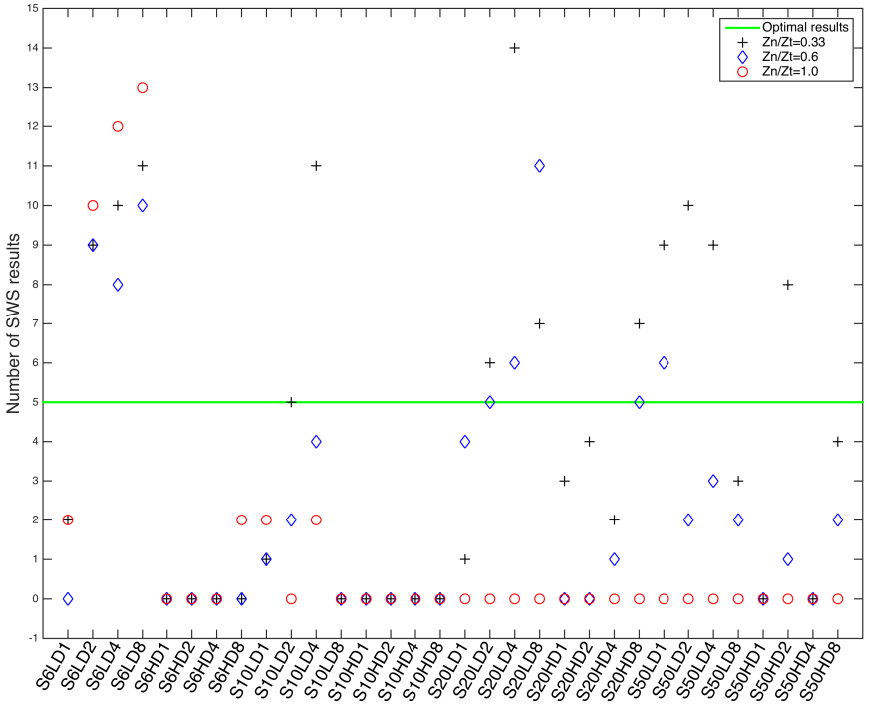

(b) Double fracture

Figure 4.9: Number of SWS results with $\mathbb{Q} \geqslant 0.75$ for each (a) single fracture set model and (b) double fracture set model.

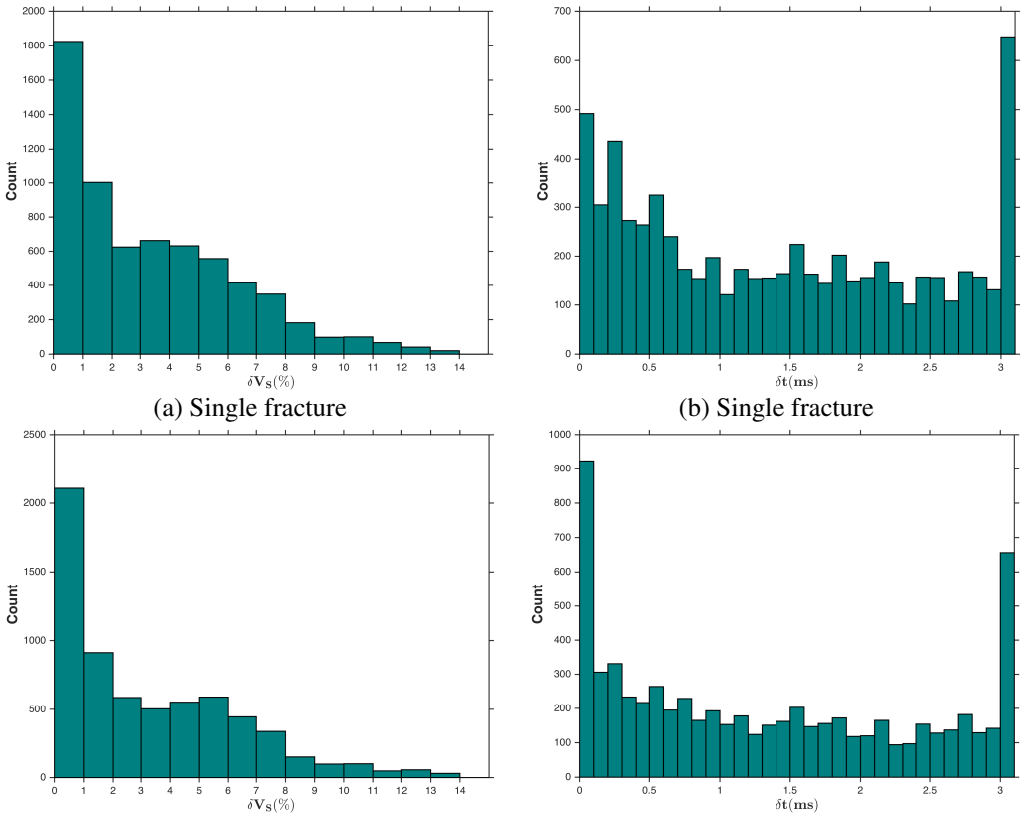

(a) Single fracture (b) Single fracture

(c) Double fracture (d) Double fracture

Figure 4.10: Histogram of δV_S and δt for the whole dataset for the single and double fracture set models (6624 measurements).

SWS (black). The dashed diagonal line in Figure 4.12 represents the inferred scale dependence of the normal or shear fracture compliance with fracture size.

From Figure 4.12, it can be observed that by increasing the fracture density ϵ the number of models with good SWS increases, particularly for small fractures. Furthermore, by increasing the compliance (Z_N and Z_T) by one order of magnitude while keeping Z_N/Z_T constant leads to models with good SWS, except for models with fracture size $a = 50$ m and $Z_N/Z_T \geq 0.60$. However, the poor SWS results are due to the fewer number of fractures (i.e., the maximum number is 3) the wave interacts with between source and receivers.

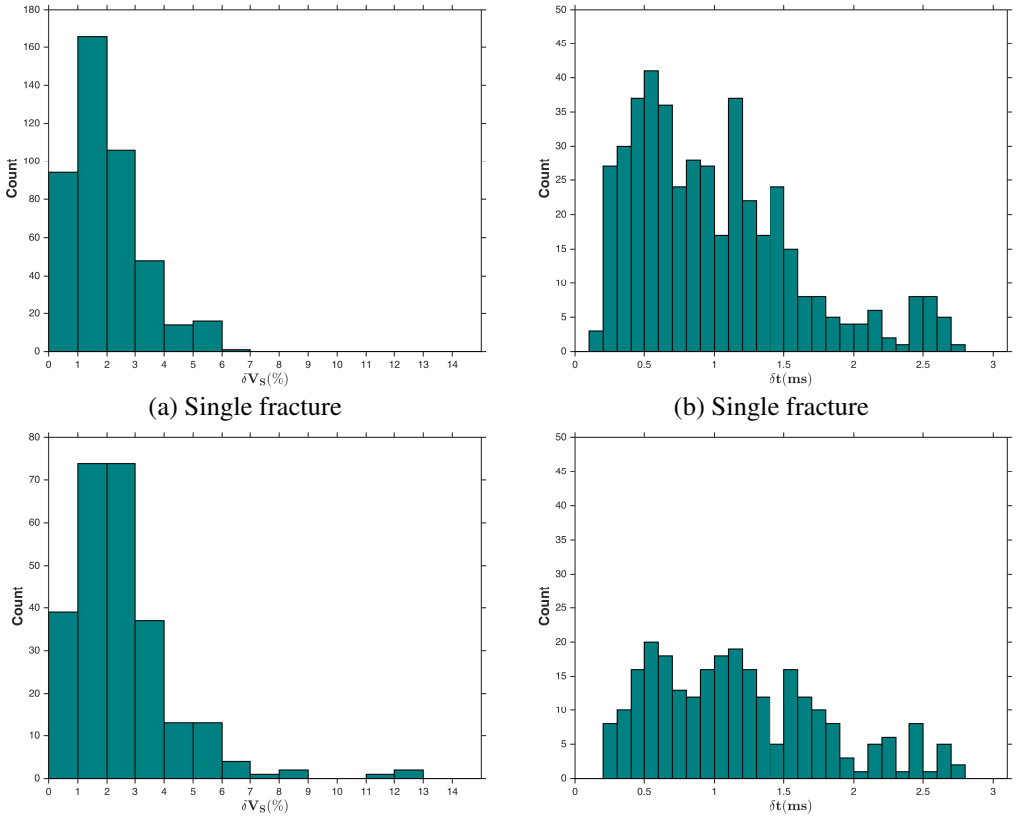

(a) Single fracture (b) Single fracture

(c) Double fracture (d) Double fracture

Figure 4.11: Histogram of δV_S and δt for the good SWS results ($\mathbb{Q} \geq 0.75$) for the single fracture set and double fracture set models.

4.4 Inversion method (INSAFF)

In this section, the inversion algorithm INSAFF (Verdon et al., 2009) is used to invert for fracture strike α and fracture density ϵ. To obtain reliable inversion results, the inversion is performed for models with at least 5 good SWS results ($\mathbb{Q} \geqslant 0.75$). To assess the inversion approach, I will first invert for the fracture properties of the single vertical fracture set models, which represent a simpler model and hence, in principle, more constrained inversion. Subsequently, I will then invert for fracture properties of

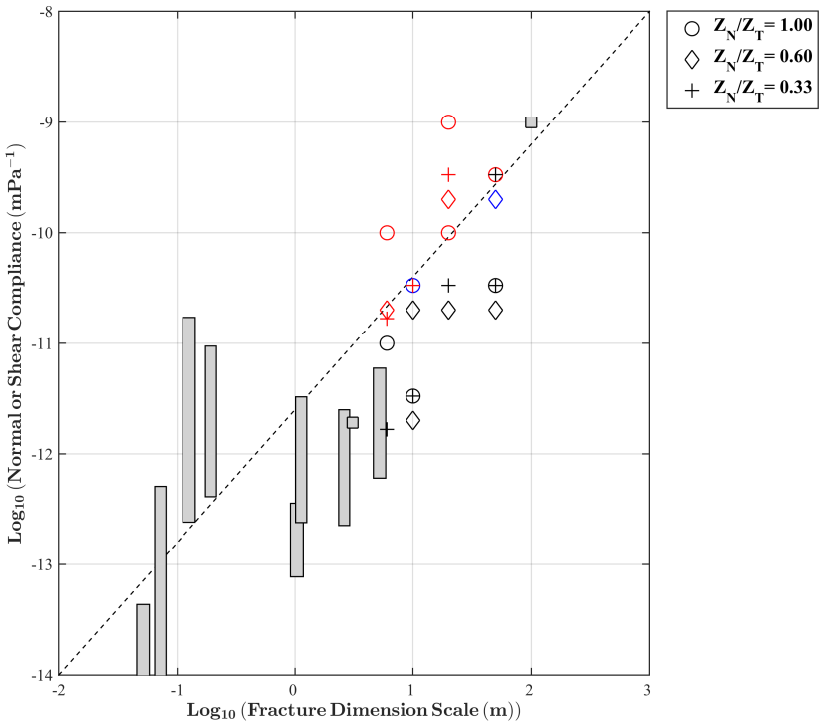

(a) ϵ = 0.02

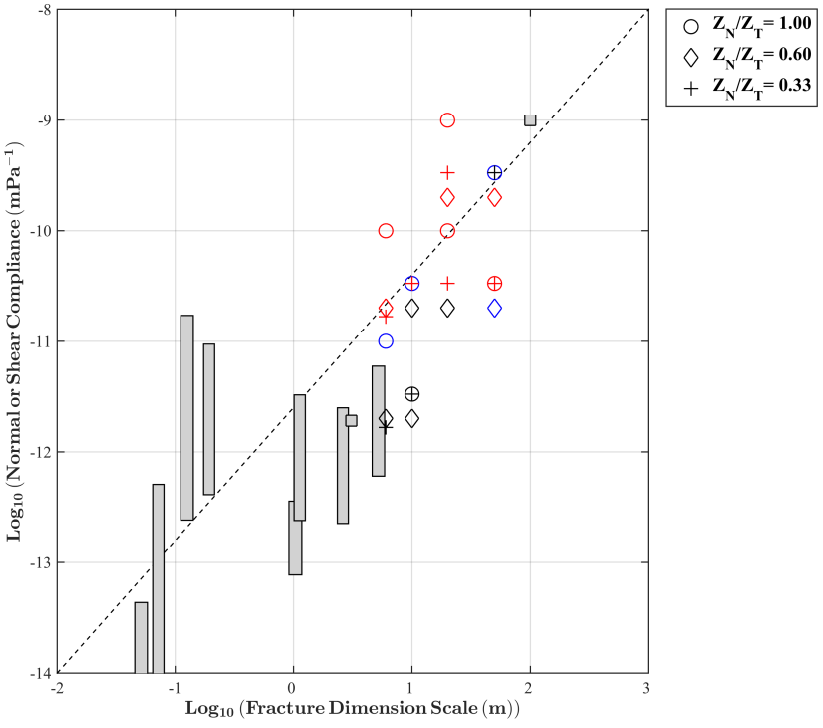

(b) ϵ = 0.04

Figure 4.12: Continued...

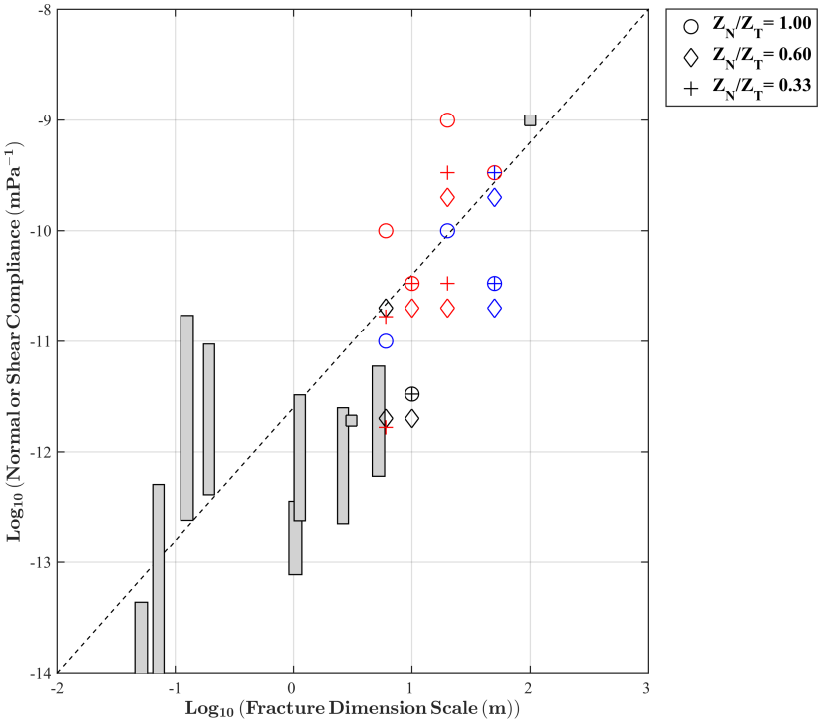

(c) $\epsilon = 0.08$

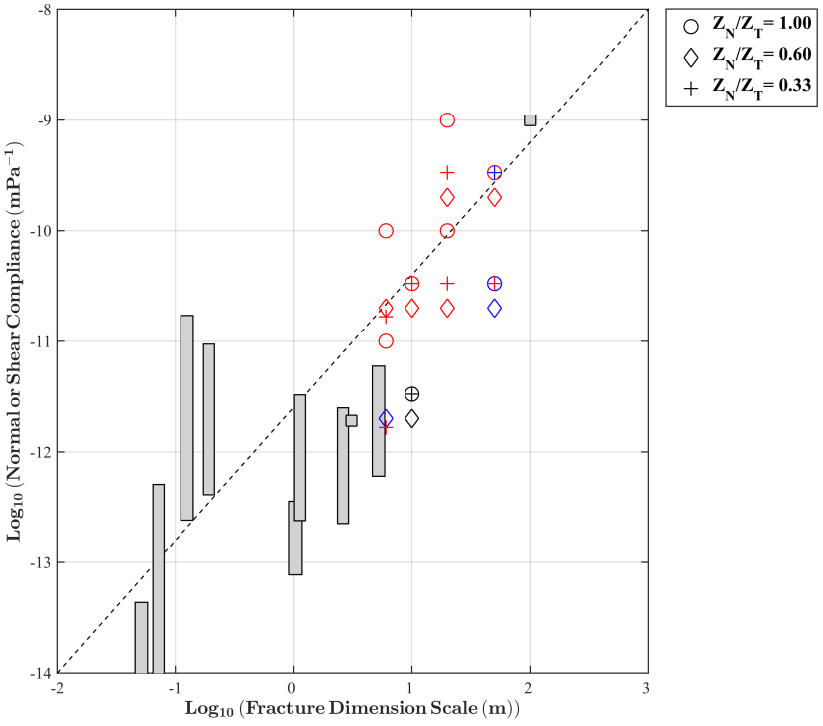

(d) $\epsilon = 0.1$

Figure 4.12: Normal compliance against fracture size. The grey rectangles are data taken from literature while the other symbols are data from this study. The colour depicts the quality of SWS: good (red); unstable (blue); no SWS (black).

the orthogonal fracture set models (orthorhombic model). INSAFF allows the inversion for background VTI anisotropy (e.g., Verdon et al., 2011b), but since the background medium is isotropic the VTI Thomsen's parameters are excluded from the inversion process. Therefore, the independent parameters in the inversion are fracture strike and fracture density for the single and double fracture set models.

In order to obtain the optimum estimates of fracture strike and fracture density and also minimise the computation time of the inversion, I limit the grid search to sensible values for these parameters. For the single fracture inversion, I allow α to vary between 0° and 180°, whereas for the double fracture inversion, I allow $\alpha 1$ and $\alpha 2$ to vary between $\alpha 1$ =-45° and 45° and $\alpha 2 = 45°$ and 135° for the first and second fracture set. Following the assumption of Crampin (1994) that fracture density is roughly equal to one hundredth of δV_S and assuming a maximum δV_S of 14% (see Figure 4.10), I set the fracture density range to be between 0.00 and 0.14 for both single and double fracture sets.

4.5 Results

4.5.1 Single fracture set

Figure 4.13 shows the lower hemisphere projection of the S-wave phase velocities as a function of propagation direction based on the best fitting elasticity tensor inverted using a single fracture set. This example is for the fracture model having fracture size 6 m, compliance ratio $Z_N/Z_T = 0.33$ and fracture density of 0.08. The inversion result for the single fracture set model has strike $\alpha = 98°$ and density $\epsilon = 0.02$, whereas the true fracture set model has strike $\alpha = 90°$ and density $\epsilon = 0.08$.

Figure 4.14 plots the inversion results of fracture strike versus fracture density for all the single fracture set models. It is clear that the inversion results for fracture strike

cluster around the true value of α =90°, but are biased to lower density estimates. The confidence in the inversion results was obtained using the F-test with 90% confidence interval (see section 3.8). In order to assess the error of the inversion results, Figure 4.15 plots the absolute error in fracture strike $\Delta\alpha(^\circ)$ against the percentage error in fracture density $\Delta\epsilon(\%)$. It is clear that the error in fracture strike $\Delta\alpha(^\circ)$ is within ±40° with standard deviation of 14°, and the error in fracture density $\Delta\epsilon(\%)$ remains between approximately 40 and 60%. The models with $Z_N/Z_T = 0.60$ have the lowest $\Delta\epsilon(\%)$ and $\Delta\alpha(^\circ)$. However, taking into account the errors in both fracture strike and density, the models with $Z_N/Z_T = 0.33$ yield the most reliable inversions.

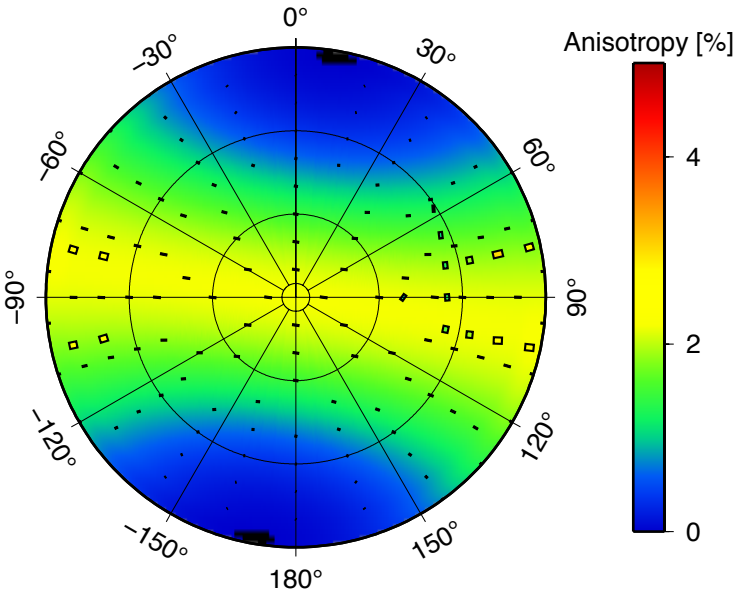

Figure 4.13: Inversion result for the single fracture set model with size 6 m and $Z_N/Z_T = 0.33$. The inverted fracture parameters have $\alpha = 98^\circ$ and $\epsilon = 0.02$ while the true values are $\alpha = 90^\circ$ and $\epsilon = 0.08$ (model S6LD8). In this figure and Figure 4.17 the thin ticks and the coloured contours are the modelled splitting results using the best fit effective medium model parameters. Also, the position of the black outlined ticks depicts the position of the azimuth and inclination of the S-wave, while the orientation shows the ϕ and the length and the colour shows the δV_S.

Figure 4.16 shows the inversion results for α and ϵ for the single fracture models in polar plot diagram, which allows comparison between the inversion results for the single and double fracture set models. The inverted fracture strikes fall within ±40° of

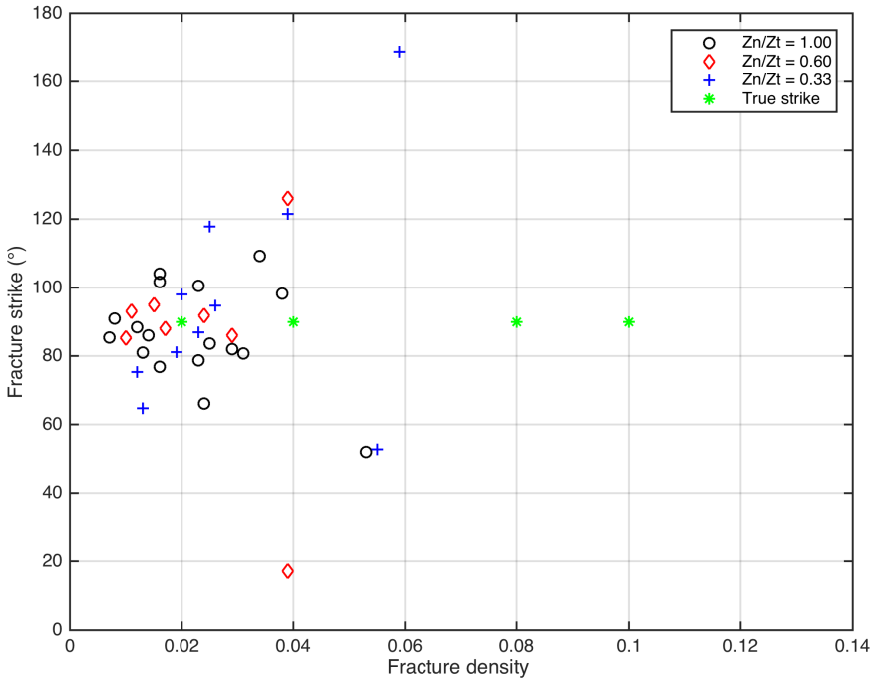

Figure 4.14: Inversion results for fracture strike versus fracture density for the single fracture set models.

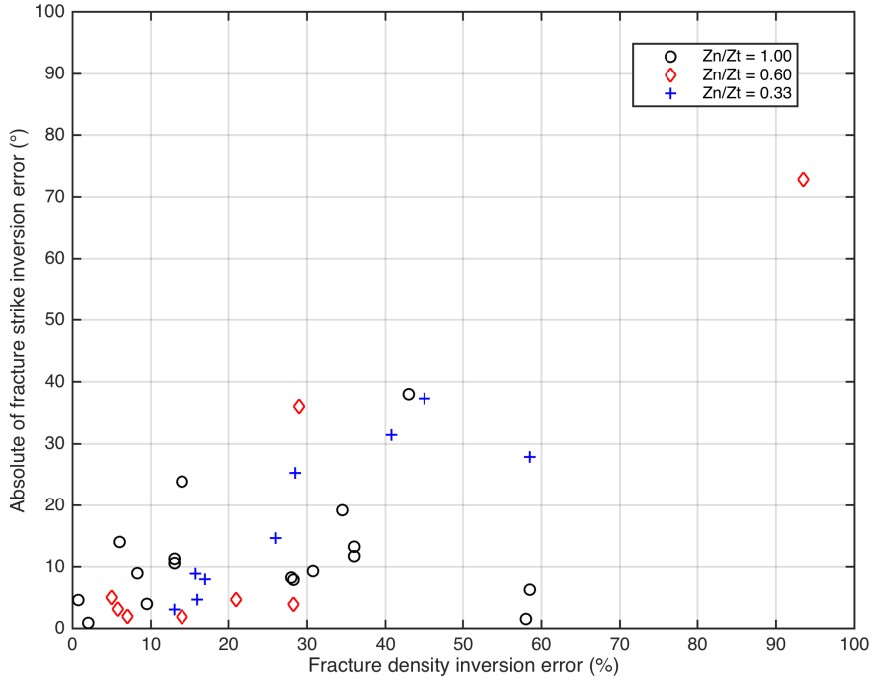

Figure 4.15: Inversion error for fracture strike inversion versus fracture density for the single fracture set models.

the true model fracture strike $\alpha = 90°$. The inverted strikes for the $Z_N/Z_T = 0.60$ are more tightly constrained around the true model. The average and standard deviation of the inversion results for the three categories of compliance ratio Z_N/Z_T are given in Table 4.3 (more detailed analysis of fracture inversion error for the single fracture set models are listed in Tables D.1-D.3 of the Appendix D). A general observation from the inversion results of the single fracture models suggests that fracture strike is much better constrained than fracture density, consistent with the results of Verdon et al. (2011b).

Z_N/Z_T	$\Delta\epsilon(\%)$	$\Delta\alpha(°)$
0.33	76.85 ± 41.62	24.00 ± 21.53
0.6	66.56 ± 25.74	16.19 ± 23.95
1.0	67.79 ± 16.36	11.40 ± 8.75

Table 4.3: Average error in fracture strike and density for the single fracture set models (given as average error $\pm$ standard deviation).

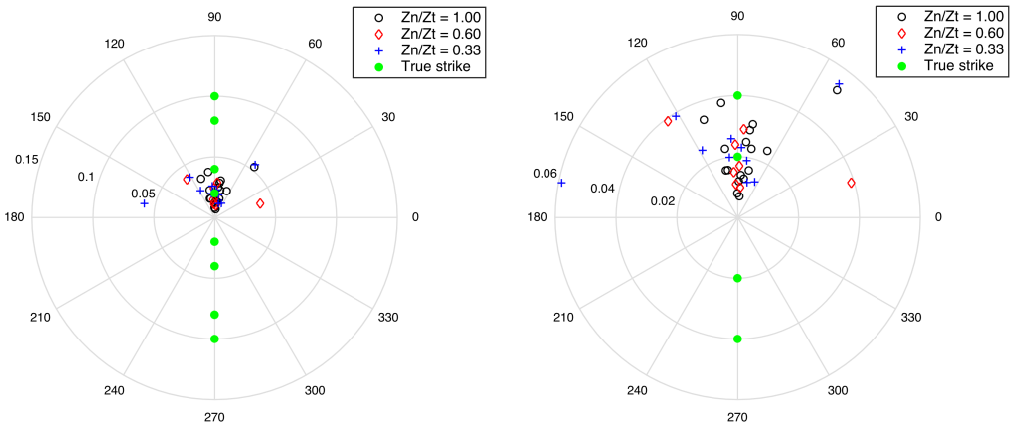

(a) (b)

Figure 4.16: Inversion results for fracture strike versus fracture density for the single fracture set models in the polar plot diagram (left) and zoom in for clear visualisation of the results (right).

4.5.2 Double fracture sets

Figure 4.17 shows the lower hemisphere projection of the S-wave phase velocity as a function of propagation direction based on the best fitting elasticity tensor for the double fracture set models with $a = 20$ m, $\epsilon = 0.08$ and $Z_N/Z_T = 0.60$ (see Table 4.2). The inverted strike and density for the first fracture set are $\alpha 1$ = -10.49° and $\epsilon 1 = 0.075$, and for the second fracture set are $\alpha 2 = 86.20°$ and $\epsilon 2 = 0.032$. The inverted fracture strikes are close to the true model fracture strikes (i.e., 0° and 90°), indicating that the inversion for strike has been successful. However, the inverted fracture densities are less accurate for the case of orthogonal fracture sets. This finding is consistent with the inverted fracture densities of Verdon et al. (2009). Furthermore, Bakulin et al. (2002) and Grechka & Tsvankin (2003) have discussed that it is possible for a broad range of fracture density models to produce equivalent effective medium stiffness tensor.

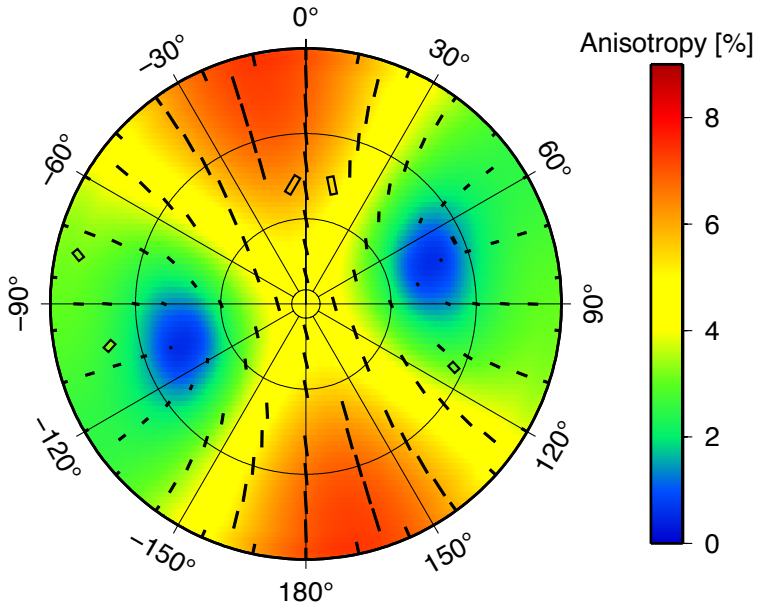

Figure 4.17: Inversion results for the double fracture set model (S20LD8) with size 20 m and Z_N/Z_T =0.60. The fracture parameters were determined to have $\alpha 1$ =-10.49° and $\epsilon 1$ =0.075 for the first fracture set and $\alpha 2$ =86.20° and $\epsilon 2 = 0.032$ for the second fracture set. The true model have have values $\alpha 1 = 0°$ and $\alpha 2 = 90°$ for strike and $\epsilon 1 = \epsilon 2 = 0.08$ for fracture density.

Figure 4.18 plots the inversion results of fracture strike versus fracture density for all the double fracture set models. The inversion results for the second fracture set (strike of 90°) are more accurate than the inversion results for the first fracture set (strike of 0°), although it is necessary to calculate the errors of inversion results for the fracture strike and density. Figure 4.19 shows the error of the inversion results for the double fracture set models in term of absolute error in fracture strike $\Delta\alpha(^\circ)$ versus percentage error in fracture density $\Delta\epsilon(\%)$. The error in fracture strike for both fracture sets ranges between 0° and 45°. For both fracture sets, the error in fracture density are approximately on the same order of magnitude ranging between 0% and 100%. Table 4.4 lists the average errors in the inversion for fracture strike and density for both fracture sets for each compliance ratio Z_N/Z_T (more detailed analyses of fracture inversion error for the double fracture set models are listed in Tables D.4-D.6 of the Appendix D).

Figure 4.20 shows the inversion results for fracture strike ($\alpha 1$ and $\alpha 2$) and fracture density ($\epsilon 1$ and $\epsilon 2$) for the double fracture set models. The results reveal that the inverted fracture strike and density for fracture set 2 are more constrained than those for fracture set 1. This is due to the optimal orientation of the MT source polarisation to illuminate the second fracture set (90°) than the first fracture set (0°). Since the fractures in the model are orthogonal, I examine the orthogonality of the inverted fracture strikes. Figures 4.21-4.22 show the histogram and polar plot diagrams of the difference in strike between the inverted fracture strikes $\Delta\alpha$. The histogram reveals that the majority of the inversions have $\Delta\alpha = 90^\circ \pm 30^\circ$. From Figure 4.22 it can be observed that the inversion results for fracture densities versus $\Delta\alpha$ are more constrained with increasing compliance ratio Z_N/Z_T. However, by decreasing Z_N/Z_T the inverted fracture densities have broader range. This seems to correlate with the number of models having different fracture parameters particularly in term of the fracture size (see Tables D.4-D.6).

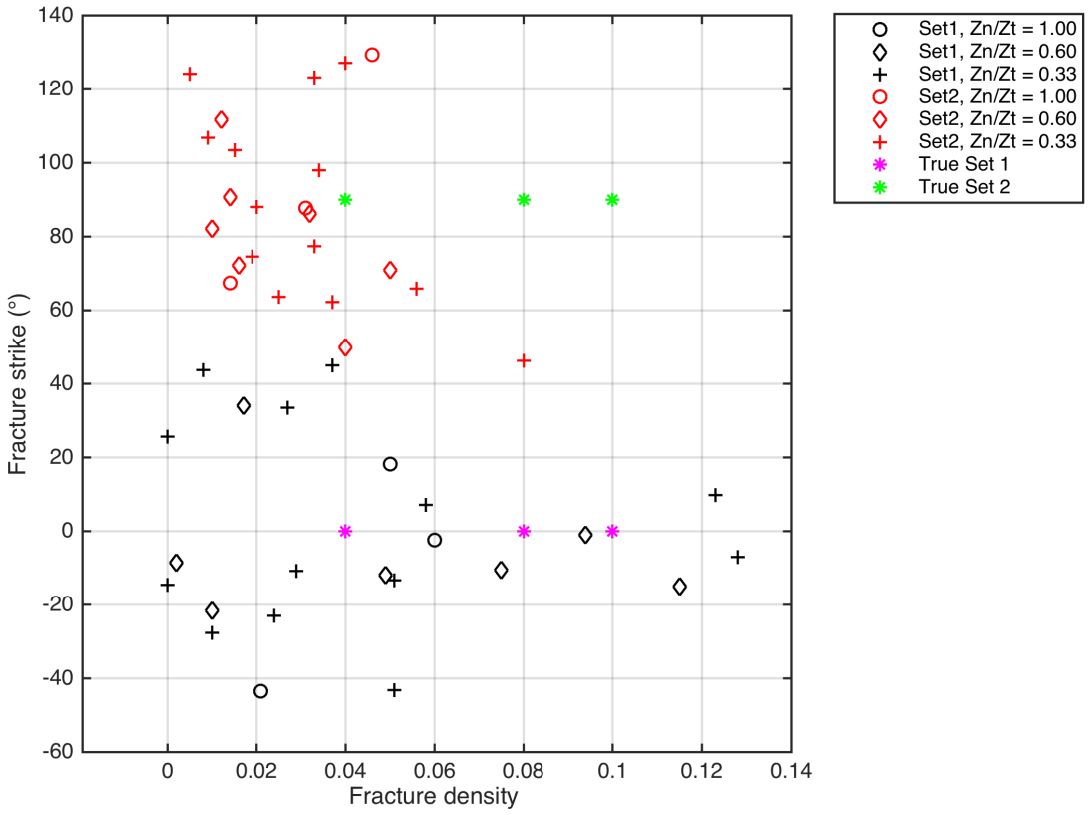

Figure 4.18: Inversion results for fracture strike versus fracture density for the double fracture set models.

Z_N/Z_T	$\Delta\epsilon 1(\%)$	$\Delta\alpha 1(^\circ)$	$\Delta\epsilon 2(\%)$	$\Delta\alpha 2(^\circ)$
0.33	88.38 $\pm$ 101.62	23.41 $\pm$ 13.73	60.21 $\pm$ 61.95	22.68$\pm$11.97
0.6	67.61 $\pm$76.84	14.68$\pm$9.78	31.64$\pm$38.04	15.88$\pm$12.39
1.0	40.83$\pm$11.24	21.37$\pm$16.93	60.08$\pm$4.57	21.39$\pm$15.15

Table 4.4: Average error in fracture strike and density error for the double fracture set models (given as average error $\pm$ standard deviation).

Figure 4.23 presents the inverted fracture strike versus fracture density for both single and double fracture set models. From this figure, it is apparent that the maximum error in the inversion for strike for the single fracture set models (i.e., 80°) is approximately double that of the double fracture set models. In contrast, the inversion error for fracture

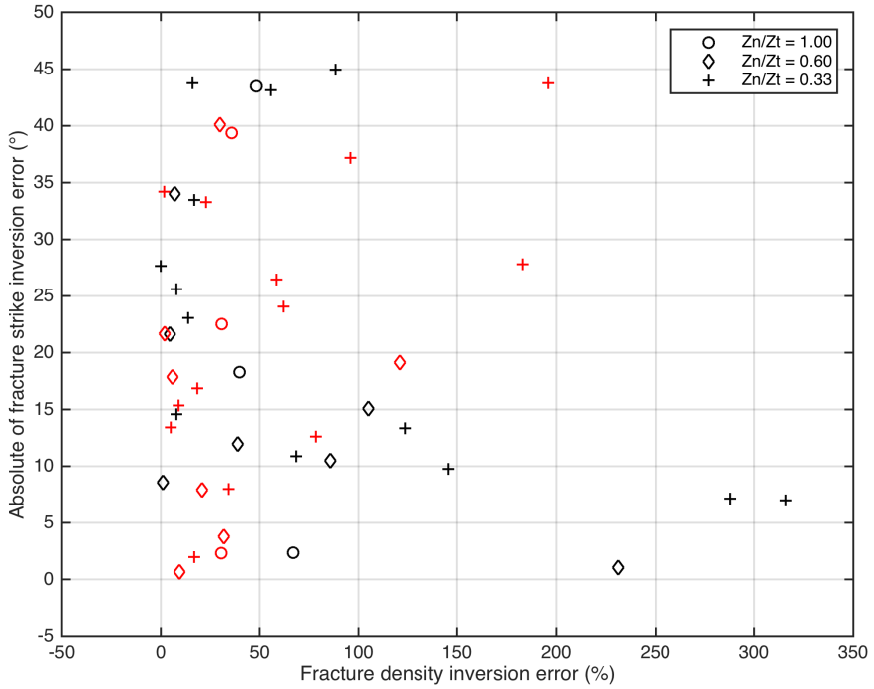

Figure 4.19: Inversion error for fracture strike versus fracture density for the double fracture set models. The results for set 1 are shown in black and for set 2 are shown in red.

density for both single and double fracture set models are generally between 40% and 100%.

4.6 Discussion

From Figures 4.14 to 4.20 it can be observed that the inversion algorithm is capable of estimating fracture strike robustly without prior knowledge of the medium fracture properties. The outliers are likely influenced by the non-linear nature of the inversion algorithm and the fact that the inversion uses only a single event to characterise a finite fracture volume. In contrast, it should be noted that the inverted fracture densities are systematically underestimated from the true value for the single fracture set (i.e., the inversion results clustered between 0.00 and 0.06), while it is systematically overestimated for the double fracture sets for the low compliance ratios (i.e., $Z_N/Z_T = 0.33$

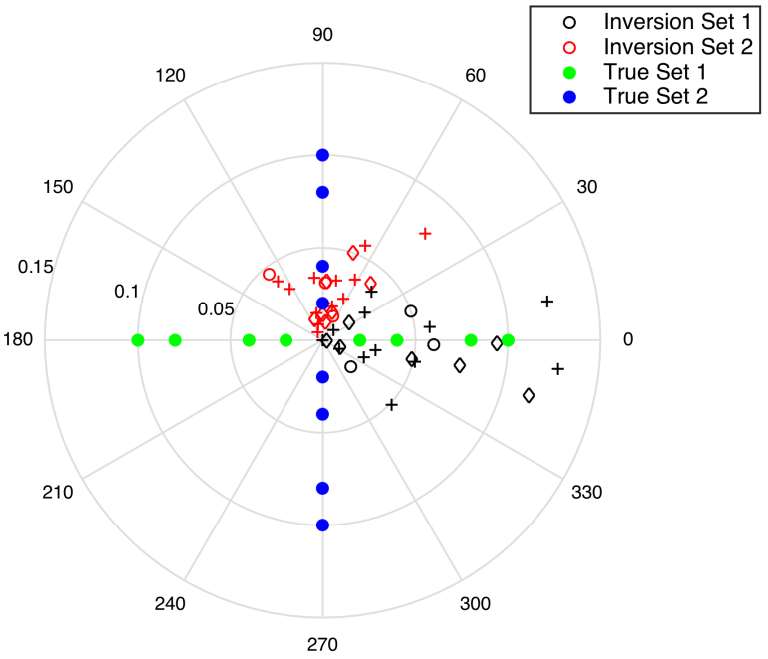

Figure 4.20: Inversion results for fracture strike versus fracture density for the double fracture set models in polar diagram.

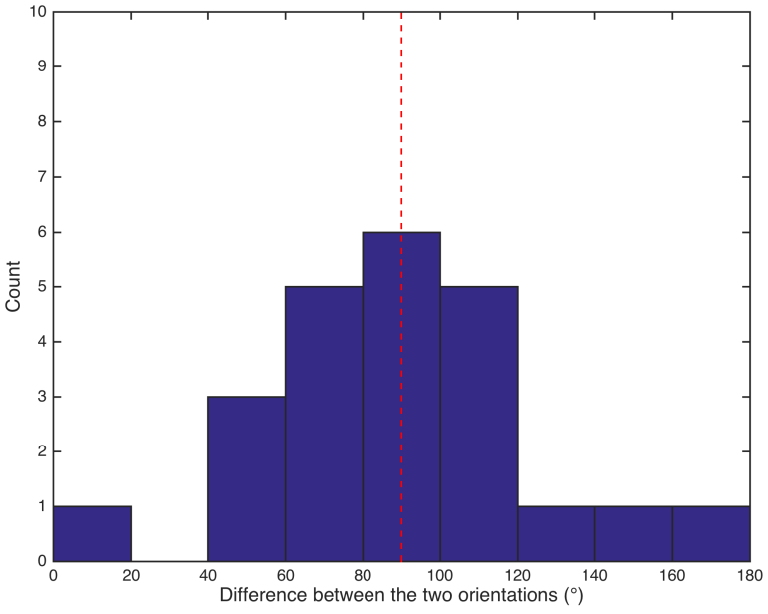

Figure 4.21: The histogram of the difference between the inverted fracture strikes of the double fracture sets.

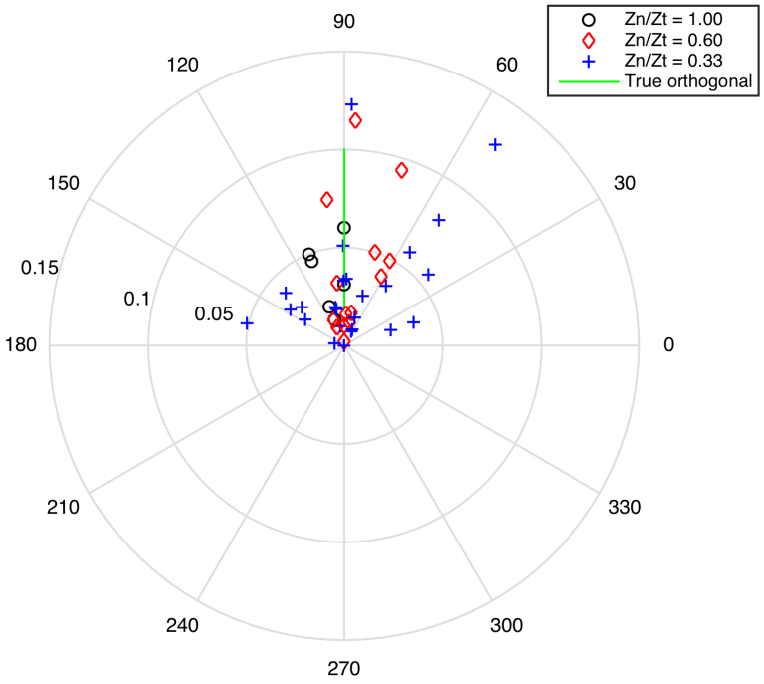

Figure 4.22: The results of difference in fracture strike inversion for the double fracture sets of in the polar coordinate for the Z_N/Z_T=1.00, 0.60 and 0.33. The radial axis and the angular axes are the fracture density and fracture strike respectively.

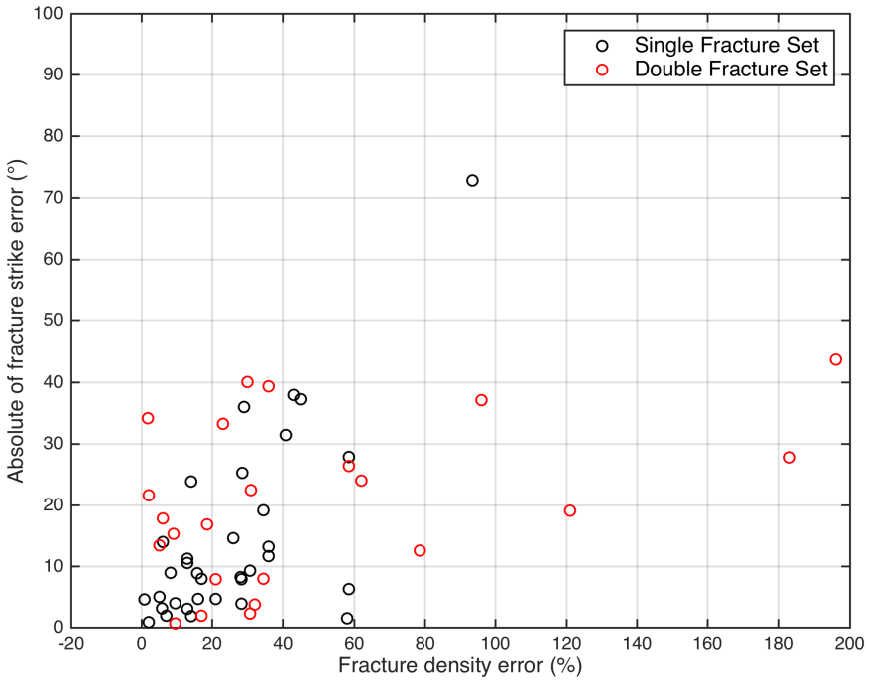

Figure 4.23: Comparison of inversion results for fracture strike versus fracture density for both the single and double fracture set models.

and 0.60). The INSAFF algorithm assumes that the whole medium in which the ray traverses is fractured, instead of only a portion of the raypath within fracture zone and so might explain the underestimate of density (Verdon et al., 2009; Verdon et al., 2011b; Wookey, 2012). Furthermore, the location of the source and orientation of failure source mechanism may be insufficient to illuminate the fracture set. However, with more sources spatially distributed around the fracture volume and more favourable (i.e, more data) it is possible that the fracture inversion would yield more accurate results (Rial et al., 2005). For the double fracture set models, the inverted strike for the 0° fracture set degrades, whereas the inverted strike for the 90° fracture set appears to be better resolved (broader but fewer outliers). In the following chapter, I will show that the inaccurate estimate of fracture density are significantly influenced by the choice of effective medium rock physics model.

4.7 Summary

In this chapter, I have shown that it is feasible to invert SWS measurements to quantitatively estimate fracture strike and qualitatively estimate fracture density assuming an effective medium fracture model. The results of the full waveform FD synthetics indicate that the source frequency of the microseismicity will be crucial in extracting reliable fracture parameters due to the relationship between scale length of the probing seismic wave and the fracture heterogeneity (i.e., size). Although the SWS results themselves are diagnostic of fracturing, the fracture inversion allows placing constraints on the physical properties of the fracture system. For real microseismic datasets, the range in magnitude of microseismicity (i.e., frequency content), spatial distribution and variable source mechanisms suggests that the inversion of fracture properties from SWS measurements is feasible. For the single seismic source case and optimum receiver array

geometry, the inversion for strike has average errors of between 11° and 25°, whereas for density has average errors between 65% and 80% for the single fracture set and 30% and 90% for the double fracture sets. Improvements on resolving strike can be made by including more microseismic sources in the inversion process. Furthermore, the improvements in resolving fracture density (or stiffness) can be achieved using a more advanced inversion approach such as anisotropic tomography in which the medium can be divided into different domains, where each domain has different anisotropic characteristics (e.g., Abt & Fischer, 2008; Wookey, 2012).

Chapter 5

Parametrisation study: Quantifying a transition from scattering to anisotropy

---

5.1 Introduction

To estimate or invert for the fracture properties a rock physics model is required to map the measured seismic anisotropy attributes (e.g., SWS) to the physical fracture properties. In general there are two approaches to model fractured rock: effective medium models (EMM) and discrete fracture models (DFM) (see Chapter 2). EMM is the most common approach for modelling the seismic behaviour of fractured rock (e.g., Hall & Kendall, 2000; Baird et al., 2013). However, there are limitations such as the applicable frequency range, the types of fracture properties which can be studied, and

non-uniform influences for example due to stress-field (e.g. Hildyard, 2007). The main restriction for EMM is that it is valid only when the dominant seismic wavelength of the propagating wave is much greater than the heterogeneity induced by the fractures; this is referred to as the LWA. Furthermore, EMM assumes the rock mass is instantaneously anisotropic and so does not allow for the transition from a scattering regime to an effective anisotropy regime.

The alternative approach is to model fracture networks as discrete elements that can encapsulate individual fracture behaviour (e.g. Hildyard, 2007). DFM allows us to reduce many assumptions about the model and enables the solution to simulate the interaction of seismic waves with fracture systems more correctly. DFM models can capture the influence of the stress state, as well as specific fracture properties such as fracture size, fill and compliance. Furthermore, DFM is not restricted by the LWA and allows the dominant seismic wavelength to be greater, less than or equal to the fracture size, allowing the characterisation of low-frequency behaviour (i.e., LWA regime) and high-frequency behaviour (i.e., ray theoretical limit). However, it is generally difficult to determine the spatial geometry of fracture systems deterministically and often the computational costs associated with modelling discrete fractures can be a barrier.

Figure 5.1 illustrates some of the uncertainties in inferring fracture properties from seismic anisotropy. Figure 5.1a shows two ray paths (P1 and P2) of equal length propagating through a fracture zone consisting of discrete fractures. The ray path perpendicular to fracture strike (P1) will experience a longer travel time than the ray path traveling along strike (P2) due to the presence of the seismic discontinuities (e.g., Babuska & Cara, 1991). This leads to an effective velocity anisotropy with seismic velocity being greater along strike than perpendicular to strike. In Figure 5.1b I include an elliptical velocity anomaly that can lead to either (i) a perceived greater seismic velocity anisotropy (if the anomaly is a high-velocity ellipse) or a perceived smaller

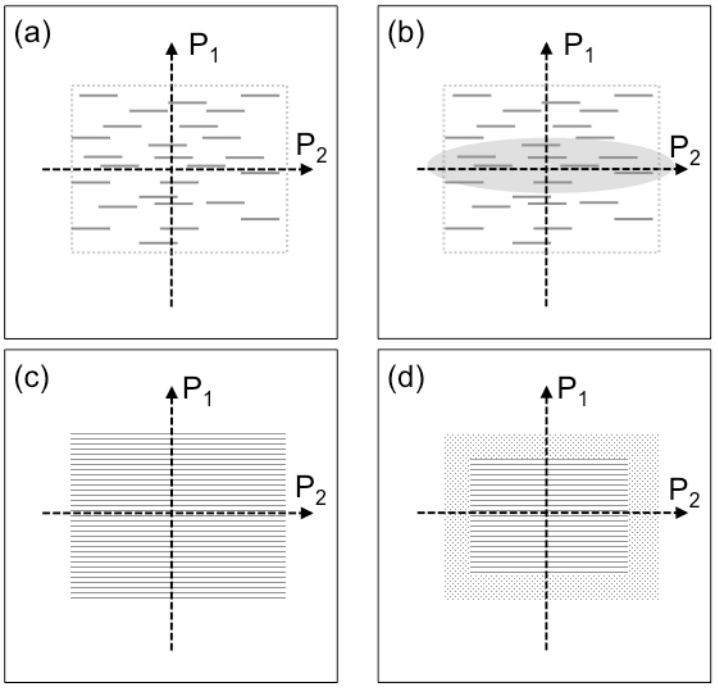

Figure 5.1: Schematic diagram of fracture induced seismic anisotropy: (a) two ray paths P_1 and P_2 (dashed arrows) travel through a fracture zone (within the dashed rectangle) with discrete fractures depicted by grey lines; (b) same as (a) but with the inclusion of a velocity anomaly (shaded ellipse); (c) same as (a) but with the discrete fracture zone represented by an effective homogeneous fracture zone; and (d) same as (c) but with the effective homogeneous fracture zone reduced in size and surrounded by a transition region (stippled region).

seismic velocity anomaly or isotropy (if the anomaly is a low-velocity ellipse). This illustrates the inherent ambiguity of traveltime anisotropic velocity analysis. In Figure 5.1c I apply the standard approach to modelling fractures by introducing a homogeneous representation of the discrete fractures with an elastically anisotropic zone based on an effective rock physics model of the fracture zone (e.g., Liu & Martinez, 2012). Since seismic anisotropy evolves as the wave propagates through a discrete fracture system, there is a region within the fracture volume where the interaction of the wave with the fractures transitions from a scattering regime to an effectively anisotropic regime. This is depicted in Figure 5.1d where I introduce a buffer zone around a smaller effective homogeneous fracture zone.

Under what conditions do fractured media become seismically anisotropic? How do

we define the transition region from scattering to anisotropy? How should we consider this transition in our quantitative estimates of fracture properties? To provide some insight into these fundamental questions, I study the development of SWS as a wave propagates through a fractured medium using the DFM approach. To do this, I model full waveform seismic synthetics using the 3D finite-difference (FD) algorithm WAVE (Hildyard, 2007) that models fracture networks as explicit discontinuity elements that can encapsulate individual fracture behaviour. By using the DFM approach I can explore the range of fracture properties that lead to effective anisotropy using heterogeneous yet coherent discontinuities by simulating the interaction of seismic waves with fractures. The DFM allows models to capture the influence of specific fracture properties, such as fracture size, stiffness and spacing (or density) on seismic SWS.

5.2 Methods

In this section, I first describe the forward modelling approach and elastic models used to generate the FD full waveform seismic synthetics. Subsequently, I summarise the approach to calculate SWS with special attention to the evaluation of the SWS quality factor.

5.2.1 Numerical FD model

I use the full waveform FD algorithm WAVE (Hildyard, 2007) to simulate wave propagation in 3D heterogeneous and isotropic media. The WAVE algorithm was previously discussed in Chapter 3. Fractures are represented using the DFM approach, where each fracture or group of fractures are explicitly defined as a displacement discontinuity. The fracture surfaces have zero-thickness, where the difference in displacements across the two surfaces is related to the stress across the interface. The stress and discontinuity in

displacement across the two surfaces are coupled by the fracture normal and tangential stiffnesses. In principal, the fracture stiffness accounts for the existence of asperities and voids between the surfaces of natural fractures (e.g., Baird et al., 2013; Petrovitch et al., 2013), leading to a finite coupling between the surfaces. Hildyard & Young (2002) benchmark WAVE and the DFM approach with laboratory experiments of ultrasonic wave propagation through natural fractures in rock (Pyrak-Nolte et al., 1990). Hildyard & Young (2002) show that the WAVE and the DFM approach accounts for frequency dependence of both the seismic velocity and the transmitted wave amplitude.

I consider a base fracture model having vertical fractures oriented along the x-axis within an isotropic background medium. The isotropic elastic medium has density ρ = 2600 kg/m^3, P-wave velocity V_P = 5700 m/s and S-wave velocity V_S = 3200 m/s (V_P/V_S = 1.78). The geometry of the model has overall dimension of (x, y, z) = (300 m, 300 m, 300 m)(see Table 4.1). Seismic waves are generated using a moment tensor source having a seismic moment magnitude of 1×10^{11} N m and a strike-slip double-couple mechanism with strike $90°$, dip of 90° and slip 45°. The source time function has a dominant source frequency of approximately 180 Hz, and so I use a grid spacing of $\Delta h = 1$ m and time increment of approximately $\Delta t = 0.08$ ms to maintain numerical stability and minimise grid dispersion for all fracture model realisations. The source is located at (x_s, y_s, z_s) = (100 m, 150 m, 140 m) outside the fracture volume having dimension (x, y, z)=(80 m, 80 m, 80 m). A single linear array of 10 three-component receivers is defined, oriented along the direction of maximum SWS (i.e., along the x-axis) and located through the fracture volume (see Figure 5.2).

I generate a suite of 48 model realisations by varying one of three explicit fracture properties (compliance ratio, fracture size and fracture density) while keeping the other two constant. I focus on compliance ratio as this parameter has been used as an indicator for fracture fluid fill as well as fracture geometry (e.g., Verdon & Wüstefeld, 2013).

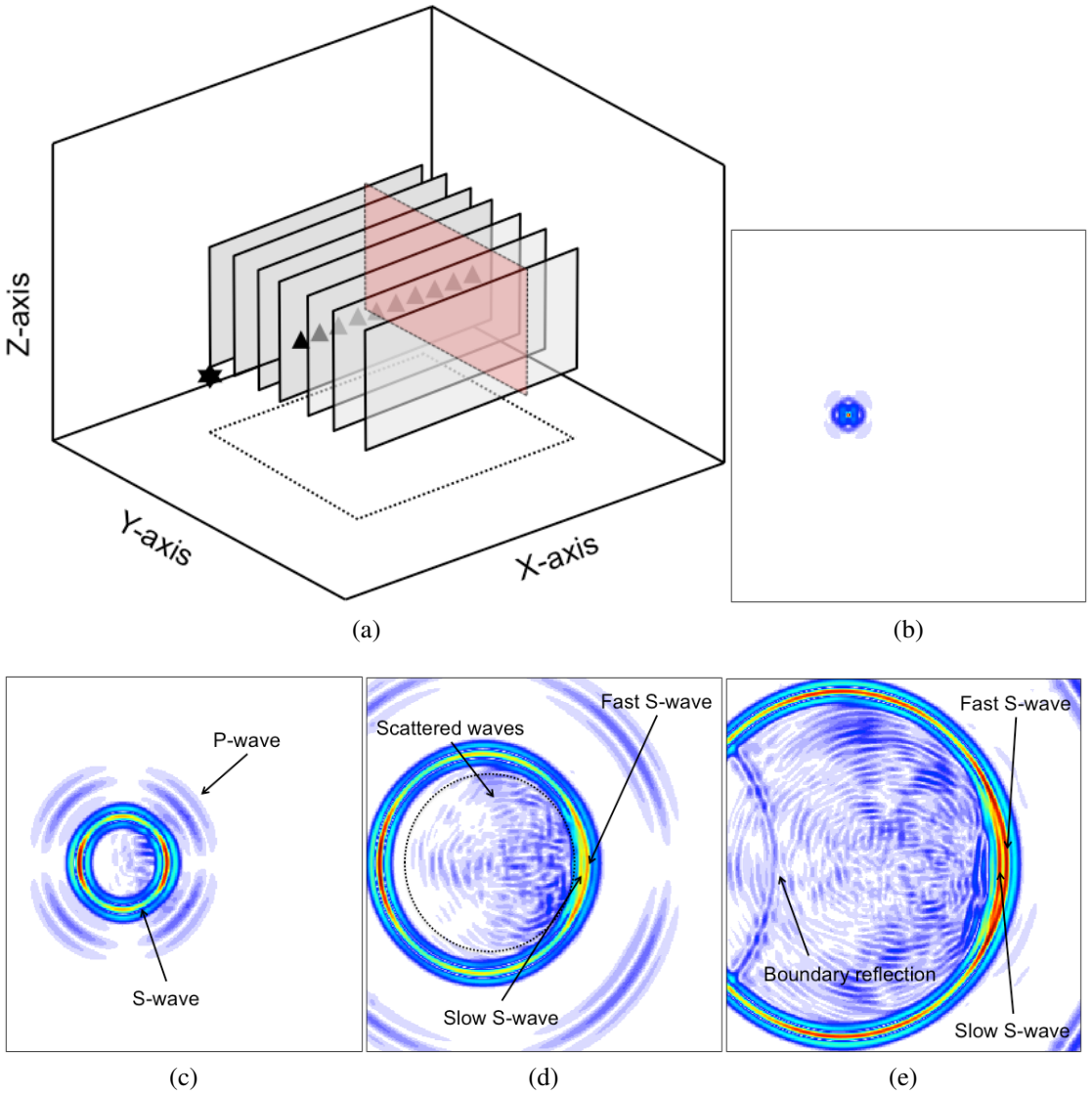

Figure 5.2: (a) Schematic view of the linear receiver array within the FD model. The star represents the source location, the triangles represent the receivers and the grey shaded rectangles represent the vertical and lateral extent of the discrete fracture zone. The red vertical plane depicts an example plane where I perform horizontal scans through the fracture volume to compute fracture spacing distribution. Snapshot of a seismic wave propagating in the x-y plane through a fractured medium for a double-couple source at time (b) t=7.9 ms, (c) t= 17.34 ms, (d) t=33.1 ms and (e) t=48.9 ms. In (d) the scattered waves are highlighted by the region within the dashed ellipse.

For compliance ratio, Z_N/Z_T, I consider values of 0.33, 0.60 and 1.00, which are consistent with the range of values observed from laboratory and field measurements (e.g., Angus et al., 2012; Verdon & Wüstefeld, 2013; Choi et al., 2014). For fracture size, a, I consider values of 6, 10, 20 and 50 m for several reasons and constrained by the dominant wavelength ($\lambda_S \approx 18$ m) of the shear-wave. For crustal rock, the size (or height) of fractures ranges on the order of between 0.01 to 10 m (e.g. Narr et al., 2006; Barton, 2007). Thus the lower end values of 6 and 10 m represent typical values observed in the field yet having size that approaches the length scale of the dominant wavelength. Values above 10 m allow us to explore the transition from conditions where EMM would be valid to conditions where EMM for fractures would not be valid. Therefore the size range of the fractures allows us to examine the transition from LWA or Rayleigh scattering where $\lambda_S/a > 1$, to Mie scattering regime where $\lambda_S/a \to 1$, and to the high frequency or geometric scattering regime ($\lambda_S/a < 1$). For fracture density, ϵ, I used values of 0.02, 0.04, 0.08 and 0.10, which is consistent with field observations of naturally occurring fracture systems (e.g., Narr et al., 2006). The values of normal and tangential stiffnesses range on the order of between 1×10^9 to 1×10^{11} Pa/m. The specific values used are consistent with the laboratory and field-scale estimates of Worthington (2008) and Verdon & Wüstefeld (2013), and are dependent on the fracture size.

Figure 5.2 shows an example of shear-wave propagation through a fracture volume at 4 time steps to highlight the evolution of SWS, where the linear array allows us to monitor the evolution of the shear wavefront as it propagates through the fracture volume. (Note that the P-wave is barely visible because the x-y section is along the null axis of the P-wave radiation pattern of the double-couple source.) As the wave propagates, the right-hand side of the wavefront begins to interact with the fracture volume, where scattering can be observed behind the primary shear-wave. At later times,

SWS can be observed on the right-hand side of the wavefront as well as significant scattering in the wavefield persisting behind the primary shear-wave within the fracture volume. The scattering that is observed is due to a combination of first-order (i.e., single) and higher-order (i.e., multiple) diffractions from fracture tips and edges as well as specular reverberations (i.e., multiply reflected energy) from fracture surfaces.

5.2.2 SWS parameters

I use the algorithm SHEBA (e.g., Teanby et al., 2004a; Wuestefeld et al., 2010) to compute the SWS parameters. The analysis of SWS requires first rotating the three component waveforms into a local ray coordinate frame, where the P-wave energy will be constrained to the ray direction (P) and the shear-wave energy on the two remaining components (S_V and S_H)(see Section 3.7.2.1). The rotation can be done either using a standard rotation algorithm based on the polarisation filter approach of Montalbetti & Kanasewich (1970) or by assuming a straight ray path between the source and receiver. I compare both approaches and found very little difference in the respective local coordinate frames for my models, and so use the straight ray path approximation to reduce processing time. After rotation into the ray coordinate, an analysis window is specified relative to the shear-wave first arrival. Typically one window size is chosen but a range of window start and end times are evaluated to cover the maximum possible time delays that could be expected. A grid search of analysis windows over these intervals allows for a much faster calculation of SWS parameters than manual picking and provides a measure of the overall SWS quality $\mathbb{Q}$ (Wuestefeld et al., 2010).

Within the algorithm the time delay between the fast and slow shear-waves and the rotation angle for maximum splitting are calculated by two XC and EV methods and compared to give a measure of quality (Teanby et al., 2004a). By comparing the similarity in the calculated time differences from the two methods a $\mathbb{Q}$ value is defined

(see Section 3.7.2.4), where values close to one represent good splitting and values close to negative one are good nulls (i.e., no SWS) (Wuestefeld et al., 2010). When the value of $\mathbb{Q}$ is close to zero, the data quality of the splitting is poor or inconclusive. Typically, with noisy data, values between -0.5 and 0.5 are discarded from further analysis. In my models, poor values would be expected due to the diffraction type scattering effects (e.g., Klem-Musatov, 2008) from the edge of the discrete fractures (see Chapter 3 for further discussion).

Previously an example of good and good null splitting was shown in Figure 4.2. That figure shows the results for a good splitting measurement, where an initial elliptical particle motion is linearised after an appropriate rotation and delay correction. The calculated delay time of 1.32 ms and fast polarisation direction of 36° is well constrained in both methods yielding $\mathbb{Q} = 0.96$. Figure 4.2 also shows the result of a null splitting example, where the initial polarisation is linear. Since there is no SWS, the solution is not well constrained yielding $\mathbb{Q} = -0.98$. For all fracture models, I apply the same SWS analysis to all receiver recordings to compute the delay time and associated quality factor.

5.3 Results

For all 48 models, I calculate the SWS parameters for all 10 receivers within the fracture volume. In Figures 5.3-5.6, I show the computed delay time δt for each station as a function of propagation length within the volume normalised by the shear wavelength (distance/λ_S). The quality of δt is given by colour contours, with $\mathbb{Q} = 1$ red, $\mathbb{Q} = 0$ green and $\mathbb{Q} = -1$ blue.

Figure 5.3 displays the SWS results for the fracture models having fracture size $a = 6$ m. For this model, the dominant wavelength of the shear-wave is 3 times greater

than the size of the fractures such that the simulation results fall within the LWA regime (e.g., Ebrom et al., 1990; Marion et al., 1994). For all compliance ratios and fracture density, there is a general trend of spurious δt measurements for receivers located close to the source within approximately one wavelength of propagation distance. For these receivers the quality of the SWS measurements is low indicating either null or inconclusive measurements. For fracture density greater than 0.04 there is a general trend of increasing δt starting from a non-zero value ($\approx$ 0.5 ms) up to approximately 3 ms with generally good SWS quality factors. For the lower fracture densities of 0.02 and 0.04, the quality of the SWS results is variable indicating that the model fracture density may not be of sufficient magnitude to induce shear-wave anisotropy. The results indicate that fracture density plays a more significant role on the evolution of SWS than compliance ratio.

Figure 5.4 displays the SWS results for the fracture models having fracture size $a = 10$ m. For fracture size $a = 10$ m the model falls close to the border of the LWA regime, where the dominant shear wavelength is less than 2 times greater than the size of the fractures. As with Figure 5.3, there is a general trend of spurious low quality δt measurements within approximately one wavelength of propagation distance. For fracture density greater than 0.04 there is a general trend of increasing δt starting from a non-zero value (≈ 0.5 ms) up to approximately 2 ms with generally good SWS quality factors for receivers beyond 2 to 3 propagation wavelengths. For the lower fracture densities of 0.02 and 0.04, the quality of the SWS results are much more variable than those for fracture size $a = 6$ m indicating that the fracture size of $a = 10$ m leads to less reliable or coherent induce shear-wave anisotropy.

Figure 5.5 displays the SWS results for the fracture models having fracture size $a = 20$ m. The dominant shear wavelength has approximately the same order of magnitude of the fracture size such that the LWA is no longer valid and where I expect

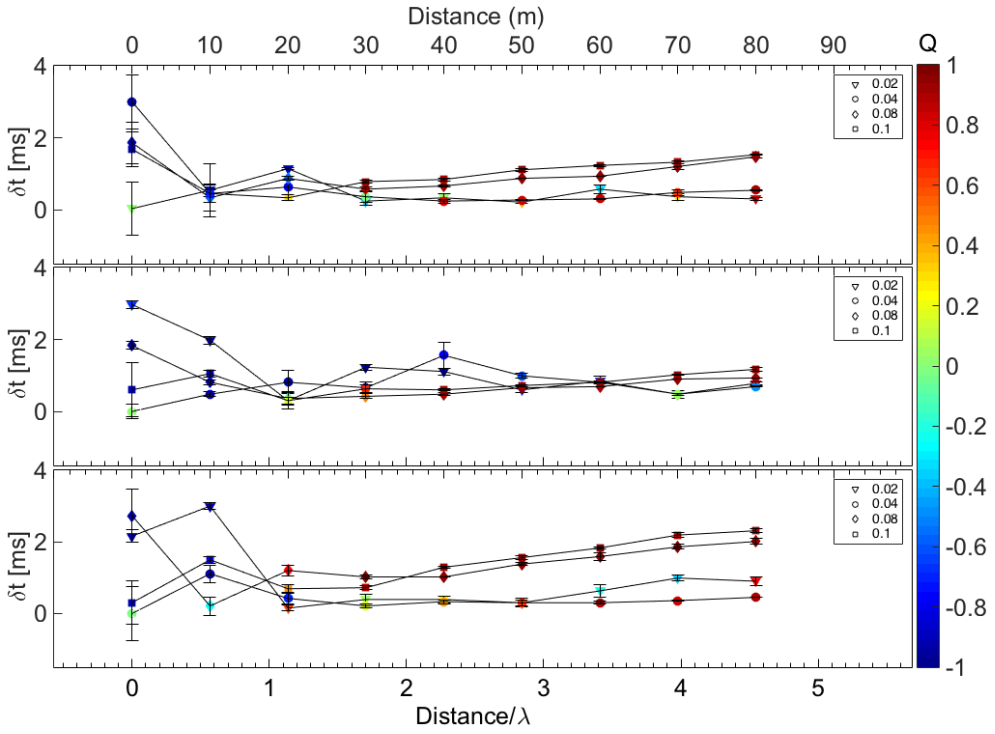

Figure 5.3: Evolution of SWS for fractures having size $a = 6$ m: (top) $Z_N/Z_T = 0.33$, (middle) $Z_N/Z_T = 0.60$ and (bottom) $Z_N/Z_T = 1.00$. The vertical axis represents the calculated delay time δt with corresponding error bars and the horizontal axis represents the propagation distance within the fracture volume normalised by the dominant wavelength $\lambda_S = 18$m. The colour contour of the symbols represents the quality factor of the SWS measurement. The fracture stiffness values are: ($Z_N/Z_T = 0.33$) $K_N = 6 \times 10^{10}$ Pa/m and $K_T = 2 \times 10^{10}$ Pa/m,($Z_N/Z_T = 0.60$) $K_N = 5 \times 10^{10}$ Pa/m and $K_T = 3 \times 10^{10}$ Pa/m, and ($Z_N/Z_T = 1.00$) $K_N = 1 \times 10^{10}$ Pa/m and $K_T = 1 \times 10^{10}$ Pa/m. The legend in the top-right corner of each subplot represents the fracture density: inverted triangle=0.02, circle=0.04, diamond=0.08 and square=0.1

to observe Mie scattering. For all compliance ratios and fracture density the SWS results are unreliable and incoherent. In Figure 5.6, I show the results for fracture models having fracture size $a = 50$ m. The ratio of shear wavelength to fracture size falls in the high-frequency approximation (HFA) region, $\lambda/a \approx 2/5$ (Ebrom et al., 1990; Marion et al., 1994) where I expect to observe geometric scattering. As with the case of fracture size $a = 20$ m, the SWS results are incoherent with the exception of two models: $Z_N/Z_T = 0.60$ and $\epsilon = 0.1$, and $Z_N/Z_T = 1.00$ and $\epsilon = 0.08$. It is important to note that the fracture models used in WAVE are generated using random fracture assemblies

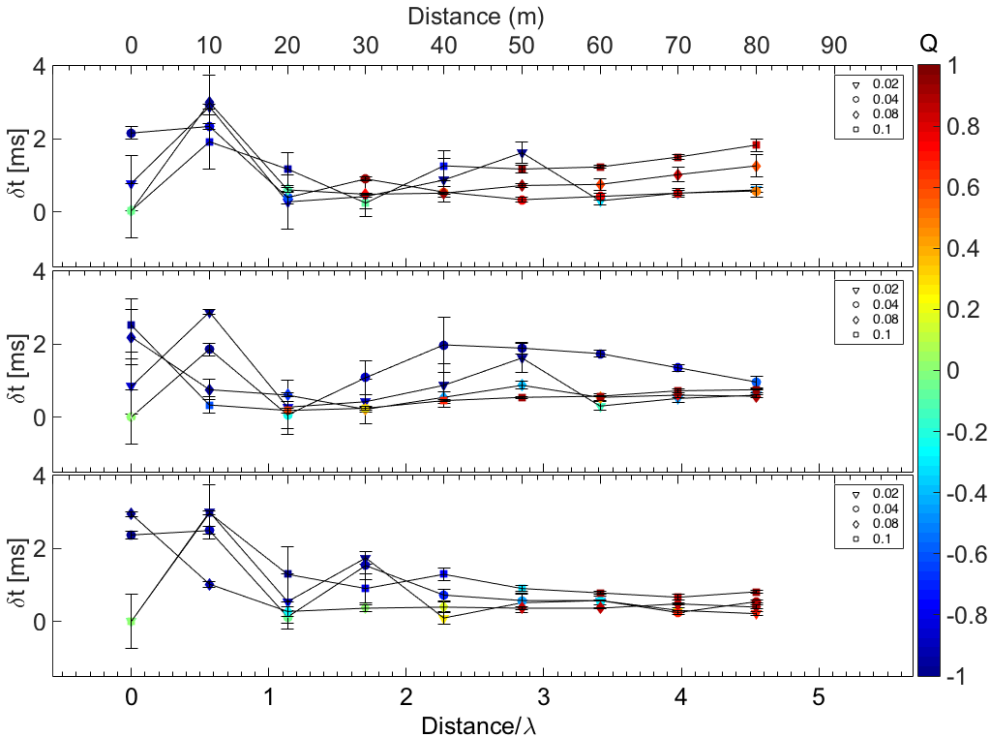

Figure 5.4: Evolution of SWS for fractures having size $a = 10$ m: (top) $Z_N/Z_T = 0.33$, (middle) $Z_N/Z_T = 0.60$ and (bottom) $Z_N/Z_T = 1.00$. The fracture stiffness values are: ($Z_N/Z_T = 0.33$) $K_N = 3 \times 10^{10}$ Pa/m and $K_T = 1 \times 10^{10}$ Pa/m, ($Z_N/Z_T = 0.60$) $K_N = 5 \times 10^{10}$ Pa/m and $K_T = 3 \times 10^{10}$ Pa/m, and ($Z_N/Z_T = 1.00$) $K_N = 3 \times 10^{10}$ Pa/m and $K_T = 3 \times 10^{10}$ Pa/m. See caption in Figure 5.3 for details.

given a range of fracture size and fracture density (Hildyard, 2007). For some of the random realisations the fracture distribution could form coherent and persistent planar features, similar to the influence of sedimentary layering that often leads to transverse isotropy (TI). Thus the interaction of the shear-wave with these large fractures could yield wave behaviour similar to that observed in TI media in the HFA regime. For larger fracture sizes or greater ray paths within the fracture volume, wave propagation would likely yield SWS having the same characteristics as that of horizontal TI media.

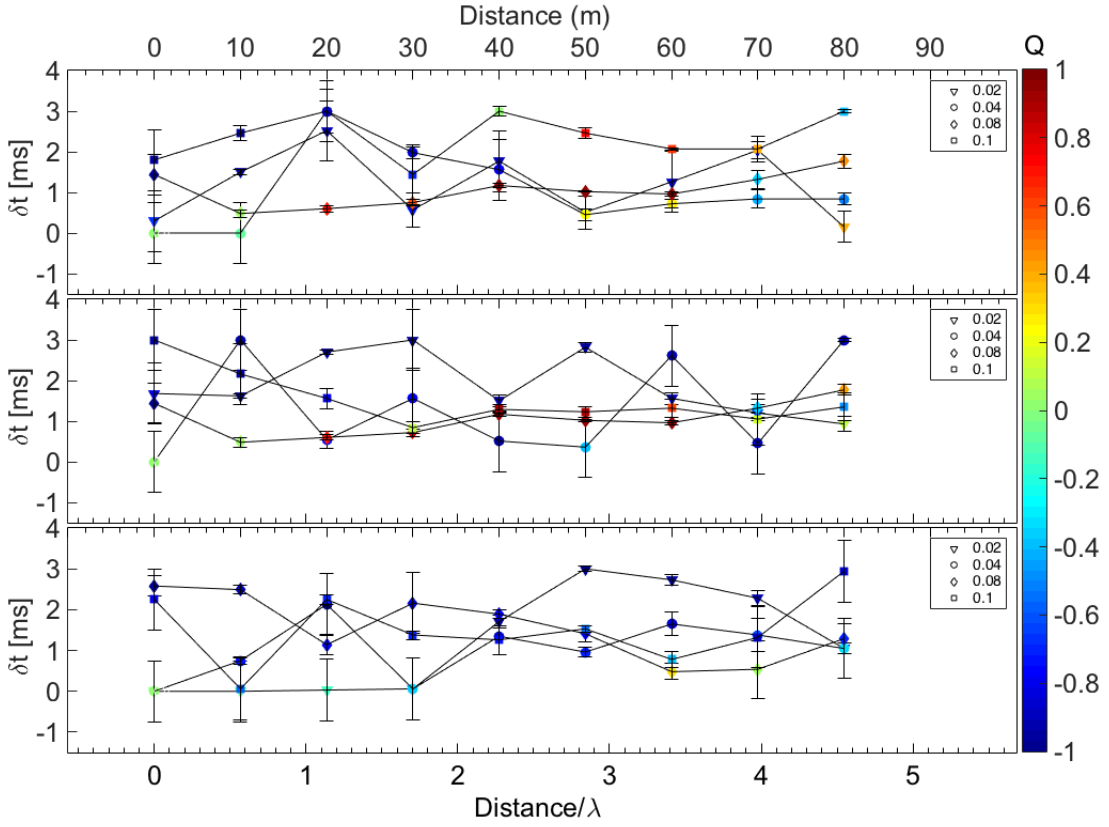

Figure 5.5: Evolution of SWS for fractures having size $a = 20$ m: (top) $Z_N/Z_T = 0.33$, (middle) $Z_N/Z_T = 0.60$ and (bottom) $Z_N/Z_T = 1.00$. The fracture stiffness values are: ($Z_N/Z_T = 0.33$) $K_N = 3{\times}10^9$ Pa/m and $K_T = 1{\times}10^9$ Pa/m, ($Z_N/Z_T = 0.60$) $K_N = 5{\times}10^9$ Pa/m and $K_T = 3 \times 10^9$ Pa/m, and ($Z_N/Z_T = 1.00$) $K_N = 1 \times 10^9$ Pa/m and $K_T = 1 \times 10^9$ Pa/m. See caption in Figure 5.3 for details.

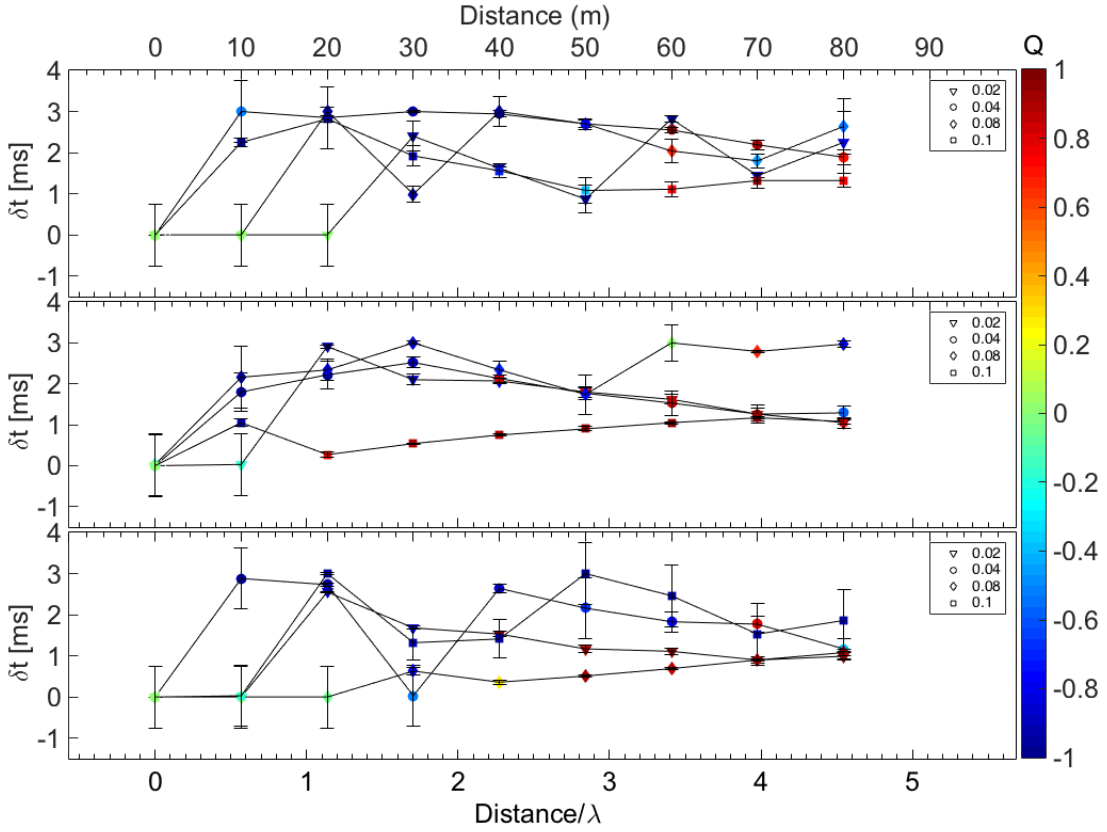

Figure 5.6: Evolution of SWS for fractures having size $a = 50$ m: (top) $Z_N/Z_T = 0.33$, (middle) $Z_N/Z_T = 0.60$ and (bottom) $Z_N/Z_T = 1.00$. The fracture stiffness values are: ($Z_N/Z_T = 0.33$) $K_N = 3{\times}10^9$ Pa/m and $K_T = 1{\times}10^9$ Pa/m, ($Z_N/Z_T = 0.60$) $K_N = 5{\times}10^9$ Pa/m and $K_T = 3 \times 10^9$ Pa/m, and ($Z_N/Z_T = 1.00$) $K_N = 3 \times 10^9$ Pa/m and $K_T = 3 \times 10^9$ Pa/m. See caption in Figure 5.3 for details.

5.4 Implications

I have addressed the question of when fracture systems become seismically anisotropic, at least for the case of shear-waves. However, I have explored the implications of the transition zone between scattering and effective anisotropy. To do this, I compare my δt observations with predictions using the LS EMM representation of Schoenberg & Sayers (1995). The LS approach is used extensively in the seismological literature to transform fracture compliance to dynamic (i.e., seismic) elasticity, primarily because of its generality (Hall & Kendall, 2000) due to the fracture compliances being rotationally

invariant (Barton, 2007).

First I compute the background stiffness matrix C_{ISO} based on the model density and isotropic P- and S-wave velocities. The background elasticity is then inverted to yield the background compliance S_{ISO}, where I can then add the excess compliance due to the presence of fractures using the approach of Schoenberg & Sayers (1995). The excess compliance matrix (ΔS) of the fractured medium requires first converting the WAVE model specific compliances Z_N and Z_T (units mPa^{-1}) to effective compliances B_N and B_T (units Pa^{-1}) using Equation 2.11.

The excess compliance matrix previously is given by Equation 2.15 (second term). If grid cells Δh in 3D FD are equal in three primary axes, so $L \equiv \Delta h$. Finally, the overall compliance in Equation 2.15 can be rewritten as,

$$S = S_{ISO} + \frac{1}{\Delta h} \begin{bmatrix} Z_N & 0 & 0 & 0 & 0 & 0 \\ 0 & 0 & 0 & 0 & 0 & 0 \\ 0 & 0 & 0 & 0 & 0 & 0 \\ 0 & 0 & 0 & 0 & 0 & 0 \\ 0 & 0 & 0 & 0 & Z_T & 0 \\ 0 & 0 & 0 & 0 & 0 & Z_T \end{bmatrix}, \tag{5.1}$$

and then inverted to yield the LS effective elastic stiffness tensor C_{EMM}.

The approach I use to compute the fracture spacing follows that of Borgos et al. (2000) and Worthington (2008). For each grid point along the ray path from the source to the receivers through the fracture volume, I define a vertical plane having dimension 36×36 m^2 (approximately the dimension of the first two Fresnel zones for a transmitted wave, e.g., see Figure 5.2a). Within the plane I compute the distribution of fracture spacing using horizontal scan lines within the plane, each line separated vertically by

the FD grid spacing Δh. Figure 5.7 shows the fracture spacing distribution for each vertical plane in the whole fracture volume as well as within the first two Fresnel zones, where the general trend shows a right (positive) skewed distribution with peak fracture spacing between 2 and 3 m. Summing the distribution for all vertical planes I get an approximate distribution of the fracture spacing: 4% for 1 m spacing, 32% for 2 m spacing, 37% for 3 m spacing, 19% for 4 m spacing, and 5% for 5 m spacing.

Figure 5.8 compares the measured SWS results for the fracture model having $a = 6$ m, $\epsilon = 0.1$ and $Z_N/Z_T = 0.33$ with several LS EMM predictions. For the simplest prediction I use an approximate average fracture spacing of 2.5 m and 6 m and observe that LS over predicts SWS. Next I compute the excess compliance based on the summed average fracture spacing distribution using 6 different means: arithmetic, geometric, harmonic, quadratic, cubic and weighted. For example, the weighted mean excess compliance is given

$$\Delta S = \frac{\sum_{i=1}^{5} w_i \Delta S_i}{\sum_{i=1}^{5} w_i}, \tag{5.2}$$

where w_i is the fractional distribution of the ith fracture spacing (i.e., $w_1 = 0.04$) and ΔS_i is the corresponding compliance. The definition of all six different means are given in Appendix E. As can be seen, most of the LS predictions do not match the observed SWS trend of the data and over predict the amount of shear-wave anisotropy. Only the weighted mean average comes close to predicting a broadly similar trend, yet under predicting the shear-wave anisotropy and having a shallower slope.

To estimate the LS EMM model parameters that would fit the data, I perform a grid search over one fracture parameter while keeping the other two constant. In the first case I assume *a priori* model fracture compliances of $Z_N = 1.7 \times 10^{-11}$ m/Pa and $Z_T = 5 \times 10^{-11}$ m/Pa (i.e., exact values from FD model) that might be available from

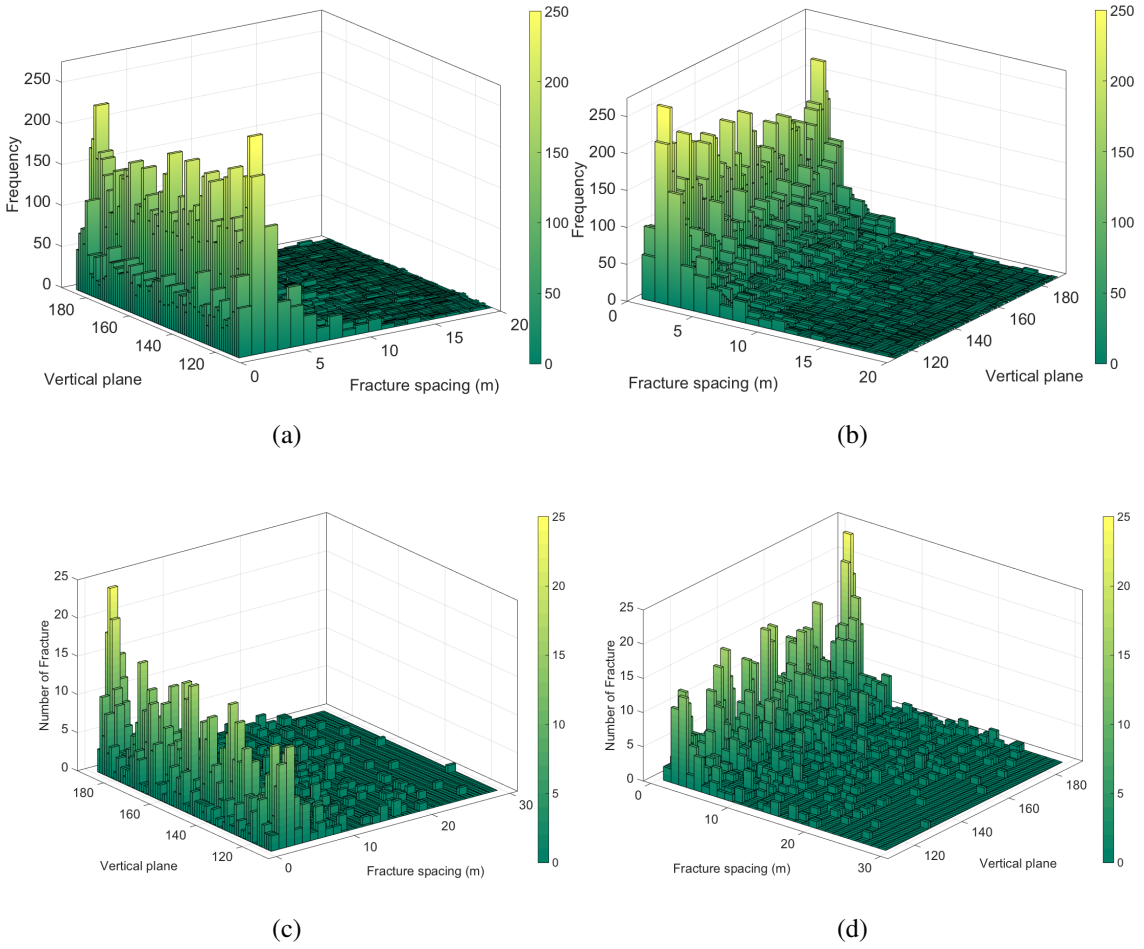

Figure 5.7: Histogram showing the distribution of fracture spacing for the whole volume (a and b) and that the shear-wave would be sensitive to as the wave propagates through the fracture volume (c and d) based on the first and second Fresnel zone. Perspective views shows (a and c) the distribution of the small fracture spacing and (b and d) the distribution of the larger spacing. Each vertical plane provides an estimate of the fracture spacing within the first two Fresnel zones ($2 \times \lambda_S \approx 36$m) tangential to the direction of wave propagation.

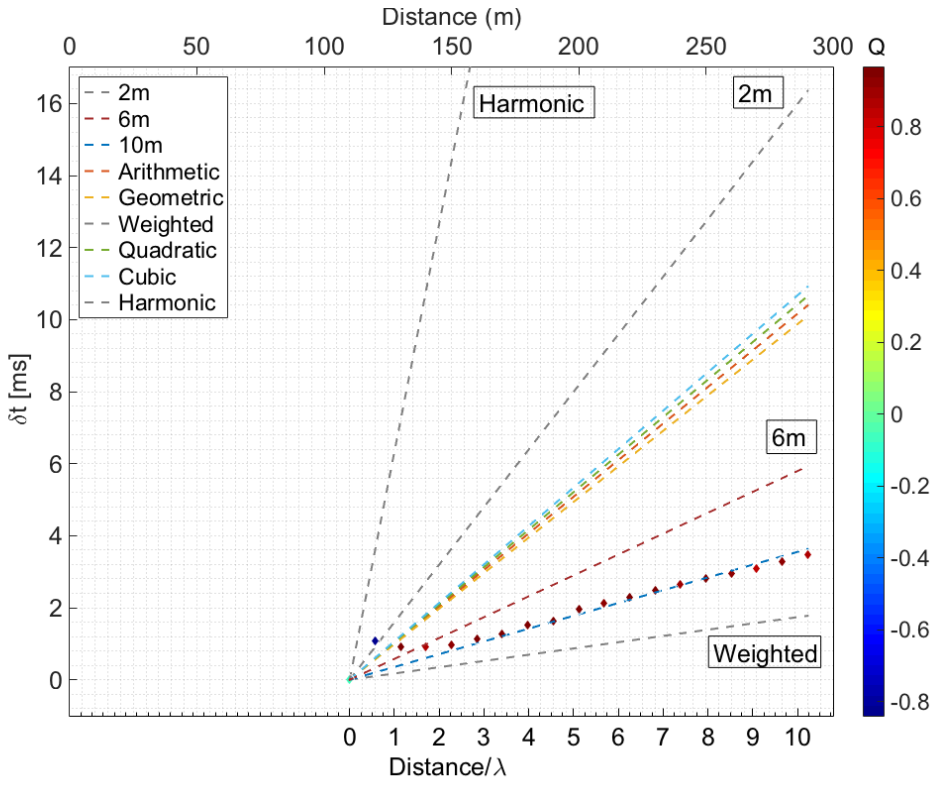

Figure 5.8: Comparison of LS EMM δt predictions with the observed SWS for the fracture model: $a = 6$ m, $\epsilon = 0.1$ and $Z_N/Z_T = 0.33$. LS EMM predictions of Schoenberg & Sayers (1995) for spacing 2 m, 6 m and 10 m (best fitting LS EMM model) as well as LS EMM predictions from the summed distribution in Figure 5.7 using 6 different means: arithmetic, geometric, harmonic, quadratic, cubic and weighted. See caption in Figure 5.3 for details.

laboratory core measurements. The best fit LS model requires a fracture spacing of 10 m. In the second case I assume *a priori* an average model fracture spacing of 2.5 m (i.e., approximate mode value for the summed distribution) and compliance ratio of $Z_N/Z_T = 0.33$ that might be available from laboratory core measurements. The best fit LS model requires fracture normal and tangential compliances of $Z_N = 2.7 \times 10^{-11}$ m/Pa and $Z_T = 8.2 \times 10^{-11}$ m/Pa, respectively. Based on these two cases, the error from using the LS EMM prediction would lead to a 400% error in fracture spacing and 60% error in fracture compliance.

There are two important implications to the results: (1) any EMM will predict that

anisotropy will develop instantaneously as the wave propagates through the model and neglects the influence of the transition zone and (2) the LS EMM significantly over predicts seismic anisotropy. The first observation suggests that EMM predictions from SWS measurements near the source will suffer from inaccuracies as seismic anisotropy will have very little time to develop. The strength of seismic anisotropy is coupled to the path length within the anisotropic volume (e.g., Savage, 1999. This is analogous to the slope ($\delta t/$distance) of the trends shown in Figure 5.8. As the distance of SWS observation moves further from the seismic source and the ray path within the zone exceeds 2 to 3 propagation wavelengths, EMM predictions will suffer less from the influence of the transition zone. This is because the slope of the best-fitting EMM prediction will approach asymptotically that of the observations (i.e., $H = 10$ m). For most observational applications it is not practical to acquire data with sensors within a fracture volume: for laboratory data this might require drilling a core through the middle of the sample to place sensors or placing sensors within a synthetic rock specimen during manufacturing whereas for field data this might require access to one or more boreholes that intersect a fracture volume where sensors could be positioned throughout the fracture system. This could be achieved on outcrop scale but would involve special processing of the seismic data to compensate for free surface effects.

The second observation is more concerning given that the LS model is used pervasively in the seismological community. Chichinina et al. (2015) analyse the limitations of Schoenberg & Sayers (1995) LS model and find that their model is not generally adequate for real rocks. Chichinina et al. (2015) note that the LS model is only valid for two conditions: (1) when $Z_N = 0$ (i.e., case of fluid-filled fractures) or (2) when the scalar crack $Z_N/Z_T = 1$ is assumed (e.g., Bakulin et al., 2000). Hildyard (2001) observed that the LS model was only accurate for high-stiffness fractures and became increasingly inaccurate as the stiffness decreased, which is consistent with the first

condition $Z_N = 0$. Regarding the second condition $Z_N/Z_T = 1$, it has been observed from laboratory (e.g., MacBeth & Schuett, 2007; Angus et al., 2012; Choi et al., 2014) and field (e.g., Worthington, 2008; Verdon & Wüstefeld, 2013) data that the scalar crack assumption is not universally consistent. Figure 5.9 compares the measured SWS results for the fracture model having $a = 6$ m, $\epsilon = 0.1$ and $Z_N/Z_T = 1.00$ with several LS EMM predictions. For this case, I observe the same misfit of the LS predictions with the synthetic data (see Figure 5.9). Thus, even for the scalar crack case, my results indicate that the LS model is inconsistent with the vast majority of real fracture behaviour. This brings us to another important limitation of the LS model, the assumption that the lateral dimension of linear slip interface be greater than the dominant seismic wavelength (e.g., Hsu & Schoenberg, 1993) or the assumption of a smooth stress field (e.g., Kachanov, 1992) thus limiting scattering within the fracture normal direction. For my models, the wavelength of the S-waves range on the order of the fracture size (i.e., the fracture size is not significantly greater than the wavelength) and so the LS model does not model the scattering from fracture edges and tips

It should be noted that the general assumption involved with the LS model is the LWA, such that $\lambda_S/a \gg 1$ (e.g., Sayers & Kachanov, 1991; Schoenberg & Sayers, 1995). In my simulations, the smallest fracture size is $a = 6$ m, which lies on the boundary of where the LWA is valid (i.e., $\lambda_S/a \approx 3$). To test LWA, I simulate a seismic source having dominant frequency of 50 Hz with a wavelength of approximately 65 m (i.e., $\lambda_S/a \approx 10$). Figure 5.10 compares the measured SWS results for the fracture model having $a = 6$ m, $\epsilon = 0.1$ and $Z_N/Z_T = 1.00$ with several LS EMM predictions. Again, I observed that at least 1 to 2 propagation wavelengths is needed before SWS develops and, even under the appropriate LWA conditions, I observe the same misfit of the LS predictions with the synthetic data (see Figure 5.10).

Thus, based on my results, I suggest that if SWS is to be used to quantify fracture

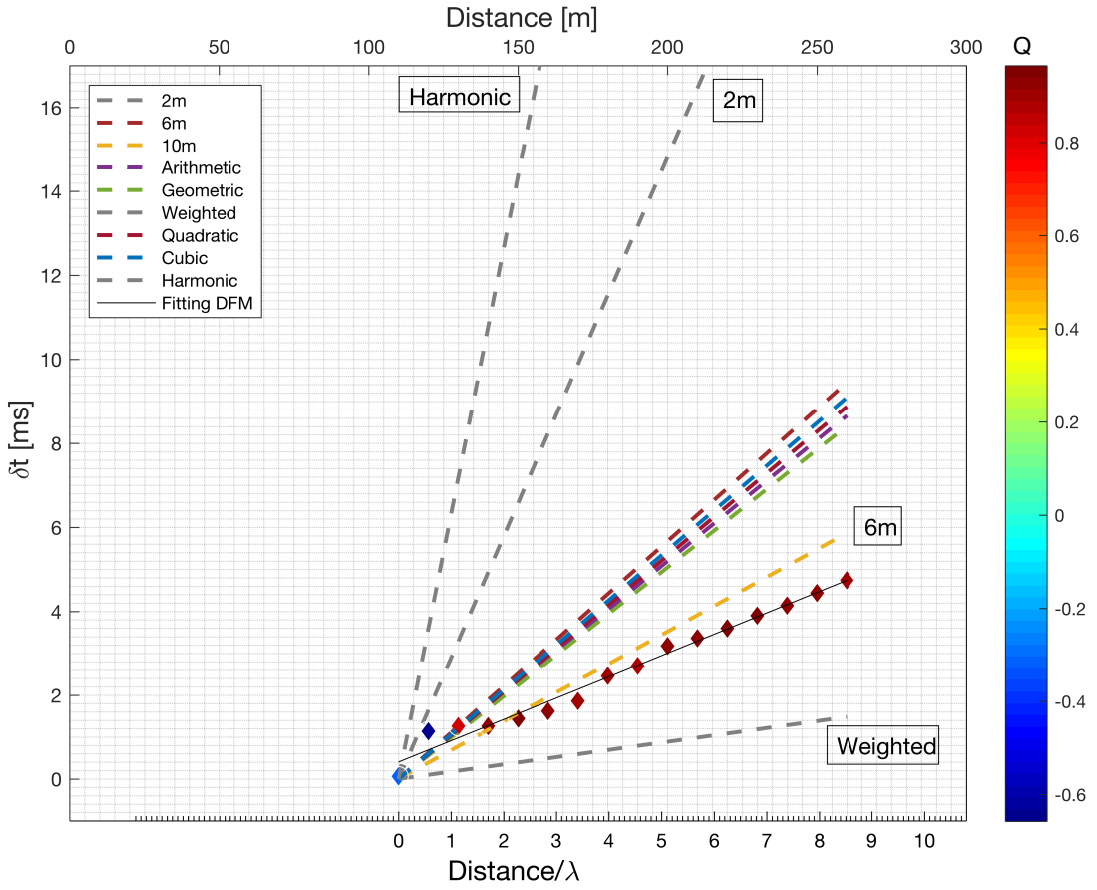

Figure 5.9: Comparison of LS EMM δt predictions with the observed SWS for the fracture model: $a = 6$ m, $\epsilon = 0.1$ and $Z_N/Z_T = 1.0$. LS EMM predictions of Schoenberg & Sayers (1995) for spacing 2 m, 6 m and 10 m (best fitting LS EMM model) as well as LS EMM predictions from the summed distribution in Figure 5.8 using 6 different means: arithmetic, geometric, harmonic, quadratic, cubic and weighted. See caption in Figure 5.3 for details.

properties the following criteria should be met:

1. Ray paths through the fracture volume should exceed 2 wavelengths to detect anisotropy and be at least 5 wavelengths to minimise the influence of the transition for quantitative estimates,

2. The ratio of dominant wavelength to expected fracture size should be greater than or equal to 3, and

3. The LS model should not be used for quantitative estimates, unless there is further

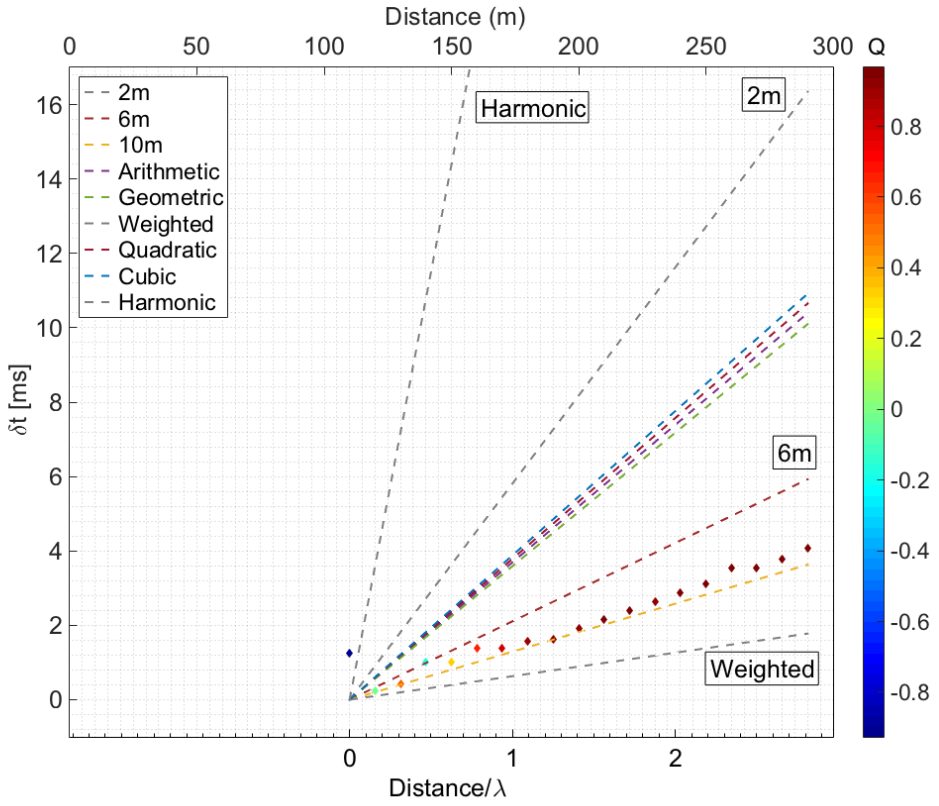

Figure 5.10: Comparison of LS EMM δt predictions with the observed SWS for dominant source frequency of 50 Hz (approximate wavelength of 60 m) for the fracture model: $a = 6$ m, $\epsilon = 0.1$ and $Z_N/Z_T = 1.0$. LS EMM predictions of Schoenberg & Sayers (1995) for spacing 2 m, 6 m and 10 m (best fitting LS EMM model) as well as LS EMM predictions from the summed distribution in Figure 5.8 using 6 different means: arithmetic, geometric, harmonic, quadratic, cubic and weighted. See caption in Figure 5.3 for details.

data to calibrate the EMM results to in situ properties.

The last point is salient since the inversion of seismic anisotropy for fracture properties is increasingly being used to populate and calibrate multi-physical models of the sub-surface (e.g., Angus et al., 2015). Significant errors in fracture property estimates will lead to over or under predicting the multi-physical response, which can have significant impact on hazard assessment and risk mitigation.

5.5 Summary

Fractures are pervasive features within the Earth's crust and have a significant influence on the multi-physical response of the subsurface. The presence of coherent fracture sets often leads to observable seismic anisotropy enabling seismic techniques to remotely locate and characterise fracture systems. In this chapter, I confirm the general scale-dependence of seismic anisotropy and provide new results specific to shear-wave splitting (SWS). I find that SWS develops under conditions when the ratio of wavelength to fracture size (λ_S/d) is greater than 3, where Rayleigh scattering from coherent fractures leads to an effective anisotropy such that effective medium model (EMM) theory is qualitatively valid. When $1 < \lambda_S/a < 3$ there is a transition from Rayleigh to Mie scattering, where no effective anisotropy develops and hence the SWS measurements are unstable. When $\lambda_S/a < 1$ I observe geometric scattering and begin to see behaviour similar to transverse isotropy. I find that seismic anisotropy is more sensitive to fracture density than fracture compliance ratio. More importantly, I observe that the transition from scattering to an effective anisotropic regime occurs over a propagation distance between 1 to 2 wavelengths depending on the fracture density and compliance ratio. The existence of a transition zone means that inversion of seismic anisotropy parameters based on EMM will be fundamentally biased. More importantly, I observe that linear slip EMM commonly used in inverting fracture properties is inconsistent with my results and leads to errors of approximately 400% in fracture spacing (equivalent to fracture density) and 60% in fracture compliance. Although EMM representations can yield reliable estimates of fracture orientation and spatial location, my results show that EMM representations will systematically fail in providing quantitatively accurate estimates of other physical fracture properties, such as fracture density and compliance. Thus more robust and accurate quantitative estimates of in situ fracture properties will require improvements to effective medium models as well as the incorporation of full waveform

inversion techniques.

Chapter 6

Scattering characteristics of shear-waves in fractured media

6.1 Introduction

Scattering of seismic waves is a phenomenon in which the seismic energy is scattered in all possible directions due to the presence of obstacles or strong lateral variation of elastic stiffness in the medium (see Figure 6.1). The scattering of seismic waves allow us to study the heterogeneous structure of the Earth's subsurface on both global and exploration scales (Margerin, 2011). Pioneering studies of seismic scattering have focused mostly on characterising the subseismic scale structure of the lithosphere, the mantle and the solid core (e.g., Shearer & Earle, 2004). Recently, the scientific community has shown an increasing interest in using seismic scattering to characterise fractured reservoirs (e.g., Shen & Toksöz, 2000; Willis et al., 2006).

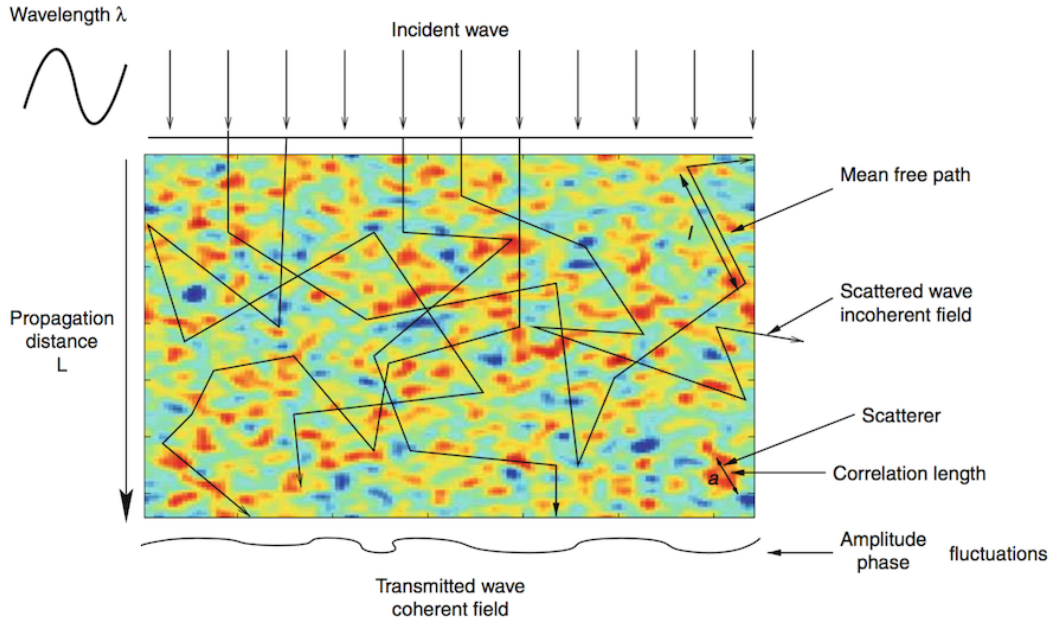

Figure 6.1: Schematic of wave propagation through a medium with typical dimension *L*. As the incident plane wave passes through the heterogeneous medium, scattering happens and deflects energy in all spatial directions. The transmitted wavefield is distorted and attenuated. Figure from Margerin (2011).

The amount of scattering, or scattering strength, due to seismic wave propagation in heterogeneous media depends on the relative size (or correlation length) of the heterogeneity a compared to the seismic wavelength λ (see Figure 6.1). A dimensionless parameter ka (wavenumber $\frac{2\pi}{\lambda}$ times a) is introduced and is referred to as the so-called normalised wave number. It describes the relative correlation length with respect to the seismic wavelength. Depending on the magnitude of ka, different scattering regimes can be classified as follows:

Quasi-homogeneous and effective elastic medium regime: $ka < 0.01$. The elastic medium can be regarded as an effective medium because the dominant wavelength is much larger than the heterogeneity scale lengths. Scattering effects are small.

Rayleigh scattering regime: $0.01 \leq ka < 0.1$. Weak fluctuation of the elastic parameters is considerable. This regime can be described using the Born approximation based

on the single scattering assumption.

Mie scattering regime: $0.1 \leq ka < 10$. Also known as resonant scattering, heterogeneity scale lengths are on the order of the dominant seismic wavelength. The prominent effect in the Mie regime is scattering at large angles with respect to the incident direction.

Forward scattering regime: $10 \leq ka$. This occurs when the correlation length is much larger than the dominant seismic wavelength and seismic energy is scattered primarily in the forward direction. In this regime backscattered energy is weak, but other phenomena such as focusing, diffraction and interference effects are important.

Heterogeneous media can been treated as either random media (e.g., Sato, 1984, 1989; Fukushima et al., 2003) or homogeneous media with discrete scatterers (e.g., Willis et al., 2004b, 2006). For the case of random heterogeneous media, the medium can be classified using five different approaches: radiative transfer theory based on the Born approximation (e.g., Sato, 1984; Shang & Gao, 1988), analytical approaches, such as using parabolic approximations (Sato, 1989; Saito et al., 2002), numerical simulation (e.g., Frankel & Clayton, 1986; Hoshiba, 2000; Fehler et al., 2000), laboratory experiments using physical models (e.g., Nishizawa et al., 1997; Fukushima et al., 2003), and empirical approaches, such as using well-log data from the shallow crust that show strong random heterogeneity but provide limited access to the nature of heterogeneities in the Earth (Wu et al., 1994).

In contrast, for the case of homogeneous media with discrete fractures, the fractured medium can be treated by a variety of different approaches. Analytical approaches can describe the propagation of elastic waves in the presence of fractures, but are only acceptable for rather simple cases, such as single cracks with simple geometries (Mal, 1970), and in most cases are valid only at far offset (Liu et al., 1997). The Born and Rytov approximations may be used for more complex situations (Wu & Aki, 1985), and

are applicable for: low frequency wave propagation and low elasticity contrasts between scatters and the host rock. These limitations are consistent when dealing with large scale inclusions or fractures, such as in some fractured reservoirs, and where seismic waves have short wavelengths compare to the large fractures. Numerical techniques are also employed to investigate the scattering of seismic waves, such as the finite-difference (FD) method (Saenger & Shapiro, 2002; Xie et al., 2013; Hildyard, 2007), finite-element (FE) method (Lysmer & Drake, 1972); pseudospectral (PS) method (e.g., Vlastos et al., 2003), boundary-element method (e.g., Pointer et al., 1998) and spectral finite-difference method (Mikhailenko, 2000). In this study I use the FD algorithm WAVE (see section 3.3) that is capable of modelling fracture networks as individual fractures defined as explicit discontinuities, where distribution of the fracture network can be populated randomly.

The scattering of elastic waves propagating in a heterogeneous medium influences the kinematic evolution (i.e., travel-times) of the seismic wavefield and can lead to amplitude attenuation and phase distortion with distance (Vinogradov et al., 1995). Thus understanding the scattering process in a heterogeneous medium is important for characterising discontinuous structures (e.g., cracks, fractures, etc.). Seismic characterisation of fractured reservoirs has the potential to not only identify fracture zones, but also estimate fracture properties. If the fracture size and spacing are substantially small relative to the seismic wavelength, then coherent fractures can lead to the rock appearing as an effective anisotropic medium with a symmetry axis normal to the strike of fractures (Liu et al., 2000). For such scenarios, application of seismic anisotropy methods (e.g., amplitude versus offset and azimuth and shear-wave splitting) can be used to extract fracture properties, such as fracture orientation and density (e.g., Willis et al., 2004b; Zhang et al., 2005, 2006). If, however, the fracture size and spacing are on the order of the seismic wavelength, then the fractures will lead to observable scatter in

the seismic energy causing complex reverberation or coda in the seismic signal (Willis et al., 2006).

Aki (1969) first showed the appearance of "wriggly" wave trains in the tail portion of a seismogram of a local earthquake and showed that this was direct evidence of random heterogeneity of the lithosphere. The coda wave can be described by an envelope where the amplitude decreases with increasing time from the onset of the direct arrivals on a recorded seismogram.

The Earth's interior has been observed to be laterally heterogeneous within the crust, mantle and core, with scale length of heterogeneity ranging from the grain size (mm) to the order of global spherical harmonics (Km). The scale length of heterogeneity a, which in this chapter means fracture size, influences the scattering response of seismic waves and hence observable seismic attributes (Snieder, 2006). The seismic attributes sensitive to scattering include travel-time anomalies, amplitude and phase fluctuations, as well as excitation in the scattered wave such as the envelope broadening phenomenon (Aki, 1988). The excitation of coda waves due to scattering means that the direct wave loses energy with increasing propagation distance (Sato et al., 2012). Furthermore, the excitation can be due to the distortion of the first-arriving seismic wave polarisation.

Recently, the distortion of the first-arriving signal has been studied in laboratory experiments using physical models (Nishizawa et al., 1997) that utilised a laser Doppler vibrometre (LDV) to measure elastic waves in the ultrasonic frequency range. Nishizawa et al. (1998) explained the principal method of measuring shear-wave particle motions by LDV. By knowing the initial source radiation pattern and comparing it with the recorded elastic waves, the relationship between scattering and medium heterogeneity can be established. Fundamentally, the P- and S-wave scattering characteristics, (i.e., P- and S-wave coda energy) are different, and the majority of studies has focused on the P-wave scattering characteristics of fractures, and so the main aim of this chapter

is analysing the effect of different fracture properties on shear-wave scattering. So, in this chapter I study the scattering characteristics of shear-waves in 3D models within an isotropic background medium with the inclusion of fracture corridors.

In order to better understand S-wave scattering and minimise the effect of the compressional P-waves, a point source is generated by using a moment tensor (MT) with optimally oriented strike-slip double couple mechanisms to enhance S-wave interaction with the fractures. The aim of this study is to investigate the scattering characteristic of shear-waves as a function of the scale length of the heterogeneity. Specifically, I consider fracture induced heterogeneity by varying the fracture size.

In this chapter, I examine the scattering characteristics of S-waves for a range of scattering regimes. First, I present the parameters of the numerical models. Next, I perform a qualitative analysis of shear-wave coda on the recorded seismograms for different source polarisations and propagation paths relative to the fracture orientation. I perform the RMS envelope analysis to examine the envelope broadening of shear-waves due to the scattering. I study the distortion of shear-wave polarisation of different fracture size against ka. Next, I perform the differential attenuation analysis of shear-wave to compare my result with Hudson (1981) and Carter & Kendall (2006) in section 6.6. Finally, I explore the frequency content of the dataset and I describe the tapering approach.

6.2 Modelling

In this chapter, I simulate wave propagation in 3D isotropic and heterogeneous media using the FD algorithm WAVE (see section 3.2). A suite of models are generated consisting of: two non-fracture models and several fracture models. All models have the same background isotropic elasticity . However, I vary the fracture properties (i.e.,

fracture size a, fracture density ϵ, and fracture compliances Z_N and Z_T) to study the scattering characteristics and sensitivity of various fracture properties.

The isotropic elastic medium has density ρ = 2600 kg/m^3, P-wave velocity V_P = 5700 m/s and S-wave velocity V_S = 3200 m/s (V_P/V_S = 1.78). The fracture models have a geometry as depicted in Figure 6.2, where the specific parameters of the various fracture models are given in Table 6.1. In general, for each fracture model there are two types of source-receiver orientations: (1) in-line receivers parallel to the fracture strike (hereafter called *Parallel*) and (2) in-line receivers normal to the fracture strike (hereafter called *Normal*). Seismic waves are generated using a moment tensor source having a seismic moment magnitude 1×10^{11} N m and a strike-slip double-couple mechanism with strike 90°, dip of 90° and slip 45° (for *Parallel*) and a 0°, dip of 90° and slip 45° (for *Normal*). These double-couple source mechanisms allow the source polarisations in the Y-Z and the X-Z planes to be equally partitioned. The source is located at (x_s, y_s, z_s) = (100 m, 150 m, 140 m) for the *Parallel* model and (x_s, y_s, z_s)=(150 m, 100 m, 150 m) for the *Normal* model. In all models the fracture volume has dimension of 80 m $\times$ 80 m $\times$ 80 m. The geometry of the model has overall dimension of 300 m $\times$ 300 m $\times$ 300 m. In both the *Normal* and *Parallel* models, only one set of discrete vertical fractures is inserted with orientation along the X-axis (see Figure 6.2). For each model, a Ricker wavelet source with a period of 5.5 ms is used. Thus, based on dispersion and stability requirements, a grid spacing of $dh = 1$ m and time increment of approximately $dt =$ 0.08 ms are used.

Following the scaling relation of Worthington & Lubbe (2007), the fracture size a dictates the allowable range of normal compliance (Z_N) and tangential compliance (Z_T) summarised in Table 6.1. A normal to tangential compliance ratio of $Z_N/Z_T = 0.33$ is chosen to represent water-filled fractures (Lubbe et al., 2008) and is representative of realistic compliance ratios of fractured reservoirs (e.g., Verdon & Wüstefeld, 2013).

Fracture density	0.02		0.04		0.08		0.1	
size (m)	$K_N\,(Pa/m)$	$K_S\,(Pa/m)$	$K_N\,(Pa/m)$	$K_S\,(Pa/m)$	$K_N\,(Pa/m)$	$K_S\,(Pa/m)$	$K_N\,(Pa/m)$	$K_S\,(Pa/m)$
6	6×10^{10}	2×10^{10}	6×10^{10}	2×10^{10}	6×10^{10}	2×10^{10}	6×10^{10}	2×10^{10}
10	3×10^{10}	1×10^{10}	3×10^{10}	1×10^{10}	3×10^{10}	1×10^{10}	3×10^{10}	1×10^{10}
20	3×10^{9}	1×10^{9}	3×10^{9}	1×10^{9}	3×10^{9}	1×10^{9}	3×10^{9}	1×10^{9}
50	3×10^{9}	1×10^{9}	3×10^{9}	1×10^{9}	3×10^{9}	1×10^{9}	3×10^{9}	1×10^{9}

Table 6.1: Summary of fracture properties for all models having $Z_N/Z_T = 0.33$.

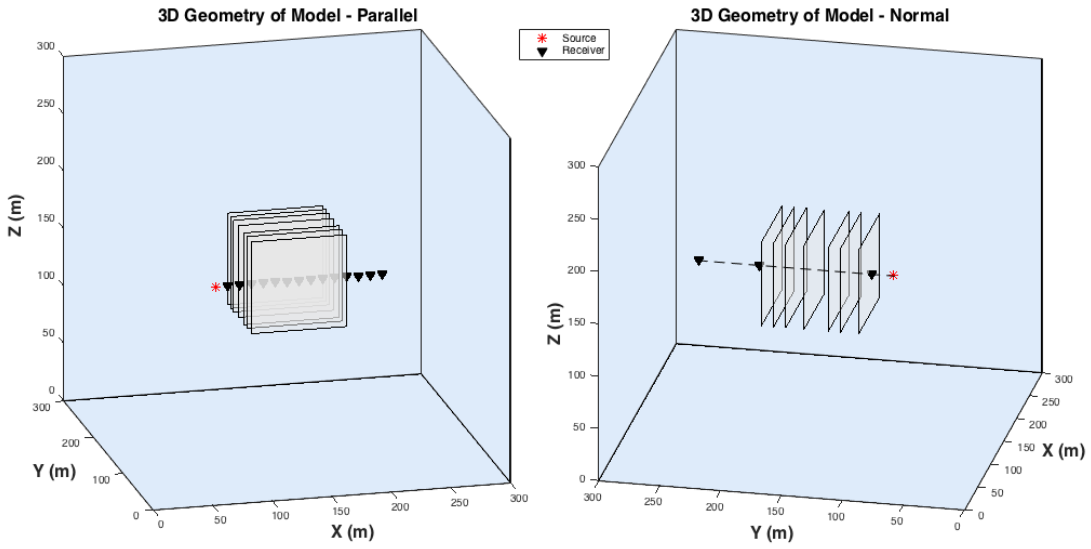

Figure 6.2: Geometry of 3D FD model. The red star shows the source location, the triangles show the receiver array and the grey rectangles within the sub-volume schematically represent the vertical fractures:(a) the linear receiver array is parallel to the fracture plane and (b) the linear receiver array is normal to the fracture plane. The receiver spacing in the *Parallel* model is 10 m while in the *Normal* model the receiver are 9 m, 100 m and 150 m far from the source.

For the $Parallel$ model, a single linear array of 15 three-component (3C) receivers is placed through the centre of model in the X-direction. The first receiver is outside fracture zone in the isotropic background medium, the subsequent 8 are within the fracture volume and the last 6 are on the outside at the other end. The receiver spacing is 10 m. This series of receivers can be used to evaluate the evolution of scattering characteristics when S-waves propagate parallel to the fractured plane. I introduce the $Normal$ model to investigate the behaviour of S-waves as they propagate in the normal direction to the fracture planes. To allow direct comparison between the $Normal$ and $Parallel$ results, the fracture geometry is kept consistent. Due to the constraints imposed by WAVE implementation, receivers could only be placed outside the fracture zone (i.e. to generate the fracture volume using CRACKGEN the receiver locations are required priori). Thus, in the $Normal$ model, the receivers are placed at distance 9 m, 100 m and 150 m respectively from the source.

Figures 6.3 and 6.4 show snapshots of the P- and S-waves from the moment tensor point source in the isotropic, homogeneous model for the *Parallel* and *Normal* geometries. The wavefronts show clear P- and S-waves with no scattering energy as well as the diagnostic radiation pattern for a double-couple source. Figures 6.3a and 6.4c represent the identity of particle velocity in these planes based on the slip 45° and the dip 90° of the source mechanism which is the same in the *Parallel* and *Normal* models.

Figure 6.5 displays snapshots of wave propagation in the X-Y horizontal plane for the *Parallel* isotropic and fracture model and *Normal* fracture model at times 33.1 and 48.9 ms. The revolution of the scattered energy is highlighted within the big circle for the fractured models. The splitting of the shear-waves in the *Parallel* model is visible (Figure 6.5d).

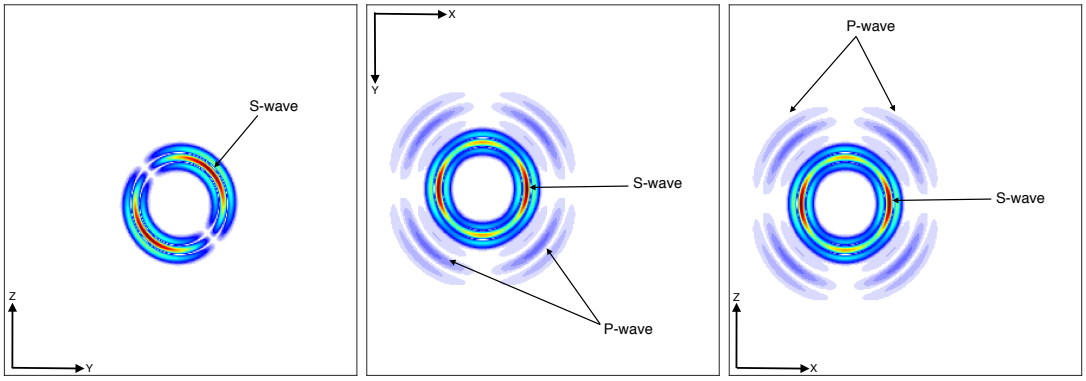

(a) (b) (c)

Figure 6.3: 2D Snapshots of particle velocity at time 17.3 ms for the double-couple source for *Parallel* type model at source location (100 m, 150 m, 140 m) in the three primary planes:(a) Y-Z plane, (b) X-Y plane and (c) X-Z plane. Red is the maximum velocity and indicates greater than 4 mm/s.

6.3 Qualitative analysis of shear-wave coda

In this section, I examine qualitatively the influence of fractures on S-waves as they propagate through a fracture volume. Before showing the results of the wavefront

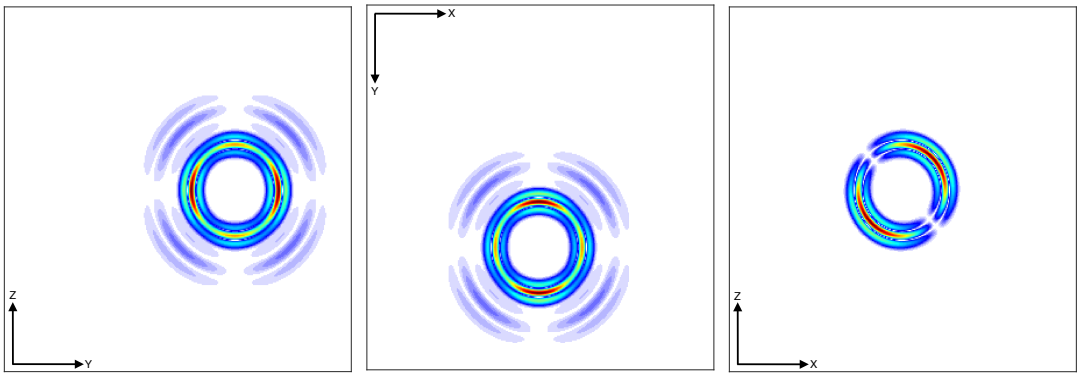

(a) (b) (c)

Figure 6.4: 2D Snapshots of particle velocity at time 17.3 ms for double-couple source for *Normal* type model at source location (150 m, 200 m, 150 m) in the three primary planes:(a) Y-Z plane, (b) X-Y plane and (c) X-Z plane.

scattering, I show the 3C signals for the isotropic model in Figures 6.6 and 6.7. With the exception of only minor P-wave contamination, the signals show a clean S-wave. Note that the visible P-wave energy is the result of the numerical implementation of the moment-tensor source. These figures verify the equal magnitude and similarity of waveforms on the Y-, Z- and X-, Z-components. Furthermore, it can be seen there is no energy on the third-component in the direction of wave propagation, as would be expected for S-wave propagation in isotropic media.

Figures 6.8-6.11 show the 15 3C seismograms for the *Parallel* models having the fracture sizes $a = 6$ m, 10 m, 20 m and 50 m. Although the MT source prescribes initial polarisations of equal magnitude on the Y- and Z-components for the *Parallel* models, small forward scattered energy can be observed on the X-component due to edge and tip diffractions.

As expected, the Y- and Z-components are initially equal at the first station, but with increasing offset there are significant changes in the waveforms, especially for $a = 20$ m, where $\lambda_S \approx 18$ m. In other words, between Figures 6.8-6.9 we see a transition from the long wave approximation (LWA) or Rayleigh scattering (where $\lambda_S/a > 1$) to the

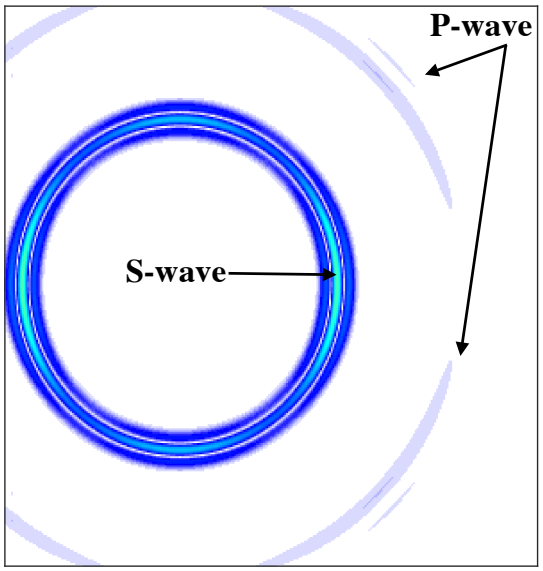

(a) Isotropic at t=33.1 ms

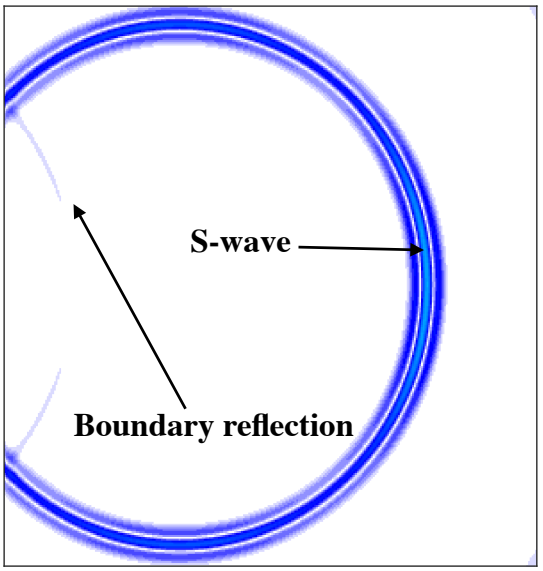

(b) Isotropic at t=48.9 ms

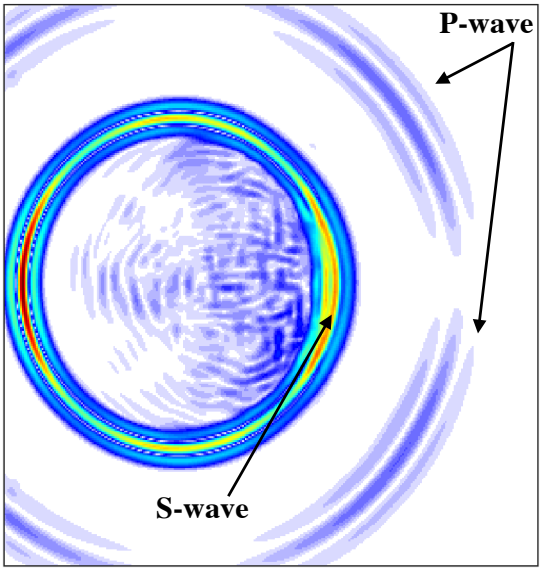

(c) *Parallel* at t=33.1 ms

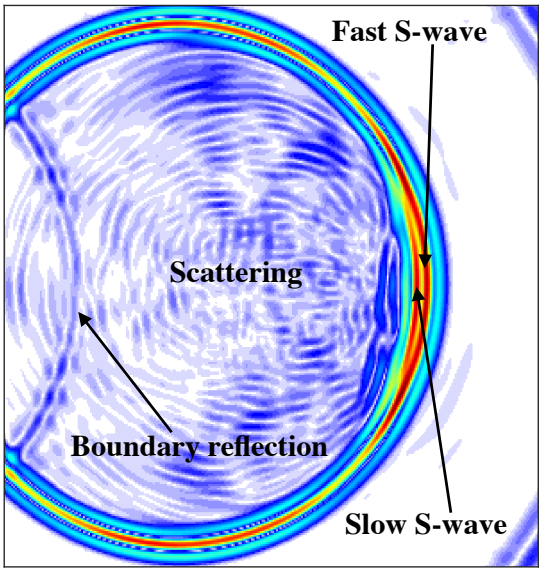

(d) *Parallel* at t=48.9 ms

Figure 6.5: Continued...

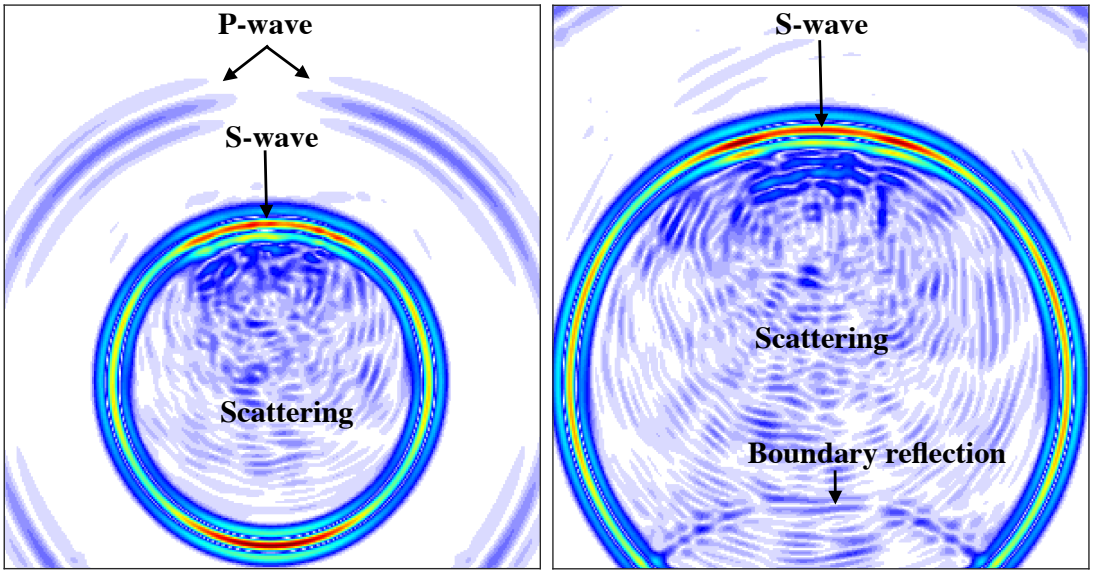

(e) *Normal* at t=33.1 ms (f) *Normal* at t=48.9 ms

Figure 6.5: 2D snapshots of seismic wave propagation in the X-Y plane at times 33.1 and 48.9 ms in the isotropic medium (a and b), and the *Parallel* (c and d) and *Normal* (e and f) fracture models.

Mie scattering regime (where $\lambda_S/a \rightarrow 1$) in Figure 6.10. In Figure 6.11, the scattering regime falls under the geometric regime, where the waveforms show similarity with those in Figures 6.8-6.9.

Figure 6.12 displays 3C seismograms for *Normal* models at the 3 stations, 9 m, 100 m and 150 m away from the source location, for all desired fracture sizes $a = 6$ m, 10 m, 20 m and 50 m. For the same reason as for the *Parallel* models, the source polarisation is equal in the X- and Z-axis for the *Normal* models as can be observed in the left-hand column of Figure 6.12.

For station 1, as the fracture size increases from 6 m to 50 m, we observe an increase in signals arriving after the primary wave. These signals are related to increasing specular reflections from the fracture zone. For station 2, we observe a substantial amount of scattering, specifically when the fracture size is comparable or larger than the wavelength of the S-wave ($\lambda_S \approx 18$ m) at $a = 20$ m and 50 m. As in the *Parallel*

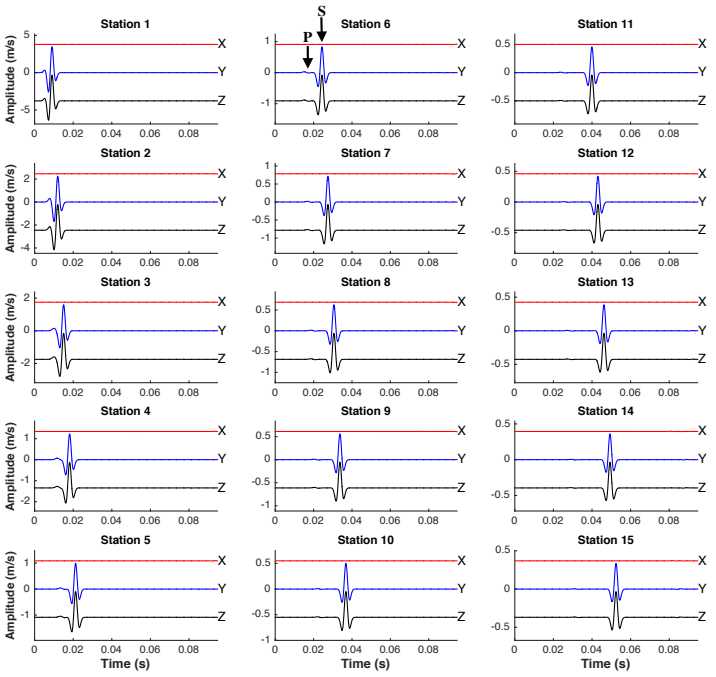

Figure 6.6: Three-component waveforms observed at the 15 stations in the *Parallel* model with no fractures (i.e., isotropic medium). Hereafter the components are depicted: X-component (red color), Y-component (blue) and Z-component (black).The arrows for the station 6 show the P- and S-wave signals. Amplitude is particle velocity in mm/s.

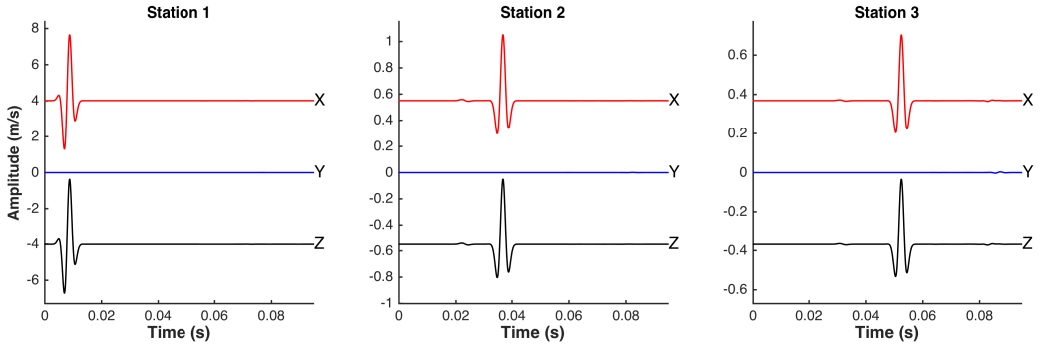

Figure 6.7: Three-component waveforms observed at the 3 stations in the *Normal* model with no fractures (i.e., isotropic medium).

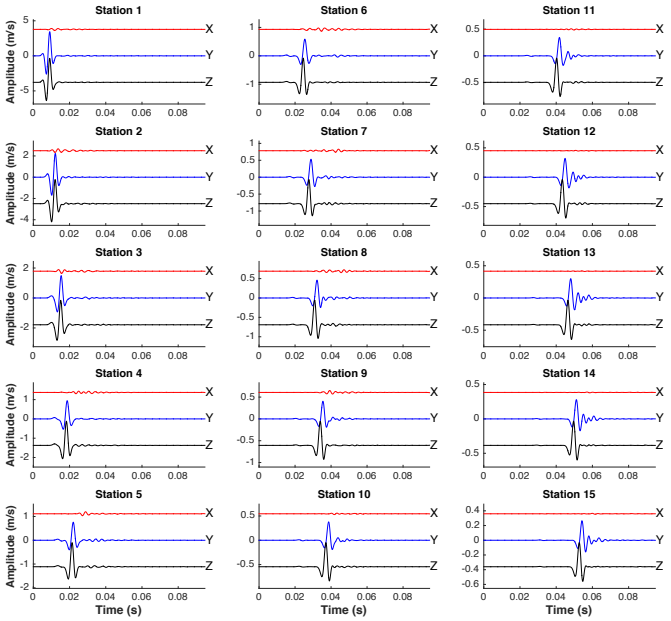

Figure 6.8: Three-component waveforms observed at 15 stations in the *Parallel* model with fracture size 6 m.

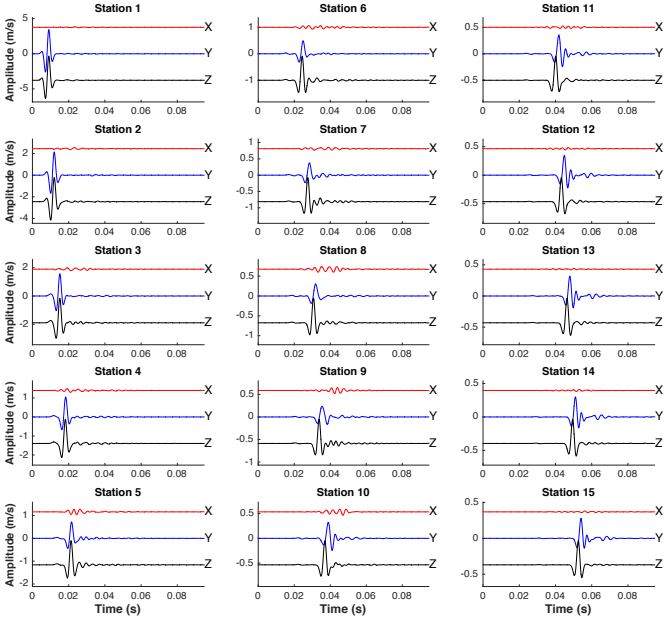

Figure 6.9: Three-component waveforms observed at 15 stations in the *Parallel* model with fracture size 10 m.

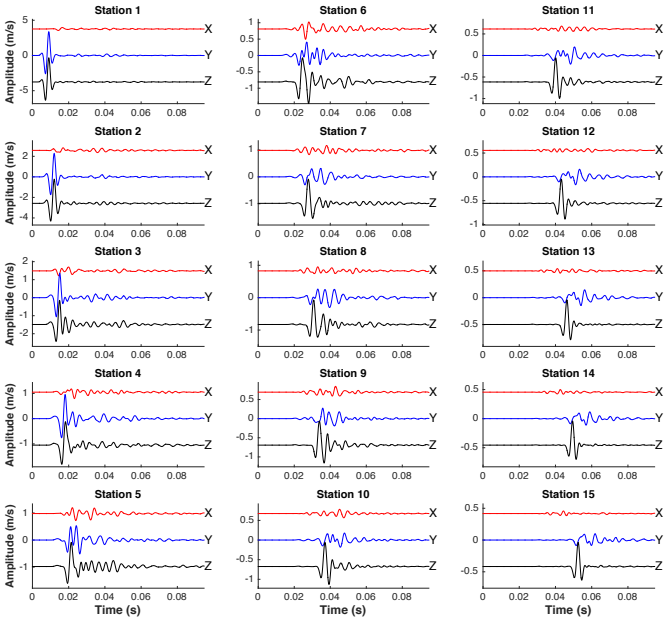

Figure 6.10: Three-component waveforms observed at 15 stations in the *Parallel* model with fracture size 20 m.

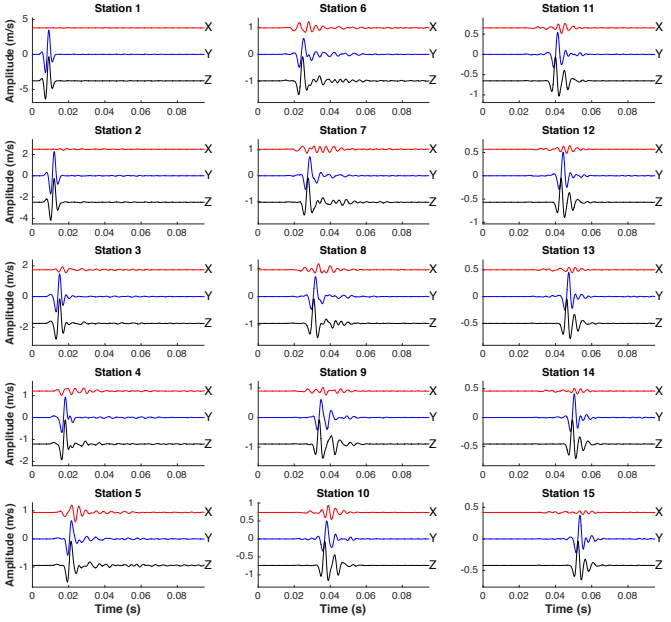

Figure 6.11: Three-component waveforms observed at 15 stations in the *Parallel* model with fracture size 50 m.

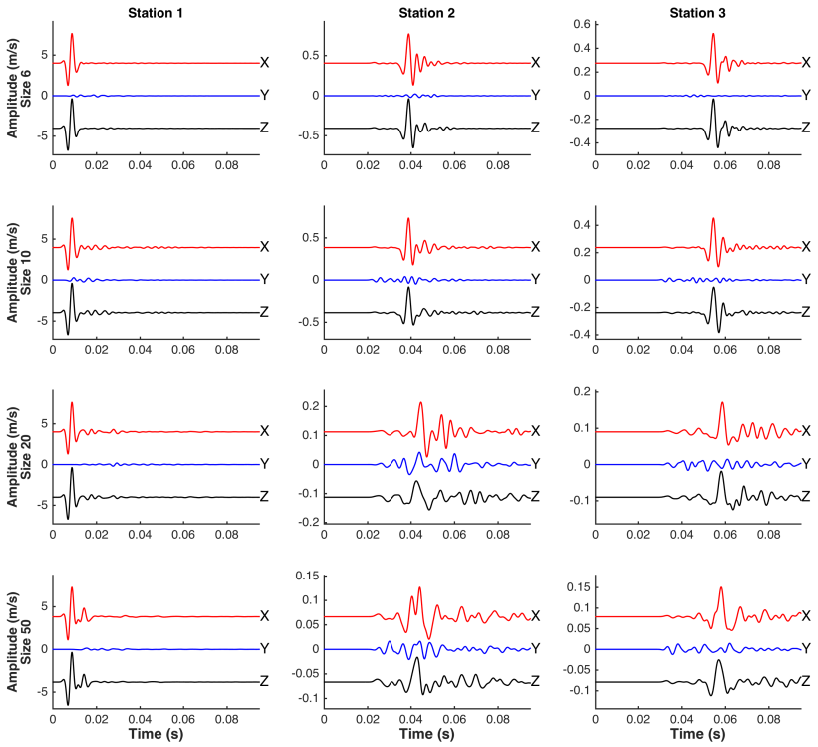

Figure 6.12: Three-component waveforms observed at 3 stations in the *Normal* models with fracture size 6 m, 10 m, 20 m, and 50 m.

models, we also observe scattering in the forward direction on the Y-component.

In the following sections, the scattering characteristics for these fracture models will be evaluated by using different techniques such as envelope broadening, amplitude spectrum and polarisation analysis.

6.4 RMS envelope analysis

This section discusses the time widening effect of wavelets due to scattering within the fractured medium. I evaluate this effect quantitatively by analysing the root-mean-square (RMS) waveform envelopes. The envelope width approach has been used previously to characterise random heterogeneities in the crust (Sato, 1989). Based on Sato (1989), the width can be qualified by the parameter t_q and depends on the intensity of velocity

fluctuation, scale length of the random heterogeneity as well as attenuation factor Q^{-1}.

The RMS envelope is estimated using the following steps:

1. Calculate the square amplitude of the waveform,
2. Average the square amplitude trace using a moving window of time length 7.9 ms (which is the width of the MS envelope),
3. Calculate the square root of step (2), and
4. Smooth the result in step (3).

To do the smoothing, I implement the method "*loess*" from the MATLAB® toolbox, which is a local regression algorithm using weighted linear least squares with a second degree polynomial mode. The strength of excitation of the scattered waves can be described by measuring the envelope width t_q, which is defined by the interval time from the onset of the shear wave to the time when the RMS envelope amplitude decreases to the half of its maximum value (see Figure 6.13).

Figure 6.13 shows the 15 3C RMS envelopes of the *Parallel* fracture model for fracture size $a = 6$ m. The RMS envelopes were calculated at 15 stations and show the evolution of the envelopes at 10 m increments. As expected in Figure 6.8, the RMS amplitude of the X-component is smaller (one order of magnitude) than the Y- and Z-components. As the shear-waves propagate through the fracture volume we observe a gradual decrease in the amplitude of the envelopes with minor changes in the shape of the envelope for the Y- and Z-components and more drastic changes for the X-component.

Figure 6.14 represents the RMS envelope for *Normal* fracture models with fracture sizes 6 m, 10 m, 20 m and 50 m for 3 stations. Similar to Figure 6.13, the components normal to wave propagation (the X- and Z-components) have approximately the same

initial RMS amplitude, whereas the component along the direction of propagation (the Y-component) displays initial RMS amplitude one order of magnitude smaller than the X- and Z-components as well as drastically different envelope shapes.

Figure 6.15 shows the result of measuring t_q against ka for the *Parallel* models with fracture density $\epsilon = 0.1$, $Z_N/Z_T = 0.33$ and fracture sizes 6 m, 10 m , 20 m and 50 m. I use the scaled wavenumber ka (product of wavenumber $\frac{2\pi}{\lambda}$ and fracture size a) to normalise the results. Thus for fracture sizes 6 m, 10 m, 20 m and 50 m, the values of ka are approximately 2.2, 3.6, 7.2 and 17.9. Parametrizing in terms of ka allows easier discussion with respect to scattering regimes. Within the near-offset, the t_q value of the first 5 stations is heavily variable. This variation is due to the fact that the propagation distance is not sufficiently long enough to allow self-averaging (Müller & Shapiro, 2001). However, for the other stations self-averaging occurs such that the value of t_q for the Y- and Z-components become stable and equal to approximately 0.013 s for fracture sizes $a = 6$ m and 10 m (i.e., $ka \approx 2.2$ and 3.6 respectively). In contrast, for $ka \approx 7.2$ and 17.9 (for stations 9-15) the t_q value increases, especially for $ka \approx 17.9$. The Y-component envelope experiences notable increases compare to the Z-component at $ka \approx 17.9$. Since the last 5 stations are placed outside the fractured corridor far from the source, the t_q values are nearly constant. This confirms the fact that the wave is propagating in the isotropic homogeneous medium and that the effect of scattering remains constant but is imprinted on the wave after station 10.

Figure 6.16 shows the t_q values for *Normal* models for all fracture sizes. At station 1, the t_q values are constant for the X- and Z-components at approximately 9 ms, while for the Y-component the t_q values are unstable due to the fact that very little energy is on this component. The results from station 2 show similar pattern to station 10 in Figure 6.15. for ka values between 2.2 and 3.6, t_q decreases and then increases to values of 21 ms, 39 ms and 15 ms for the X-, Y- and Z-components, respectively. Station 3 shows

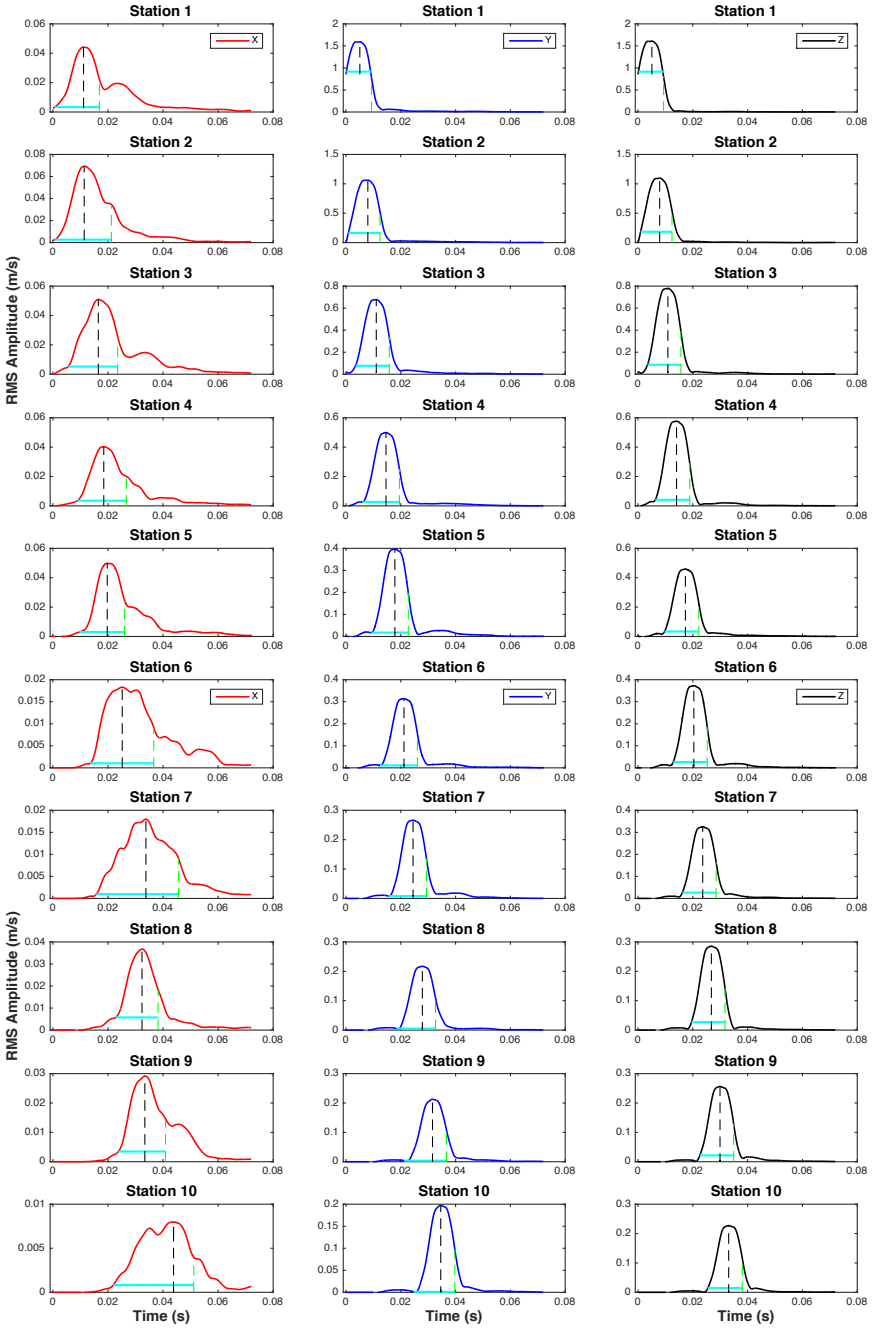

Figure 6.13: Continued...

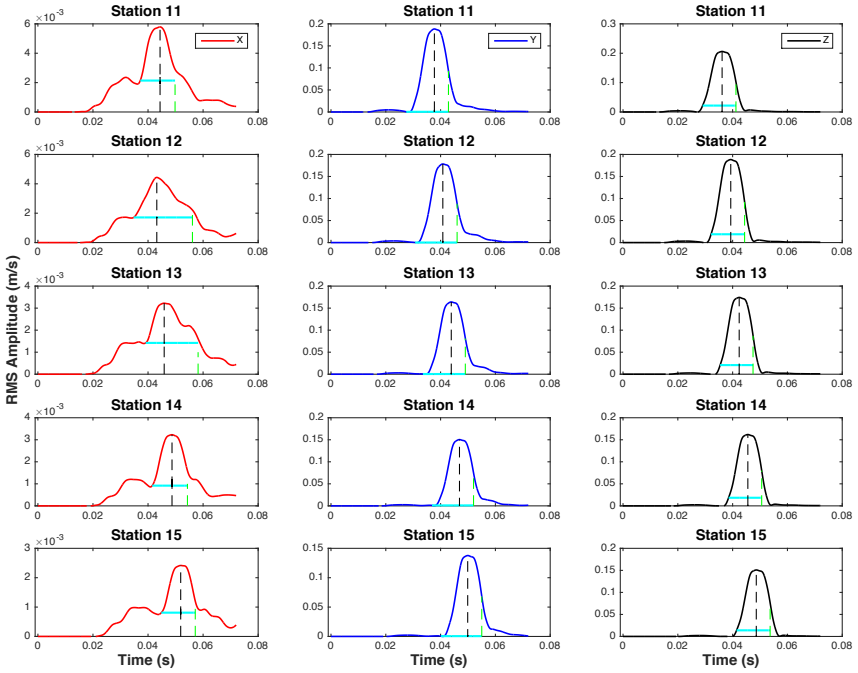

Figure 6.13: Three-component RMS envelopes observed at 15 stations in the fractured medium (*Parallel*) with fracture size 6 m. The black dashed line shows the maximum RMS envelope, and thick cyan line depicts the envelope width time t_q.

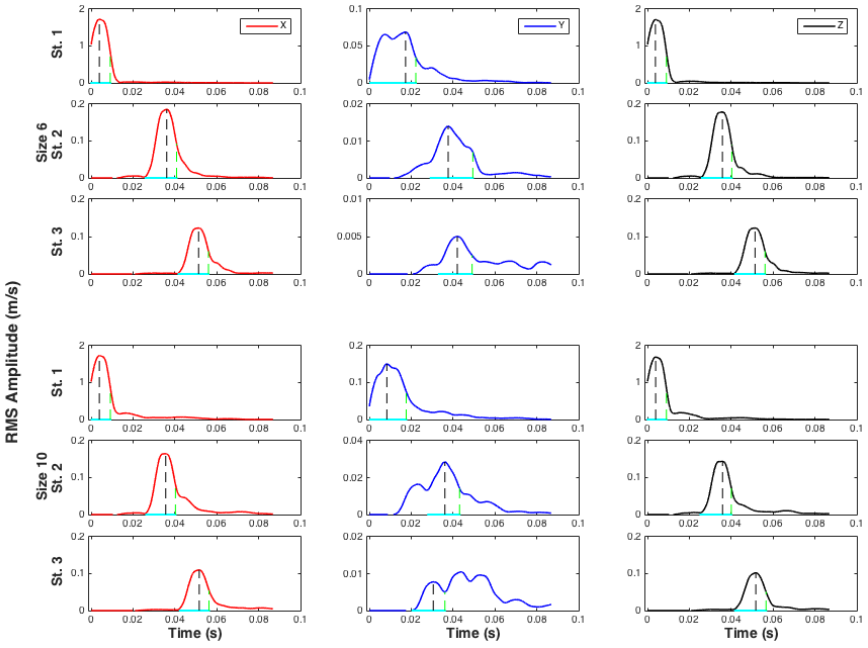

Figure 6.14: Continued...

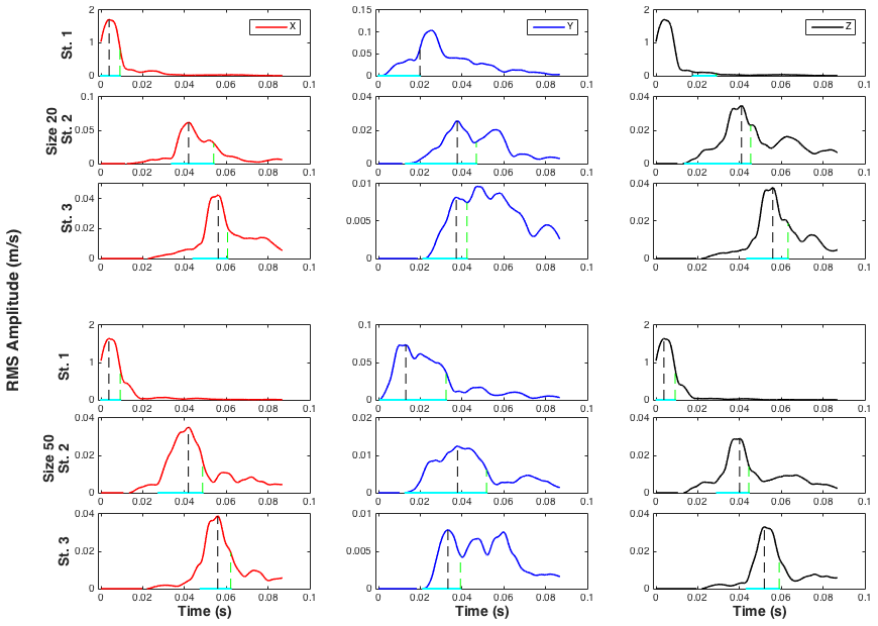

Figure 6.14: Three-component RMS envelopes observed at 3 stations in the fractured medium (*Normal*) with fracture size 6 m, 10 m, 20 m and 50 m. The black dashed line shows the maximum RMS envelope, and thick cyan line depicts the envelope width time t_q.

similar pattern to station 2 for ka between 2.2 and 7.2, but with lower maximum values of 16.4 ms, 20.9 ms and 19.6 ms for $ka = 7.2$. Displaying a different pattern to station 2, t_q values for $ka = 17.9$ at station 3 are smaller. Again we observe a reduction in the t_q values indicating that wavefront healing is occurring.

To remove the effect of geometrical spreading in my analysis, the t_q values for each station in the *Parallel* and *Normal* models are divided by the t_q values of the corresponding isotropic homogeneous models. Figure 6.17 displays the normalised t_q values (hereafter called $\overline{t_q}$) against the scaled wavenumber ka for the Y- and Z-components. The RMS values are zero for the X-component in *Parallel* model with no fractures, and so the X-component is not normalised and hence is not available in this figure. The first 5 stations reveal that the $\overline{t_q}$ values are nearly equal to 1 for all ka values, indicating an equivalent homogeneous medium. There is a gradual increase over stations 6-10 where the Y-component shows much larger values than the Z-component.

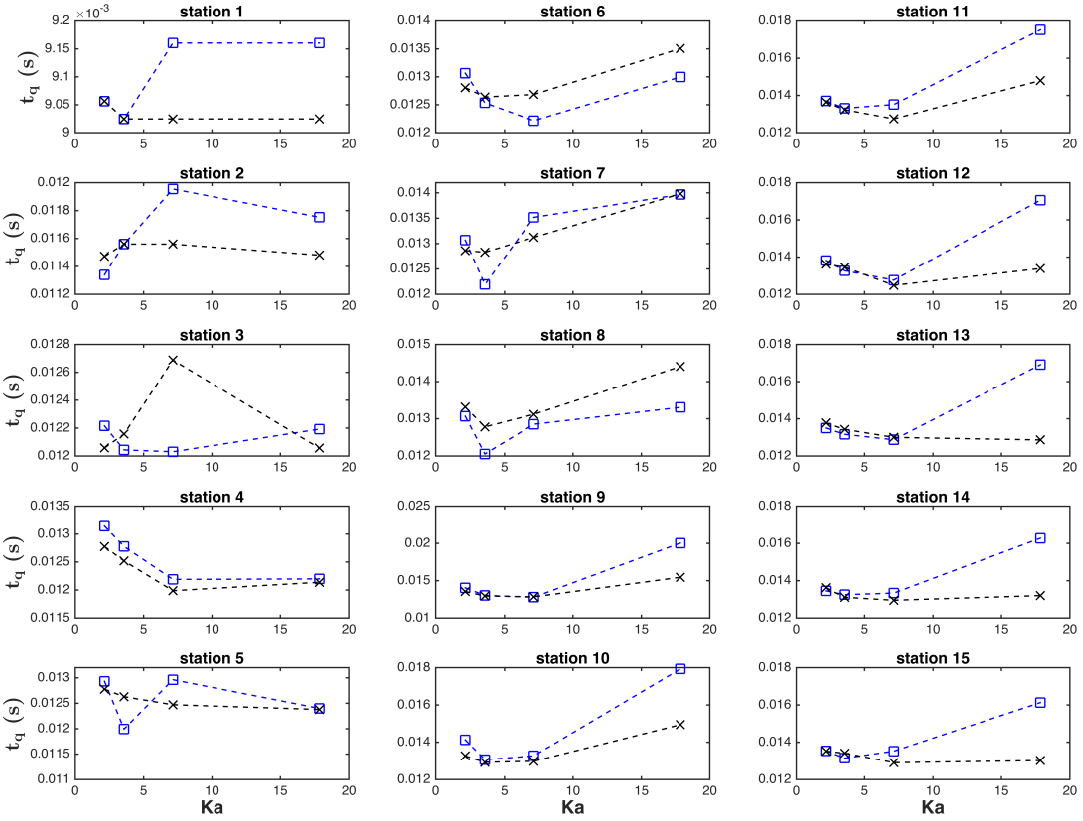

Figure 6.15: Plot of the envelope width t_q against ka for the fracture sizes 6 m,10 m, 20 m and 50 m (*Parallel*). The t_q are shown for Y-component (blue) and Z-component (black).

The $\overline{t_q}$ values for $a = 50$ m ($ka \approx 17.9$) ranges between 1.2 to 1.6. The results of the last 5 stations remain almost stable as expected as wave propagates within the homogeneous section of the model. There is very little change in the $\overline{t_q}$ value for the Z-component which is polarised in the direction of the fracture plane. However, there is significant change in the $\overline{t_q}$ value for the Y-component which is polarised normal to plane.

For the *Normal* models, the $\overline{t_q}$ value versus ka is plotted in the Figure 6.18 for the X- and Z-components. Similar to the X-component in the *Parallel* model, the results for Y-component are excluded in this figure. The results are close to 1.0 at station 1 for all ka values as expected as this station is within the isotropic homogeneous medium before the fracture zone. For station 2, we observe similar behaviour to that shown in Figure

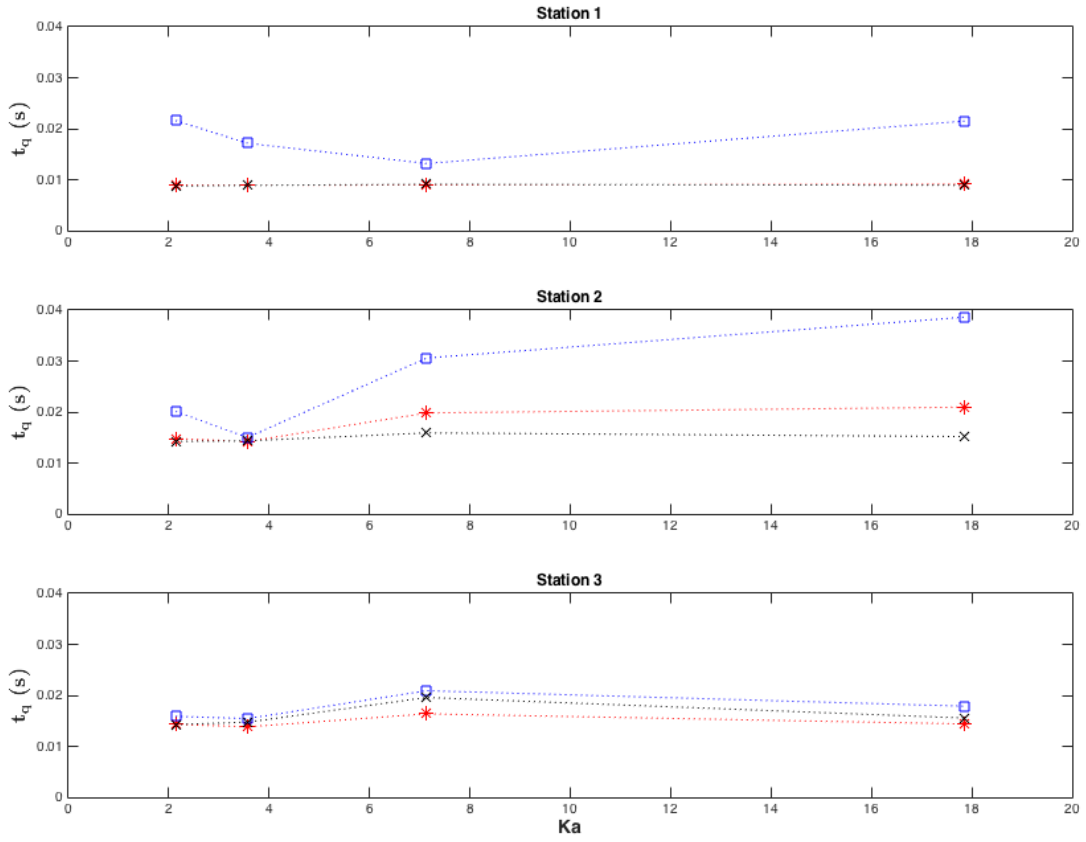

Figure 6.16: Plot of the envelope width t_q against ka for the fracture sizes 6 m,10 m, 20 m and 50 m (*Normal*). The t_q are shown for X-component (red star), Y-component (blue square) and Z-component (black cross).

6.17, yet where we observe both components having an increase in $\overline{t_q}$ values, especially for $ka \approx 7.2$ and 17.9. In principal we would expect the increase for both components to be equal (both components are polarised tangential to the fracture planes). However, we notice that the X-component is larger than Z-component at station 2 and vice versa at station 3. Since the fracture distribution is generated randomly, this particular realisation yields more heterogeneity in the X-direction. It is expected that including significantly more random realisations we would expect, statistically, that the X- and Z-components would behave similarly.

As the seismic moment magnitude of the source is equal in the *Parallel* and *Normal* models, it is useful to compare the results of the $\overline{t_q}$ values for the three primary axes

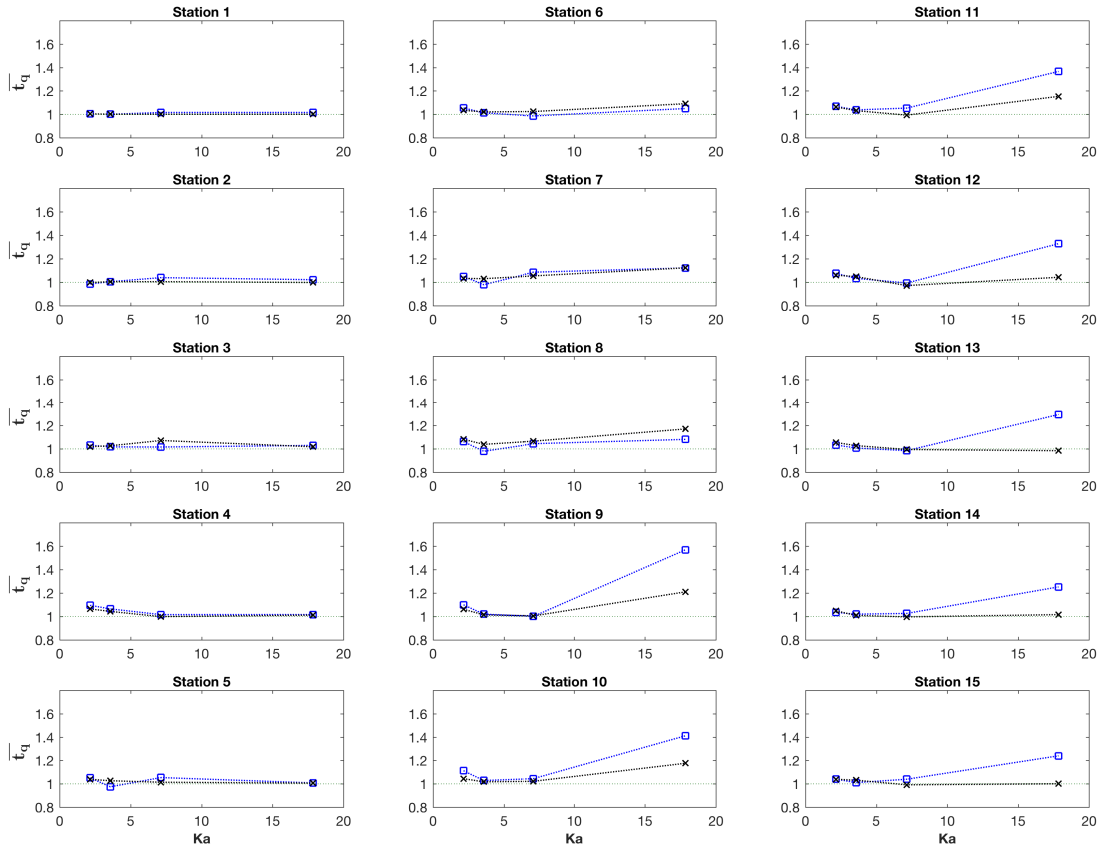

Figure 6.17: Plot of the normalised envelope width $\overline{t_q}$ against ka for the fracture sizes 6 m,10 m, 20 m and 50 m (*Parallel*).

of polarisation, X-, Y-, and Z-axes. In Figure 6.19, the $\overline{t_q}$ results for the X- and Z-components from the *Normal* model and the Y- and Z-components from the *Parallel* model are shown together. I compare the values for station 1 of both *Parallel* and *Normal* models, which show the result of the wave prior to entering the fracture zone. I also show the values for stations 10 and 15 of the *Parallel* model and stations 2 and 3 of the *Normal* model, which show the results of the wave after exiting the fracture volume. Here after, I refer to station 1 as the proximal station, station 2 in *Normal* model and station 10 in *Parallel* model as the exit station and station 3 in the *Normal* model and station 15 in the *Parallel* model as the distal station. At the proximal station, the $\overline{t_q}$ values are approximately 1.0, while at the exit station the $\overline{t_q}$ values increase, with

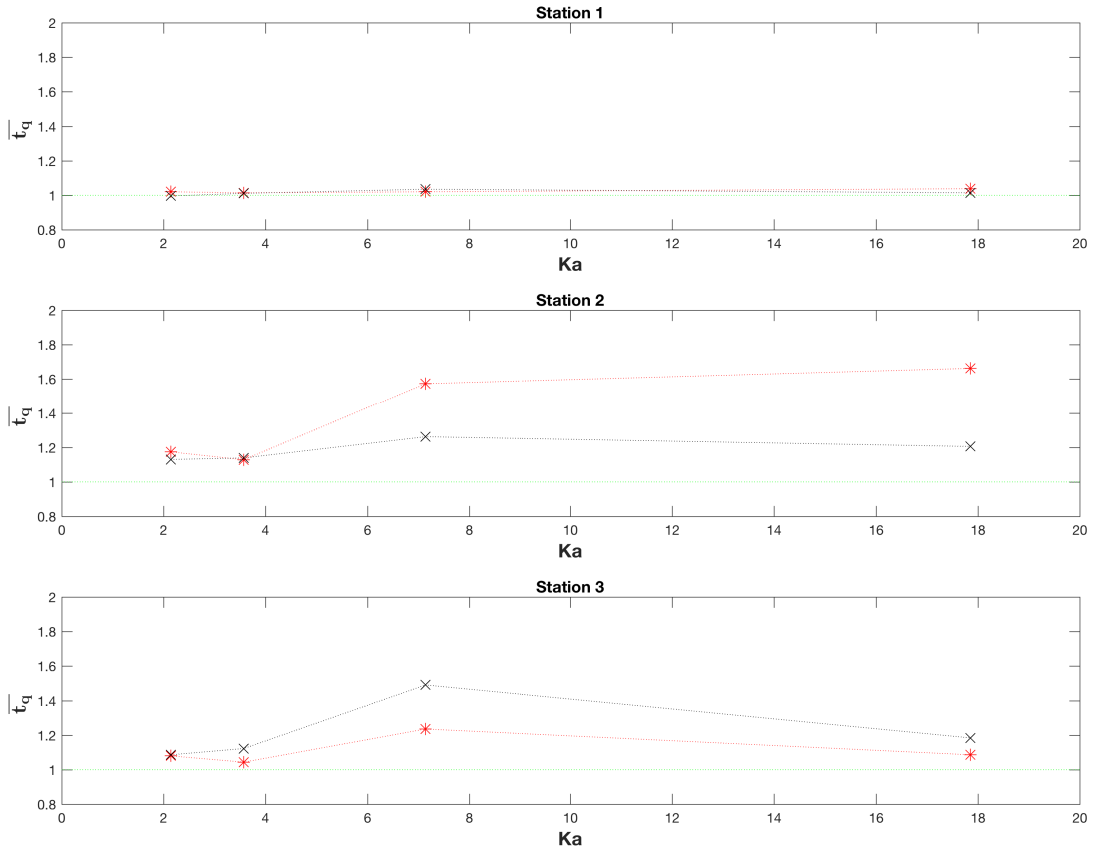

Figure 6.18: Plot of the normalised envelope width $\overline{t_q}$ against ka for the fracture sizes 6 m,10 m, 20 m and 50 m (*Normal*).

more significant increase for $ka > 3$. The $\overline{t_q}$ values between ka 7.2 to 17.9 decrease for *Normal* model at the distal station in comparison with the those at the exit station except for the Z-component. In general, the $\overline{t_q}$ values for the *Normal* model, with propagation direction normal to the fracture plane, are larger than those for the Parallel model. This can be explained by the fact that in the normal direction the wavefront interacts to a much larger extent with the fracture surfaces and so experiences much greater edge and tip diffractions. For propagation parallel to the fracture surface the wavefront still interacts with the fracture surface, but to a lesser extent.

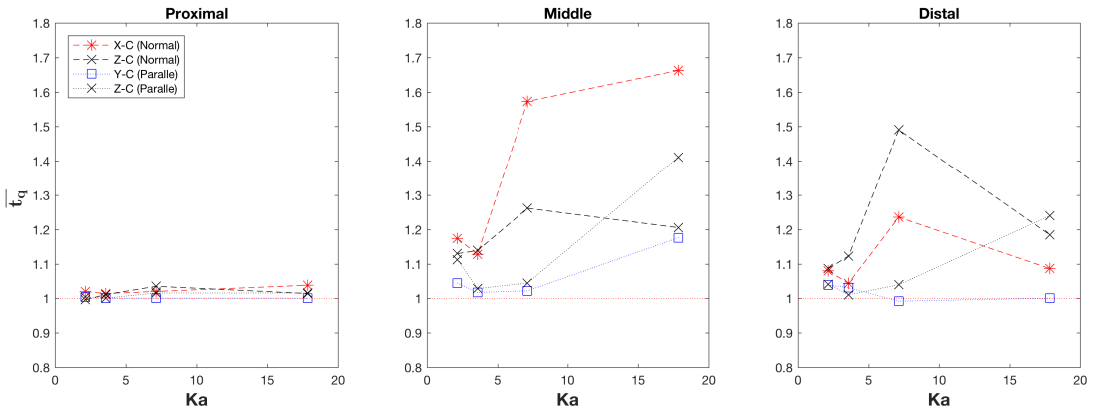

Figure 6.19: Plot of normal envelope width $\overline{t_q}$ against ka for the fracture sizes 6 m,10 m, 20 m and 50 m (*Parallel* and *Normal*).

6.5 Distortion of shear-wave polarisation

In a homogeneous isotropic medium, the particle motion of the P-wave is normal to the spherical wavefront and the polarisation of the S-wave is confined to within the wavefront (i.e., normal to the propagation direction) and defined by the source radiation pattern. However, in a heterogeneous medium, P-wave particle motion and S-wave polarisation can deviate from linearity. The deviation from linearity (or waveform distortion) can be assessed by tracking the trajectory of the waveform particle motion. The shape of the time evolution of the particle motion (or hodogram) can be diagnostic of the seismic waveform distortion. A number of earlier studies have shown the usefulness of hodograms for detecting heterogeneity (e.g., Nishizawa et al., 1983; Nishimura, 1996; Fukushima et al., 2003).

Figures 6.20-6.23 display the particle motion of the direct S-waves in the Y-Z plane for the *Parallel* model with fracture sizes a = 6 m, 10 m, 20 m and 50 m for all 15 stations. The figures are plotted for a time window encompassing two cycles of the dominant period (11 ms) of the S-wave. The first station shows a linear particle motion as expected for a homogeneous isotropic medium. With increasing distance from the source, the waveforms become increasingly distorted and deviate from linear motion.

After station 10 the hodograms remain steady. In Figures 6.20-6.21, the particle motion of the S-waves display typical behaviour of orthogonal fast and slow shear-waves (i.e., shear-wave splitting). In Figures 6.22-6.23, the polarisation is not consistent with that of shear-wave splitting and shows a more random behaviour.

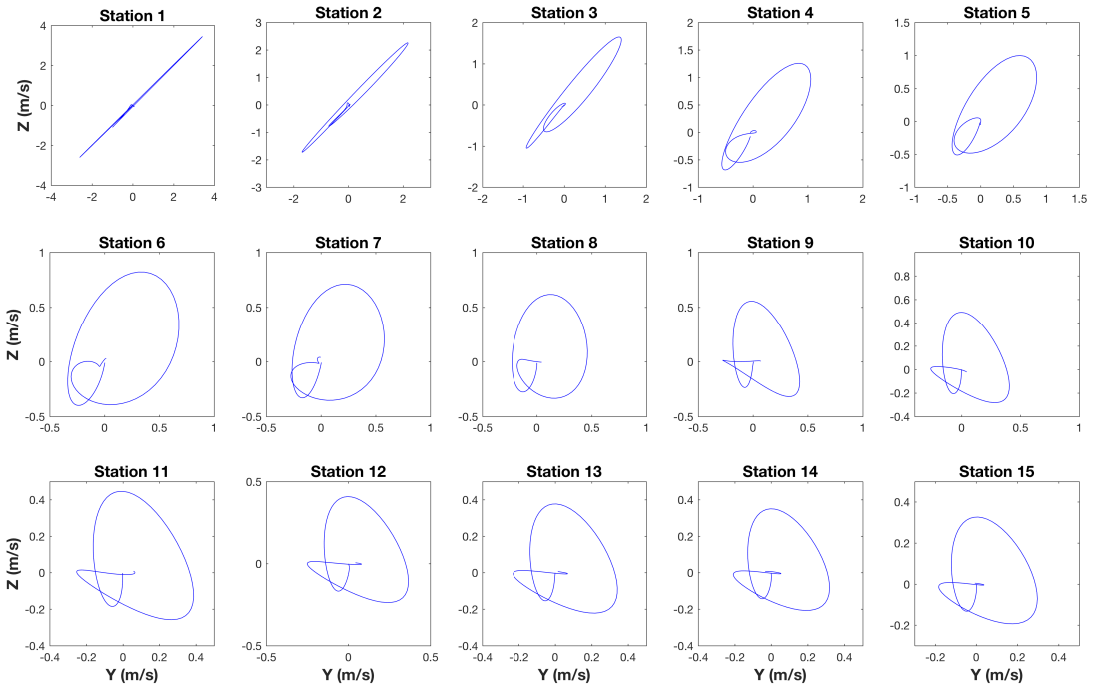

Figure 6.20: Particle motion of S-waves in the Y-Z plane for the *Parallel* model with fracture sizes 6 m. In this figure and Figures 6.21-6.23, the time window is set from the onset of the S-wave and has a time length two times the period of the Ricker source wavelet.

Figure 6.24 displays the particle motion for the *Normal* model for all fracture sizes at the 3 stations. For all fracture sizes at station 1, the particle motions are linear as expected. At stations 2 and 3 by increasing fracture size the distortion from linearity also increases. For wave propagation normal to the fracture planes shear-wave splitting will not develop. Although the waveform envelopes where shown to increase (i.e., waveform broadening) in the previous section, the actual polarisation of the shear-waves remain relatively unaffected for scenarios where $ka \leqslant 3$. For $ka > 3$, we observe significant deviation from linearity, primarily as a result of the multiple reverberations

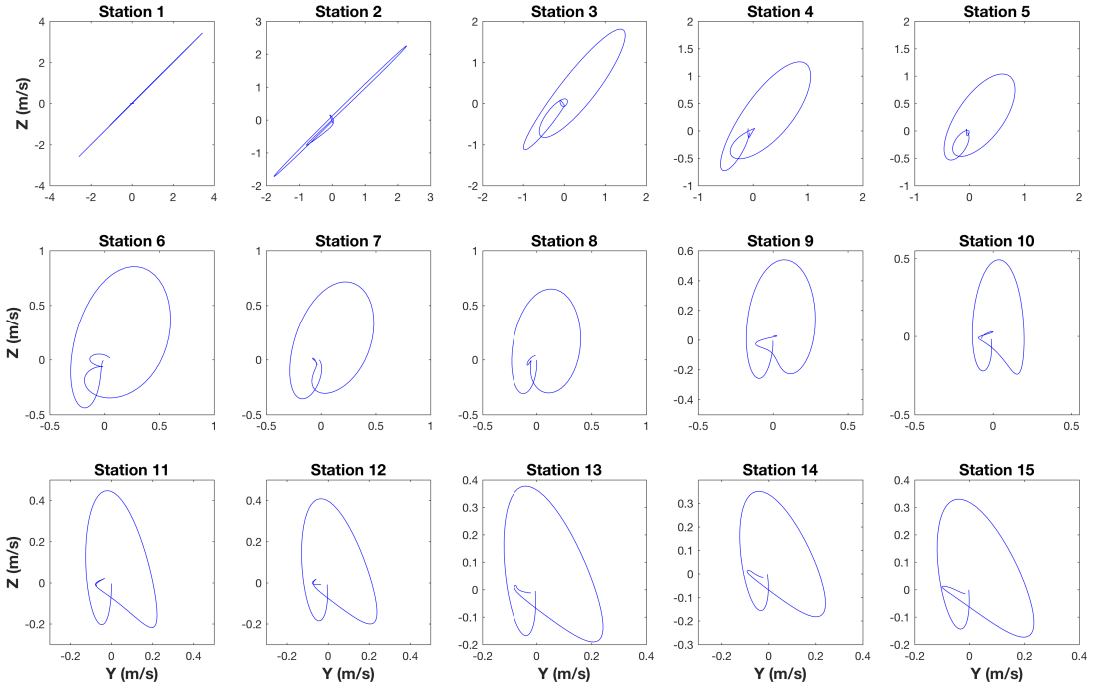

Figure 6.21: Particle motion of S-waves in the Y-Z plane for the *Parallel* model with fracture sizes 10 m.

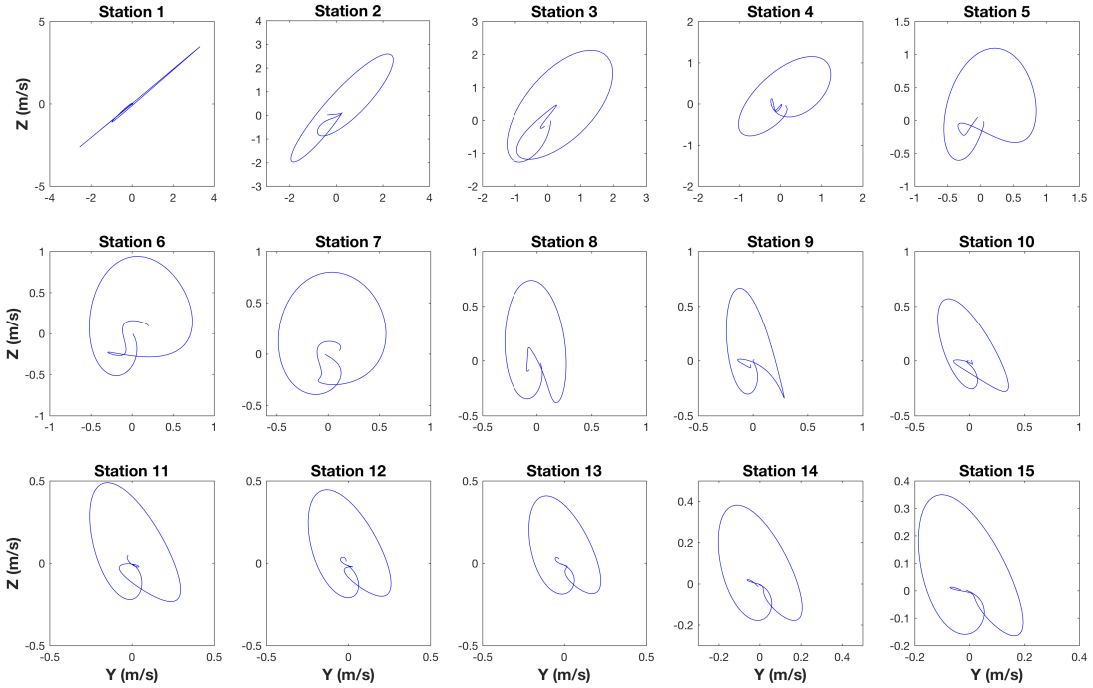

Figure 6.22: Particle motion of S-waves in the Y-Z plane for the *Parallel* model with fracture sizes 20 m.

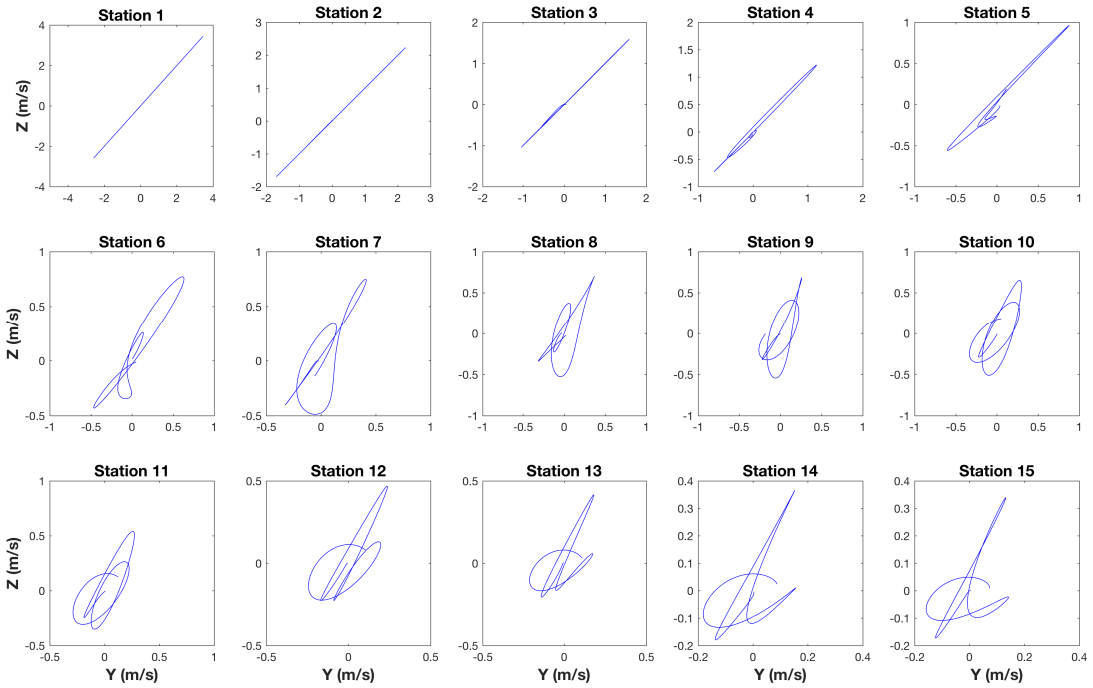

Figure 6.23: Particle motion of S-waves in the Y-Z plane for the *Parallel* model with fracture sizes 50 m.

due to specular type reflections from the interaction of the spherical wavefront and the fracture surfaces (i.e., stronger coherent scattering).

To quantitatively evaluate the distortion of the direct shear-waves, the RMS amplitude ratio between the Y- and Z-components for *Parallel* models, and the X- and Z-components for *Normal* models are calculated. The RMS amplitude ratios are calculated according to

$$\chi_{Parallel} = \sqrt{\frac{\sum_i RMS_{z_i}}{\sum_i RMS_{y_i}}}, \tag{6.1}$$

$$\chi_{Normal} = \sqrt{\frac{\sum_i RMS_{z_i}}{\sum_i RMS_{x_i}}}, \tag{6.2}$$

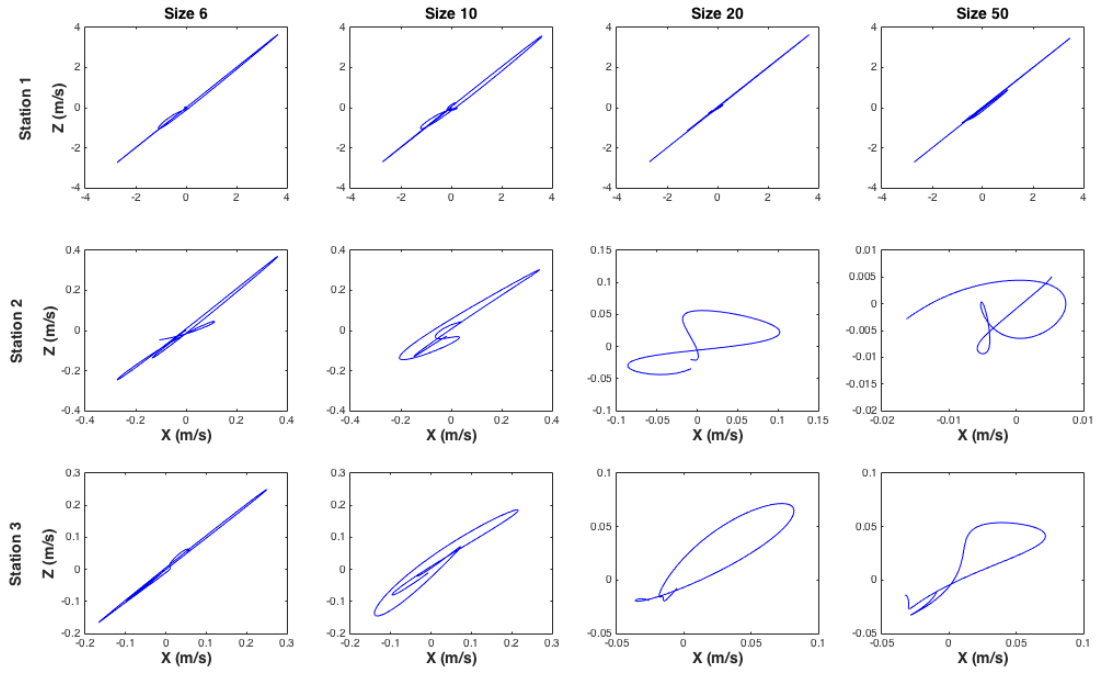

Figure 6.24: Particle motion of S-waves in the X-Z plane for the *Normal* model with fracture sizes 6 m, 10 m, 20 m, 50 m. The time window is set from the onset of the S-wave and has a time length two times the period of the Ricker source wavelet.

where RMS_{x_i}, RMS_{y_i} and RMS_{z_i} are the RMS amplitudes of X, Y and Z components at time t_i, respectively. The summation is evaluated over a time window that is two times the dominant period (11 ms) of the S-wave source from the onset.

Figures 6.25 and 6.26 show the RMS amplitude ratio for *Parallel* $\chi_{Parallel}$ and *Normal* χ_{Normal} models, respectively, against ka for all the fracture sizes in this study. As shown in Figure 6.25, for $a = 6$ m and all stations the values of $\chi_{Parallel}$ are very close to 1, which indicates that the same amount of the energy is partitioned into the Y- and Z-components. Also, for all fracture sizes for the first 5 stations the values of $\chi_{Parallel}$ remain nearly equal to 1. For fracture sizes $a = 10$ m, 20 m and 50 m (i.e. $ka = 3.6$, 7.2 and 17.9 respectively), the values of $\chi_{Parallel}$ are noticeably larger than 1, especially when $ka = 17.9$. However, for $ka = 3.6$ and 7.2 the $\chi_{Parallel}$ values fluctuate in a more or less random pattern between stations 6-10. Outside the fracture zone (stations 11-15) the $\chi_{Parallel}$ values rise for increasing ka to about 1.5 (at $ka = 7.2$) and

then fall to about 1.2 at $ka = 17.9$.

The results for the χ_{Normal} calculations are shown in Figure 6.26 for the 3 stations. Similar to $\chi_{Parallel}$ at station 1, for all fracture sizes the χ_{Normal} values are about 1, but at station 2 the χ_{Normal} values increase with increasing ka to 1.8 at $ka = 7.2$ and then decrease to 1.3 at $ka = 17.9$. From Figures 6.25 and 6.26, it can seen that the largest distortion occurs when the fracture size a is comparable to the dominant wavelength λ_S (i.e., a =20 m) in the Mie scattering regime.

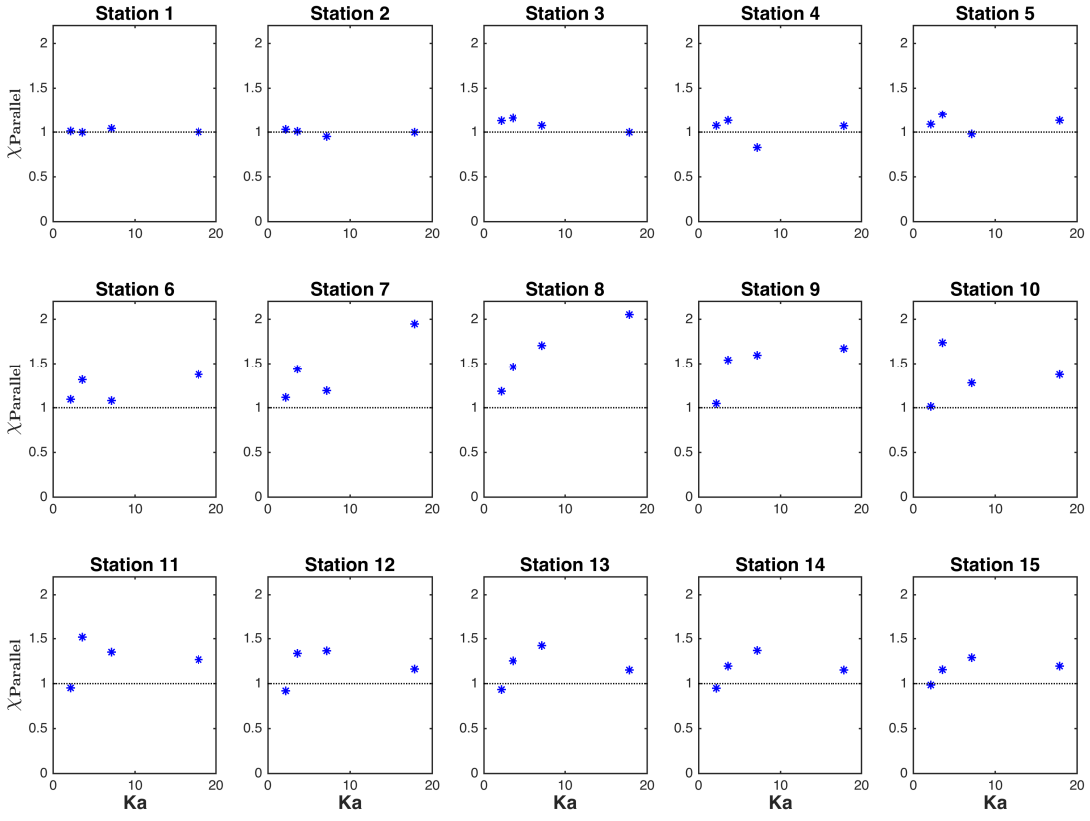

Figure 6.25: Plot of the RMS ratio $\chi_{Parallel}$ against ka for the fracture sizes 6 m,10 m, 20 m and 50 m.

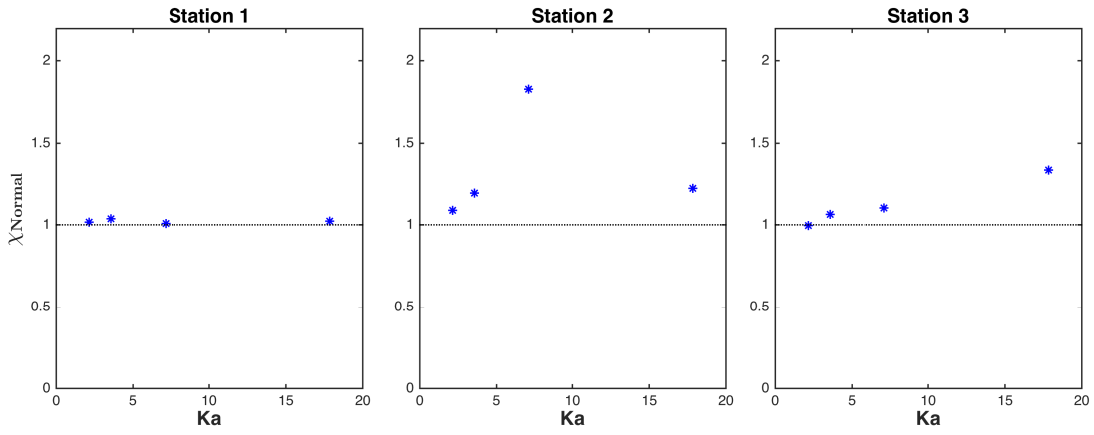

Figure 6.26: Plot of the RMS ratio χ_{Normal} against ka for the fracture sizes 6 m,10 m, 20 m and 50 m.

6.6 Differential attenuation analysis

There are several techniques to measure wave attenuation, such as the centroid frequency shift method (e.g., Quan & Harris, 1997), the dominant frequency shift method (Barnes, 1993) and the spectral ratio method (e.g., Båth, 1974). In this section, I first consider the waveform frequency content of both the *Parallel* and *Normal* models and then discuss and implement the spectral analysis method to quantify attenuation.

6.6.1 Amplitude spectrum analysis

In the previous section, I analysed the effects of scattering in the time-domain. In this section, I examine the data in the frequency domain. Analysis in the frequency domain allows me to apply filters much more easily as well as analyse the whole signal as a spectrum in the frequency domain rather than at specific points in time around the onset of the direct P- or S-waves. Analysis in the frequency domain allows comparison of waveforms frequency content such as dominant or central frequency and their respective amplitude. The comparison can be unambiguous and allow comparison between stations and components.

Figures 6.27-6.30 show the amplitude spectrum for the *Parallel* models for all fracture sizes for Z- and Y-components. To eliminate the effect of geometrical spreading, each component has been normalised by its corresponding station component in the model with no fractures. A Hanning window has been used to taper the shear-waves prior to Fourier transformation into the frequency domain. The window length varies depending on the model fracture size. For all fracture sizes, the amplitude spectrum of the Y-component is more attenuated at higher frequencies than Z-component (this is expected as the Y-component is polarised normal to the fracture surface whereas the Z-component is polarised parallel to the fracture surface). With increasing distance from the source in the fracture zone for all models, attenuation increases and the frequency content of all waveforms is reduced. The results remain relatively constant for stations 10-15, where the receivers are located in the isotropic homogeneous background. I compute the peak (maximum) frequency as well as the dominant frequency at each station and for each component.The dominant frequency as defined by (Barnes, 1993) is given

$$f_d^2 = \frac{\int_0^\infty f^4 P(f) df}{\int_0^\infty f^2 P(f) df}, \tag{6.3}$$

where f_d is the dominant frequency and $P(f)$ is the power spectrum.

To facilitate the results of the spectral analysis of the *Parallel* models for all fracture sizes, I combined all the results for station 15 as well as the spectrum for the isotropic medium (orange colour) in Figure 6.31. In this figure it can be observed that for the Z-component, attenuation is greater for the smaller fracture sizes and the peak frequency is approximately 210 Hz. However, for the Y-component the most attenuation is obtained for $a = 10$ m and 20 m (blue and green dashed line respectively) and the peak frequency has shifted to a lower frequency ($\approx$ 173 Hz). Furthermore, the Y-component shows larger attenuation than the Z-component. The results indicate that a larger number

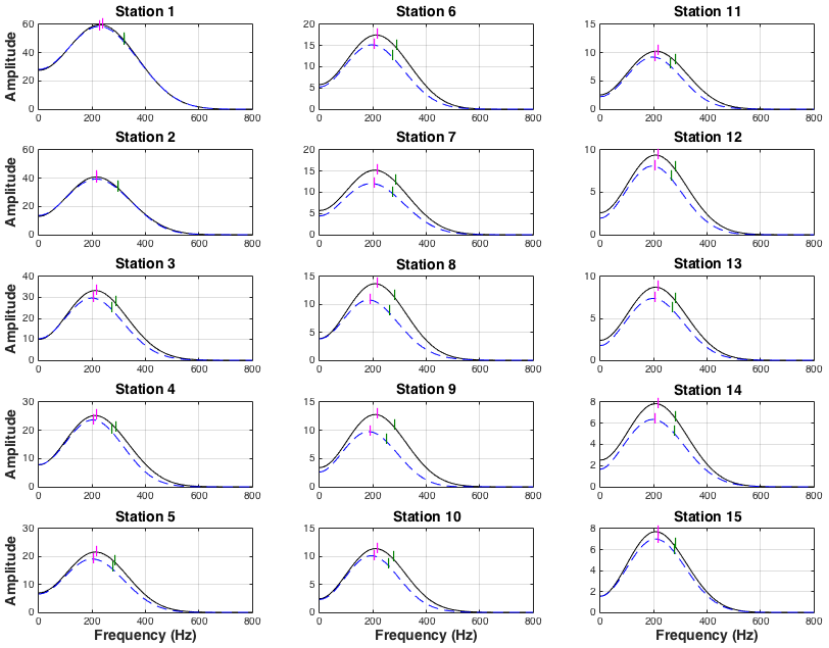

Figure 6.27: Fourier amplitude spectrum for model having fracture density 0.1 and fracture size 6 m (*Parallel*). For this figure and Figures 6.28-6.30 the solid black line depicts the Z-component, the blue dashed line depicts the Y-components (Figures 6.27-6.30) and the small green and magenta bars, respectively show the dominant and peak frequencies of spectra.

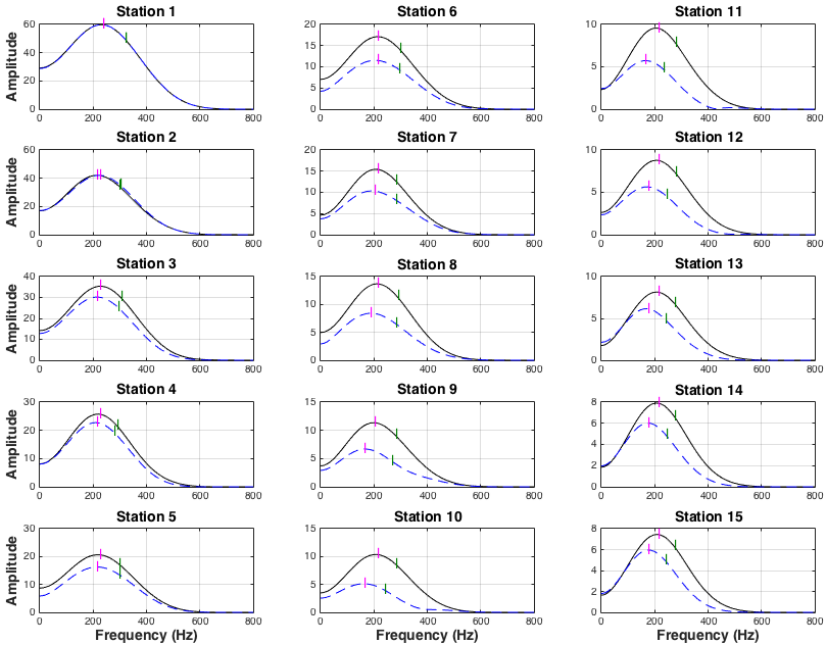

Figure 6.28: Fourier amplitude spectrum of model having fracture density of 0.1 and fracture size 10 m (*Parallel*).

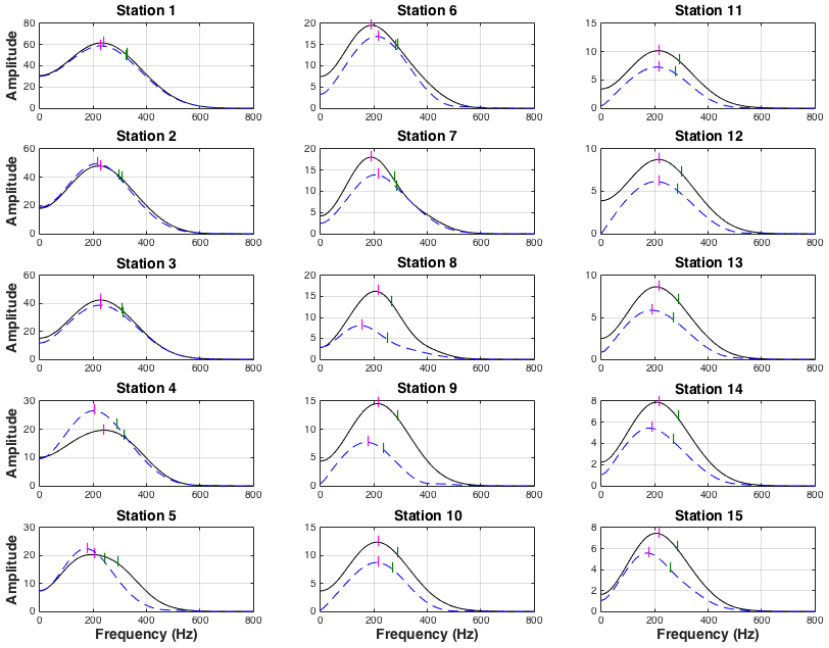

Figure 6.29: Fourier amplitude spectrum of model having fracture density of 0.1 and fracture size 20 m (*Parallel*).

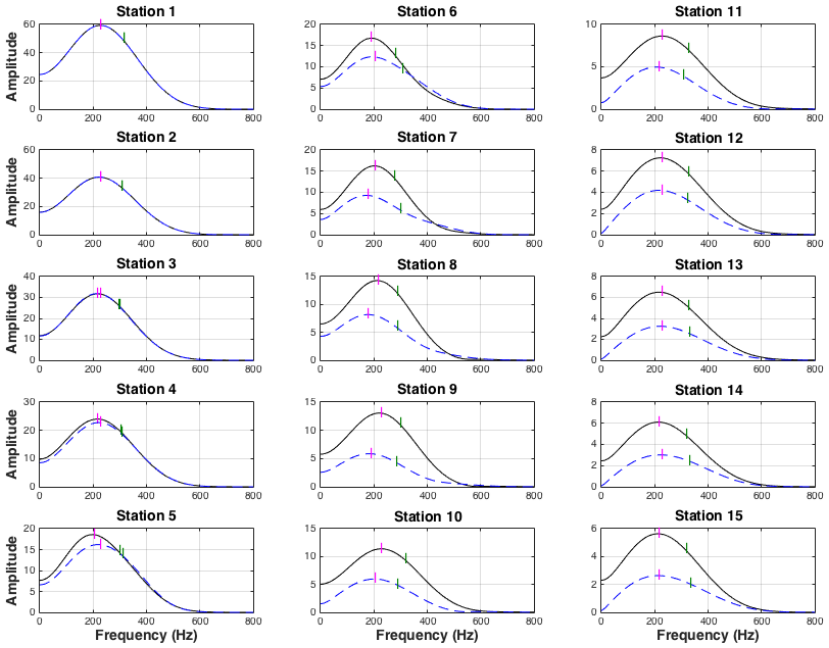

Figure 6.30: Fourier amplitude spectrum of model having fracture density of 0.1 and fracture size 50 m (*Parallel*).

of small fractures causes higher attenuation than a small number of large fractures. Moreover, the medium with small fracture size behaves as a low pass filter. Furthermore, there is discrepency between peak frequency of the signal for the isotrpic medium ($\approx$ 200 Hz) and for the fratured media ($\approx$ 210 Hz) due to (1) some possible numerical dispersion although the optimal FD grid parameters are used (e.g., Wang et al., 2015) and (2) some observed distortion of input wavelets when using finite-difference moment tensor implementation on numerical grids.

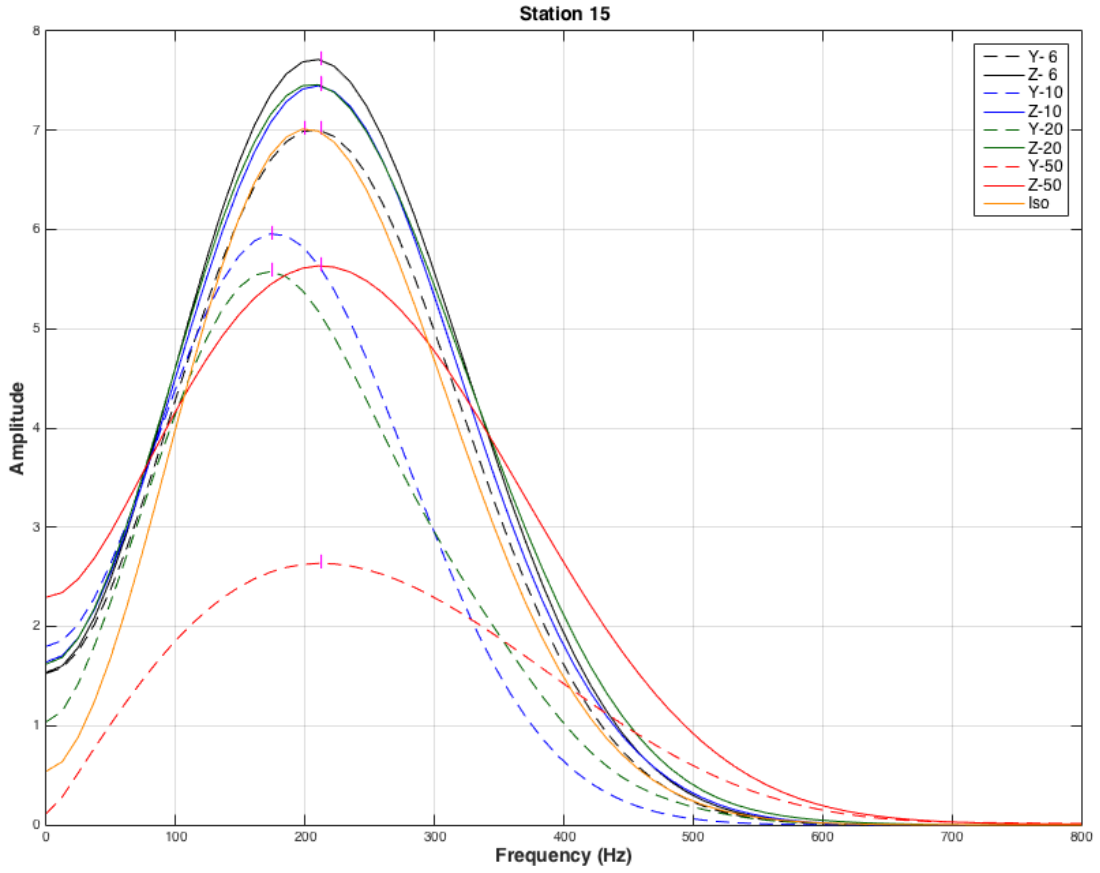

Figure 6.31: Amplitude spectra of Y- and Z-velocities of *Parallel* with $\epsilon = 0.1$ and a =10 m, 20 m and 50 m at the station 15. The small magenta bars show the peak frequency of spectra.

Figure 6.32 shows the amplitude spectra for the *Normal* models at the 3 stations for all fracture sizes. With the exception of the first station (where the spectra results are very closely equal) the remaining stations reveal that the Z-component is more

attenuated at higher frequencies than the X-component. For both components, the peak frequencies have shifted to lower frequencies; the shift being greatest for models with larger fracture size.

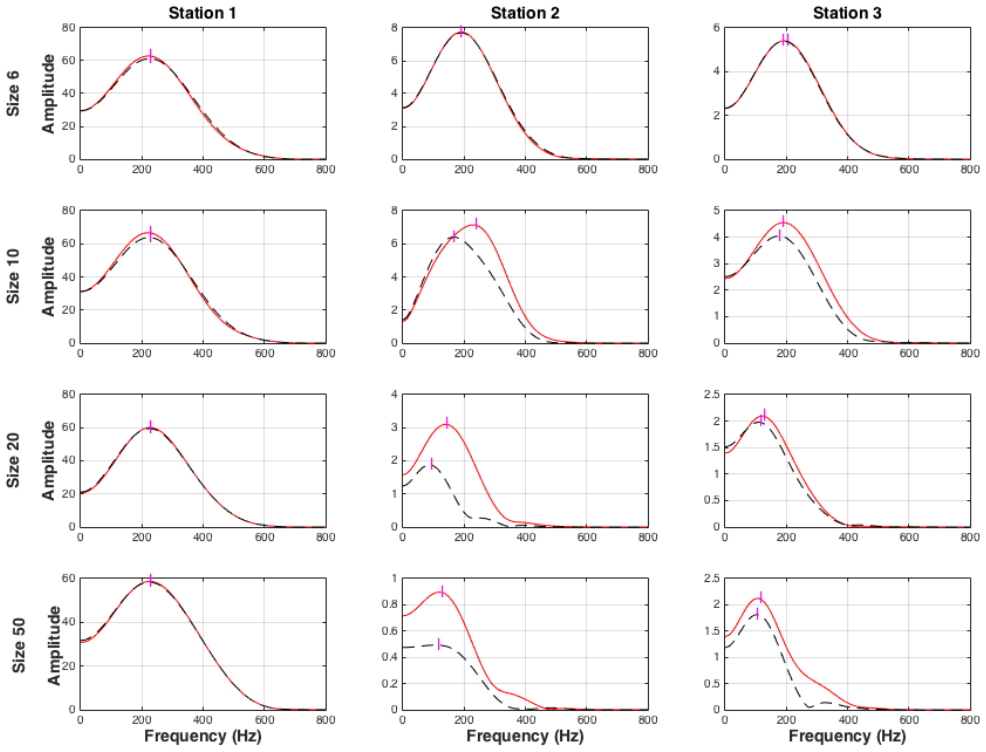

Figure 6.32: Fourier amplitude spectrum of models having fracture density of 0.1 and fracture sizes 6 m, 10 m, 20 m and 50 m (*Normal*). The solid red line depicts the X-component and the black dashed line depicts the Z-components.

6.6.2 Amplitude spectral ratio

In section 6.2 it was mentioned that the presence of discrete fractures leads to elastic heterogeneity. If fractures or cracks form within coherent and subparallel patterns, the seismic velocity will be dependent on the direction of wave propagation. For instance, P-waves propagating parallel to the fracture planes will travel faster than P-waves propagating normal to the fracture planes. The velocity between these two directions depends on several variables, such as the medium elastic constants, pore-fluid properties

and saturation, the fracture density as well as the distribution and shape of fractures (Carter & Kendall, 2006). The presence of aligned fracture sets often results in seismic anisotropy, although there is a transition where a fractured medium evolves from a scattering to anisotropic regime (Yousef & Angus, 2016).

Velocity anisotropy is theoretically formulated for various types of anisotropic symmetries, such as transverse isotropy (TI), azimuthal anisotropy and fracture-induced anisotropy. Yet, velocity anisotropy alone is not sufficient to reveal the reasons that lead to elastic anisotropy. For instance, crystal scale lattice preferred orientation (LPO) and aligned fractures can theoretically result in the same observed anisotropy. However, attenuation anisotropy can differ between these two causes of observed anisotropy and this is due to frequency-dependent mechanisms. For instance, when the scale length of heterogeneity is smaller than the seismic wavelength, low frequency waves have longer splitting times than high frequency waves (Carter & Kendall, 2006). For media where the shear-wave velocity is frequency-dependent, the medium elasticity is required to be dispersive. Furthermore, there is a relation between dispersion and intrinsic attenuation (e.g., Aki & Richards, 1980; Hudson, 1981).

Hudson (1981) studied velocity and attenuation anisotropy of vertically fractured media with low fracture density and introduced a model valid in the high frequency limit, where wavelengths are larger than fracture size. The Hudson (1981) model predicts that the slow shear-wave will be more attenuated at higher frequencies relative to the fast shear-wave. Chapman et al. (2003) extended the Hudson (1981) model and showed the dependency of shear-wave splitting on waveform frequency and fracture size. Carter & Kendall (2006) tested the Hudson (1981) model on several microseismic datasets of shear-waves splitting to predict attenuation of the split shear-waves. However, Carter & Kendall (2006) observed that sometimes the fast shear-wave was more attenuated at higher frequencies than the slow shear-wave.

In this section I implement the spectral ratio method for the Y- and Z-components for the *Parallel* models and the X- and Z-components for the *Normal* models for the model with fracture density $\epsilon = 0.1$ and fracture sizes $a = 6$ m, 10 m, 20 m and 50 m. To do this, the intrinsic attenuation Q^{-1} is assumed to be a constant. For the *Parallel* models, where the propagation direction is along the strike of the fracture planes and for the initial prescribed source polarisation orientation, shear-wave splitting has the potential to develop in the synthetic data. Hence, the calculation of differential attenuation ΔQ^{-1}_{Z-Y} for the *Parallel* models might provide a measure of shear-wave scattering attenuation. Differential attenuation is the difference in the loss of energy per cycle experienced by pairs shear-components along the fractured part of the raypath. The measurement of the quality factor is not a true value, rather it approximates Q^{-1}, and is refereed as specific attenuation.

The amplitude of the shear-wave can be written as a function of frequency f,

$$A_n(f) = G_n(f)S_n(f)R_n(f)exp(\frac{-\pi t_n f}{Q_n}), \tag{6.4}$$

where $A_n(f)$ is the amplitude spectrum at a particular station, n is the component (i.e., X, Y or Z), $G_n(f)$ is the transfer function between source and station, $S_n(f)$ is the amplitude at the source, $R_n(f)$ is the effective transfer function of the receiver (i.e., including rotation, the coupling, the impulse response of the receiver and the recording system response) and t is the traveltime between source and receiver.

Assuming the pairs of shear-wave components have the same transfer function, the same effective transfer function and the same spectral frequency at the source, then the spectral ratio method (Båth, 1974) can provide a measure of the relative attenuation between two orthogonal components. The calculation of the $\log_e$ amplitude spectral ratio (LASR) for the *Paralel* and *Normal* models, respectively, are formed,

$$ln\left(\frac{A_Z(f)}{A_Y(f)}\right) = -\pi\left(\frac{t_Z}{Q_Z} - \frac{t_Y}{Q_Y}\right)f + c. \tag{6.5a}$$

$$ln\left(\frac{A_Z(f)}{A_X(f)}\right) = -\pi\left(\frac{t_Z}{Q_Z} - \frac{t_X}{Q_X}\right)f + c. \tag{6.5b}$$

The c term is a constant value that results from the frequency-independent differences in the G_n, S_n and R_n values in Equation 6.4. The t_n values for the *Parallel* and the *Normal* model represent the arrival time for each component. For the *Parallel* model $t_Z \leqslant t_Y$ ($t_Z = t_Y$ if no shear-wave splitting and $t_Z < t_Y$ if there is shear-wave splitting, where the Z-component is the fast shear-wave). For the *Normal* model the $t_Z = t_X$. If attenuation Q^{-1} is constant, the LASR should be approximately linear with frequency over the signal bandwith. Figures 6.33-6.36 display the LASR for the *Parallel* models against frequency. Regression is performed over a limited bandwidth (black dashed line). The differential attenuation for the *Parallel* and *Normal* models, respectively, can be defined as

$$\Delta Q^{-1}_{Z-Y} = \pi t_Z\left(\frac{t_Y}{t_Z Q_Y} - \frac{1}{Q_Z}\right) \tag{6.6a}$$

$$\Delta Q^{-1}_{Z-X} = \pi t_Z\left(\frac{t_X}{t_Z Q_X} - \frac{1}{Q_Z}\right). \tag{6.6b}$$

The term πt_Z is positive, so the remaining term can be either positive or negative. If Equation 6.6a is negative, the Z-component is more attenuated than the Y-component since t_Y/t_Z is greater than or equal to one. However, when Equation 6.6a is positive, we can not strictly say which component has been more attenuated. Without a measurement of either Q_Z^{-1} or Q_Y^{-1}, it is not possible to know which component has experienced more attenuation at high frequencies due to the trade-off between the additional travel time of the slow shear-wave spent in the attenuative medium and the magnitude of

attenuation affecting the slow component being larger than the fast component (i.e., the slow shear-wave has experienced a greater attenuation per cycle).

In section 6.6.1 I show that the Y-component (slow shear-wave) has larger attenuation than the Z-component (fast shear-wave), which is consistent with results of Hudson (1981). However, Carter & Kendall (2006) observe that the fast shear-wave can experience larger attenuation than the slow shear-wave. Carter & Kendall (2006) note that the relative peak amplitude of the split shear-waves depends more on the initial polarization of the incident shear-wave than on the relative levels of frequency-dependent attenuation.

Figures 6.33-6.36 show the LASR for *Parallel* models for all fracture sizes. The regression lines (black dashed lines) reveal a positive gradient over the bandwidth of 0-200 Hz. The positive gradient suggests that the Y-component is more attenuated than the Z-component. As well in Figures 6.27-6.30 the difference between peak frequency of the shear-waves is positive ($f_{p_Z} - f_{p_Y} > 0$) indicating that the Y-component is more attenuated. However, it is not possible to determine whether $Q_Z > Q_Y$ or whether $Q_Z \approx Q_Y$ since the Y-component could be more attenuated due to the longer travel time in fractured medium.

The LASR for the *Normal* model can be simplified based on the assumption that the shear-wave onset times will be equal ($t_X = t_Z$)

$$\Delta Q^{-1}_{Z-X} = \pi t_Z \left(\frac{1}{Q_X} - \frac{1}{Q_Z} \right). \tag{6.7}$$

The term πt_Z is positive and the remaining term in brackets can be either positive or negative. If Equation 6.7 is positive, the X-component is more attenuated than Z-component ($Q_X^{-1} > Q_Z^{-1}$). Equation 6.7 intuitively reveals that differences in attenuation between the X- and Z-components in the *Normal* model is not influenced by differential

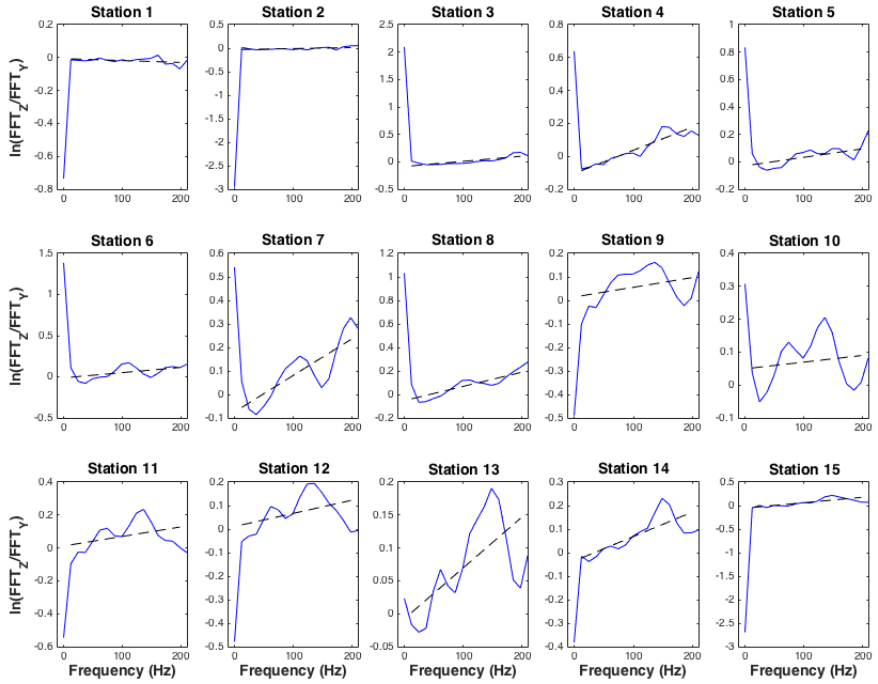

Figure 6.33: Amplitude spectral ratio of Y- and Z-axis $Log_e(A_Z(f)/A_Y(f))$ of *Parallel* with ϵ =0.1 and $a = 6$ m. The dashed line shows the regression line over limited bandwidth.

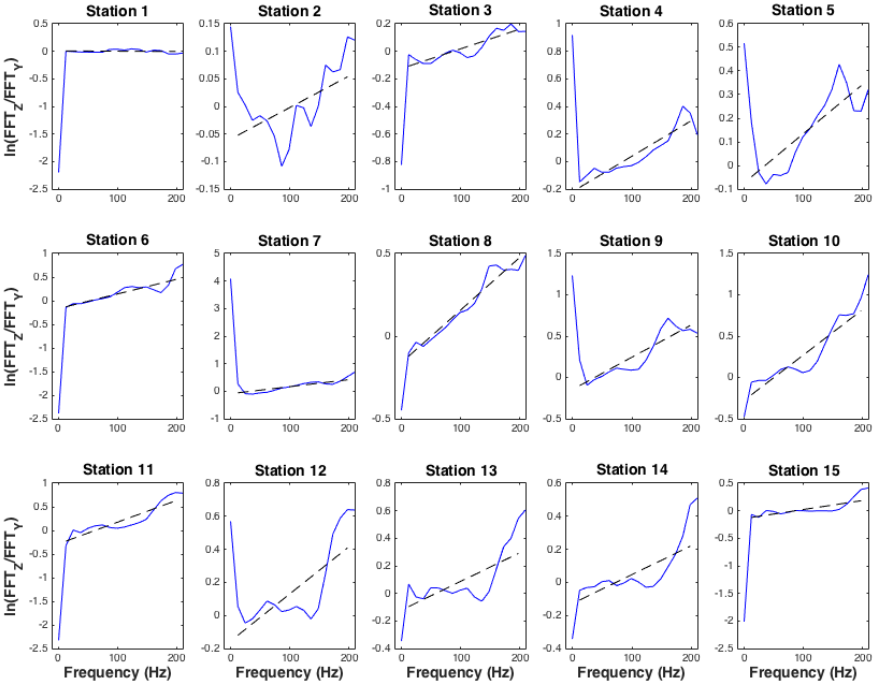

Figure 6.34: Amplitude spectral ratio of Y- and Z-axis $Log_e(A_Z(f)/A_Y(f))$ of *Parallel* with ϵ =0.1 and $a = 10$ m. The dashed line shows the regression line over limited bandwidth.

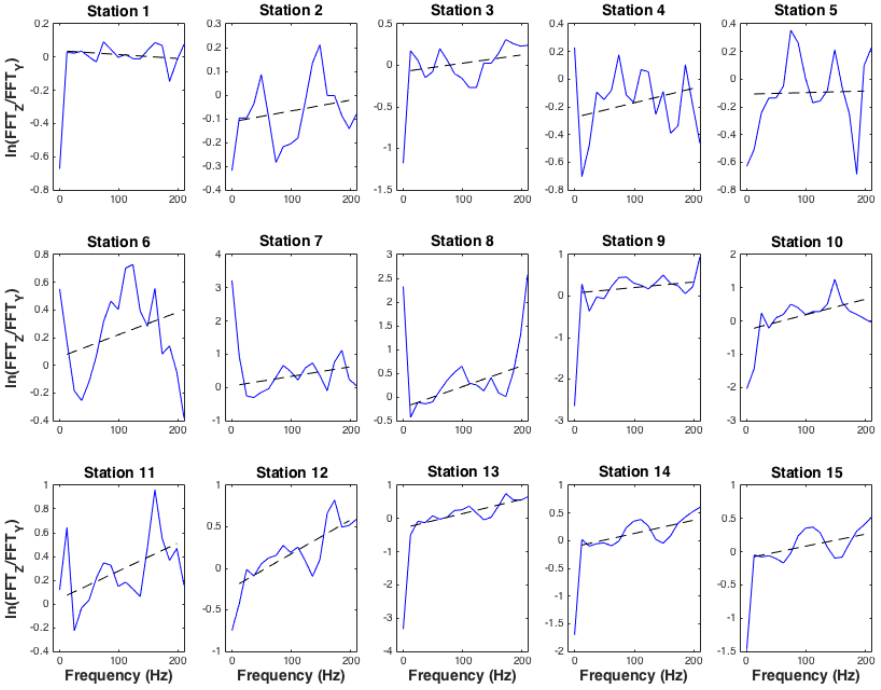

Figure 6.35: Amplitude spectral ratio of Y- and Z-axis $Log_e(A_Z(f)/A_Y(f))$ of *Parallel* with ϵ =0.1 and $a = 20$ m. The dashed line shows the regression line over limited bandwidth.

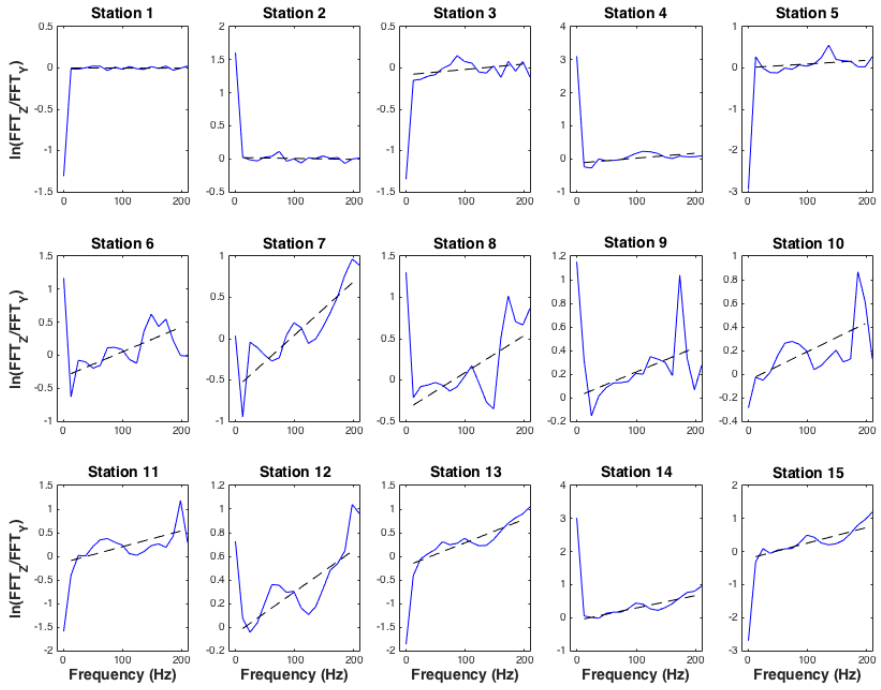

Figure 6.36: Amplitude spectral ratio of Y- and Z-axis $Log_e(A_Z(f)/A_Y(f))$ of *Parallel* with $\epsilon = 0.1$ and $a = 50$ m. The dashed line shows the regression line over limited bandwidth.

travel times. The LASR for the Z- and X-components of the *Normal* model is shown in Figure 6.37, where the regression gradient lines (black dashed line) for almost all the stations is negative. The negative regression line implies that $Q_Z^{-1} > Q_X^{-1}$. However, with the exception of a few frequency notches, the slopes are approximately horizontal. We would expect that the X- and Z-component attenuation to be identical and so my results could be influenced by focusing and defocusing of discrete frequency bands.

Figures 6.38-6.39 depict the differential attenuations (ΔQ_{Z-Y}^{-1} and $f_{p_Z} - f_{p_Y}$) against the difference in the peak frequencies $f_{p_Z} - f_{p_Y}$ and the dominant frequency $f_{d_Z} - f_{d_Y}$ respectively. From Figures 6.38-6.39 it can be seen that the differential attenuation in the *parallel* model $\Delta Q_{Z-Y}^{-1} > 0$ is consistent with the observation of a shift in the peak frequency $f_{p_Z} - f_{p_Y} \geqslant 0$. However, it can be seen that for the *Normal* model the differential attenuation $\Delta Q_{Z-X}^{-1} < 0$, while $f_{p_Z} - f_{p_X} \leqslant 0$. These results implies that the differential attenuation method is adequate to examine the attenuation of each component individually, except when $\Delta Q_{Z-Y}^{-1} > 0$. In addition, differential attenuation is an appropriate method and is compatible with method of peak frequency shift.

6.7 Summary

In this chapter, I examined the widening effect of wavelets due to scattering within a fractured medium by using several different approaches. The examination was performed by implementing numerical modelling of wave propagation in discrete fracture models with a desired high fracture density and for various fracture sizes. I used different methods including the RMS envelope analysis, shear-wave polarisation distortion, differential attenuation analysis and peak frequency shifting to assess the scattering behaviour of those parametrised models in which the propagation direction is either normal or parallel to the fracture surfaces.

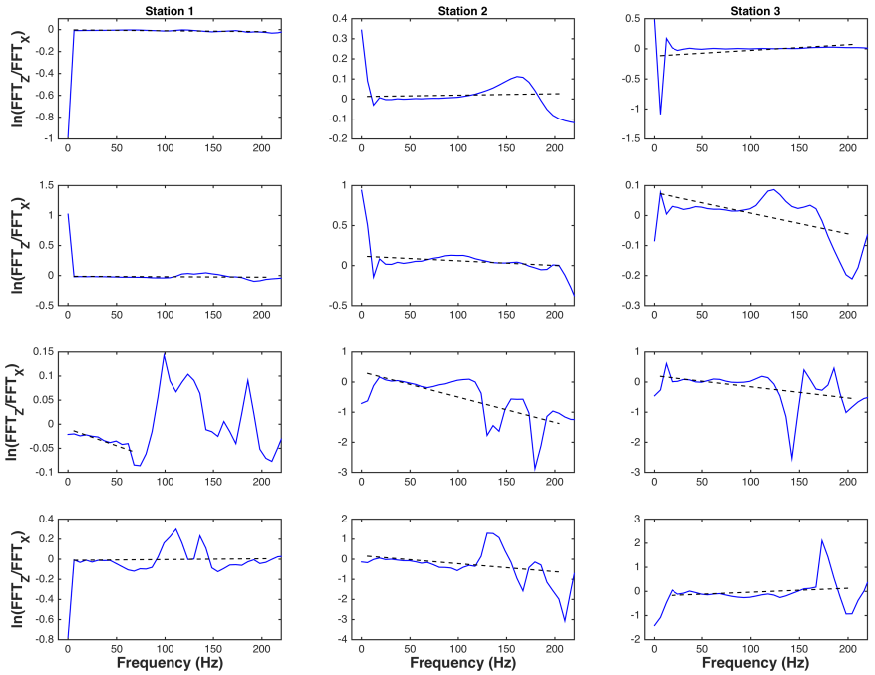

Figure 6.37: Amplitude spectral ratio of X- and Z-axis $Log_e(A_Z(f)/A_X(f))$ of *Parallel* with $\epsilon = 0.1$ and $a = 6$ m, 10 m, 20 m and 50 m from top to bottom. The dashed line shows the regression line over limited bandwidth.

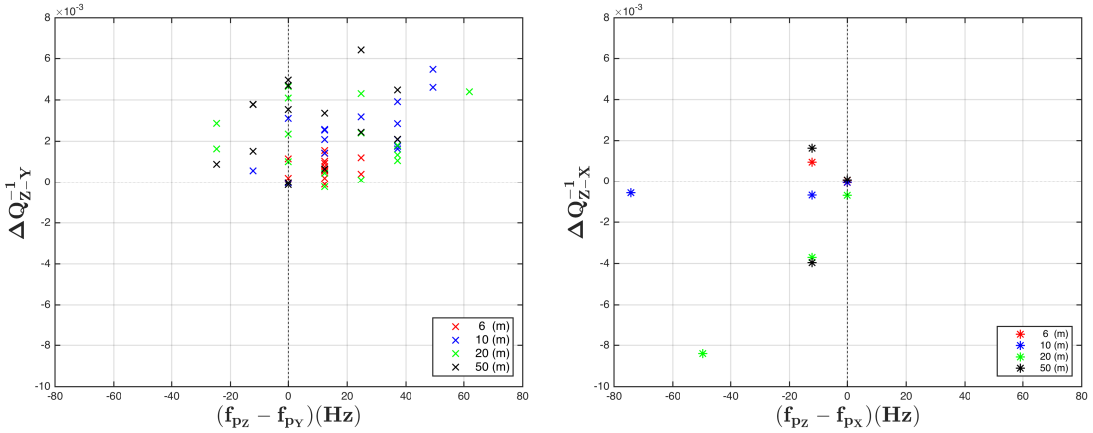

(a) (b)

Figure 6.38: Differential attenuation plotted against difference in peak frequency, $f_{pZ} - f_{pY}$ for the *Parallel* (a) model and $f_{pZ} - f_{pX}$ for the *Normal* model (b).

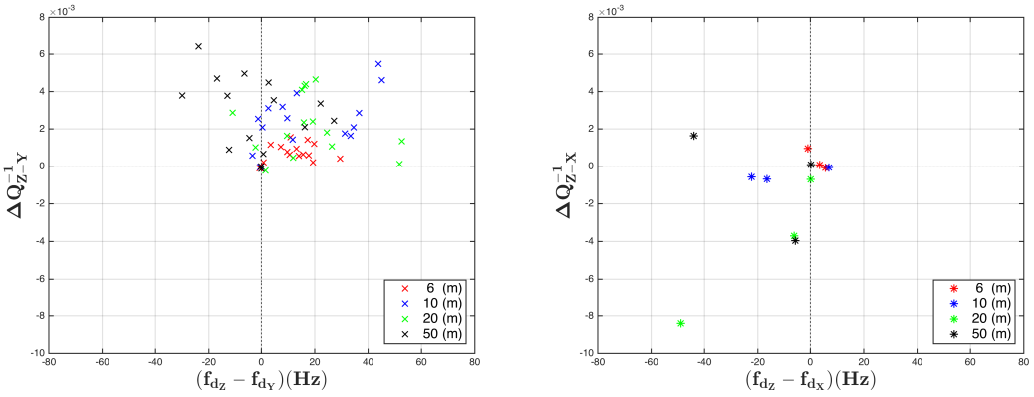

(a) (b)

Figure 6.39: Differential attenuation plotted against difference in peak frequency, $f_{d_Z} - f_{d_Y}$ for the *Parallel* (a) model and $f_{d_Z} - f_{d_X}$ for the *Normal* model (b).

For the Parallel model the largest $\overline{t_q}$ was obtained for the largest fracture size ($a =$ 50 m), while for the *Normal* model the largest $\overline{t_q}$ occurred for fracture size, $a = 20$ m (where a is approximately equal to the λ_S). Neerhoff & Van der Hijden (1984) and Van Der Hijden & Neerhoff (1984) theoretically examined the scattering characteristics of shear-waves of planar cracks of finite width for $ka \geqslant 3$. Based on their results, scattering is prominent when the shear-wave propagates perpendicular to the fracture planes. In general, the average $\overline{t_q}$ values for the *Normal* model were generally larger than the *Parallel* model. This is consistent with theory and is likely due to the wavefront interactions with fracture surfaces that result in diffraction from the tip and edge of fractures.

By using the shear-wave propagation distortion approach, I observed that the particle motion qualitatively shows a distortion from linearity. This is symptomatic of orthogonal shear-wave splitting that occurs in the *Parallel* model for small fracture sizes (6 and 10 m) relative to the λ_S. For the *Normal* model there is no splitting but there is observable distortion for fracture sizes larger 10 m (i.e., $ka \geqslant 3.6$). The $\chi_{Parallel}$ and χ_{Normal} values for the direct shear-waves for the *Parallel* and *Normal* models increased by $ka \approx$

7.2 and then decreased at $ka \approx 17.9$. In other words, the transition occurs when the fracture size a =20 m is comparable to the dominant shear wavelength λ_S in the Mie scattering regime.

The amplitude spectral analysis for the *Parallel* model indicated that the Y-component was attenuated more than the Z-component, which is consistent with the observed difference in dominant frequency of the shear-waves being positive ($f_{d_Z} - f_{d_Y} > 0$). Also, for the *Parallel* model the attenuation of Z-component is greater for the smaller fracture sizes (see Figure 6.31). However, for the Y-component the largest attenuation appeared for the small fracture sizes $a = 6$ and 10 m. Moreover, the medium with larger number of small fractures led to higher attenuation than the model with sparse fractures. For the *Normal* model, the Z-component experienced broader attenuation than the X-component, which is due to the spatial distribution of the randomly generated fracture model realisation.

The gradient of regression line of amplitude spectral ratio over the limited bandwith of 0-200 Hz was positive for the *Parallel* model (ΔQ^{-1}_{Z-Y}) and negative for the *Normal* model (ΔQ^{-1}_{Z-X}). The LASR method was compatible to the result of peak frequency shifting of direct shear-waves, where for the *Normal* models is negative($f_{d_Z} - f_{d_X} < 0$). Stochastically, the result for the *Normal* models would be expected be equal for the X- and Z-components as the result intuitively depend on the fracture geometry in the fracture volume for the consistent source polarisation.

Although the results from this chapter remain inconclusive in terms of using shear-wave scattering phenomena as means of imaging fracture properties, previous works suggest that considering the frequency-dependent response can provide constraint of fracture size and fracture infill (e.g., Chapman et al., 2003; Maultzsch, 2005; Baird et al., 2013). Further work should include performing the analysis in discrete frequency bands as well as a range of different source dominant frequencies.

Chapter 7

Discussion

7.1 Fracture parameter inversion from SWS

Assessing the inversion of SWS measurements for fracture properties using full waveform seismic synthetic using DFM represents a novel contribution. Previous feasibility studies of fracture property inversion have been performed assuming the whole medium in which the ray propagates is an effective fractured medium (Verdon et al., 2009, 2011a). For instance, Verdon et al. (2009) noted that there is a potential pitfall in the inversion for fracture strike and density when using SWS data from only sub-vertical arrivals and that SWS data from a medium with two sets of fractures can only be inverted for one set of fractures. They suggested a wider range of arrivals, including sub-horizontal arrivals, is required to precisely characterise the fractured medium, particularly the anisotropic parameters. However, Verdon et al. (2009, 2011a) did not validate the methodology of using an effective medium approximation with realistic band-limited full waveform

seismic data.

In this thesis, I designed the receiver array and model geometry to yield the most suitable arrivals, specifically sub-horizontal arrivals (see Figure 4.5). Despite this, there is no azimuth coverage between 0° and 40° as well as 140° and 180° since the raypaths do not travel through the fracture volume where SWS would develop. This is due to the single microseismic source implemented at one side, which allows the raypaths to travel through the fracture volume. This may be crucial for the models with double fracture sets, where the number of good SWS results ($\mathbb{Q} \geq 0.75$) falls to approximately half ($\approx 4\%$) in comparison to those models with a single fracture set ($\approx 7\%$). In addition, the number of good SWS is a key factor in the inversion process, and thus I choose a minimum of 5 good SWS, leading to a stable inversion (see Figure 4.9).

The assumption that the whole medium is an effective fractured medium in the inversion algorithm is a significant limitation. Alternative approaches that allow spatial variation in anisotropy and isotropic regimes exist (Abt & Fischer, 2008; Wookey, 2012), but they tend to be underdetermined problems due to requiring significantly more model parameters (Verdon et al., 2009). This may result in the inversion process to be computationally time consuming, as well as requiring a priori assumptions of the medium.

Figure 4.6 shows a histogram of the SWS measurement quality $\mathbb{Q}$ of 6624 SWS measurements. The largest volume of SWS data for both single and double fracture set models are in the category good null ($\approx 4\%$ and 7%, respectively). My results validate the automated approach showing that the approach can be successful in recognising unreliable SWS measurements that typically would require manual inspection. The good category $\mathbb{Q}$ can be shifted to the higher values if the volume of the data is large enough and/or if the S-wave is of very good quality. The method is applicable for the large microseismic data (e.g., Jones, 2010; Wuestefeld et al., 2010).

The separation of $\mathbb{Q}$ into different categories through implementation of the automated approach leads to the detection of null SWS measurements (see Figure 4.6). The null measurements can potentially characterise the anisotropy symmetry system of the probing medium. However, it is necessary to take into consideration that the interpretation of the null data is controversial as the null measurements can be due to the low signal-to-noise ratio or the coincidence of the initial S-wave polarisation with the symmetry plane (see Figure 3.8). Figure 4.7 plots the distribution of $\mathbb{Q}$ against the difference between the initial S-wave polarisation and the fast polarisation direction ϕ in the shear-wave plane (i.e., SV-SH plane). Reliable measurements are found to have 20° separation from the null direction (i.e., 0° and 90°). Furthermore, another cause of null measurements can be due to the medium being isotropic. However, detailed examination of null measurements is beyond the scope of this PhD, as the null measurements are ignored in the inversion approach of Verdon et al. (2009).

Worthington & Lubbe (2007) investigated the relationship between fracture length scale and compliance. Figure 7.1 plots a compilation of laboratory and field estimates of fracture compliance against fracture length scale. A compilation of Z_N/Z_T measurements is reviewed by Verdon & Wüstefeld (2013) in which the majority of measurements are from laboratory studies. The models in this thesis are consistent with the fracture sizes, observed in hydrocarbon reservoirs. There is a lack of upscaled measurements between 10 and 100 m fracture length (Figure 2.6). This study fills the gap of fracture size which has not examined in the literature and is important in the reservoir characterisation. Figure 4.12 shows that the compliances of the models are compatible with the findings of Worthington & Lubbe (2007). Worthington & Lubbe (2007) discussed that the fracture compliances of the laboratory scale are certainly smaller at least one order of magnitude than the fracture compliances of the field scale data. Therefore, for each model parameter I set two different compliances (see Table

4.2). Figure 4.12 indicates that by increasing compliance by one order of magnitude while keeping Z_N/Z_T constant leads to models with good SWS.

The Z_N/Z_T measurement is sensitive to both the fracture fluid infill and the fracture structure itself (Foord et al., 2015). However, in this thesis the examination of fracture infill structure is ignored even though the study of fracture infill is of great interest.

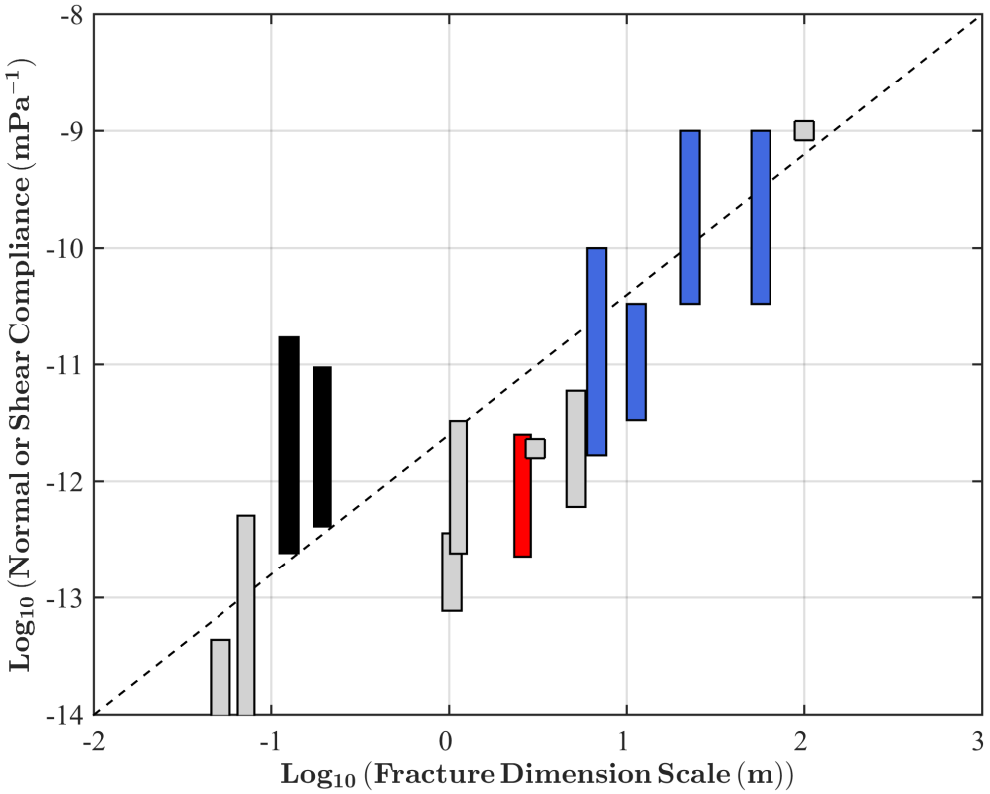

Figure 7.1: Fracture compliance as a function of fracture length scale. Grey is the compilation of laboratory and filed data by Worthington (2008). Black bars are data from Far (2011). Red is data from Verdon & Wüstefeld (2013). Blue represents the data from this study. Figure is modified from Worthington (2008).

7.1.1 Errors in inverted fracture parameters

From Figures 4.14 to 4.20 it can be observed that the inversion algorithm is capable of estimating fracture strike robustly without prior knowledge of the medium fracture

properties. The outliers are likely influenced by the non-linear nature of the inversion algorithm and the fact that the inversion uses only a single event to characterise a finite fracture volume. In contrast, it should be noted that the inverted fracture densities are systematically underestimated from the true value for the single fracture set (i.e., the inversion results clustered between 0.00 and 0.06), while it is systematically overestimated for the double fracture sets for the low compliance ratios (i.e., $Z_N/Z_T = 0.33$ and 0.60). The underestimation of fracture density is addressed by Verdon et al. (2009, 2011b) due to the inversion algorithm assumptions that the whole medium is fractured and also for non-orthogonal fracture sets there is a trade-off between the inverted fracture densities. Also, the problem of non-uniqueness has been observed by Bakulin et al. (2002) for fracture densities of orthogonal fracture sets. Furthermore, for the double fracture set models, the inverted strike is more constrain for the 90° than the 0° (Figures 4.18 and 4.20). This is likely due to the fact that most raypaths with good SWS are sub/parallel to the fracture strike 90°. Moreover, for the double fracture set models the estimation of the orthogonality of fracture sets is 90 ± 30 (Figures 4.21-4.22). This suggests that the inversion method can determine the orthogonality of fracture strike precisely than the absolute fracture strike of each fracture set. However, by increasing Z_N/Z_T the orthogonality of fracture strike is more constrained. This is a potential approach to distinguish between scalar fracture (i.e., $Z_N/Z_T = 1.00$) and fracture fluid infill.

7.2 Quantifying a transition from scattering to anisotropy

I have shown the scale-dependence of seismic anisotropy with new results specific to SWS. I explore the influence of Rayleigh, Mie and geometric scattering on shear-wave propagation through explicit fracture volumes. I find that SWS develops under conditions when the ratio of wavelength to fracture size is greater than 3 (Rayleigh scattering),

where scattering from coherent fractures leads to an effective anisotropy. When the ratio of wavelength to fracture size is between 1 and 3, the scattering regime transitions from Rayleigh to Mie and no effective anisotropy develops. Within the Mie scattering regime the SWS measurements are unstable and of poor quality. When wavelength to fracture size is less than 1, geometric scattering occurs where I have potentially observe behaviour similar to transverse isotropy. In terms of fracture properties, I observe that seismic anisotropy is more sensitive to fracture density than fracture compliance ratio. I observe that the transition from scattering to an effective anisotropic regime occurs over a propagation distance between 1 to 2 wavelengths and as such indicates that the inversion of seismic anisotropy parameters based on EMM will be biased. More importantly, I find that the linear slip effective medium model is inconsistent with my results. I show that the application of the linear slip model to predict fracture properties leads to errors of approximately 400% in fracture spacing (equivalent to fracture density) and 60% in fracture compliance.

It should be noted that numerous studies based on the linear slip EMM representation have yielded reliable estimates fracture orientation and the spatial location of fracture systems. However, my results indicate that the linear slip model will systematically fail in providing quantitatively accurate estimates of physical fracture properties, such as fracture density and compliance. EMM approaches are still valuable, especially in terms of identifying the location and orientation of fracture sets as well as semi-quantitatively estimates of temporal variations in fracture properties, such as compliance ratio. For accurate and robust quantitative estimates of in situ fracture properties, improvements to effective medium models will be required as well as the incorporation of a full waveform inversion techniques that enable capturing the influence of stress state as well as specific fracture properties such as fracture size, filling and compliance.

7.3 Scattering characteristics of shear-waves in fractured media

7.3.1 Envelope broadening

The scattering characteristic of S-wave can be used as an additional attribute (rather than P-wave) to characterise fractured media. In Chapter 6, the different techniques such as envelope broadening, amplitude spectrum and polarisation analysis have been used to evaluate the S-wave scattering characteristics. Fukushima et al. (2003) study the S-wave scattering of rock samples in the lab. However, the study makes no attempts to include a different scale length of discrete fractured medium. Furthermore, their study are limited to the ka smaller than 1.5 which can not explain the transitional behaviour of scattering regimes. Figures 6.17-6.18 display the normalised envelope width $\overline{t_q}$ against ka for the *Parallel* and *Normal* models, respectively. The $ka \approx 1$ for the first 5 stations in the *Parallel* model indicate that for the near offsets (i.e., approximately 3 times the wavelength of the S-wave $\lambda_S \approx 18$ m), the medium behaves as an equivalent homogeneous medium. For stations 6-10 larger coda excitation occurs for the Y-component (i.e, normal to the fracture plane) than the Z-component (i.e., parallel to the fracture plane). For both the *Parallel* and *Normal* models, larger excitation happens for $ka > 3$ which is much larger than the findings of Fukushima et al. (2003) (i.e, in the sample of gabbro rock $ka \approx 1.4$ and in the granite rock $ka \approx 0.4$). However, the largest $\overline{t_q}$ occurs for the *Normal* models as shown in Figure 6.19 and suggests that in the *Normal* models the wavefronts interact to a much larger extent with fracture surfaces and so undergo much greater edge and tip diffractions. This is compatible with the results of Fukushima et al. (2003) for their rock samples. Moreover, Figure 6.19 indicates that in general larger excitation happens for $ka \approx 7.2$ instead of 17.9. Willis et al. (2006)

introduce a techniques of scattering index SI for the detection of the fracture strike and spacing for the range of the random discrete fracture models (10 m, 25 m, 35 m, 50 m and 100 m) in which the maximum SI happens for fracture length size $a = 35$ m, where the fracture size is 0.35 times the P-wavelength ($\lambda_P = 100$ m) and 0.6 times the S-wavelength ($\lambda_S = 58$ m). Moreover, the large $\overline{t_q}$ for $ka > 5$ in Figure 6.19 is consistent with the theoretical findings of the Neerhoff & Van der Hijden (1984) and Van Der Hijden & Neerhoff (1984), where they investigate the scattering characteristics of S-waves due to planar crack of finite length having $ka \geqslant 3$. This is consistent for the *Normal* model, where the back-angle scattering results in large envelope broadening for the $ka > 5$.

Coda wave excitation is addressed in field observations for a frequency range of 2-30 Hz (Fukushima et al., 2003), where the scattering observations are due to the forward modelling ($ka \geqslant 10$) as the wavelength is much smaller than the characteristic length of heterogeneity of the media (Sato et al., 2012; Fehler et al., 2000; Sato, 1989). However, the results in this thesis show that envelope broadening happens for $ka < 5$. This seems to be due to the large angle scattering rather than the multiple forward scattering when the scale of the crack size is smaller or comparable to the wavelength.

7.3.2 Distortion of shear-wave polarisation

The distortion of shear-wave particle motion for the *Parallel* models show typical behaviour of shear-wave splitting for fracture sizes $a = 6$ m and 10 m as shown in Figures 6.20-6.21, whereas for the larger fracture sizes (i.e., $a = 20$ m and 50 m) the shear-wave particle motions display more random behaviour (see Figures 6.22-6.23). However, for the *Normal* models, as the wave is normal to the fracture plane, there is no development of shear-wave splitting. For the *Normal* model, the waveform envelop increases and the shear-wave polarisation remains relatively unaffected for

$ka \leqslant 3$ (see Figure 6.24). However, for $ka > 3$, a significant deviation from linearity happens, essentially as a result of reverberations due to the specular reflections from the interaction of the spherical wavefronts and the fracture surfaces (i.e, string coherent scattering).

The distortion of shear-wave polarisation in the *Parallel* $\chi_{Parallel}$ and *Normal* models χ_{Normal} (see Figures 6.25-6.26) is noticeable for $ka > 3$ (i.e. for $ka = 3.6$, 7.2 and 17.9). The high $\chi_{Parallel}$ is consistent with the broadening envelope and indicates large scattering when $ka > 3$. The largest $\chi_{Parallel}$ values for the station outside the fracture zone (stations 11-15) happens at $ka = 7.2$ which is in the Mie scattering regime. For the *Normal* models by increasing ka from 7.2 to 17.9 the shear-wave distortion χ_{Normal} decreases and then increases between stations 2 and 3, while $\overline{t_q}$ shows an increase and then decrease (see Figure 6.19). This may be due to the random distribution of the fractures, specifically at $ka = 7.2$ in Mie scattering regime.

7.4 Differential attenuation analysis

7.4.1 Amplitude spectrum

The amplitude spectrum for the Y-component is more attenuated at higher frequencies than the Z-component for the *Parallel* models. This is expected as the Y-component is polarised normal to the fracture planes whereas the Z-component is polarised parallel to the fracture planes. Attenuation increases and thereby the frequency content decreases by increasing the source-receiver distance in the fracture zone for all *Parallel* models (see Figures 6.27-6.30). For the Z-component attenuation is increased with decreasing fracture size (Figure 6.31); however, for the Y-component the largest attenuation happenes for fracture sizes $a = 10$ m and 20 m. The findings of attenuation analysis indicate that the large number of small fractures lead to larger wave attenuation than a

small number of larger fractures. Furthermore, the medium with small fracture size acts as a low pass filter which is consistent with the results of amplitude spectral analyses for P-waves by Al-Rajhi (2012).

In contrast, for the *Normal* models, the amplitude spectrum for the Z-component is more attenuated than the Y-component, which I would expect to be equal as both wave components propagate normal to the fracture surface. The most likely explanation is due to the random distribution of the fractures. Moreover, the attenuation is larger and thereby the dominant frequency is shifted more to the lower frequencies with increasing fracture size. The most attenuation occurs in the forward scattering regime, where the wavefront interacts in a reverberation pattern with the fractures.

7.4.2 Amplitude spectral ratio

I perform an analysis of the amplitude spectral ratio for the pair of shear-waves in the ray frame for both the *Parallel* and the *Normal* models based on the assumption that the intrinsic attenuation Q^{-1} is constant between the source and receivers (see Figures 6.33-6.37). The amplitude spectral method is based on the linear regression of $\log_e$ amplitude spectral ratio (LASR). However, the LASR measurements are limited to where the regression lines are linear over the limited range of 20-180 Hz. I exclude the analyses beyond this frequency range as the LASRs are non-linear. The non-linearity of the LASRs is likely due to the scattering of some frequencies which can lead to the highly inaccurate results.

The differential attenuation measurements for the *Parallel* models ΔQ^{-1}_{Z-Y} are positive, and as such it is not possible to strictly say whether the Y-component or the Z-component is more attenuated. The results of amplitude spectral analysis indicate that the Y-component, (i.e., slow shear-wave S_2) is attenuated more than the Z-component (i.e., fast shear S_1 component). However, Carter & Kendall (2006) point out that

sometimes the S_1 component can be poorer in high frequency than the S_2, which is contrary to the attenuation anisotropy predicted by the effective medium models of Hudson (1981) for the elastic moduli.

The differential attenuation measurements for the *Normal* models ΔQ^{-1}_{Z-X} are almost all negative, which implies that $Q^{-1}_Z > Q^{-1}_X$. However, there are a few regression lines which are horizontal. This is implies that the attenuation of the X- and Z-components are identical and is expected due to the focusing and defocusing of discrete frequency bands.

Chapter 8

Conclusions and recommendations

8.1 Conclusions

8.1.1 Seismic imaging of fractured media

Imaging and characterising fractures based on inverting microseismic SWS measurements is a relatively new method in the field of petroleum production. Thus, in Chapter 4 I studied the robustness of inverting SWS measurements from a suite of synthetic microseismic data from fractured media with known fracture parameters. The synthetic fractured media are simulated for a single fracture set and a more complicated double fracture set. By using a 3D FD algorithm I simulate the propagation of shear wave in the fractured media based on an appropriate geometry of source and receivers in order to acquire numerous high $\mathbb{Q}$ SWS measurements which are used in the fracture inversion process. There are five important findings: (1) based on the results of the full waveform

FD synthetics the dominant frequency of the microseismicity is crucial in extracting reliable fracture parameters due to the relationship between the scale length of the probing seismic wave and the fracture size; (2) the automated SWS approach is capable of detecting unreliable SWS measurements; (3) increasing fracture density leads to a greater number of the models with good SWS, particularly for small fractures; (4) by increasing normal and tangential compliances by one order of magnitude while keeping Z_N/Z_T constant leads to models with good SWS, except for models with fracture size $a = 50$ m and $Z_N/Z_T \leqslant 0.60$ (see Figure 4.12); and (5) the inversion for fracture strike is more constrained than fracture density as the average errors for the fracture strike are between 11° and 25°, whereas for density the average errors are between 65% and 80% for the single fracture set and 30% and 90% for the double fracture sets. In summary, it is possible to image discrete fractures feasibly based upon some conditions: wide azimuthal and large inclination coverage of high quality SWS measurements.

8.1.2 Quantifying a transition from scattering to anisotropy

I have shown the scale-dependence of seismic anisotropy with new results specific to SWS. I explored the influence of Rayleigh, Mie and geometric scattering on shear-wave propagation through explicit fracture volumes. I found that SWS develops under conditions when the ratio of wavelength to fracture size is greater than 3 (Rayleigh scattering), where scattering from coherent fractures leads to an effective anisotropy. When the ratio of wavelength to fracture size is between 1 and 3, the scattering regime transitions from Rayleigh to Mie scattering and no effective anisotropy develops. Within the Mie scattering regime the SWS measurements are unstable and of poor quality. When the wavelength to fracture size is less than 1, geometric scattering occurs and I potentially observed behaviour similar to transverse isotropy. In terms of fracture properties, I observed that seismic anisotropy is more sensitive to fracture density than

fracture compliance ratio. I observed that the transition from scattering to an effective anisotropic regime occurs over a propagation distance between 1 to 2 wavelengths and as such indicates that the inversion of seismic anisotropy parameters based on EMM will be biased. More importantly, I found that the linear slip effective medium model is inconsistent with my results. I showed that the application of the linear slip model to predict fracture properties leads to errors of approximately 400% in fracture spacing (equivalent to fracture density) and 60% in fracture compliance.

It should be noted that numerous studies based on the linear slip EMM representation have yielded reliable estimates fracture orientation and the spatial location of fracture systems. However, my results indicate that the linear slip model will systematically fail in providing quantitatively accurate estimates of physical fracture properties, such as fracture density and compliance. EMM approaches are still valuable, especially in terms of identifying the location and orientation of fracture sets as well as semi-quantitatively estimates of temporal variations in fracture properties, such as compliance ratio. For accurate and robust quantitative estimates of in situ fracture properties, improvements to effective medium models will be required as well as the incorporation of a full waveform inversion technique that enable capturing the influence of stress state as well as specific fracture properties such as fracture size, filling and compliance.

8.1.3 Scattering characterisation of shear-wave in fractured media

I examined the widening effect of wavelets due to scattering within a fractured medium by using several different approaches. The examination was performed by implementing numerical modelling of wave propagation in discrete fracture models with a desired fracture density and for various fracture sizes. I used different methods including the RMS envelope analysis, shear-wave polarisation distortion, differential attenuation analysis and peak frequency shifting to assess the scattering behaviour of those parametrised

models in which the propagation direction is either normal or parallel to the fracture surfaces. The quantitative measurements showed strong observable deviations for fracture sizes of the order of or greater than the dominant seismic wavelength within the Mie and geometric scattering regime for both propagation normal and parallel to fracture strike. In other words, this occurs when the ka exceeds 5 for both the *Parallel* and the *Normal* models. The results suggest that strong scattering is symptomatic of fractures having size on the same order of the probing seismic wave. Furthermore, the distortion of the shear-wave polarisation happens when ka exceeds 3 for both the *Parallel* and the *Normal* models.

Two different source polarisations and two different source-receiver orientations were used to study propagation normal and parallel to the fracture surface. The results indicated that scattering is notable for the *Normal* models where shear-wave propagates perpendicular to the aligned fracture surface.

The amplitude spectrum analysis for the *Parallel* models reveals that by increasing the fracture size both the fast and slow shear-waves are less attenuated, whereas this is contrary to the *Normal* models. The results also indicate that the slow shear-wave attenuation undergoes higher attenuation than the fast shear-wave for the *Normal* models.

The amplitude spectral ratio, based on the calculation of the gradient of regression line over limited frequency bandwith, was performed for both models. It was concluded that the differential attenuation in both models are consistent with their relative difference in the peak/dominant frequency.

8.2 Recommendations for future study

In this PhD research, a parametrisation study was performed through modelling numerous fractured media with different fracture parameters. This led to an examination of the

capability of a fracture inversion approach by placing quantitative constraints on fracture strike and fracture density. The 3D FD algorithm WAVE is limited to orthogonal planar fractures limited to the three primary axes and thus greater efforts are required to develop the algorithm to incorporate different fracture shapes and orientations. Moreover, it would be useful to assess the effects of different random spatial distributions of fractures, such as Gaussian distribution, exponential distribution and Gamma distribution (Vlastos et al., 2003) in the study of seismic fractured characterisation.

There are some inaccuracies in terms of inverted fracture strike and fracture density. For instance, there is high uncertainty in fracture density inversion. Thus improvements are needed in the inversion approach. It is suggested that incorporating more micro-seismic events around the receivers and fracture volume as well as implementing more advanced inversion approach. Anisotropic tomography allows the medium to be divided into different domains, where each domain has different anisotropic characteristics (e.g., Wookey, 2012). Although anisotropic tomography is computationally intensive, it would be expected to yield more precise and accurate results.

In this study the null SWS measurements have been excluded, whereas these measurements can be used to reveal more information about the medium background and also where the raypaths are normal to the fracture surfaces. However, such data must filter out any null data due to high signal noise. Therefore, using null measurements in anisotropic tomography can constrain the inversion parameters.

The study in chapter 5 shows that the findings are more sensitive to the fracture density than the compliance ratio. Thus it would be interesting to examine the study of scattering shear-wave for the models with broad value of fracture density and also for different fracture compliance ratio. Although the application of the linear slip model in quantitative estimates could be accurate if further data are available to calibrate the EMM results to in situ properties, improvements could be made to the model to

incorporate realistic scattering effects.

Bibliography

Abt, D. L., & Fischer, K. M. (2008). Resolving three-dimensional anisotropic structure with shear wave splitting tomography. *Geophysical Journal International*, *173*(3), 859–886.

Aguilera, R. (1998). Geologic aspects of naturally fractured reservoirs. *The Leading Edge*, *17*(12), 1667–1670.

Aki, K. (1969). Analysis of the seismic coda of local earthquakes as scattered waves. *Journal of geophysical research*, *74*(2), 615–631.

Aki, K. (1988). *Scattering and attenuation of seismic waves, Part 1*. Springer.

Aki, K., & Richards, P. (1980). *Quantitative seismology*, vol. 1424. Freeman San Francisco.

Aki, K., & Richards, P. G. (2002). *Quantitative Seismology, 2nd Ed.*. University Science Books.

Al-Anboori, A. S. (2005). *Anisotropy, focal mechanisms, and state of stress in an oilfield: Passive seismic monitoring in Oman*. Ph.D. thesis, University of Leeds.

Al-Harrasi, O., Al-Anboori, A., Wüstefeld, A., & Kendall, J. M. (2011). Seismic anisotropy in a hydrocarbon field estimated from microseismic data. *Geophysical Prospecting*, *59*(2), 227–243.

Al-Harrasi, O. H. (2010). *Fractured reservoir characterisation using shear-wave splitting in microseismic data: A case study form Oman*. Ph.D. thesis, University of Bristol.

Al-Rajhi, M. (2012). *studied the petrophysical and seismic characteristics of tight-gas reservoirs and is currently at Petroleum Development Oman*. Thesis, Leeds University.

Ando, M., & Ishikawa, Y. (1980). S-wave anisotropy in the upper mantle under a volcanic area in japan. *Nature*, *286*, 43–46.

Angus, D., Dutko, M., Kristiansen, T., Fisher, Q., Kendall, J.-M., Baird, A., Verdon, J., Barkved, O., Yu, J., & Zhao, S. (2015). Integrated hydro-mechanical and seismic modelling of the valhall reservoir: a case study of predicting subsidence, avoa and microseismicity. *Geomechanics for Energy and the Environment*, *2*, 32–44.

Angus, D. A., Fisher, Q. J., & verdon, J. P. (2012). Exploring trends in microcrack properties of sedimentary rocks: An audit of dry and water saturated sandstone core velocity-stress measurements. *International Journal of Geosciences*, *3*(4), 822–833.

Angus, D. A., Thomson, C. J., & Pratt, R. G. (2004). A one-way wave equation for modelling variations in seismic waveforms due to elastic anisotropy. *Geophysical Journal International*, *156*(3), 595–614.

Angus, D. A., Verdon, J. P., Fisher, Q. J., & Kendall, J.-M. (2009). Exploring trends in microcrack properties of sedimentary rocks: An audit of dry-core velocity-stress measurements. *Geophysics*, *74*(5), E193–E203.

Arne Johansen, T., Ole Ruud, B., & Jakobsen, M. (2004). Effect of grain scale alignment on seismic anisotropy and reflectivity of shales. *Geophysical Prospecting*, *52*(2), 133–149.

Aster, R. C., Shearer, P. M., & Berger, J. (1990). Quantitative measurements of shear wave polarizations at the anza seismic network, southern california: Implications for shear wave splitting and earthquake prediction. *Journal of Geophysical Research: Solid Earth*, *95*(B8), 12449–12473.

Babuska, V., & Cara, M. (1991). *Seismic anisotropy in the Earth*, vol. 10. Springer Science & Business Media.

Backus, G. E. (1962). Long-wave elastic anisotropy produced by horizontal layering. *Journal of Geophysical Research*, *67*(11), 4427–4440.

Baird, A., Verdon, J., Kendall, J., Foord, G., Stork, A., & Usher, P. (2014). Field estimates of fracture compliances using active & passive seismics. In *Fifth EAGE Passive Seismic Workshop*.

Baird, A. F., Kendall, J.-M., & Angus, D. A. (2013). Frequency-dependent seismic anisotropy due to fractures: Fluid flow versus scattering. *Geophysics*, *78*(2), WA111–WA122.

Bakulin, A., Grechka, V., & Tsvankin, I. (2000). Estimation of fracture parameters from reflection seismic data-part ii: Fractured models with orthorhombic symmetry. *Geophysics*, *65*(6), 1803–1817.

Bakulin, A., Grechka, V., & Tsvankin, I. (2002). Seismic inversion for the parameters of two orthogonal fracture sets in a vti background medium. *Geophysics*, *67*(1), 292–299.

Barnes, A. E. (1993). Instantaneous spectral bandwidth and dominant frequency with applications to seismic reflection data. *Geophysics*, *58*(3), 419–428.

Barton, N. (2007). *Rock quality, seismic velocity, attenuation and anisotropy*. CRC press.

Båth, B. (1974). *Spectral analysis in geophysics*. Amsterdam: Elsevier.

Booth, D. C., & Crampin, S. (1985b). Shear-wave polarizations on a curved wavefront at an isotropic free surface. *Geophysical Journal International*, *83*(1), 31–45.

Booth, D. C., Crampin, S., Evans, R., & Roberts, G. (1985a). Shear-wave polarizations near the north anatolian fault–i. evidence for anisotropy-induced shear-wave splitting. *Geophysical Journal International*, *83*(1), 61–73.

Borgos, H. G., Cowie, P. A., & Dawers, N. H. (2000). Practicalities of extrapolating one-dimensional fault and fracture size-frequency distributions to higher-dimensional samples. *Journal of Geophysical Research: Solid Earth*, *105*(B12), 28377–28391.

Bratton, T., Canh, D. V., Van Que, N., Duc, N. V., Gillespie, P., Hunt, D., Li, B., Marcinew, R., Ray, S., Montaron, B., et al. (2006). The nature of naturally fractured reservoirs. *Oilfield Review*, *18*(2), 4–23.

Brown, R. J., & Korringa, J. (1975). On the dependence of the elastic properties of a porous rock on the compressibility of the pore fluid. *Geophysics*, *40*(4), 608–616.

Buchbinder, G. G. (1985). Shear-wave splitting and anisotropy in the charlevoix seismic zone, quebec. *Geophysical Research Letters*, *12*(7), 425–428.

Carcione, J. M., Herman, G. C., & Ten Kroode, A. (2002). Seismic modeling. *Geophysics*, *67*(4), 1304–1325.

Carter, A. J., & Kendall, J. M. (2006). Attenuation anisotropy and the relative frequency content of split shear waves. *Geophysical Journal International*, *165*(3), 865–874.

Chapman, C. t., & Pratt, R. (1992). Traveltime tomography in anisotropic media-II. theory. *Geophysical Journal International*, *109*(1), 1–19.

Chapman, M., Maultzsch, S., Liu, E., & Li, X.-Y. (2003). The effect of fluid saturation in an anisotropic multi-scale equant porosity model. *Journal of Applied Geophysics*, *54*(3), 191–202.

Cheng, C. (1993). Crack models for a transversely isotropic medium. *Journal of Geophysical Research: Solid Earth*, *98*(B1), 675–684.

Chevrot, S. (2000). Multichannel analysis of shear wave splitting. *Journal of Geophysical Research: Solid Earth*, *105*(B9), 21579–21590.

Chichinina, T., Obolentseva, I., Dugarov, G., et al. (2015). Effective-medium anisotropic models of fractured rocks of ti symmetry: analysis of constraints and limitations in linear slip model. In *2015 SEG Annual Meeting*. Society of Exploration Geophysicists.

Chichinina, T., Sabinin, V., & Ronquillo-Jarillo, G. (2006). Qvoa analysis: P-wave attenuation anisotropy for fracture characterization. *Geophysics*, *71*(3), C37–C48.

Choi, M.-K., Bobet, A., & Pyrak-Nolte, L. J. (2014). The effect of surface roughness and mixed-mode loading on the stiffness ratio κ_x/κ_z for fractures. *Geophysics*, *79*(5), D319–D331.

Coates, R. T., & Schoenberg, M. (1995). Finite-difference modeling of faults and fractures. *Geophysics*, *60*(5), 1514–1526.

Crampin, S. (1978). Seismic-wave propagation through a cracked solid: polarization as a possible dilatancy diagnostic. *Geophysical Journal International*, *53*(3), 467–496.

Crampin, S. (1981). A review of wave motion in anisotropic and cracked elastic-media. *Wave motion*, *3*(4), 343–391.

Crampin, S. (1984). An introduction to wave propagation in anisotropic media. *Geophysical Journal International*, *76*(1), 17–28.

Crampin, S. (1994). The fracture criticality of crustal rocks. *Geophysical Journal International*, *118*(2), 428–438.

Crampin, S., Evans, R., Üçer, B., Doyle, M., Davis, J. P., Yegorkina, G. V., & Miller, A. (1980). Observations of dilatancy-induced polarization anomalies and earthquake prediction. *Nature*, *286*(5776), 874–877.

Crampin, S., & Peacock, S. (2005). A review of shear-wave splitting in the compliant crack-critical anisotropic earth. *Wave motion*, *41*(1), 59–77.

Crampin, S., & Zatsepin, S. V. (1997). Modelling the compliance of crustal rock-II. response to temporal changes before earthquakes. *Geophysical Journal International*, *129*(3), 495–506.

Crampin, S., et al. (1983). Shear wave polarizations: A plea for three-component recording. In *1983 SEG Annual Meeting*. Society of Exploration Geophysicists.

Daehnke, A., Rossmanith, H., & Knasmillner, R. (1996). Using dynamic photoelasticity to evaluate the influence of parting planes on stress waves interacting with stopes. *International journal for numerical and analytical methods in geomechanics*, *20*(2), 101–117.

Dershowitz, W., La Pointe, P., Doe, T., et al. (2004). Advances in discrete fracture network modeling. In *Proceedings of the US EPA/NGWA fractured rock conference, Portland*, (pp. 882–894).

Dricker, I., Vinnik, L., Roecker, S., & Makeyeva, L. (1999). Upper-mantle flow in eastern europe. *Geophysical research letters*, *26*(9), 1219–1222.

Ebrom, D., Tatham, R. H., Sekharan, K., McDonald, J., Gardner, G., et al. (1990). Dispersion and anisotropy in laminated versus fractured media: An experimental comparison. In *1990 SEG Annual Meeting*. Society of Exploration Geophysicists.

Emerman, S. H., Schmidt, W., & Stephen, R. (1982). An implicit finite-difference formulation of the elastic wave equation. *Geophysics*, *47*(11), 1521–1526.

Engelder, T., Lash, G. G., & Uzctegui, R. S. (2009). Joint sets that enhance production from middle and upper devonian gas shales of the appalachian basin. *AAPG bulletin*, *93*(7), 857–889.

Far, M. E. (2011). *Seismic Characterization of Naturally Fractured Reservoirs*. Ph.D. thesis, UNIVERSITY OF HOUSTON.

Far, M. E., & Hardage, B. (2016). Fracture characterization using converted waves. *Geophysical Prospecting*, *64*(2), 287–298.

Fehler, M., Sato, H., & Huang, L.-J. (2000). Envelope broadening of outgoing waves in 2d random media: a comparison between the markov approximation and numerical simulations. *Bulletin of the Seismological Society of America*, *90*(4), 914–928.

Foord, G., Verdon, J. P., & Kendall, J.-M. (2015). Seismic characterization of fracture compliance in the field using p-and s-wave sources. *Geophysical Journal International*, *203*(3), 1726–1737.

Fornberg, B. (1998). *A practical guide to pseudospectral methods*, vol. 1. Cambridge university press.

Fossen, H. (2010). *Structural geology*. Cambridge University Press.

Frankel, A., & Clayton, R. W. (1986). Finite difference simulations of seismic scattering: implications for the propagation of short-period seismic waves in the crust and models of crustal heterogeneity. *Journal of Geophysical Research B*, *91*(B6), 6465–6489.

Fukao, Y. (1984). Evidence from core-reflected shear waves for anisotropy in the earth's mantle. *Nature*, *309*, 695–698.

Fukushima, Y., Nishizawa, O., Sato, H., & Ohtake, M. (2003). Laboratory study on scattering characteristics of shear waves in rock samples. *Bulletin of the seismological Society of America*, *93*(1), 253–263.

Galvin, R. J., & Gurevich, B. (2015). Frequency-dependent anisotropy of porous rocks with aligned fractures. *Geophysical Prospecting*, *63*(1), 141–150.

Garbin, H., & Knopoff, L. (1973). The compressional modulus of a material permeated by a random distribution of circular cracks. *Quarterly of Applied Mathematics*, *30*(4), 453–464.

Gilbert, F. (1971). Excitation of the normal modes of the earth by earthquake sources. *Geophysical Journal International*, *22*(2), 223–226.

Gilbert, F. (1973). Derivation of source parameters from low-frequency spectra. *Philosophical Transactions of the Royal Society of London. Series A, Mathematical and Physical Sciences*, *274*(1239), 369–371.

Grandi Karam, S. (2008). *Multiscale determination of in situ stress and fracture properties in reservoirs*. Ph.D. thesis, Massachusetts Institute of Technology.

Graves, R. W. (1996). Simulating seismic wave propagation in 3d elastic media using staggered-grid finite differences. *Bulletin of the Seismological Society of America*, *86*(4), 1091–1106.

Grechka, V., & Tsvankin, I. (2003). Feasibility of seismic characterization of multiple fracture sets. *Geophysics*, *68*(4), 1399–1407.

Groenenboom, J., & Falk, J. (2000). Scattering by hydraulic fractures: Finite-difference modeling and laboratory data. *Geophysics*, *65*(2), 612–622.

Guest, W., & Kendall, J. (1993). Modelling seismic waveforms in anisotropic inhomogeneous media using ray and maslov asymptotic theory: applications to exploration seismology. *Canadian Journal of Exploration Geophysics*, *29*(1), 78–92.

Hall, S. A., & Kendall, J.-M. (2000). Constraining the interpretation of avoa for fracture characterisation. *Anisotropy 2000: Fractures, converted waves, and case studies*, (pp. 107–144).

Hall, S. A., Kendall, J.-M., Maddock, J., & Fisher, Q. (2008). Crack density tensor inversion for analysis of changes in rock frame architecture. *Geophysical Journal International*, *173*(2), 577–592.

Han, D.-h., Nur, A., & Morgan, D. (1986). Effects of porosity and clay content on wave velocities in sandstones. *Geophysics*, *51*(11), 2093–2107.

Hardin, E., Cheng, C., Paillet, F., & Mendelson, J. (1987). Fracture characterization by means of attenuation and generation of tube waves in fractured crystalline rock at mirror lake, new hampshire. *Journal of Geophysical Research: Solid Earth (19782012)*, *92*(B8), 7989–8006.

Herrmann, R. B. (1975). A students guide to the use of p and s wave data for focal mechanism determination. *Seismological Research Letters*, *46*(4), 29–39.

Hess, H. (1964). Seismic anisotropy of the uppermost mantle under oceans. *Nature*, *203*, 629–631.

Hildyard, M. (2007). Manuel rocha medal recipient wave interaction with underground openings in fractured rock. *Rock Mechanics and Rock Engineering*, *40*(6), 531–561.

Hildyard, M., & Young, R. (2002). Modelling seismic waves around underground openings in fractured rock. *Pure & Applied Geophysics*, *159*(1-3), 247.

Hildyard, M. W. (2001). *Wave interaction with underground openings in fractured rock*. Thesis, University of Liverpool.

Hildyard, M. W., Daehnke, A., & Cundall, P. A. (1995). Wave: A computer program for investigating elastodynamic issues in mining. *Rock Mechanics - Proceedings of the 35th U.S. Symposium*, (pp. 519–524).

Hobday, C., & Worthington, M. (2012). Field measurements of normal and shear fracture compliance. *Geophysical Prospecting*, *60*(3), 488–499.

Honda, H. (1962). Earthquake mechanism and seismic waves. *Journal of Physics of the Earth*, *10*(2), 1–97.

Hood, J. A. (1991). A simple method for decomposing fracture-induced anisotropy. *Geophysics*, *56*(8), 1275–1279.

Hornby, B. E., Schwartz, L. M., & Hudson, J. A. (1994). Anisotropic effective-medium modeling of the elastic properties of shales. *Geophysics*, *59*(10), 1570–1583.

Horne, S., & MacBeth, C. (1994). Inversion for seismic anisotropy using genetic algorithms1. *Geophysical prospecting*, *42*(8), 953–974.

Hoshiba, M. (2000). Large fluctuation of wave amplitude produced by small fluctuation of velocity structure. *Physics of the earth and planetary interiors*, *120*(3), 201–217.

Hou, S. (2014). *Seismic imaging and inversion in the presence of fracture-induced anisotropy*. Ph.D. thesis, University of Edinburgh.

Hsu, C.-J., & Schoenberg, M. (1993). Elastic waves through a simulated fractured medium. *Geophysics*, *58*(7), 964–977.

Hudson, J. (1980). Overall properties of a cracked solid. In *Mathematical Proceedings of the Cambridge Philosophical Society*, vol. 88, (pp. 371–384). Cambridge Univ Press.

Hudson, J., Liu, E., & Crampin, S. (1996). The mechanical properties of materials with interconnected cracks and pores. *Geophysical Journal International*, *124*(1), 105–112.

Hudson, J. A. (1981). Wave speeds and attenuation of elastic-waves in material containing cracks. *Geophysical Journal of the Royal Astronomical Society*, *64*(1), 133–150.

Hudson, J. A., & Liu, E. (1999). Effective elastic properties of heavily faulted structures. *Geophysics*, *64*(2), 479–485.

Hudson, J. A., Pointer, T., & Liu, E. (2001). Effective-medium theories for fluid-saturated materials with aligned cracks. *Geophysical Prospecting*, *49*(5), 509–522.

Johnston, J., & Christensen, N. (1993). Compressional to shear velocity ratios in sedimentary rocks. *International journal of rock mechanics and mining sciences*, *30*, 751–754.

Jones, I. F. (2010). *An introduction to: Velocity model building*. Eage Publications.

Jost, M. u., & Herrmann, R. (1989). A students guide to and review of moment tensors. *Seismological Research Letters*, *60*(2), 37–57.

Kachanov, M. (1992). On continuum characterization of crack arrays and its limits. In *Recent advances in damage mechanics and plasticity*, vol. 132, (pp. 103–113).

Kanamori, H., & Given, J. W. (1981). Use of long-period surface waves for rapid determination of earthquake-source parameters. *Physics of the Earth and Planetary interiors*, *27*(1), 8–31.

Kanamori, H., & Given, J. W. (1982). Use of long-period surface waves for rapid determination of earthquake source parameters 2. preliminary determination of source mechanisms of large earthquakes (ms$\geq$6.5) in 1980. *Physics of the Earth and Planetary Interiors*, *30*(2-3), 260–268.

Kelly, K., Ward, R., Treitel, S., & Alford, R. (1976). Synthetic seismograms: a finite-difference approach. *Geophysics*, *41*(1), 2–27.

Kendall, J.-M., Fisher, Q., Crump, S. C., Maddock, J., Carter, A., Hall, S., Wookey, J., Valcke, S., Casey, M., & Lloyd, G. (2007). Seismic anisotropy as an indicator of reservoir quality in siliciclastic rocks. *Geological Society, London, Special Publications*, *292*(1), 123–136.

Kendall, J.-M., & Silver, P. (1998). Investigating causes of d ?anistropy. *The core-mantle boundary region*, (pp. 97–118).

Kendall, R. R., & Kendall, J.-M. (1996). Shear-wave amplitude anomalies in south-central wyoming. *The Leading Edge*, *15*(8), 913–920.

King, M., Myer, L., & Rezowalli, J. (1986). Experimental studies of elastic-wave propagation in a columnar-jointed rock mass. *Geophysical prospecting*, *34*(8), 1185–1199.

Klem-Musatov, K. D. (2008). *Edge and tip diffractions: Theory and applications in seismic prospecting*, vol. 14. SEG Books.

Knopoff, L., & Randall, M. J. (1970). The compensated linear-vector dipole: A possible mechanism for deep earthquakes. *Journal of Geophysical Research*, *75*(26), 4957–4963.

Kosloff, D. D., & Baysal, E. (1982). Forward modeling by a fourier method. *Geophysics*, *47*(10), 1402–1412.

Lay, T., Williams, Q., & Garnero, E. J. (1998). The core–mantle boundary layer and deep earth dynamics. *Nature*, *392*(6675), 461–468.

Leary, P., & Abercrombie, R. (1994). Frequency dependent crustal scattering and absorption at 5–160 hz from coda decay observed at 2.5 km depth. *Geophysical Research Letters*, *21*(11), 971–974.

Liu, E., Crampin, S., & Hudson, J. (1997). Diffraction of seismic waves by cracks with application to hydraulic fracturing. *Geophysics*, *62*(1), 253–265.

Liu, E., & Martinez, A. (2012). *Seismic fracture characterization: Concepts and practical applications*. EAGE Publication.

Liu, E., Queen, J., Li, X., Chapman, M., Maultzsch, S., Lynn, H., & Chesnokov, E. (2003). Observation and analysis of frequency-dependent anisotropy from a multicomponent vsp at bluebell-altamont field, utah. *Journal of Applied Geophysics*, *54*(3), 319–333.

Liu, E. R., Hudson, J. A., & Pointer, T. (2000). Equivalent medium representation of fractured rock. *Journal of Geophysical Research-Solid Earth*, *105*(B2), 2981–3000.

Liu, K. H., & Gao, S. S. (2013). Making reliable shear-wave splitting measurements. *Bulletin of the Seismological Society of America*, *103*(5).

Long, M. D., & van der Hilst, R. D. (2006). Shear wave splitting from local events beneath the ryukyu arc: trench-parallel anisotropy in the mantle wedge. *Physics of the earth and planetary interiors*, *155*(3), 300–312.

Lubbe, R. (2005). A field and laboratory investigation of the compliance of fractured rock. *DPhil thesis*, *Oxford University*.

Lubbe, R., Sothcott, J., Worthington, M. H., & McCann, C. (2008). Laboratory estimates of normal and shear fracture compliance. *Geophysical Prospecting*, *56*(2), 239–247.

Lubbe, R., & Worthington, M. H. (2006). A field investigation of fracture compliance. *Geophysical Prospecting*, *54*(3), 319–331.

Lynn, H. B. (2004). The winds of change. *The Leading Edge*, *23*(12), 1258–1268.

Lynn, H. B., Cox, D., et al. (2003). P-wave avoa interpretation needs the input of additional information. In *2003 SEG Annual Meeting*. Society of Exploration Geophysicists.

Lynn, H. B., Simon, K. M., & Bates, C. R. (1996). Correlation between p-wave avoa and s-wave traveltime anisotropy in a naturally fractured gas reservoir. *The Leading Edge*, *15*(8), 931–935.

Lynn, H. B., Simon, K. M., Bates, C. R., Layman, M., Schneider, R., & Jones, M. (1995). Use of anisotropy in p-wave and s-wave data for fracture characterization in a naturally fractured gas reservoir. *The Leading Edge*, *14*(8), 887–893.

Lysmer, J., & Drake, L. A. (1972). A finite element method for seismology. *Methods of computational physics*, *11*, 181–216.

MacBeth, C. (1991). Inverting shear-wave polarizations for anisotropy using three-component offset vsps: synthetic seismograms. *Geophysical journal international*, *107*(3), 571–583.

MacBeth, C. (1999). Azimuthal variation in p-wave signatures due to fluid flow. *Geophysics*, *64*(4), 1181–1192.

MacBeth, C., & Schuett, H. (2007). The stress dependent elastic properties of thermally induced microfractures in aeolian rotliegend sandstone. *Geophysical Prospecting*, *55*(3), 323–332.

Madariaga, R. (1976). Dynamics of an expanding circular fault. *Bulletin of the Seismological Society of America*, *66*(3), 639–666.

Mal, A. K. (1970). Interaction of elastic waves with a griffith crack. *International Journal of Engineering Science*, *8*(9), 763–776.

Margerin, L. (2011). Seismic waves, scattering. In H. Gupta (Ed.) *Encyclopedia of Solid Earth Geophysics*. Springer.

Marion, D., Mukerji, T., & Mavko, G. (1994). Scale effects on velocity dispersion: From ray to effective medium theories in stratified media. *Geophysics*, *59*(10), 1613–1619.

Maultzsch, S. (2005). *Analysis of frequency-dependent anisotropy in VSP data*. Ph.D. thesis, University of Edinburgh.

Maultzsch, S., Chapman, M., Liu, E., & Li, X. Y. (2003). Modelling frequency-dependent seismic anisotropy in fluid-saturated rock with aligned fractures: implication of fracture size estimation from anisotropic measurements. *Geophysical Prospecting*, *51*(5), 381–392.

Mavko, G., Mukerji, T., & Dvorkin, J. (2009). *The rock physics handbook: Tools for seismic analysis of porous media*. Cambridge university press.

Menke, W., & Levin, V. (2003). The cross-convolution method for interpreting sks splitting observations, with application to one and two-layer anisotropic earth models. *Geophysical Journal International*, *154*(2), 379–392.

Mikhailenko, B. G. (2000). Seismic modeling by the spectral-finite difference method. *Physics of the Earth and Planetary Interiors*, *119*(1), 133–147.

Moczo, P., Robertsson, J. O., & Eisner, L. (2007). The finite-difference time-domain method for modeling of seismic wave propagation. *Advances in Geophysics*, *48*, 421–516.

Montalbetti, J. F., & Kanasewich, E. R. (1970). Enhancement of teleseismic body phases with a polarization filter. *Geophysical Journal International*, *21*(2), 119–129.

Mufti, I. (1985). Seismic modeling in the implicit mode*. *Geophysical prospecting*, *33*(5), 619–656.

Müller, T. M., & Shapiro, S. A. (2001). Most probable seismic pulses in single realizations of two-and three-dimensional random media. *Geophysical Journal International*, *144*(1), 83–95.

Napier, J., & Malan, D. (1997). A viscoplastic discontinuum model of time-dependent fracture and seismicity effects in brittle rock. *International Journal of Rock Mechanics and Mining Sciences*, *34*(7), 1075–1089.

Narr, W., Schechter, D. W., & Thompson, L. B. (2006). *Naturally fractured reservoir characterization*. Richardson, TX: Society of Petroleum Engineers.

Nataf, H.-C., Nakanishi, I., & Anderson, D. L. (1984). Anisotropy and shear-velocity heterogeneities in the upper mantle. *Geophysical Research Letters*, *11*(2), 109–112.

Neerhoff, F., & Van der Hijden, J. (1984). Diffraction of elastic waves by a sub-surface crack (anti-plane motion). *Journal of Sound and Vibration*, *93*(4), 523–536.

Nelson, R. (2001). *Geologic Analysis of Naturally Fractured Reservoirs*. Elsevier Gulf.

Nichols, D., Muir, F., Schoenberg, M., et al. (1989). Elastic properties of rocks with multiple sets of fractures. In *Proceedings of the 63rd Annual International Meeting of the Society of Exploration Geophysicists, Extended Abstracts*, (pp. 471–474).

Nihei, K., Nakagawa, S., Myer, L., & Majer, E. (2002). Finite difference modeling of seismic wave interactions with discrete, finite length fractures. *cell*, *1*, 2.

Nihei, K. T., Yi, W., Myer, L. R., Cook, N. G., & Schoenberg, M. (1999). Fracture channel waves. *Journal of Geophysical Research: Solid Earth*, *104*(B3), 4769–4781.

Nishimura, T. (1996). Horizontal layered structure with heterogeneity beneath continents and island arcs from particle orbits of long-period p waves. *Geophysical Journal International*, *127*(3), 773–782.

Nishizawa, O., Pearson, C., & Albright, J. (1983). Properties of seismic wave scattering around water injection well at fenton hill hot dry rock geothermal site. *Geophysical Research Letters*, *10*(1), 101–104.

Nishizawa, O., Satoh, T., & Lei, X. (1998). Detection of shear wave in ultrasonic range by using a laser doppler vibrometer. *Review of scientific instruments*, *69*(6), 2572–2573.

Nishizawa, O., Satoh, T., Lei, X., & Kuwahara, Y. (1997). Laboratory studies of seismic

wave propagation in inhomogeneous media using a laser doppler vibrometer. *Bulletin of the Seismological Society of America*, *87*(4), 809–823.

Nur, A., & Simmons, G. (1969). Stress-induced velocity anisotropy in rock: An experimental study. *Journal of Geophysical Research*, *74*(27), 6667–6674.

O'Connell, R. J., & Budiansky, B. (1974). Seismic velocities in dry and saturated cracked solids. *Journal of Geophysical Research*, *79*(35), 5412–5426.

Pearce, F. D. (2003). *Seismic scattering attributes to estimate reservoir fracture density: a numerical modeling study*. Master's thesis, Massachusetts Institute of Technology.

Pérez, M. A., Gibson, R. L., & Toksöz, M. N. (1999). Detection of fracture orientation using azimuthal variation of p-wave avo responses. *Geophysics*, *64*(4), 1253–1265.

Petrovitch, C. L., Nolte, D. D., & Pyrak-Nolte, L. J. (2013). Scaling of fluid flow versus fracture stiffness. *Geophysical Research Letters*, *40*(10), 2076–2080.

Pointer, T., Liu, E., & Hudson, J. A. (1998). Numerical modelling of seismic waves scattered by hydrofractures: application of the indirect boundary element method. *Geophysical Journal International*, *135*(1), 289–303.

Press, W. H. (1989). *Numerical recipes in Pascal: the art of scientific computing*, vol. 1. Cambridge University Press.

Pyrak-Nolte, L., Cook, N., & Myer, L. (1987). Seismic visibility of fractures. In *The 28th US Symposium on Rock Mechanics (USRMS)*. American Rock Mechanics Association.

Pyrak-Nolte, L. J., Myer, L. R., & Cook, N. G. (1990). Transmission of seismic waves across single natural fractures. *Journal of Geophysical Research: Solid Earth*, *95*(B6), 8617–8638.

Pyrak-Nolte, L. J., & Roy, S. (2000). Monitoring fracture evolution with compressional-mode interface waves. *Geophysical research letters*, *27*(20), 3397–3400.

Qian, Z., Li, X., & Chapman, M. (2007). *Azimuthal variations of PP- and PS-wave attributes: A synthetic study*, (pp. 184–188). Society of Exploration Geophysicists.

Quan, Y., & Harris, J. M. (1997). Seismic attenuation tomography using the frequency shift method. *Geophysics*, *62*(3), 895–905.

Rathore, J., Fjaer, E., Holt, R., & Renlie, L. (1994). P-and s-wave anisotropy of a synthetic sandstone with controlled crack geometryl1. *Geophysical Prospecting*, *43*(6), 711–728.

Rathore, J., Fjaer, E., Holt, R., & Renlie, L. (1995). Pand swave anisotropy of a synthetic sandstone with controlled crack geometryl1. *Geophysical Prospecting*, *43*(6), 711–728.

Restivo, A., & Helffrich, G. (1999). Teleseismic shear wave splitting measurements in noisyenvironments. *Geophysical Journal International*, *137*(3), 821–830.

Rial, J. A., Elkibbi, M., & Yang, M. (2005). Shear-wave splitting as a tool for the characterization of geothermal fractured reservoirs: lessons learned. *Geothermics*, *34*(3), 365–385.

Rüger, A. (1997). P-wave reflection coefficients for transversely isotropic models with vertical and horizontal axis of symmetry. *Geophysics*, *62*(3), 713–722.

Ryall, A., & Savage, W. U. (1974). S-wave splitting: Key to earthquake prediction? *Bulletin of the Seismological Society of America*, *64*(6), 1943–1951.

Saenger, E. H., & Shapiro, S. A. (2002). Effective velocities in fractured media: A

numerical study using the rotated staggered finite-difference grid. *Geophysical Prospecting*, *50*(2), 183–194.

Saito, T., Sato, H., & Ohtake, M. (2002). Envelope broadening of spherically outgoing waves in three-dimensional random media having power law spectra. *Journal of Geophysical Research: Solid Earth*, *107*(B5).

Sato, H. (1984). Attenuation and envelope formation of threecomponent seismograms of small local earthquakes in randomly inhomogeneous lithosphere. *Journal of Geophysical Research: Solid Earth*, *89*(B2), 1221–1241.

Sato, H. (1989). Broadening of seismogram envelopes in the randomly inhomogeneous lithosphere based on the parabolic approximation: Southeastern honshu, japan. *J. geophys. Res*, *94*(B12), 17735–7747.

Sato, H., Fehler, M. C., & Maeda, T. (2012). *Seismic wave propagation and scattering in the heterogeneous earth*, vol. 484. Springer.

Savage, M. (1999). Seismic anisotropy and mantle deformation: what have we learned from shear wave splitting? *Reviews of Geophysics*, *37*(1), 65–106.

Savage, M., Shih, X., Meyer, R., & Aster, R. (1989). Shear-wave anisotropy of active tectonic regions via automated s-wave polarization analysis. *Tectonophysics*, *165*(1), 279–292.

Sayers, C., & Kachanov, M. (1991). A simple technique for finding effective elastic constants of cracked solids for arbitrary crack orientation statistics. *International Journal of Solids and Structures*, *27*(6), 671–680.

Sayers, C. M. (1999). Stress-dependent seismic anisotropy of shales. *Geophysics*, *64*(1), 93–98.

Sayers, C. M. (2010). *Geophysics Under Stress*. Society of Exploration Geophysicists and European Association of Geoscientists and Engineers.

Sayers, C. M., & Han, D.-H. (2002). The effect of pore fluid on the stress-dependent elastic wave velocities in sandstones. In *2002 SEG annual meeting*. Society of Exploration Geophysicists.

Sayers, C. M., & Kachanov, M. (1995). Microcrack-induced elastic wave anisotropy of brittle rocks. *Journal of Geophysical Research*, *100*(B3), 4149–4156.

Sayers, C. M., & Rickett, J. E. (1997). Azimuthal variation in avo response for fractured gas sands. *Geophysical Prospecting*, *45*(1), 165–182.

Schlue, J. (1979). Finite element matrices for seismic surface waves in three-dimensional structures. *Bulletin of the Seismological Society of America*, *69*(5), 1425–1438.

Schoenberg, M. (1980). Elastic wave behavior across linear slip interfaces. *Journal of the Acoustical Society of America*, *68*(5), 1516–1521.

Schoenberg, M., & Douma, J. (1988). Elastic wave propagation in media with parallel fractures and aligned cracks. *Geophysical Prospecting*, *36*(6), 571–590.

Schoenberg, M., & Muir, F. (1989). A calculus for finely layered anisotropic media. *Geophysics*, *54*(5), 581–589.

Schoenberg, M., & Sayers, C. M. (1995). Seismic anisotropy of fractured rock. *Geophysics*, *60*(1), 204–211.

Shang, T., & Gao, L. (1988). Transportation theory of multiple scattering and its application to seismic coda waves of impulsive source. *Scientia Sinica (series B)*, *31*, 1503–1514.

Shearer, P. M. (2009). *Introduction to seismology*. Cambridge University Press.

Shearer, P. M., & Earle, P. S. (2004). The global short-period wavefield modelled with a monte carlo seismic phonon method. *Geophysical Journal International*, *158*(3), 1103–1117.

Shen, F., & Toksöz, M. N. (2000). Scattering characteristics in heterogeneously fractured reservoirs from waveform estimation. *Geophysical Journal International*, *140*(2), 251–266.

Shih, X. R., Meyer, R. P., & Schneider, J. F. (1989). An automated, analytical method to determine shear-wave splitting. *Tectonophysics*, *165*(1-4), 271–278.

Šílenỳ, J., & Plomerová, J. (1996). Inversion of shear-wave splitting parameters to retrieve three-dimensional orientation of anisotropy in continental lithosphere. *Physics of the earth and planetary interiors*, *95*(3), 277–292.

Silver, P. G. (1996). Seismic anisotropy beneath the continents: probing the depths of geology. *Annual review of earth and planetary sciences*, *24*, 385–432.

Silver, P. G., & Chan, W. W. (1988). Implications for continental structure and evolution from seismic anisotropy.

Silver, P. G., & Chan, W. W. (1991). Shear wave splitting and subcontinental mantle deformation. *Journal of Geophysical Research: Solid Earth*, *96*(B10), 16429–16454.

Snieder, R. (2006). The theory of coda wave interferometry. *Pure and Applied Geophysics*, *163*(2-3), 455–473.

Tannehill, J., Anderson, D., & Pletcher, R. (1997). *Computational fluid mechanics and heat transfer*. Taylor & Francis.

Teanby, N., Kendall, J.-M., Jones, R., & Barkved, O. (2004b). Stress-induced temporal variations in seismic anisotropy observed in microseismic data. *Geophysical Journal International*, *156*(3), 459–466.

Teanby, N., Kendall, J.-M., & Van der Baan, M. (2004a). Automation of shear-wave splitting measurements using cluster analysis. *Bulletin of the Seismological Society of America*, *94*(2), 453–463.

Thomsen, L. (1986). Weak elastic anisotropy. *Geophysics*, *51*(10), 1954–1966.

Thomsen, L. (2002). *Understanding seismic anisotropy in exploration and exploitation*, vol. 5. Society of Exploration Geophysicist.

Tsvankin, I. (1997). Anisotropic parameters and p-wave velocity for orthorhombic media. *Geophysics*, *62*(4), 1292–1309.

Tsvankin, I., & Grechka, V. (2011). *Seismology of azimuthally anisotropic media and seismic fracture characterization*. Society of Exploration Geophysicists.

Valcke, S. L. A., Casey, M., Lloyd, G. E., Kendall, J. M., & Fisher, Q. J. (2006). Lattice preferred orientation and seismic anisotropy in sedimentary rocks. *Geophysical Journal International*, *166*(2), 652–666.

Van Der Hijden, J., & Neerhoff, F. (1984). Scattering of elastic waves by a plane crack of finite width. *Journal of Applied Mechanics*, *51*(3), 646–651.

Van der Pluijm, B. A., & Marshak, S. (2005). Earth structure. *Physics of the Earth and Planetary Interiors*, *149*, 133–153.

Vecsey, L., Plomerová, J., Kozlovskaya, E., & Babuška, V. (2007). Shear wave splitting as a diagnostic of variable anisotropic structure of the upper mantle beneath central fennoscandia. *Tectonophysics*, *438*(1), 57–77.

Verdon, J., Kendall, J.-M., & Wüstefeld, A. (2009). Imaging fractures and sedimentary fabrics using shear wave splitting measurements made on passive seismic data. *Geophysical Journal International*, *179*(2), 1245–1254.

Verdon, J. P., Angus, D. A., Kendall, J. M., & Hall, S. A. (2008). The effect of microstructure and nonlinear stress on anisotropic seismic velocities. *Geophysics*, *73*(4), D41–D51.

Verdon, J. P., Kendall, J., et al. (2011a). Detection of multiple fracture sets using observations of shear-wave splitting in microseismic data. *Geophysical Prospecting*, *59*(4), 593–608.

Verdon, J. P., Kendall, J. M., White, D. J., & Angus, D. A. (2011b). Linking microseismic event observations with geomechanical models to minimise the risks of storing co2 in geological formations. *Earth and Planetary Science Letters*, *305*(1-2), 143–152.

Verdon, J. P., & Wüstefeld, A. (2013). (zn/zt) during hydraulic fracture stimulation using s-wave splitting data. *Geophysical Prospecting*, *61*(s1), 461–475.

Vernik, L. (1993). Microcrack-induced versus intrinsic elastic anisotropy in mature hc-source shales. *Geophysics*, *58*(11), 1703–1706.

Vidale, J. E. (1986). Complex polarization analysis of particle motion. *Bulletin of the Seismological society of America*, *76*(5), 1393–1405.

Vinnik, L., Kind, R., Kosarev, G., & Makeyeva, L. (1989). Azimuthal anisotropy in the lithosphere from observations of long-period s-waves. *Geophysical Journal International*, *99*(3), 549–559.

Vinogradov, S., Troitskiy, P., & Solovieva, M. (1995). Scattering of longitudinal and shear waves by a single crack. *Physics of the Solid Earth*, *31*, 437–440.

Virieux, J. (1986). P-sv wave propagation in heterogeneous media: Velocity-stress finite-difference method. *Geophysics*, *51*(4), 889–901.

Vlastos, S., Liu, E., Main, I., & Li, X. (2003). Numerical simulation of wave propagation in media with discrete distributions of fractures: effects of fracture sizes and spatial distributions. *Geophysical Journal International*, *152*(3), 649–668.

Wang, M., Xu, S., et al. (2015). Time dispersion prediction and correction for wave propagation. In *2015 SEG Annual Meeting*. Society of Exploration Geophysicists.

White, J. E. (1983). *Underground sound: Application of seismic waves*, vol. 253. Elsevier Amsterdam.

Willis, M., Burns, D., Rao, R., Minsley, B., & Zhang, Y. (2004a). Characterizing seismic scattering from discrete fracture systems. In *SEG Research Workshop on Fractured Reservoirs*.

Willis, M., Pearce, F., Burns, D., Byun, J., & Minsley, B. (2004b). Reservoir fracture orientation and density from reflected and scattered seismic energy. In *66th EAGE Conference & Exhibition*.

Willis, M. E., Burns, D. R., Rao, R., Minsley, B., Toksöz, M. N., & Vetri, L. (2006). Spatial orientation and distribution of reservoir fractures from scattered seismic energy. *Geophysics*, *71*(5), O43–O51.

Willis, M. E., Burns, D. R., Rao, R. V., & Minsley, B. J. (2003). Characterization of scattered waves from fractures by estimating the transfer function between reflected

events above and below each interval. Report, Massachusetts Institute of Technology. Earth Resources Laboratory.

Winterstein, D. F. (1990). Velocity anisotropy terminology for geophysicists. *Geophysics*, *55*(8), 1070–1088.

Wolfe, C. J., & Silver, P. G. (1998). Seismic anisotropy of oceanic upper mantle: Shear wave splitting methodologies and observations. *Journal of Geophysical Research: Solid Earth*, *103*(B1), 749–771.

Wookey, J. (2012). Direct probabilistic inversion of shear wave data for seismic anisotropy. *Geophysical Journal International*, *189*(2), 1025–1037.

Worthington, M. (2008). Interpreting seismic anisotropy in fractured reservoirs. *First Break*, *26*(7).

Worthington, M., & Hudson, J. (2000). Fault properties from seismic q. *Geophysical Journal International*, *143*(3), 937–944.

Worthington, M., & Lubbe, R. (2007). The scaling of fracture compliance. *Geological Society, London, Special Publications*, *270*(1), 73–82.

Wu, R., & Aki, K. (1985). Scattering characteristics of elastic waves by an elastic heterogeneity. *Geophysics*, *50*(4), 582–595.

Wu, R. S., Xu, Z., & Li, X. P. (1994). Heterogeneity spectrum and scale-anisotropy in the upper crust revealed by the german continental deep-drilling (ktb) holes. *Geophysical Research Letters*, *21*(10), 911–914.

Wuestefeld, A., Al-Harrasi, O., Verdon, J. P., Wookey, J., & Kendall, J. M. (2010). A strategy for automated analysis of passive microseismic data to image seismic anisotropy and fracture characteristics. *Geophysical Prospecting*, *58*(5), 755–773.

Wuestefeld, A., Verdon, J. P., Kendall, J.-M., Rutledge, J., Clarke, H., & Wookey, J. (2011). Inferring rock fracture evolution during reservoir stimulation from seismic anisotropy. *Geophysics*, *76*(6), WC157–WC166.

Wüstefeld, A., & Bokelmann, G. (2007). Null detection in shear-wave splitting measurements. *Bulletin of the Seismological Society of America*, *97*(4), 1204–1211.

Wüstefeld, A., Bokelmann, G., Zaroli, C., & Barruol, G. (2008). Splitlab: A shear-wave splitting environment in matlab. *Computers & Geosciences*, *34*(5), 515–528.

Xian, C., Nolte, D. D., & Pyrak-Nolte, L. J. (2001). Compressional waves guided between parallel fractures. *International Journal of Rock Mechanics and Mining Sciences*, *38*(6), 765–776.

Xie, X.-B., et al. (2013). Seismic wave scattering in 3d random media: A finite-difference simulation and slowness domain analysis. In *2013 SEG Annual Meeting*. Society of Exploration Geophysicists.

Yang, M., Elkibbi, M., & Rial, J. A. (2005). An inversion scheme to model subsurface fracture systems using shear wave splitting polarization and delay time observations simultaneously. *Geophysical Journal International*, *160*(3), 939–947.

Yi, W., Nakagawa, S., Nihei, K. T., Rector, J. W., Myer, L., & Cook, N. G. (1998). Numerical investigation of fracture channel waves. In *Expanded Abstracts of the 68th SEG Annual Meeting*.

Yousef, B., Angus, D., Hildyard, M., Verdon, J., & Perry, M. (2013). Full waveform model validation of microseismic shear-wave splitting fracture parameter inversion. In *Second EAGE Workshop on Naturally Fractured Reservoirs*.

Yousef, B. M., & Angus, D. A. (2016). When do fractured media become seismically anisotropic? some implications on quantifying fracture properties. *Earth and Planetary Science Letters*, *444*, 150–159.

Yousef, B. M., Angus, D. A., Hildyard, M. W., Verdon, J. P., & Perry, M. (2014). Measuring shear-wave splitting using seismic anisotropy. In *76th EAGE Conference and Exhibition 2014*.

Zatsepin, S. V., & Crampin, S. (1997). Modelling the compliance of crustal rock-i. response of shear-wave splitting to differential stress. *Geophysical Journal International*, *129*(3), 477–494.

Zhang, Y., Chi, S., Willis, M. E., Burns, D., & Nafi, T. M. (2005). Comparison of discrete fracture and effective media representation of fractures on azimuthal avo. *75th Annual Meeting of the Society of Exploration Geophysicists (SEG 2006)*.

Zhang, Y., Chi, S., Willis, M. E., Toksoz, M. N., & Burns, D. R. (2006). Orientation estimation for multiple large fractures by scattering energy. Report, Massachusetts Institute of Technology. Earth Resources Laboratory.

Appendix A

Software and programmes in the thesis

1. Programmes

The Programmes used in this PhD are listed below:

- **WAVE**

  The WAVE is a 3D FD programme developed by Hildyard et al. (1995) which is capable of accurately modelling diffraction, refraction, reflection and transmission of stress waves.

- **WVPLOT**

  The WVPLOT is a post-processing package developed by Hildyard et al. (1995) to plot and or print the WAVE programme's outputs such as snapshot and time series. I used this Programme only for inspection of the results on the screen.

- **SHEBA**

  SHEBA (SHEar-wave Birefringence Analysis) is an algorithm developed by Teanby et al. (2004a) to conduct the analysis of shear-wave splitting.

- **INSAFF**

  The INSAFF is an inversion programme by Verdon et al. (2009) to invert for fractured medium anisotropy parameters such as fracture strike, density, Thomsen's parameters and compliance ratio. The programme is based on effective medium theory.

2. Software

The software used in this PhD are listed below:

- **DosBox**

  DosBox is a open-source DOS-emulator sofware that emulates graphics and sound cards. I used DosBox to visualise the result from WAVE by implementing the GUI WVPLOT.

- **CorelDRAW**

  CorelDRAW is commercial software for general graphic design. I use it for displaying some figures in Chapter 2.

- **Matlab**

  Matlab is a commercial software package that has broad applications in numerical computing, signal processing, 2D/3D visualization, etc. I use it for the picking of direct P- and S-waves for the SWS analysis. Furthermore, it is used for the scattering analysis in chapter 6 and general result visualisation.

Appendix B

Effective elastic constants of fractured media- Hudson's model

The Hudson (1980, 1981) models predict the effective properties of embedded fractures with small, thin and penny-shaped ellipsoidal cracks or inclusion in an isotropic background medium. His model is based on a scattering theory analysis of the mean wavefield. The effective stiffness matrix is expressed by Mavko et al. (2009),

$$\mathbf{C}_{ij}^{eff} = \mathbf{C}_{ij}^{0} + \mathbf{C}_{ij}^{1} + \mathbf{C}_{ij}^{2}, \tag{B.1}$$

where $\mathbf{C}_{ij}^{0}$ $(i, j = 1 - 6$ using Voigt notation) is the isotropic background stiffness tensor. $\mathbf{C}_{ij}^{1}$ and $\mathbf{C}_{ij}^{2}$ are the first- and second-order corrections, respectively. ϵ is the crack density defined in Chapter 3. For a single fracture set with normal oriented along the 3-axis, the $\mathbf{C}_{ij}^{l}$ components are expressed as,

$$\mathbf{C}_{11}^{1} = -\frac{\lambda^2}{\mu}\epsilon\mathbf{U}_3, \tag{B.2a}$$

$$\mathbf{C}^1_{13} = -\frac{\lambda(\lambda+2\mu)}{\mu}\epsilon\mathbf{U}_3, \tag{B.2b}$$

$$\mathbf{C}^1_{33} = -\frac{(\lambda+2\mu)^2}{\mu}\epsilon\mathbf{U}_3, \tag{B.2c}$$

$$\mathbf{C}^1_{44} = -\lambda\epsilon\mathbf{U}_1, \tag{B.2d}$$

$$\mathbf{C}^1_{66} = 0, \tag{B.2e}$$

$$\mathbf{C}^2_{11} = \frac{b}{15}\frac{\lambda^2}{(\lambda+2\mu)}(\epsilon\mathbf{U}_3)^2, \tag{B.2f}$$

$$\mathbf{C}^2_{13} = \frac{b}{15}\lambda(\epsilon\mathbf{U}_3)^2, \tag{B.2g}$$

$$\mathbf{C}^2_{33} = \frac{b}{15}(\lambda+2\mu)(\epsilon\mathbf{U}_3)^2, \tag{B.2h}$$

$$\mathbf{C}^2_{44} = \frac{2}{15}\frac{\mu(3\lambda+8\mu)}{\lambda+2\mu}(\epsilon\mathbf{U}_1)^2, \tag{B.2i}$$

$$\mathbf{C}^2_{66} = 0, \tag{B.2j}$$

where

$b = 15\frac{\lambda^2}{\mu^2} + 28\frac{\lambda}{\mu} + 28,$

$\epsilon = \frac{N}{V}a^3.$

The isotropic background moduli are λ and μ. and a is crack radius. The symmetry conditions can be applied for corrections $\mathbf{C}^1_{ij}$ and $\mathbf{C}^2_{ij}$ like for elastic tensor $\boldsymbol{C}$ of an elastic media (see Equation 3.21).

The terms $\mathbf{U}_1$ and $\mathbf{U}_3$ depend on the crack conditions. For dry cracks

$$\mathbf{U}_1 = \frac{16(\lambda+2\mu)}{3(3\lambda+4\mu)} \qquad \mathbf{U}_3 = \frac{4(\lambda+2\mu)}{3(\lambda+\mu)} \tag{B.3}$$

For cracks filled with weak materials whose bulk and shear moduli are K' and μ',

$$\mathbf{U}_1 = \frac{16(\lambda + 2\mu)}{3(3\lambda + 4\mu)(1 + M)} \qquad \mathbf{U}_3 = \frac{4(\lambda + 2\mu)}{3(\lambda + \mu)(1 + \mathcal{K})} \tag{B.4}$$

where

$$M = \frac{4\mu'}{\pi\alpha_a\mu}\frac{(\lambda + 2\mu)}{(3\lambda + 4\mu)} \qquad \mathcal{K} = \frac{(K' + \frac{4}{3}\mu')(\lambda + \mu)}{\pi\alpha_a\mu(\lambda + \mu)} \tag{B.5}$$

The criteria for an inclusion to be weak depend on its shape or aspect ratio α_a as well as on the relative moduli of the inclusion and matrix material. Dry cracks can be modelled by setting the inclusion material moduli to zero. Fluid-saturated cracks can be modelled by setting the inclusion shear modulus to zero.

Appendix C

Effective elastic constants of fractured media- Liu's model

Based on LS theory, which there is liner relation between displacement discontinuity and the stress traction in DFM, Liu et al. (2000) classify that the natural fractures into three type models as explained in 2.2.1. when the fracture normal is aligned the unit norm $\mathbf{n} = (1,0,0)$, the effective compliance matrix is

$$\mathbf{C}_{eff} = \begin{bmatrix} C_{11} & C_{12} & \frac{C_{12}}{1+E_N} & 0 & 0 & 0 \\ C_{12} & C_{11} & \frac{C_{12}}{1+E_N} & 0 & 0 & 0 \\ \frac{C_{12}}{1+E_N} & \frac{C_{12}}{1+E_N} & \frac{C_{11}}{1+E_N} & 0 & 0 & 0 \\ 0 & 0 & 0 & \frac{C_{44}}{1+E_T} & 0 & 0 \\ 0 & 0 & 0 & 0 & \frac{C_{44}}{1+E_T} & 0 \\ 0 & 0 & 0 & 0 & 0 & C_{44} \end{bmatrix} = \begin{bmatrix} \lambda+2\mu & \lambda & \frac{\lambda}{1+E_N} & 0 & 0 & 0 \\ \lambda & \lambda+2\mu & \frac{\lambda}{1+E_N} & 0 & 0 & 0 \\ \frac{\lambda}{1+E_N} & \frac{\lambda}{1+E_N} & \frac{\lambda+2\mu}{1+E_N} & 0 & 0 & 0 \\ 0 & 0 & 0 & \frac{\mu}{1+E_T} & 0 & 0 \\ 0 & 0 & 0 & 0 & \frac{\mu}{1+E_T} & 0 \\ 0 & 0 & 0 & 0 & 0 & \mu \end{bmatrix} \quad \text{(C.1)}$$

where $E_N = (\lambda + 2\mu)Z_N$ and $E_T = \mu Z_T$ are related to the fracture model. For model (a),

$$E_N = \left(\frac{N^c a_c^3}{H}\right)\left(\frac{\lambda+2\mu}{\mu}\right) U_3 \left[1 + \pi U_3 (N^c a_c^2)^{3/2}(1 - \frac{\mu}{\lambda+2\mu})\right], \tag{C.2a}$$

$$E_T = \left(\frac{N^c a_c^3}{H}\right) U_1 \left[1 + \frac{\pi}{4} U_1 (N^c a_c^2)^{3/2}(3 - \frac{2\mu}{\lambda+2\mu})\right], \tag{C.2b}$$

and for (b) model,

$$E_N = \frac{(\lambda+2\mu)^2}{4\mu(\lambda+\mu)(N^w H b)}\left(1 + 2\sqrt{N^w b^2}\right)^{-1}, \tag{C.3a}$$

$$E_T = \frac{(3\lambda+4\mu)}{8\mu(\lambda+\mu)(N^w H b)}\left(1 + 2\sqrt{N^w b^2}\right)^{-1}, \tag{C.3b}$$

where a_c is crack radius, N^c is the number density of cracks on the fault surface and H is the average fault spacing. Note that Equation C.2a is valid only for small ($N^c a^2$) and also N^w is the number density of welded regions and Equation C.3a is valid for small ($N^w b^2$) as well. The terms U_1 and U_3 are related to the internal crack conditions (Hudson & Liu, 1999; Liu et al., 2000):

for dry crack, i.e., a crack filled with inviscid gas with high compressibility,

$$U_1 = \frac{16(\lambda+2\mu)}{3(3\lambda+4\mu)} = \frac{16}{3}\frac{1-\nu}{2-\nu} \qquad U_3 = \frac{4(\lambda+2\mu)}{3(\lambda+\mu)} = \frac{8}{3}(1-\nu), \tag{C.4}$$

$$\frac{Z_N}{Z_T} = \frac{3\lambda+4\mu}{4(\lambda+\mu)} = 1 - \frac{\nu}{2}, \tag{C.5}$$

where $\nu = \lambda/2(\lambda+\mu)$ is the Poisson's ratio for the isotropic background (Liu et al., 2000). The compliance ration $Z_N/Z_T \approx 1$ when ν is small in the range ($0.1 \leqslant \nu \leqslant 0.25$).

for infinity thin liquid infill cracks (filled with inviscid liquid of low compressibility),

$$U_1 = \frac{16(\lambda + 2\mu)}{3(3\lambda + 4\mu)} \qquad U_3 = 0, \tag{C.6}$$

Therefore, $Z_N = 0$ and $Z_N/Z_T = 0$.

Appendix D

Inversion results for single and double fracture set models

Size (m)	ϵ	$K_N(Pa/m)$	#	ϵ	$\alpha(^\circ)$	$\Delta\epsilon(\%)$	$\Delta\alpha(^\circ)$
6	0.1	6×10^{11}	17	0.023	86.92	77.00	3.08
6	0.04	6×10^{10}	12	0.012	75.35	70.00	14.65
6	0.08	6×10^{10}	16	0.02	98.00	75.00	8.00
10	0.1	3×10^{10}	13	0.026	94.72	74.00	4.72
10	0.04	3×10^{10}	6	0.013	64.70	67.50	25.29
10	0.08	3×10^{10}	14	0.019	81.12	76.25	8.89
20	0.1	3×10^{9}	10	0.055	52.69	45.00	37.31
20	0.02	3×10^{9}	7	0.059	168.80	195.00	78.80
20	0.08	3×10^{9}	6	0.039	121.45	51.25	31.45
50	0.04	3×10^{10}	13	0.025	117.86	37.50	27.86
Average						76.85	24.00
Standard deviation						41.62	21.536

Table D.1: Fracture inversion results for the single fracture model having Z_N/Z_T = 0.33 and a minimum of 5 SWS results with $\mathbb{Q} \geqslant 0.75$. The average and standard deviation of the error was shown at the bottom of the table.

Size (m)	ϵ	$K_N(Pa/m)$	#	ϵ	$\alpha(^\circ)$	$\Delta\epsilon(\%)$	$\Delta\alpha(^\circ)$
6	0.1	5×10^{10}	20	0.017	88.04	83.00	1.96
6	0.04	5×10^{10}	8	0.01	85.30	75.00	4.70
10	0.1	5×10^{10}	8	0.015	95.02	85.00	5.02
10	0.08	5×10^{10}	11	0.011	93.14	86.25	3.14
20	0.1	5×10^{9}	12	0.039	126.03	61.00	36.03
20	0.08	5×10^{9}	5	0.029	86.06	63.75	3.94
50	0.1	5×10^{9}	6	0.024	91.88	76.00	1.88
50	0.04	5×10^{9}	5	0.039	17.15	2.50	72.85
Average						66.56	16.19
Standard deviation						25.74	23.95

Table D.2: Fracture inversion results for the single fracture model having Z_N/Z_T = 0.6 and a minimum of 5 SWS results with $\mathbb{Q} \geqslant 0.75$. The average and standard deviation of the error was shown at the bottom of the table.

Size (m)	ϵ	$K_N(Pa/m)$	#	ϵ	$\alpha(^\circ)$	$\Delta\epsilon(\%)$	$\Delta\alpha(^\circ)$
6	0.1	1×10^{10}	23	0.038	98.24	62.00	9.12
6	0.1	1×10^{11}	12	0.008	90.91	92.00	0.51
6	0.02	1×10^{10}	10	0.012	88.49	40.00	1.84
6	0.04	1×10^{10}	15	0.016	76.78	60.00	14.74
6	0.08	1×10^{10}	17	0.031	80.69	61.25	10.32
6	0.08	1×10^{11}	8	0.007	85.37	90.00	15.68
10	0.1	3×10^{10}	13	0.016	104.04	79.00	33.54
10	0.08	3×10^{10}	8	0.013	81.04	83.75	9.79
20	0.1	1×10^{9}	9	0.053	52.00	65.00	15.24
20	0.1	1×10^{10}	9	0.023	100.57	78.00	0.22
20	0.04	1×10^{9}	8	0.025	83.67	37.50	7.03
20	0.04	1×10^{10}	5	0.016	101.67	60.00	11.23
20	0.08	1×10^{9}	7	0.023	78.74	77.00	3.16
20	0.08	1×10^{10}	6	0.014	86.00	82.05	4.40
50	0.1	3×10^{9}	7	0.023	78.74	77.00	3.16
50	0.1	3×10^{10}	6	0.024	66.08	76.00	27.03
50	0.08	3×10^{9}	7	0.029	82.06	63.75	8.90
Average						67.79	11.40
Standard deviation						16.36	8.75

Table D.3: Fracture inversion results for the single fracture model having Z_N/Z_T = 1.0 and a minimum of 5 SWS results with $\mathbb{Q} \geqslant 0.75$. The average and standard deviation of the error was shown at the bottom of the table.

Size (m)	ϵ	$K_N(Pa/m)$	#	$\epsilon 1$	$\alpha 1(^\circ)$	$\epsilon 2$	$\alpha 2(^\circ)$	$\Delta\epsilon 1(\%)$	$\Delta\alpha 1(^\circ)$	$\Delta\epsilon 2(\%)$	$\Delta\alpha 2(^\circ)$
6	0.1	6×10^{10}	11	0.01	-27.67	0.02	74.63	0.00	27.67	9.00	15.37
6	0.04	6×10^{10}	9	0.01	43.78	0.01	106.86	16.00	43.78	18.50	16.86
6	0.08	6×10^{11}	10	0.00	-14.59	0.02	88.04	8.00	14.59	17.00	1.96
10	0.04	3×10^{10}	5	0.128	-6.98	0.08	46.24	316.00	6.98	150.00	62.69
10	0.08	3×10^{10}	11	0.123	9.75	0.034	97.98	145.75	9.75	34.50	7.98
20	0.1	3×10^{9}	7	0.0248	-23.06	0.033	123.27	14.00	23.06	23.00	33.27
20	0.1	3×10^{10}	7	0.027	33.47	0.015	103.44	17.00	33.47	5.00	13.44
20	0.04	3×10^{9}	6	0.051	-13.34	0.033	77.40	123.50	13.34	78.50	12.61
20	0.08	3×10^{9}	14	0.051	-43.14	0.005	124.21	55.75	43.14	1.75	34.21
50	0.02	3×10^{9}	9	0.058	7.14	0.037	62.20	288.00	7.14	183.00	27.80
50	0.04	3×10^{9}	10	0.037	44.96	0.025	63.56	88.50	44.96	58.50	26.44
50	0.04	3×10^{10}	8	0.063	143.68	0.03	34.32	57.50	20.18	22.50	61.87
50	0.08	3×10^{9}	9	0.029	-10.86	0.040	127.16	57.50	20.18	22.50	61.87
Average								88.38	23.41	60.21	22.69
Standard deviation								101.62	13.73	61.94	11.97

Table D.4: Fracture inversion results for the double fracture model having Z_N/Z_T = 0.33 and a minimum of 5 SWS results with $\mathbb{Q} \geqslant 0.75$. The average and standard deviation of the error was shown at the bottom of the table.

Size (m)	ϵ	$K_N(Pa/m)$	#	$\epsilon 1$	$\alpha 1(^\circ)$	$\epsilon 2$	$\alpha 2(^\circ)$	$\Delta\epsilon 1(\%)$	$\Delta\alpha 1(^\circ)$	$\Delta\epsilon 2(\%)$	$\Delta\alpha 2(^\circ)$
6	0.1	5×10^{10}	10	0.017	33.99	0.012	111.67	7.00	33.99	2.00	21.67
6	0.04	5×10^{10}	9	0.002	-8.57	0.01	82.09	1.00	8.56	21.00	7.91
6	0.08	5×10^{10}	8	0.010	-21.63	0.014	90.66	4.50	21.63	9.50	0.66
20	0.1	5×10^{10}	11	0.049	-11.94	0.04	49.91	39.00	11.94	30.00	40.10
20	0.1	5×10^{9}	5	0.115	-15.04	0.016	72.15	105.00	15.04	6.00	17.85
20	0.04	5×10^{9}	5	0.094	-1.03	0.050	70.86	231.00	1.03	121.00	19.14
20	0.08	5×10^{9}	6	0.075	-10.49	0.032	86.20	85.75	10.49	32.00	3.80
Average								67.61	14.68	31.64	15.87
Standard deviation								76.84	9.78	38.04	12.40

Table D.5: Fracture inversion results for the double fracture model having Z_N/Z_T = 0.6 and a minimum of 5 SWS results with $\mathbb{Q} \geqslant 0.75$. The average and standard deviation of the error was shown at the bottom of the table.

Size (m)	ϵ	$K_N(Pa/m)$	#	$\epsilon 1$	$\alpha 1(^\circ)$	$\epsilon 2$	$\alpha 2(^\circ)$	$\Delta\epsilon 1(\%)$	$\Delta\alpha 1(^\circ)$	$\Delta\epsilon 2(\%)$	$\Delta\alpha 2(^\circ)$
6	0.1	1×10^{10}	13	0.050	18.28	0.046	129.36	50.00	18.28	54.00	39.36
6	0.04	1×10^{10}	10	0.021	-43.48	0.014	67.48	47.50	43.48	65.00	22.52
6	0.08	1×10^{10}	12	0.060	-2.35	0.031	87.70	25.00	2.35	61.25	2.30
Average								40.83	21.37	60.08	21.39
Standard deviation								11.24	16.93	4.56	15.15

Table D.6: Fracture inversion results for the double fracture model having Z_N/Z_T = 1.0 and a minimum of 5 SWS results with $\mathbb{Q} \geqslant 0.75$. The average and standard deviation of the error was shown at the bottom of the table.

Appendix E

Excess compliance computations from different means

In Chapter 5, I compute the excess compliance based on the summed average fracture spacing distribution using 6 different means: arithmetic, geometric, harmonic, quadratic, cubic and weighted. The definition of each mean is formulated as following

(1) **Weighted**:

$$\Delta S = \frac{\sum_{i=1}^{n} w_i \Delta S_i}{\sum_{i=1}^{n} w_i}, \tag{E.1}$$

where w_i is the fractional distribution of the i-th fracture spacing (i.e., $w_1 = 0.04$) and ΔS_i is the corresponding compliance.

(2) **Arithmetic**:

$$\Delta S = \frac{1}{n} \sum_{i=1}^{n} \Delta S_i, \tag{E.2}$$

(3) **Geometric**:

$$\Delta S = \sqrt[n]{\Delta S_1 \, \Delta S_1 \ldots \Delta S_n}, \tag{E.3}$$

(4) **Quadratic**:

$$\Delta S = \sqrt[n]{\frac{1}{n} \sum_{i=1}^{n} {\Delta S_i}^2}, \tag{E.4}$$

(5) **Cubic**:

$$\Delta S = \sqrt[n]{\frac{1}{n} \sum_{i=1}^{n} {\Delta S_i}^3}, \tag{E.5}$$

(6) **Harmonic**:

$$\Delta S = \frac{n}{\sum_{i=1}^{n} \Delta C_i}, \tag{E.6}$$

where $\Delta C_i = \dfrac{1}{\Delta S_i}$.